

UNIVERSITÉ MOULAY ISMAÏL
ÉCOLE NATIONALE SUPÉRIEURE D'ARTS ET MÉTIERS -
MEKNÈS

CENTRE D'ÉTUDES DOCTORALES
RECHERCHE ET INNOVATION POUR LES SCIENCES DE
L'INGÉNIEUR

THÈSE

Présentée pour l'obtention du

Diplôme de Doctorat

Discipline : **Science de l'ingénieur**

Spécialité : **Mathématiques Appliquées**

Par : **Khadija TALALI**

Titre :

MODÉLISATION MATHÉMATIQUE ET NUMÉRIQUE DE MODÈLES
D'INTRUSION MARINE DANS LES NAPPES CÔTIÈRES

Date prévue pour la soutenance : le **17 Décembre 2021 à 10h, à la salle de**
Conférences, Génie Mécanique, devant le jury composé des Professeurs :

| | | |
|------------------|---------------------------|------------------------|
| Mme. Z. MGHAZLI | PES, FS/UIT/KENITRA | Présidente/Rapporteure |
| Mme. C. ROSIER | PES, ULCO/CALAIS (France) | Rapporteure |
| M. A. TAAKILI | PH, ENSAM/UMI/MEKNÈS | Rapporteur |
| M. M. AFIF | PES, FS/UCA/MARRAKECH | Examineur |
| M. A. AHARMOUCH | PES, FS/USMB/FÈS | Examineur |
| M. A. EZZIANI | PH, FSJES/UH2/CASABLANCA | Examineur |
| M. M. EL OSSMANI | PES, ENSAM/UMI/MEKNÈS | Directeur de thèse |
| M. B. AMAZIANE | MC-HDR, UPPA/Pau (France) | Co-directeur de thèse |

Remerciements

Le travail présenté dans ce mémoire rentre dans le cadre d'une co-direction de thèse entre l'Université Moulay Ismail, École Nationale Supérieure d'Arts et Métiers, Meknès, Maroc et l'Université de Pau et des Pays de l'Adour, Laboratoire de Mathématiques et leurs Applications, Pau, France. Ce travail a bénéficié du soutien financier du CNRS via l'IRN (International Research Networks) GE2MI (Groupement Euro-Maghrébin de Mathématiques et de leurs Interactions).

Je remercie sincèrement les membres du Jury : Mesdames Z. Mghazli et C. Rosier et Monsieur A. Taakili d'avoir accepté d'être mes rapporteurs. Je leur exprime toute ma gratitude pour leurs remarques pertinentes et constructives qui m'ont permis d'améliorer ce document. J'exprime ma gratitude à Z. Mghazli pour m'avoir fait l'honneur de présider ce Jury. Des remerciements particuliers sont adressés à Messieurs M. Afif et A. Ezziani, qui ont gentiment accepté d'être membres de mon Jury. J'exprime toute ma reconnaissance à Monsieur A. Aharmouch pour ses discussions fructueuses, sa collaboration et pour sa participation au Jury.

Je tiens à remercier tout particulièrement mes directeurs de thèse, Messieurs M. El Ossmani et B. Amaziane, pour m'avoir proposé ce sujet et pour m'avoir accompagné dans ma formation de Mathématiques Appliquées. Tout au long de ce travail, j'ai bénéficié de leurs compétences scientifiques en mathématiques appliquées, notamment en analyse numérique, en programmation C++ et en simulation numérique. Leur profonde humanité m'a beaucoup encouragée et m'a permis de préparer cette thèse dans les meilleures conditions possibles. Je leur suis très reconnaissante de m'avoir permis de participer à des conférences internationales. Je n'oublierai pas non plus la gentillesse et le soutien de Monsieur E. Ahusborde pour son aide pour l'initiation et durant le développement des codes dans la plateforme DuMuX.

Je remercie également mes collègues en France et au Maroc : M. Id Moulay, S. Hamidi, S. Eddamiri, Y. Zehraoui, S. Raaidi, L. Lkadi pour l'ambiance de travail, leur disponibilité et leur bonne compagnie. Cela a été un véritable plaisir de partager avec vous des activités conviviales.

D'une manière plus générale, je remercie infiniment le Laboratoire de Modélisation Mathématique, Simulation et Smart Systèmes (ENSAM-Meknès) et le Laboratoire de Mathématiques et de leurs Applications (UPPA-Pau) de m'avoir accueilli et donner l'opportunité de découvrir un univers tant riche sur le plan scientifique que sur le plan humain. Parallèlement, je remercie tous mes enseignants de la FST-Fès, FST Errachidia et le centre INRIA de Paris qui ont contribué à ma réussite, mon épanouissement culturelle et scientifique.

Une attention très particulière à ma famille, ma mère, mes sœurs, mes frères et mes grands-parents pour m'avoir épaulé, encouragé et sans lesquels je ne serai pas là où je suis aujourd'hui. Un grand merci à mon mari SalahEddine, pour son soutien et ses encouragements permanents. Finalement, je dédie ce travail à mon trésor, ma mère Fatima Hamidi, et mon père pour leur soutien inestimable, leur amour inconditionnel.

Abstract

Numerical modeling and simulation of marine intrusion in coastal aquifers has been an interesting research topic and different approaches and appropriate strategies have been developed to predict seawater intrusion. Such a problem is modeled by a coupled system of two parabolic partial differential equations. This thesis aims to develop and implement robust and accurate finite volume schemes, based on recent and efficient tools, for two (sharp and sharp-diffuse) seawater intrusion models in coastal aquifers. Moreover, we focus in this work on the numerical analysis of a finite volume method for the mixed sharp-diffuse interfaces model. The thesis is organized in six chapters.

The general context of the thesis and a literature review were the subject of the first chapter. In the second one, we present a state of the art on existing approaches for modeling marine intrusion in coastal aquifers. Afterwards, we present the derivation of the sharp interface 2D model, which assumes that freshwater and saltwater are immiscible and separated by a sharp interface. Chapter 3 is devoted to the numerical resolution of this model. In this context, we have considered a fully coupled, fully implicit finite volume TPFA (Two Point Flux Approximation) method for performing numerical simulations using this approach. The numerical scheme is implemented in the [DuMu^X](#) framework. Our code is validated on several 1D and 2D test cases, including two realistic cases: the Souss-Chtouka plain in Morocco and Tripoli aquifer in Lebanon. The comparison of our numerical results with others presented in the literature proves the ability of our module to predict seawater intrusion in large-scale aquifers.

Then in chapter 4, we consider an extension of the sharp interface approach to take into account the dynamics of transition (mixing) zones to the so-called sharp-diffuse interfaces 2D model. The mathematical formulation, recently introduced, of this approach is briefly described. As in the previous chapter, this model is discretized by a fully implicit TPFA method and implemented in [DuMu^X](#). The proposed module is validated on several test cases and proved its capacity to deal with physical and hydrological phenomena like tidal fluctuations. Thereafter, we compared the numerical result for the 2D model with those obtained with the classical 3D model for miscible displacements. The numerical results showed that this approach yields physically realistic and performance results.

To predict seawater intrusion into heterogeneous and anisotropic coastal aquifers, we have considered in chapter 5 a numerical method, based on a MPFA (Multi-Point Flux Approximation) method of the sharp-diffuse interfaces model. The study of the numerical analysis of the scheme is presented. The non-negativity of the discrete solution is proved and an existence result is shown using a fixed point theorem. Based on recent compactness tools, we have proved the strong convergence of the approximate solution to the weak solution of the continuous problem. The MPFA numerical scheme is further implemented in the [DuMu^X](#) framework. The accuracy and efficiency of our method in a strongly heterogeneous case are examined by performing 2D numerical simulations. Lastly, some concluding remarks and perspectives are forwarded.

Keywords: *Saltwater intrusion, finite volume, TPFA, MPFA, DuMu^X, numerical simulation, numerical analysis, convergence, heterogeneity, porous media.*

Résumé

La modélisation et la simulation numérique de l'intrusion marine dans les aquifères côtiers ont été un sujet de recherche important et différentes approches et stratégies appropriées ont été développées pour prédire l'intrusion d'eau salée. Un tel problème est modélisé par un système couplé de deux équations aux dérivées partielles paraboliques. Cette thèse vise à développer des schémas volumes finis robustes et précis, basés sur des outils récents et efficaces, pour deux modèles (interface nette et nette-diffuse) d'intrusion marine dans des aquifères côtiers. En plus, on s'intéresse dans ce travail à l'analyse numérique d'une méthode volume finis pour le modèle d'interface nette-diffuse. La thèse est organisée en six chapitres.

Le contexte général de la thèse et une revue de la littérature ont fait l'objet du premier chapitre. Dans le second chapitre, nous présentons un état de l'art sur les approches existantes pour la modélisation de l'intrusion marine dans les aquifères côtiers. Ensuite, nous présentons la dérivation du modèle 2D d'interface nette, qui suppose que l'eau douce et l'eau salée sont immiscibles et séparées par une interface nette. Le chapitre 3 est consacré à la résolution numérique de ce modèle. Dans ce contexte, nous avons considéré une méthode volumes finis TPFA (Two Point Flux Approximation) totalement couplée et implicite pour effectuer des simulations numériques en utilisant cette approche. Le schéma numérique est implémenté dans la plateforme [DuMu^X](#). Notre code est validé sur plusieurs cas tests 1D et 2D dont deux cas sont réalistes : la plaine du Souss-Chtouka au Maroc et l'aquifère de Tripoli au Liban. La comparaison de nos résultats numériques avec d'autres présentés dans la littérature montre la capacité de notre module à prédire l'intrusion marine dans des aquifères à grande échelle.

Dans le chapitre 4, nous avons considéré une extension, récemment introduite, permettant de prendre en compte la dynamique des zones de transition. Cette approche est nommée modèle d'interface nette-diffuse. La formulation mathématique de ce modèle est brièvement décrite. Comme dans le chapitre précédent, ce modèle est discrétisé par une méthode TPFA totalement implicite et implémenté dans [DuMu^X](#). Ce second module est validé sur plusieurs cas tests et a montré sa capacité à traiter des phénomènes physiques et hydrologiques comme les fluctuations des marées. Ensuite, nous avons comparé les résultats numériques du modèle 2D avec ceux obtenus avec le modèle 3D classique pour les déplacements miscibles. Les résultats numériques ont montré que cette approche donne des résultats physiquement réalistes et performants.

Pour prédire l'intrusion marine dans des aquifères hétérogènes et anisotropes, nous avons développé dans le chapitre 5 une méthode numérique, basée sur une approximation MPFA (Multi Point Flux Approximation) du modèle d'interface nette-diffuse. L'étude de l'analyse numérique du schéma est présentée. La positivité de la solution discrète est prouvée et un résultat d'existence est montré en utilisant un théorème de point fixe. En se basant sur des outils de compacité récents, nous avons prouvé la convergence forte de la solution approchée vers la solution faible du problème continu. Le schéma numérique MPFA est implémenté dans [DuMu^X](#). La précision et l'efficacité de la méthode dans un cas fortement hétérogène sont examinées en effectuant des simulations numériques 2D. Enfin, une conclusion et perspectives sont présentées.

Mots clés: *Intrusion marine, volumes finis, TPFA, MPFA, DuMu^X, simulation numérique, analyse numérique, convergence, hétérogénéité, milieux poreux.*

Table of contents

| | | |
|----------|-------------------------------------------------------------------------------------|-----------|
| 1 | General introduction | 1 |
| 1.1 | Introduction | 1 |
| 1.2 | Motivation and problem setting | 2 |
| 1.3 | The objective of the thesis | 3 |
| 1.3.1 | The sharp interface module | 4 |
| 1.3.2 | The sharp-diffuse interfaces module | 4 |
| 1.4 | Thesis structure | 5 |
| 2 | Mathematical modeling of seawater intrusion in coastal aquifers | 9 |
| 2.1 | Introduction | 9 |
| 2.2 | A state of the art on marine intrusion models | 10 |
| 2.2.1 | Sharp interface approach | 11 |
| 2.2.2 | Variable density approach | 12 |
| 2.2.3 | Sharp-diffuse interfaces approach | 13 |
| 2.3 | Mathematical modeling of the sharp interface model | 14 |
| 2.3.1 | Continuity equation | 14 |
| 2.3.2 | Darcy's law | 15 |
| 2.3.3 | Assumptions | 15 |
| 2.3.4 | Integration of the equations | 16 |
| 2.3.5 | Mathematical model of the sharp interface problem | 20 |
| 2.4 | Conclusion | 21 |
| 3 | A finite volume method for numerical simulation of the sharp interface model | 23 |
| 3.1 | Introduction | 23 |
| 3.2 | A fully implicit finite volume numerical scheme | 24 |
| 3.2.1 | Discretization and basic notations | 25 |
| 3.2.2 | Resolution of the nonlinear system | 29 |
| 3.3 | Implementation of the numerical scheme | 32 |

| | | |
|----------|----------------------------------------------------------------------------------------------|-----------|
| 3.4 | Numerical simulations | 32 |
| 3.4.1 | Test 1: The rotating interface problem | 33 |
| 3.4.2 | Test 2: a field-scale free aquifer problem | 37 |
| 3.4.2.1 | Test description | 37 |
| 3.4.2.2 | Numerical convergence | 38 |
| 3.4.2.3 | Numerical results | 43 |
| 3.4.3 | Test 3: Souss-Chtouka case study | 47 |
| 3.4.3.1 | Geographical location | 47 |
| 3.4.3.2 | The studied domain and discretization | 48 |
| 3.4.3.3 | Physical parameters and boundary conditions | 50 |
| 3.4.3.4 | Numerical results | 53 |
| 3.4.4 | Test 4: Tripoli aquifer case study | 60 |
| 3.4.4.1 | Geographical location | 60 |
| 3.4.4.2 | The studied domain and physical parameters | 61 |
| 3.4.4.3 | Numerical results | 63 |
| 3.5 | Conclusion | 67 |
| 4 | A finite volume method for numerical simulation of the sharp-diffuse interfaces model | 69 |
| 4.1 | Introduction | 69 |
| 4.2 | Mathematical model of the sharp-diffuse interfaces problem | 70 |
| 4.3 | Numerical simulations of the sharp-diffuse interfaces model | 72 |
| 4.3.1 | Test 1: Pumping of freshwater | 72 |
| 4.3.1.1 | Test description | 72 |
| 4.3.1.2 | Numerical convergence | 73 |
| 4.3.1.3 | Numerical results | 76 |
| 4.3.2 | Test 2: Tidal effects | 78 |
| 4.3.2.1 | Test description | 78 |
| 4.3.2.2 | Numerical results | 78 |
| 4.3.3 | Test 3: 3D variable density test | 82 |
| 4.3.3.1 | Test description | 83 |
| 4.3.3.2 | Numerical results | 84 |
| 4.4 | Conclusion | 89 |

| | | |
|----------|-------------------------------------------------------------------------------------------------------------------------|------------|
| 5 | Numerical analysis of a multi-point flux approximation finite volume scheme for a sharp-diffuse interfaces model | 91 |
| 5.1 | Introduction | 91 |
| 5.2 | Mathematical model | 92 |
| 5.3 | Finite volume discretization | 93 |
| 5.3.1 | Discretization and notations | 94 |
| 5.3.2 | Fully coupled fully implicit finite volume scheme | 95 |
| 5.4 | Discrete maximum principle | 98 |
| 5.5 | Energy estimates and compactness results | 101 |
| 5.5.1 | A priori estimates | 101 |
| 5.5.2 | Existence of the discrete solution | 107 |
| 5.5.3 | Space and time translates estimates | 109 |
| 5.6 | Convergence results | 112 |
| 5.7 | Numerical results | 116 |
| 5.7.1 | Studied domain and physical data | 117 |
| 5.7.2 | Test case 1: homogeneous aquifer | 118 |
| 5.7.3 | Test case 2: fractured aquifer | 120 |
| 5.8 | Conclusion | 121 |
| 6 | Conclusion and perspectives | 125 |
| | Bibliography | 127 |

Table of Figures

| | | |
|------|-------------------------------------------------------------------------------------------------------------------------------------------------------------------|----|
| 1.1 | Saltwater intrusion into coastal water wells. Source: http://imag.slid.com | 2 |
| 2.1 | Sharp interface model. Source: https://www.solinst.com | 11 |
| 2.2 | Groundwater flow patterns and the dispersion zone in a homogeneous coastal aquifer. Source: http://water.usgs.gov/ | 13 |
| 2.3 | Schematic representation of a coastal aquifer [70]. | 17 |
| 3.1 | Geometry of the domain Ω | 25 |
| 3.2 | Discretisation by a cell-centred finite volume method. | 26 |
| 3.3 | Position of the interface obtained with the present model and the analytical solution at different simulation times. | 34 |
| 3.4 | The progress of the numerical and analytical toe. | 34 |
| 3.5 | Evolution of the salt interface at different times. | 35 |
| 3.6 | Rotary character of the freshwater/saltwater interface at times $t = 10, 20, 100, 400$ and 800 days. | 35 |
| 3.7 | Evolution of the groundwater surface Z_T and the salt front Z in an injection (left) and pumping (right) process at time: $t=1.5$ and 10 days. | 36 |
| 3.8 | Left: Injection process. Right: pumping scenario. | 36 |
| 3.9 | Schematic of the well screen in an unconfined aquifer [84]. | 38 |
| 3.10 | Convergence of solutions on different grids to the reference solution during 30 years of activity on the main section $(0, 10) - (500, 10)$ | 40 |
| 3.11 | Evolution of the solutions on each grid and convergence to the reference solution for 30 years at the point of pumping $(350, 10)$ | 41 |
| 3.12 | Variation of the salt front while changing the pumping rate and fixing the position of the well. | 44 |
| 3.13 | Evolution of the salt front by varying the depth of the well and fixing the pumping rate at $Q_t = 0.1 \text{ m}^3/\text{day}$ | 45 |
| 3.14 | Evolution of the salt front by varying the depth of the well and fixing the pumping rate at $Q_t = 0.07 \text{ m}^3/\text{day}$ | 45 |

| | | |
|------|-------------------------------------------------------------------------------------------------------------------------------------------------------------------------------------------------------------------------------------------------------------------|----|
| 3.15 | Evolution of the salt front for Sc-1, Sc-7, Sc-8 and Sc-9 scenarios, while changing the longitudinal positions of the wells. | 46 |
| 3.16 | The situation of the Souss-Massa basin and the Souss-Chtouka groundwater. | 48 |
| 3.17 | 3D representation of the studied domain. | 49 |
| 3.18 | Left: geometry and boundaries of the aquifer and well locations. Right: mesh for the aquifer. | 49 |
| 3.19 | Left: hydraulic conductivity (\mathbf{D}_f) of the aquifer. Right: porosity (ϕ) of the soil. | 50 |
| 3.20 | Left: the freshwater storage coefficient S_f . Right: comparison between our developed module $2p$ -SWI model and the measured piezometric map of 1968. | 51 |
| 3.21 | Topography of the aquifer bottom. | 52 |
| 3.22 | Plan view of the piezometry of the plain Souss-Chtouka before (left) and after (right) solicitation. | 53 |
| 3.23 | Contours representing the freshwater potential of the Souss-Chtouka plain illustrated on the bottom of the aquifer in 1968 (left) and 2048 (right). | 54 |
| 3.24 | Plan view of the piezometry of the saltwater in its initial state in 1968 (left) and after 80 years of exploitation (right). | 55 |
| 3.25 | Position of the interface freshwater/saltwater in 1968 (black line) and in 2048 (red line). | 56 |
| 3.26 | Left: Plan view of level positions. Right: vertical cross section showing the interface position (red line), the free surface position (blue line) and the variation of the saltwater hydraulic head (green line) for different time: cut on the level 1. | 56 |
| 3.27 | Vertical cross section showing the interface position (red line), the free surface position (blue line) and the variation of the saltwater hydraulic head (green line), for different time: cut on the levels 2 (left) and 3 (right). | 57 |
| 3.28 | Vertical cross section showing the interface position (red line), the free surface position (blue line) and the variation of the saltwater hydraulic head (green line), for different times: cut on the levels 4 (left) and 5 (right). | 58 |
| 3.29 | Evolution in time of the salt front (top right) freshwater head (left) and saltwater head (right). | 59 |
| 3.30 | Position of the Tripoli aquifer, study zone and wells position (cf. [56]). | 60 |
| 3.31 | Geological map and stratigraphy of Tripoli (cf. [56]). | 61 |
| 3.32 | Geometry and Boundaries of the aquifer (left). The mesh of the studied domain (right). | 62 |

| | | |
|------|-------------------------------------------------------------------------------------------------------------------------------------------------------------------------------------------------------------------------------------------------------------------------------------------------------|----|
| 3.33 | Location of pumping zones (cf. [56]). The rectangle in blue corresponds to the private wells and the public wells are represented by a yellow zone. The yellow zone in the south of the aquifer contain 4 wells in Bhsas while the two other wells are in El-jisir and Malouleh respectively. | 63 |
| 3.34 | Evolution of the saltwater/freshwater interface in 2008. "NOP" scenario | 64 |
| 3.35 | Evolution of the saltwater/freshwater interface in 2018 with a rate of 150 L/day as recommended by the water authorities. | 64 |
| 3.36 | Evolution of the saltwater/freshwater interface in 2018 with a rate of 250 L/day. | 65 |
| 3.37 | Evolution of the saltwater/freshwater interface in 2028 with a rate of 250 L/day. | 65 |
| 3.38 | Evolution of the piezometric head of freshwater in 2008. | 66 |
| 3.39 | Position of the freshwater head scenarios. a) After 10 years of pumping with 150 L/day: "REC" scenario. b) After 10 years of pumping with 250 L/day: "10Y" scenario. c) After 20 years of pumping with 250 L/day: "20Y" scenario. | 67 |
| 4.1 | Schematic representation of a coastal aquifer. | 71 |
| 4.2 | Convergence of solutions on each grid to the reference solution during 3 days of pumping on cross-section $(-50, 0) - (50, 0)$ | 74 |
| 4.3 | Evolution of the solutions on each grid and convergence to the reference solution for 3 days at the point $(-10, 0)$ | 74 |
| 4.4 | Conservation of the total amount of freshwater pumped | 75 |
| 4.5 | Evolution of the elevation of sharp-diffuse interfaces (left) and the freshwater head (right) in 1, 2 and 3 days. | 77 |
| 4.6 | Velocity of freshwater (left) and saltwater (right) flows during 3 days of pumping. | 77 |
| 4.7 | Convergence of the interface obtained with the present model towards the analytical solution derived from Ferris model. Times $T = 0.5$ day (left) and $T = 1$ day (right). | 79 |
| 4.8 | Evolution of the freshwater head and the salt front elevation in different times without any external forces. $T = 0.1, 0.5$ and 1 day. | 80 |
| 4.9 | Displacement of the freshwater head and the salt front elevation in different times during a pumping scenario. $T = 0.1, 0.5, 1$ day. | 80 |
| 4.10 | Oscillations on the salt front elevation, predicted by the hydrograph artifacts ($\delta = 0$ (left) and $\delta \neq 0$ (right)) and comparison between both models. | 81 |
| 4.11 | Sea oscillations effects on the freshwater head u . Simulations with $\delta = 0$ and $\delta \neq 0$ | 82 |
| 4.12 | Evolution of the freshwater head u with and without oscillations in the boundary. | 82 |

| | | |
|------|-----------------------------------------------------------------------------------------------------------------------------------------------------------------------------------------|-----|
| 4.13 | Initial conditions : initial salt concentration for the 3D model (left) and initial position of the transition zone between freshwater/saltwater for the 2D model (right). | 83 |
| 4.14 | 3D presentation of the initial position of the interface. | 84 |
| 4.15 | Evolution of the freshwater and saltwater flows in the normal conditions during $T = 10$ days. | 84 |
| 4.16 | Representation of sharp-diffuse interfaces and 3D density variable results (50 % salinity contour and 5 % and 95% salinity contour) for $T=5$ days. | 85 |
| 4.17 | The velocity field in the rotating interface problem at $t = 10$ days. | 85 |
| 4.18 | Numerical results for pumping scenario: $x_2 = 0.5$ (top) $x_2 = 1.5$ (center) and $x_2 = 2.5$ (below). | 86 |
| 4.19 | Evolution of the concentration (3D model) and the salt front (2D model) under a large amount of pumping: slice on $x_2 = 1.5$. | 86 |
| 4.20 | Numerical results during an injection experiment. $x_2 = 0.5$ (top), $x_2 = 1.5$ m (center) and $x_2 = 0.5$ (bottom). | 87 |
| 4.21 | Initial conditions: initial salt concentration for 3D model (left) and initial position of the salt front for the 2D model (right). | 88 |
| 4.22 | Numerical results for double pumping wells. Slice $x_2 = 0.5$ m (top), slice $x_2 = 1.5$ m (center) and slice $x_2 = 2.5$ m. | 88 |
| 4.23 | Numerical results: injection and pumping, $T = 10.5$ days $\gamma = 0.00025$. | 89 |
| 5.1 | The control volume K and associated notations. | 94 |
| 5.2 | Structured mesh of a homogeneous aquifer (21164 cells). | 118 |
| 5.3 | Displacement of the freshwater/saltwater transition zone at vertical cross-section through pumping wells in the homogeneous case after 3 <i>days</i> (left) and 10 <i>days</i> (right). | 119 |
| 5.4 | Freshwater flow velocity in the homogeneous case after 10 <i>days</i> . | 119 |
| 5.5 | Displacement of the freshwater/saltwater interface 2D plot in the homogeneous case after 3 <i>days</i> (left) and 10 <i>days</i> (right). | 119 |
| 5.6 | Evolution of the freshwater head 2D plot in the homogeneous case after 3 <i>days</i> (left) and 10 <i>days</i> (right). | 120 |
| 5.7 | Unstructured mesh in the heterogenous case with two intersecting fractures (20651 cells). | 120 |
| 5.8 | Displacement of the freshwater/saltwater transition zone for different sections in the heterogeneous case after 3 <i>days</i> (left) and 10 <i>days</i> (right). | 121 |
| 5.9 | Freshwater flow velocity in the heterogeneous case after 10 <i>days</i> . | 122 |
| 5.10 | Displacement of the freshwater/saltwater interface 2D plot in the heterogeneous case after 3 <i>days</i> (left) and 10 <i>days</i> (right). | 122 |

5.11 Evolution of the freshwater head 2D plot in the heterogeneous case
after 3 *days* (left) and 10 *days* (right). 122

List of Tables

| | | |
|------|--------------------------------------------------------------------------------------------|-----|
| 3.1 | Parameter values for the rotating interface problem. | 33 |
| 3.2 | Parameters and properties of the aquifer. | 38 |
| 3.3 | Different pumping scenarios. | 38 |
| 3.4 | Grids considered in the study of the numerical convergence. | 39 |
| 3.5 | Numerical convergence of the scheme in l^2 -relative norm. | 42 |
| 3.6 | Numerical convergence of the scheme in l^∞ -relative norm. | 42 |
| 3.7 | Order of convergence for the l^2 -relative norm. | 42 |
| 3.8 | Order of convergence for the l^∞ -relative norm. | 43 |
| 3.9 | CPU time taken for each simulation. | 43 |
| 3.10 | Well position and associated rates. | 52 |
| 3.11 | Parameters and properties of the aquifer (cf. [56]) | 62 |
| 3.12 | Wells position and associated rates. | 63 |
| | | |
| 4.1 | Parameter values for the pumping scenario. | 73 |
| 4.2 | Different grids used in the numerical convergence. | 73 |
| 4.3 | Numerical convergence of the scheme in l^2 -relative norm. | 75 |
| 4.4 | Numerical convergence of the scheme in l^∞ norm | 75 |
| 4.5 | Order of convergence | 75 |
| 4.6 | CPU time and the number of iterations required by Newton's method to converge | 76 |
| 4.7 | Parameters and properties of the aquifer | 83 |
| | | |
| 5.1 | Parameters and properties of the aquifer. | 118 |

Chapter 1

General introduction

Contents

| | |
|-----------------------------------------------------|----------|
| 1.1 Introduction | 1 |
| 1.2 Motivation and problem setting | 2 |
| 1.3 The objective of the thesis | 3 |
| 1.3.1 The sharp interface module | 4 |
| 1.3.2 The sharp-diffuse interfaces module | 4 |
| 1.4 Thesis structure | 5 |

1.1 Introduction

In this thesis, we are interested in the mathematical modeling and numerical simulation of seawater intrusion into coastal aquifers. Thus, this chapter presents a general introduction of this manuscript while outlining the objective, the structure and the different developments and improvements made in the context of this work.

We introduce the motivation and the problematic of this research in section 1.2. Due to accelerated urbanization and the population explosion and industrial activities, the exploitation of water resources becomes more and more considerable, particularly in coastal regions which are pole of attraction. Therefore, the potential of freshwater decreases and the seawater advances towards the land-side which degrade the quality of freshwater. A good management of these areas requires the use of appropriate strategies and efficient tools for the simulation and prediction of seawater intrusion in these zones. Different approaches used in the modeling of marine intrusion are discussed and presented. After that, we present in section 1.3 the main results achieved in this thesis. In this work, two marine intrusion modules, based on recent and efficient tools, are developed and integrated in the platform [DuMu^X](#). A brief description of these modules is presented and the different developments done in the implementation of the finite volume numerical methods is explained. The structure of this manuscript is explained in section 1.4.

1.2 Motivation and problem setting

Groundwater is an essential source of water that represents only 3% of the world total water. Most groundwater is in contact with saltwater. These valuable resources suffer from drought and contamination by seawater. Freshwater extraction is increasing with population growth and industrial activity. The water potential of the aquifers is threatened, both qualitatively and quantitatively, by the significant decline in peizometric levels and ocean intrusion due to high pumping rates. A good management of these resources is becoming an important issue and a major challenge, see for instance [91, 92].

The coastal regions are often, poles of attraction for industrial, agricultural and tourist activities. The large increase in demand for drinking water due to population growth and the expansion of economic activities in these areas presents a significant challenge to the hydraulic potential of coastal aquifers. Over-exploitation and excessive pumping of these resources lead to the invasion of aquifers by salt water. As a consequence, seawater moves towards the landside under freshwater because of its important density compared to freshwater. Indeed, over-pumping from wells located in sensitive areas of the water table can cause the advancement of the saltwater wedge and thus cause the degradation of the quality of the water in the coastal water table. Figure 1.1 represents seawater intrusion phenomena into coastal aquifers.

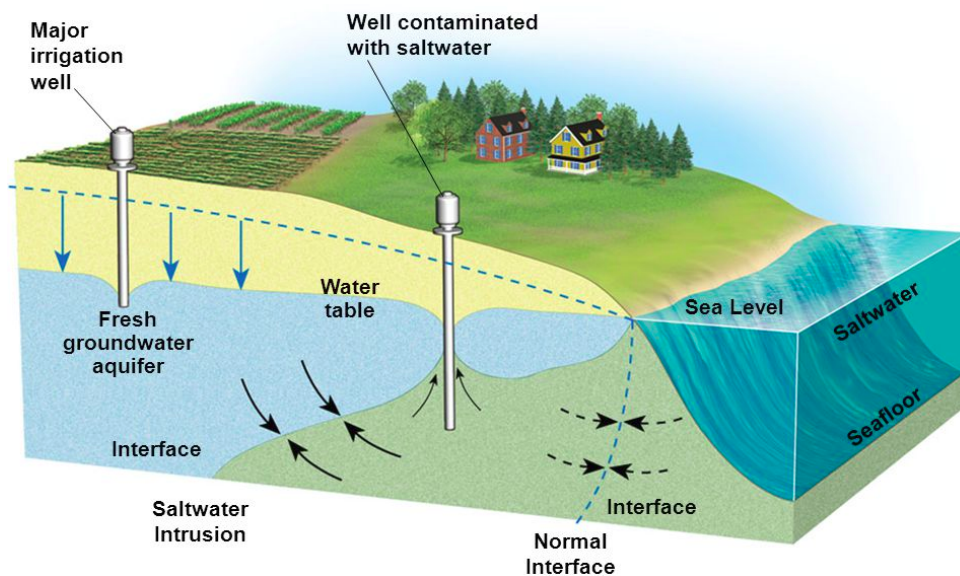


Figure 1.1: Saltwater intrusion into coastal water wells. Source: <http://imag.slid.com>

The prediction of the hydrodynamics of freshwater and saltwater and the implementation of efficient tools is essential for a good management of these resources in the coastal zones, because once contaminated, the freshwater hardly recovers its state before the pollution, hence the importance of prediction.

The numerical modeling and simulation of marine intrusion in coastal aquifers has been a significant research topic and different approaches have been developed to

predict seawater intrusion. Two classical approaches are often employed to tackle marine intrusion problems. We refer to the books [14, 15, 16, 21, 22, 36].

The first one is the 2D sharp interface approach [15] which assumed that the freshwater and saltwater fluids do not interact with each other and are separated by an abrupt interface. In this case, flow at the saltwater and freshwater zones is considered and no mass transfer occurs at the transition zones. In natural conditions where external forces are neglected, saltwater is supposed to be immobile; and only the freshwater movement is then considered. In such case, we are simulating only freshwater flow.

Secondly, the 3D variable density flow and solute transport approach [14, 36] which considers that the two fluids are miscible. Two processes then govern the transport of the dissolved salt, namely convection and dispersion. This approach seems more credible to track movement and changes in the freshwater/saltwater transition zone, but no interface is defined to determine the area of saltwater wedge occupation or that of the water table which may be moved by pumping. In this case, the vertical variation of the fluids is considered. Furthermore, in terms of CPU time, this approach (3D model) is expensive compared to the sharp interface approach and produces significant numerical diffusion in the transition zones between freshwater and saltwater, and saturated and unsaturated zones.

In the coastal areas, the thickness of the aquifer is insignificant compared to its horizontal thickness. The problem is simplified and reduced to a 2D model since the fluids flow is assumed to be horizontal. In such case, the sharp interface approach can be adopted and extended to deal with large scale aquifers and to provide physically efficient results. In this context, a new approach (2D model) coupling the physical sides of the 3D variable density model and the simplicity of the sharp interface approach is introduced in [25]. The dynamic of the diffusive zones is tacking into account.

1.3 The objective of the thesis

The purpose of this research is the development and implementation of finite volume numerical schemes for seawater intrusion models into coastal aquifers. This study is based mainly on the of an efficient and robust numerical framework simulating seawater intrusion models and able to take into account various hydraulic and hydrogeological phenomena. Furthermore, we are interested in the numerical analysis of a conservative finite volume method for the flow of two immiscible fluids in an anisotropic and heterogeneous porous medium.

In this section, we describe the different development done in the implementation of our finite volume seawater intrusion numerical schemes. We have adopted a fully coupled, fully implicit approach for the resolution of freshwater and saltwater flows into coastal aquifers. We employ an Euler implicit scheme for the discretisation in time and a *Cell Centered* finite volume method to discretize in space. We linearise the coupled systems using Newton's method in each time step wherein each iteration, a linear system is solved using iterative Krylov methods. We use mainly BiCGSTAB (Biconjugate gradient stabilized method) solvers combined with

a preconditioner (ILU) and GMRES (Generalized minimal residual method) solver coupled with a preconditioned (AMG Backend). Numerical differentiation techniques are used to approximate the derivatives in the calculation of the Jacobian matrix.

We have developed and implemented two modules in the the framework of the parallel open source `DuMuX`, based on the Distributed and Unified Numerics Environment (`DUNE`), allowing simulations for large-scale field applications involving seawater intrusion in coastal aquifers. The two modules called respectively "2p-SWI" (for the sharp interface approach) and "2pdiff-SWI" (for the sharp-diffuse interfaces approach). The object-oriented code provides recent and efficient numerical tools and allows us to predict marine intrusion while taking into account various hydraulic and hydrogeological phenomena. All our recent developments have been implemented in `DuMuX` versions 2.12 and 3.0.

1.3.1 The sharp interface module

The 2p-SWI module is based on a TPFA (See [37, 42]) numerical finite volume scheme by means of the sharp interface approach. The validation of the integrated module is performed on different 1D, 2D test cases, in particular the Souss-Chtouka plain in Morocco. In the case of a confined aquifer, we have compared our numerical results with an analytical solution proposed in [61]. The numerical results feet well with those presented in [8, 67]. The efficiency and accuracy of our module in the case of a free aquifer are investigated by performing the numerical convergence of the scheme. Afterwards, we have extent our module to deal with heterogenous and realistic test cases. We have applied our method to two real test cases: "the field scale free aquifer" presented in [71], the Souss-Chtouka plain [5] and the Tripoli aquifer test case [57]. Numerical simulations for the long-term demonstrate the applicability of our developed approach in highly heterogeneous coastal aquifers, and proved that our module is efficient and able to solve numerically 2D seawater intrusion problem using the sharp interface approach. Chapter 3 summarizes all the numerical illustrations of these test cases.

The extension of the methodology to more advanced models, like the mixte sharp-diffuse interfaces model recently introduced in [25] will be the subject of the next section.

1.3.2 The sharp-diffuse interfaces module

Firstly, we have extended the sharp interface module to more general module which take into account the width of the transition zones. It is based on a TPFA finite volume numerical method. This module provides more informations about the position of the diffusion zones and yields physically realist results. To ensure the validity of our module, we proceed to the study of the numerical convergence of the scheme and compared our numerical results with an analytical solution presented in [45]. The ability of our 2D module to provide an efficient and accurate results is checked by comparing the numerical results with the classical 3D model for miscible displacements.

After that, we have developed the "2pdiff-SWI" module to deal with the anisotropy and the heterogeneity of the coastal aquifer and to provide accurate results. The developed module uses an MPFA [37] finite volume numerical method, where the subfluxes are approximated on the half-edges of the control volume. In fact, this method tackles the non-linearity of the problem, the anisotropy and the heterogeneity of the aquifer on unstructured mesh, which improves the efficiency and accuracy of the numerical computations of the system of equations. Numerical results for a test case showed the impact of various hydraulic and hydrogeological phenomena on the displacement of the freshwater and saltwater flows.

1.4 Thesis structure

The purpose of this section is to present the general structure of the thesis, which is divided into six chapters.

Chapter 2 is devoted to the mathematical modeling of seawater intrusion in coastal aquifers. First, we present a state of the art on the existing approaches modeling marine intrusion. After that, we describe the derivation of the governing equations modeling saltwater and freshwater flows using the sharp interface model. The set of physical assumptions used in the formulation of the mathematical model is presented.

In chapter 3, we develop a fully coupled, fully implicit finite volume method for the numerical resolution of the sharp interface model. To discretize in time, we use an implicit Euler method and a TPFA finite volume method (See [37, 42]) in space. The coupled system is linearized using Newton's method, wherein each iteration a linear system is solved. In this context, we have integrated "2p-SWI" module in the framework of DuMuX. A brief description of the platform is presented. Afterwards, we illustrate the numerical results obtained in the validation of our module. The module is first tested on a reference case concerning the evolution of the interface under density contrast in a confined aquifer. The efficiency of the module is examined by conducting the numerical scheme study in the case of a free aquifer. We applied the method to different test cases presented in [8, 67, 71]. The results obtained are in good agreement, which guarantees the validity of our implemented module. Moreover, we test our module in a two realistic cases corresponding to the Souss-Chtouka plain [5] in Morocco and Tripoli aquifer [57] in Lebanon. The numerical model is based on available hydrogeological data in real scale by simulating the progress of seawater intrusion for several years. Numerical results have proved the ability of our developed module to predict water table and salt front elevations under various stress conditions and its ability to yield physically accurate and efficient solutions. Part of the results of this chapter have been published in [4].

Chapter 4 aims to develop a finite volume method for the numerical simulation of the sharp-diffuse interfaces model. First, we briefly outline the derivation of the mathematical model. Then, we present different numerical results used for the validation of our module. First, we proceed to the study of the numerical convergence of the scheme. After that, we consider a test case which concerns a

free aquifer subjected to tidal fluctuations where the analytical solution is known. The numerical results are compared to the analytical solution and proved a good agreement with those presented in [7, 25]. Both test cases show that our fully implicit approach is suitable to simulate a seawater intrusion problem taking into account the dynamics of transition zones. In addition, we propose to compare the numerical results of the 2pdiff-SWI module (2D model) with those provided by the classical 3D model for miscible displacements. The numerical results have shown that this approach yields physically realistic and performant results.

Chapter 5 is devoted to the study of the convergence of an MPFA finite volume scheme for the sharp-diffuse interfaces model in an anisotropic and heterogeneous free aquifer. We develop a fully coupled, fully implicit approach finite volume method to discretize the coupled system on an unstructured mesh. The numerical scheme ensures a discrete maximum principle taking into account the heterogeneity and anisotropy of the aquifer. Using a fixed point theorem, we have established the existence of the discrete solution. Based on a priori estimates and compactness arguments, we prove the convergence of the numerical approximation to the weak solution of the continuous problem. Furthermore, we have integrated the numerical scheme in the DuMu^X framework. Numerical results proving the robustness and the ability of our module to deal with heterogeneity of the aquifer are presented.

In chapter 6, we conclude and summarize the work carried out in this thesis and give some research perspectives in the context of modeling seawater intrusion in coastal aquifers.

Notations

- **General variables**

- t : Time variable [s],
- x : Space variable [m],
- $i = f, s$: Phase index f= freshwater and s= saltwater.

- **The main unknowns of the system**

- u : The freshwater head [m],
- v : The saltwater head [m],
- Z : The salt front elevation [m].

- **Physical parameters**

- ϕ : porosity of medium [-],
- κ : Intrinsic permeability tensor [m²],
- μ_i : Dynamic viscosity [kg.m⁻¹.s⁻¹],
- ρ_i : Density of the fluid i [kg · m⁻³],
- \vec{q}_i : Darcy's velocity of the fluid i [m.s⁻¹],
- Q_i : Quantity of water injected or pumped per unit of VER [s⁻¹],
- g : Gravitational acceleration [m.s⁻²],
- \mathbf{D} : Hydraulic conductivity of freshwater [m/day]
- \mathbf{D}_i : Hydraulic conductivity of the fluid i [m/day]
- $\alpha = \frac{\rho_f}{\rho_s - \rho_f}$: Density contrast [-],
- $\gamma = \frac{\rho_s - \rho_f}{\rho_f}$,
- Z_B : Bottom of the aquifer [m],
- Z_T : Water table elevation [m],
- δ : Width of the transition zones [m].

- **Functions**

- $b_f = Z_T - Z_B$: Thickness of freshwater [m],
- $b_s = Z - Z_B$: Thickness of saltwater [m],
- $\varphi(u) = \frac{1}{2}(u - Z_B)^2$,
- $\varphi(Z) = \frac{1}{2}(Z - Z_B)^2$.

Chapter 2

Mathematical modeling of seawater intrusion in coastal aquifers

Contents

| | | |
|------------|-----------------------------------------------------------|-----------|
| 2.1 | Introduction | 9 |
| 2.2 | A state of the art on marine intrusion models | 10 |
| 2.2.1 | Sharp interface approach | 11 |
| 2.2.2 | Variable density approach | 12 |
| 2.2.3 | Sharp-diffuse interfaces approach | 13 |
| 2.3 | Mathematical modeling of the sharp interface model | 14 |
| 2.3.1 | Continuity equation | 14 |
| 2.3.2 | Darcy's law | 15 |
| 2.3.3 | Assumptions | 15 |
| 2.3.4 | Integration of the equations | 16 |
| 2.3.5 | Mathematical model of the sharp interface problem | 20 |
| 2.4 | Conclusion | 21 |

2.1 Introduction

In this chapter, we are interested in the mathematical modeling of seawater intrusion in coastal aquifers. In section 2.2, we present an overview of marine intrusion models. We consider two classical approaches. The sharp interface approach (2D model), see for instance [14, 15, 16, 21, 22, 36], which assumes that freshwater and saltwater are immiscible and separated by a sharp interface. Furthermore, we have the variable density approach (3D model) which supposes that the two fluids are miscible and a mixing zone caused by dispersion is considered. In this context, another approach modeling saltwater intrusion in coastal aquifers (2D model) has recently been introduced in [25]. It is based on the assumption that the two fluids are immiscible and takes into account the dynamics of transition zones.

In section 2.3, we present the mathematical formulation of the equations modeling marine intrusion using the sharp interface model. The hydraulic flow of freshwater and saltwater is governed by Darcy's law and the mass conservation equation of each fluid. We define the main unknowns and physical parameters of the aquifer and subsequently introduce the laws that contribute in the construction of the mathematical system. Furthermore, we consider two hypotheses, corresponding to Dupuit's approximation [38], which suppose that the flow is horizontal and Bear's hypothesis [13], where the vertical variation of the fluids is neglected. Thereafter, we present the sharp interface seawater intrusion model in a coastal aquifer. Such flows are governed by a coupled non-linear system of two parabolic equations simulating freshwater and saltwater heads respectively. Finally, section 2.4 contains concluding remarks.

2.2 A state of the art on marine intrusion models

Groundwater is the main source of drinking water in coastal areas, and better management of these resources is becoming a major challenge, see e.g. [92]. With the population explosion and increased economic activities in these areas, the high demand for drinking water is threatening the water potential of coastal aquifers, both in terms of quantity and quality. Indeed, over-exploitation can lead to the invasion of aquifers by seawater, thus degrading groundwater quality. Marine intrusion is caused by excessive pumping from the water table, thus reducing the load of freshwater and destabilizing the prevailing balance between freshwater and saltwater. Therefore, seawater progresses towards the land side as a saltwater bevel under freshwater because of its high density compared to freshwater. The implementation of appropriate strategies for the management of coastal aquifers is a requirement. Much work is also being done to develop technical tools to determine the amount of water that can be pumped without causing such a negative impact.

There are many reference books, see for instance [14, 15, 16, 21], and different theses, such as [6, 34, 56, 74, 75, 95] on the modeling of marine intrusion in coastal aquifers. Two approaches have been adopted. The first one is the variable density flow and solute transport approach, which assumes that freshwater and saltwater are miscible and a mixing zone caused by dispersion is taken into account. We can mention in this case [29, 43, 53, 77]. The second method is based on an abrupt approximation, see e.g. [13, 55]. This approach assumes that the two fluids are immiscible, therefore separated by a sharp interface.

Models with a sharp interface can be divided into two main categories. Models considering only freshwater flow and saltwater are assumed to be stationary. In this case, we are talking about the one fluid dynamics approach of freshwater [9, 39, 40]. This approach remains valid for long-term predictions under steady-state conditions but suffers from an insufficient description of the behavior of the freshwater-saltwater interface in the short term. Secondly, we have the two-fluid dynamics approach [17, 55] considering the dynamics of the two fluids (freshwater and saltwater). Different analytical models are derived from the sharp interface approach for the prediction of marine intrusion [45, 47, 61, 86, 88] but they are limited to very simple geometries and to situations where the Ghyben-Herzberg

hypothesis is satisfied. Under simplified conditions, these analytical solutions are used as a test case to validate numerical codes.

Recently, several studies [7, 8, 23, 25, 26] have focused on saline intrusion modeling with a new method called sharp-diffuse interfaces approach. The last one combines the simplicity of the sharp interface model with the physical accuracy of models with a diffuse interface. The modeling of the transition zone is based on a phase-field theory developed in [10] and used for the description of the exchange between freshwater and saltwater. A detailed description of the derivation of the mathematical model is given in [23].

2.2.1 Sharp interface approach

The sharp interface approach assumes that saltwater and freshwater are immiscible separated by an abrupt interface. This approximation is all the more legitimate as the vertical dimension of the aquifer is very small in front of the horizontal dimensions of the aquifer, see for instance [13, 40]. For the same reasons, the interface between the saturated and unsaturated zone is assumed to be abrupt in the case of a free aquifer. The presentation of the sharp interface approach is shown in Figure 2.1.

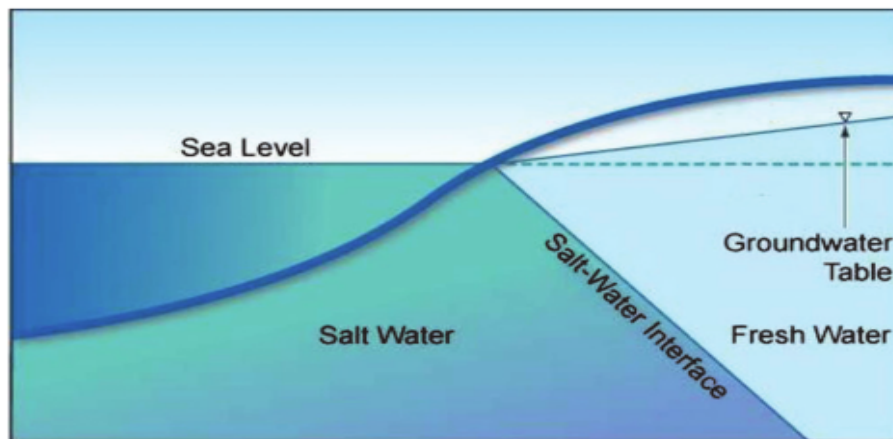


Figure 2.1: Sharp interface model. Source: <https://www.solinst.com>

In steady state conditions, according to a hypothesis proposed in [31], there is an approximate relationship between the thickness of freshwater above sea level and that of freshwater below sea level. In hydrostatic conditions, they assumed that saltwater is static and freshwater is the only fluid in dynamic. According to this relation, if the water table in an unconfined coastal aquifer is lowered by 1 m, the saltwater interface will rise 40 m. In [90], a density difference factor was modified in the relationship introduced in [31]. The developed method is used as an analytical solution to predict seawater intrusion in steady-state conditions in [91].

Unlike previous two-fluid flow models that were established using freshwater and saltwater hydraulic heads as variables, the model introduced in [55] used a mixed formulation with one fluid potential and a Pseudosaturation as double variables.

The numerical solution solved by the finite element method was verified against the analytical solution proposed in [86]. In the same context, another mathematical formulation of the sharp interface model is proposed in [67]. It is based on the mathematical model presented in [40] which simulates freshwater and saltwater heads, therefore the position of the interface is calculated using the continuity of the flux on the interface. The variables of the proposed model are the depth of the salt front and the capillary fringe.

In the case of confined aquifers, the validity of the sharp interface model was assessed in [80] according to four factors: infiltration factor, dispersion/advection ratio, geometric ratio, and time scale factor. The results have shown that the abrupt interface is applicable in steady and unsteady state conditions provided that advection is dominant. Similarly, its validity was discussed in [66] by comparison with the diffusive approach in a free aquifer subjected to pumping. Considering the mathematical formulation presented in [40], a numerical model based on a finite volume method is performed to predict seawater intrusion in Llobregat Delta [17, 18].

Recent work has examined other factors that increased seawater intrusion in a coastal aquifer. The impact of Sea-Level Rise (SLR) on seawater intrusion has been investigated in [60, 87] for a single aquifer and in [69] for multi-layer aquifer. The location of the toe (intersection of the interface with the base of the aquifer) is assessed in [60] under the impact of SLR combined with the Land Surface inundation and the Aquifer Bed Slope. The pumping impact was studied in [48, 70, 84] according to two parameters: the pumping quantity and the position of the wells. Several scenarios are presented to visualize the motion of the salt front while the effect of the random heterogeneity of the aquifer structure on saline intrusion was investigated in [32]. The resolution of the system in a multilayer aquifer is considered as a kind of heterogeneity of the medium [55, 69, 71]. The impact of the population increase on the exploitation of freshwater potential in the Tripoli aquifer was examined in [58]. Results for different pumping scenarios and their impact on the evolution of the freshwater/saltwater interface are presented.

Many works are presented for the application of the sharp groundwater model in complex and realistic examples. We can cite the case of Tongatapu Island [11], the Tripoli Aquifer in Lebanon [58], the Qom aquifer in Iran [79], the Greek Island Kalymnos [63], the Llobregat aquifer in Spain [17], the Soquel-Aptos basin - Santa Cruz Country in California [40], the Walawe River basin in Sri Lanka [78], Yermasogia aquifer in Cyprus and the Crau aquifer in France [46].

2.2.2 Variable density approach

In the variable density approach, the two volumes of water are considered to interact with each other, thus forming a transition zone characterized by variations in salt concentration. This interface is, in fact, a diffuse zone in which freshwater and saltwater mix. It is called a dispersion zone (or transition zone) (Figure 2.2). This approach seems more realistic and represents physical reality since fresh and saltwater are miscible. The vertical section is then considered and the salt concentration is expressed in 3D. The density is considered as a function of salt concentration.

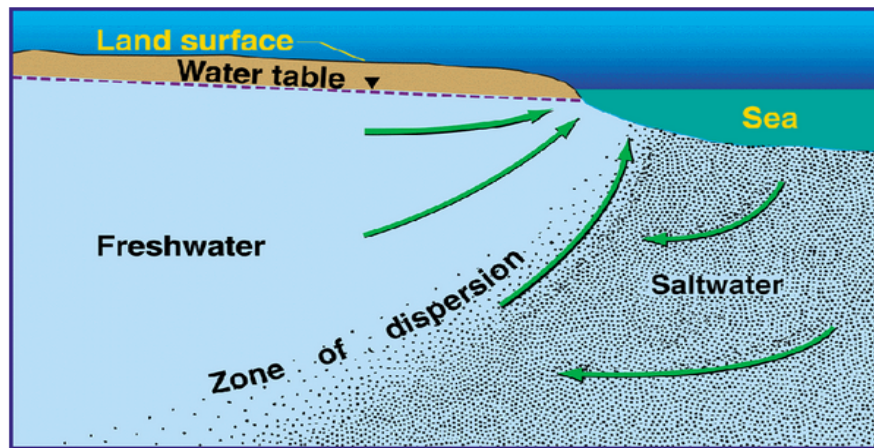


Figure 2.2: Groundwater flow patterns and the dispersion zone in a homogeneous coastal aquifer. Source: <http://water.usgs.gov/>

During the last decades, many simulation models were developed with finite elements and finite difference techniques using this approach [28, 29, 51, 59, 60], also the finite volume methods [12, 50, 65]. In the same context, different works are devoted to the development of software for the problem with variable density such as SEAWAT [49], SUTRA [89] based on finite element methods, FEMWATER [64], MODFLOW [68], MOCDENS-3D [81] and FEFLOW [35].

Under steady-state conditions, a semi-analytical solution proposed in [52] for the variable density diffusion problem in a confined aquifer. The classical problem of saltwater intrusion in a coastal aquifer using the variable density approach under simplified conditions, introduced in [52], is widely used for the validation of numerical models. All semi-analytical methods proposed in previous works [44, 62, 93, 94, 95] for the resolution of Henry's problem are limited to homogeneous and isotropic cases that have recently extended to a heterogeneous and anisotropic coastal aquifer [43]. This model has many applications in randomly heterogeneous aquifers [85] and fractured media [82]. For the application of the method in realistic case, we can mention, the Kocaeli-Darica plain in Turkey [59], the Wadi Ham aquifer in the Fujairah Emirate of the UAE [54], the Gooburrum-Bundaberg-Queensland aquifers in Australia [65].

2.2.3 Sharp-diffuse interfaces approach

A new model combined between the sharp interface approach and the diffusive approach has recently been introduced in [25]. The freshwater and saltwater zones are modeled using the Dupuit approach which assumes that all fluid movements are essentially horizontal.

The modeling of the diffusive interface (resp. between the saturated and unsaturated zone) is derived from a model based on the phase field theory. However, the latter was initially developed in [10] for the description of the transition phenomena between freshwater and seawater. The reader can consult [6, 34, 74] for

documentation including an overview of the sharp-diffuse modeling approach and the mathematical formulation of the proposed model. It combines the simplicity of the abrupt interface with the realism of diffuse interface models. Furthermore, the model takes into account the dynamics of the diffuse interface. In [23], a numerical comparison between the results given by this model with those obtained from the variable-density flow and solute transport model, is proposed. Several scenarios, including pumping and injection processes, were considered to demonstrate that the diffuse interface provided by this model passes through the middle of the transition zone. The salt concentration in the transition zone is assumed to be half that of the saltwater zone.

Another comparison between this model and the classical sharp interface approach is proposed in [25] to assess the validity of the mixed approach. The diffusive interface given by the mixed approach coincides with that provided by the sharp interface model when the width of the transition zone is small. Tidal effects on the saltwater front were studied in [25] using this model. The effect of the width of the transition zone was also investigated in the same reference. In [7], the authors approximate the sharp-diffuse model using finite volume and finite element methods in unconfined aquifers. The numerical results were compared and showed good agreement.

2.3 Mathematical modeling of the sharp interface model

In this section, we present the basic equations used in the derivation of the mathematical model, including the mass conservation equations and Darcy's law. The governing flow equations are provided firstly in 3D. Based on different assumptions, presented in subsection 2.3.3, the equations are vertically integrated and the problem is reduced to a 2D model. Afterwards, the system of equations is closed by evaluating the flow and the pressure continuity on the sharp interface.

2.3.1 Continuity equation

The continuity equation of a fluid in movement on a Representative Elementary Volume (REV) is given by the following equation, see e.g. [14, 16]

$$\frac{\partial(\phi\rho)}{\partial t} + \text{div}(\rho\vec{q}) = \rho Q, \quad (2.3.1)$$

with:

- ϕ : porosity [-],
- ρ : fluid density [$\text{kg} \cdot \text{m}^{-3}$],
- \vec{q} : Darcy's velocity [$\text{m} \cdot \text{s}^{-1}$],
- Q : quantity of water injected per unit of VER [s^{-1}].

We define the coefficient of compressibility of the soil and the fluid respectively by

$$\beta_P = \frac{1}{(1-\phi)} \frac{\partial\phi}{\partial P} \quad \text{and} \quad \alpha_P = \frac{1}{\rho} \frac{\partial\rho}{\partial P}. \quad (2.3.2)$$

with P is the pressure [Pa]. By replacing (2.3.2) in (2.3.1), we obtain

$$\begin{aligned}\frac{\partial(\phi\rho)}{\partial t} &= \left(\phi \frac{\partial\rho}{\partial P} + \rho \frac{\partial\phi}{\partial P} \right) \frac{\partial P}{\partial t}, \\ &= \phi\rho\alpha_P \frac{\partial P}{\partial t} + \rho\beta_P(1-\phi) \frac{\partial P}{\partial t}, \\ &= \rho \left(\phi\alpha_P + \beta_P(1-\phi) \right) \frac{\partial P}{\partial t}.\end{aligned}$$

Therefore, the mass conservation equation (2.3.1) is written as follows

$$\rho \left(\phi\alpha_P + \beta_P(1-\phi) \right) \frac{\partial P}{\partial t} + \rho \operatorname{div}(\vec{q}) + \nabla\rho \cdot \vec{q} = \rho Q. \quad (2.3.3)$$

2.3.2 Darcy's law

Darcy's law describes the flow of a fluid through a porous medium in a macroscopic context. It expresses the flow velocity as a function of the gradient of the hydraulic head. It is given by the following equation:

$$\vec{q} = -\frac{\kappa}{\mu} (\nabla P + \rho g \nabla x_3), \quad (2.3.4)$$

where

- κ : intrinsic permeability tensor [m²],
- μ : dynamic viscosity [kg.m⁻¹.s⁻¹],
- g : gravitational acceleration [m.s⁻²],
- x_3 : the vertical dimension [m].

We define the macroscopic hydraulic head by

$$\Phi[\text{m}] = \frac{P}{\rho g} + x_3. \quad (2.3.5)$$

The freshwater and the saltwater are incompressibles with a constant density. In this case, the hydraulic head is identified at the piezometric level. Equation (2.3.4) is, therefore, written as a function of the hydraulic head:

$$\vec{q} = -\mathbf{D}\nabla\Phi, \quad (2.3.6)$$

where \mathbf{D} [m.s⁻¹] = $\frac{\kappa\rho g}{\mu}$ is the tensor of the hydraulic conductivity.

2.3.3 Assumptions

In this subsection, we present different assumptions used in the derivation of the sharp interface model. Some hypotheses are related to the nature of the soil and the fluids and others are used for the up-scaling of the 3D problem to a 2D model. The aquifer is supposed weakly deformable and the elastic behavior of the soil is

very weak. Moreover, freshwater and saltwater are both weakly compressible fluids. Therefore, the compressibility coefficient of the fluid and the soil, defined in (2.3.2), are neglected, i.e. $(\beta_p, \alpha_P \ll 1)$.

Two main assumptions are also applied: Dupuit's approximation where the movement of the fluids is horizontal since the thickness of many coastal aquifers is neglected compared to its horizontal surface. This has been used and discussed in [13, 38]. In this concept, the transition zone between freshwater and saltwater (resp. saturated and unsaturated zone in the case of a free aquifer) is presumed an abrupt interface. The problem is thereby reduced to a 2D model describing the freshwater and saltwater flows separated by an abrupt interface. In a second step, we consider Bear's hypothesis [13], which consists to ignore the density variation in the flow direction.

2.3.4 Integration of the equations

This subsection aims to present different details of the derivation of the mathematical model. The mass conservation equation (2.3.3) and Darcy's equation (2.3.4) for each fluid can be rewritten as follows

$$\begin{cases} \underbrace{\rho \rho g (\phi \alpha_P + \beta_P (1 - \phi))}_S \frac{\partial \Phi}{\partial t} + \rho \operatorname{div}(\vec{q}) + \nabla \rho \cdot \vec{q} = \rho Q, \\ \vec{q} = -\mathbf{D} \nabla \Phi, \end{cases} \quad (2.3.7)$$

with $S = \rho g (\phi \alpha_P + \beta_P (1 - \phi))$ is the storage coefficient representing the capacity of the aquifer to contain groundwater. Usually, its value is very small due to the low compressibility of the soil and the fluid. i.e, $(\beta_P \ll 1$ and $\alpha_P \ll 1)$.

Using Bear's hypothesis, the term $\nabla \rho \cdot \vec{q}$ in equation (2.3.7) is negligible. One has

$$\rho S \frac{\partial \Phi}{\partial t} + \rho \operatorname{div}(\vec{q}) + \underbrace{\nabla \rho \cdot \vec{q}}_{=0} = \rho Q, \quad \text{with} \quad \vec{q} = -\mathbf{D} \nabla \Phi. \quad (2.3.8)$$

We introduce specific indices for freshwater (f) and saltwater (s) in (2.3.8). The governing freshwater and saltwater flows are as follows

$$S_f \frac{\partial \Phi_f}{\partial t} + \operatorname{div}(\vec{q}_f) = Q_f, \quad S_f = \rho_f g (\phi \alpha_P + \beta_P (1 - \phi)), \quad \vec{q}_f = -\mathbf{D}_f \nabla \Phi_f. \quad (2.3.9)$$

$$S_s \frac{\partial \Phi_s}{\partial t} + \operatorname{div}(\vec{q}_s) = Q_s, \quad S_s = \rho_s g (\phi \alpha_P + \beta_P (1 - \phi)), \quad \vec{q}_s = -\mathbf{D}_s \nabla \Phi_s. \quad (2.3.10)$$

We consider a coastal aquifer represented by a domain $\Omega \times (Z_B, Z_T)$ with $\Omega \subset \mathbb{R}^2$ is a part of its horizontal surface (see Figure 4.1). The function Z_B [m] describes its lower topography while Z_T [m] represents the elevation of the top of the aquifer.

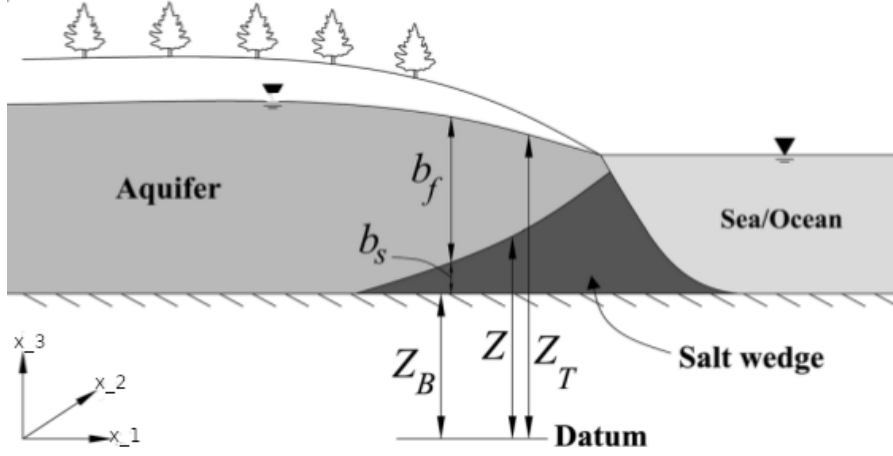


Figure 2.3: Schematic representation of a coastal aquifer [70].

The sharp interface between freshwater and saltwater is noted by Z [m]. The physical parameters $b_f = Z_T - Z$ and $b_s = Z - Z_B$ are the thicknesses of the freshwater and saltwater zones respectively. Equations (2.3.9) and (2.3.10) are expressed in 3D. However, the vertical dimension of a coastal aquifer is very small compared to its horizontal dimension. We, therefore, use Dupuit's approximation. In the following, we will present all the steps of upscaling the 3D problem to a 2D model. In this part, we refer to the work performed in [34].

We integrate equation (2.3.9) between Z and Z_T . We obtain

$$\int_Z^{Z_T} \left(S_f \frac{\partial \Phi_f}{\partial t} + \text{div}(\vec{q}_f) \right) dx_3 = \int_Z^{Z_T} Q_f dx_3. \quad (2.3.11)$$

According to the Leibniz formula, we have

$$\begin{aligned} \int_Z^{Z_T} S_f \frac{\partial \Phi_f}{\partial t} dx_3 &= S_f \int_Z^{Z_T} \frac{\partial \Phi_f}{\partial t} dx_3, \\ &= S_f \frac{\partial}{\partial t} \left(\int_Z^{Z_T} \Phi_f dx_3 \right) - S_f \Phi_f(Z_T) \frac{\partial Z_T}{\partial t} + S_f \Phi_f(Z) \frac{\partial Z}{\partial t}. \end{aligned} \quad (2.3.12)$$

Let $\bar{\Phi}_f$ be the vertical average of Φ_f :

$$\bar{\Phi}_f(x_1, x_2) = \frac{1}{b_f} \int_Z^{Z_T} \Phi_f(x_1, x_2, x_3) dx_3, \quad \forall (x_1, x_2) \in \Omega.$$

Since

$$\begin{aligned} S_f \frac{\partial}{\partial t} \left(\int_Z^{Z_T} \Phi_f dx_3 \right) &= S_f \frac{\partial}{\partial t} (b_f \bar{\Phi}_f), \\ &= S_f b_f \frac{\partial \bar{\Phi}_f}{\partial t} + S_f \bar{\Phi}_f \frac{\partial b_f}{\partial t}, \end{aligned}$$

equation (2.3.12) becomes

$$\int_Z^{Z_T} S_f \frac{\partial \Phi_f}{\partial t} dx_3 = S_f b_f \frac{\partial \bar{\Phi}_f}{\partial t} + S_f (\bar{\Phi}_f - \Phi_f(Z_T)) \frac{\partial Z_T}{\partial t} - S_f (\bar{\Phi}_f - \Phi_f(Z)) \frac{\partial Z}{\partial t}.$$

Similarly, applying the Leibniz formula to the second term on the right-hand side of equation (2.3.11), we obtain

$$\begin{aligned} \int_Z^{Z_T} \operatorname{div}(\vec{q}_f) &= \int_Z^{Z_T} \left(\frac{\partial q_{fx_1}}{\partial x_1} + \frac{\partial q_{fx_2}}{\partial x_2} \right) dx_3 + \int_Z^{Z_T} \frac{\partial q_{fx_3}}{\partial x_3} dx_3, \\ &= \nabla' \cdot \left(\int_Z^{Z_T} \vec{q}'_f dx_3 \right) - \vec{q}'_f(Z_T) \cdot \nabla'(Z_T) + \vec{q}'_f(Z) \cdot \nabla'(Z) + q_{fx_3}(Z_T) - q_{fx_3}(Z), \\ &= \nabla' \cdot (b_f \bar{q}'_f) - \vec{q}'_f(Z) \cdot \left(\nabla'(Z_T) - \partial_{x_3} x_3 \right) + q_f(Z) \cdot \left(\nabla'(Z) - \partial_{x_3} x_3 \right), \end{aligned}$$

where:

$$\begin{aligned} \vec{q}'_f &= (q_{fx_1}, q_{fx_2}, q_{fx_3}) & \vec{q}'_f &= (q_{fx_1}, q_{fx_2}) \\ \nabla' \cdot () &= \frac{\partial ()}{\partial x_1} + \frac{\partial ()}{\partial x_2} + \frac{\partial ()}{\partial x_3}, & \nabla' \cdot () &= \frac{\partial ()}{\partial x_1} + \frac{\partial ()}{\partial x_2}. \end{aligned}$$

The vertical average of freshwater flux is given by

$$\bar{q}'_f \simeq \frac{1}{b_f} \int_Z^{Z_T} \vec{q}'_f dx_3 \simeq -\bar{\mathbf{D}}_f \nabla' \bar{\Phi}_f,$$

with

$$\bar{\mathbf{D}}_f(x_1, x_2) = \frac{1}{b_f} \int_Z^{Z_T} \mathbf{D}_f(x_1, x_2, x_3) dx_3, \quad \forall (x_1, x_2) \in \Omega, \text{ and } x_3 \in (Z, Z_T)$$

Using Dupuit's assumption, the following approximations hold up $\Phi_f(x_1, x_2, x_3) \simeq \bar{\Phi}_f(x_1, x_2)$ and $Q_f(x_1, x_2, x_3) \simeq Q_f = (x_1, x_2)$ with $(x_1, x_2) \in \Omega$ and $x_3 \in (Z, Z_T)$. One obtains the equation modeling freshwater flow process [39, 40]

$$S_f b_f \frac{\partial \bar{\Phi}_f}{\partial t} - \operatorname{div}(b_f \bar{\mathbf{D}}_f \nabla' \bar{\Phi}_f) + \vec{q}'_f(Z_T) \cdot \nabla'(x_3 - Z_T) - \vec{q}'_f(Z) \cdot \nabla'(x_3 - Z) = Q_f. \quad (2.3.13)$$

Likewise, using $Q_s(x_1, x_2, x_3) \simeq Q_s = (x_1, x_2)$ and integrating between Z_B and Z the equation (2.3.10), leads to the following equation describing the saltwater flow

$$S_s b_s \frac{\partial \bar{\Phi}_s}{\partial t} - \operatorname{div}(b_s \bar{\mathbf{D}}_s \nabla' \bar{\Phi}_s) + \vec{q}'_s(Z) \cdot \nabla'(x_3 - Z) - \vec{q}'_s(Z_B) \cdot \nabla'(x_3 - Z_B) = Q_s. \quad (2.3.14)$$

The vertical averages of Φ_s and \mathbf{D}_s are given by

$$\bar{\Phi}_s(x_1, x_2) = \frac{1}{b_s} \int_{Z_B}^Z \Phi_s(x_1, x_2, x_3) dx_3, \quad \text{and} \quad \bar{\mathbf{D}}_s(x_1, x_2) = \frac{1}{b_s} \int_{Z_B}^Z \mathbf{D}_s(x_1, x_2, x_3) dx_3.$$

The derived system (2.3.13)-(2.3.14) is composed of two equations with four unknowns ($\bar{\Phi}_f$, $\bar{\Phi}_s$, Z and Z_T). To reduce the number of unknowns, we close the system by approaching the fluxes at the interfaces. More precisely, we use the continuity of the fluxes and the pressure at the interfaces.

Pressure continuity at the interface

We assume the continuity of the pressure at the interface. The salt front elevation Z can be written as a function of the hydraulic head (2.3.5)

$$\begin{aligned} P_f|_{x_3=Z} = P_s|_{x_3=Z} &\iff \rho_f(\bar{\Phi}_f - Z) = \rho_s(\bar{\Phi}_s - Z), \\ &\iff Z = \left(1 + \frac{\rho_f}{\rho_s - \rho_f}\right) \bar{\Phi}_s - \frac{\rho_f}{\rho_s - \rho_f} \bar{\Phi}_f, \\ &\iff Z = (1 + \alpha) \bar{\Phi}_s - \alpha \bar{\Phi}_f, \end{aligned} \quad (2.3.15)$$

with $\alpha = \frac{\rho_f}{\rho_s - \rho_f}$ is the density contrast.

Approximation of the flux $\vec{q}_s|_{x_3=Z_B} \cdot \nabla(x_3 - Z_B)$

The base layer of the aquifer is impermeable. There is, therefore, no flow between the salt zone and the bottom $x_3 = Z_B$. One has

$$\vec{q}_s|_{z=Z_B} \cdot \nabla(x_3 - Z_B) = 0.$$

The base of the aquifer Z_B is assumed spatially variable.

Approximation of the flux $\vec{q}_i|_{x_3=Z} \cdot \nabla(x_3 - Z), i = f, s$

In the case of the sharp interface approach, the normal components of the velocity at the interface are equal in each zone. This corresponds to no transfer of mass across the interface. Thus, we obtain

$$\left(\frac{\vec{q}_f|_{x_3=Z}}{\phi} - \vec{v}\right) \cdot \vec{n} = \left(\frac{\vec{q}_s|_{x_3=Z}}{\phi} - \vec{v}\right) \cdot \vec{n} = 0,$$

where \vec{n} is the normal unit vector with respect to the abrupt interface, \vec{v} [m.s⁻¹] is the interface velocity. We get

$$\vec{q}_f|_{x_3=Z} \cdot \nabla(x_3 - Z) = \vec{q}_s|_{x_3=Z} \cdot \nabla(x_3 - Z) = \phi \frac{\partial Z}{\partial t}.$$

Approximation of the flux $\vec{q}_f|_{x_3=Z_T} \cdot \nabla(x_3 - Z_T)$

The modeling of the upper surface depends on the nature of the aquifer, we will distinguish between free and confined aquifers.

In the case of a confined aquifer, the upper surface of the aquifer is impermeable, so there is no flow between the roof and the freshwater area. The flux through the upper interface of the aquifer is given by:

$$\vec{q}_f|_{x_3=Z_T} \cdot \nabla(x_3 - Z_T) = 0.$$

In the case of a free aquifer, the upper surface consists of a permeable layer, which can be crossed by water at reasonable speeds. This limit corresponds to the piezometric surface where there are exchanges with the outside world such as injections and rainwater supply. The flow is given by

$$\vec{q}_f|_{x_3=Z_T} \cdot \nabla(x_3 - Z_T) = \phi \frac{\partial \bar{\Phi}_f}{\partial t}.$$

We introduce a parameter β to combine the two cases of the confined and unconfined aquifer,

$$\beta = \begin{cases} 1 & \text{if the aquifer is free,} \\ 0 & \text{if the aquifer is confined.} \end{cases}$$

By replacing the flux in the equations (2.3.13) and (2.3.14) and Z by its formula, we obtain a 2D system modeling freshwater and saltwater flows

$$\begin{cases} \left\{ S_f b_f + (\beta + \alpha) \phi(x) \right\} \frac{\partial \bar{\Phi}_f}{\partial t} - (1 + \alpha) \phi(x) \frac{\partial \bar{\Phi}_s}{\partial t} - \operatorname{div} (b_f \bar{\mathbf{D}}_f \nabla \bar{\Phi}_f) & = Q_f, \\ \left\{ S_s b_s + (1 + \alpha) \phi(x) \right\} \frac{\partial \bar{\Phi}_s}{\partial t} - \alpha \phi(x) \frac{\partial u}{\partial t} - \operatorname{div} (b_s \bar{\mathbf{D}}_s \nabla \bar{\Phi}_s) & = Q_s. \end{cases}$$

The thicknesses of freshwater and saltwater are respectively $b_f = Z_T - Z$ and $b_s = Z - Z_B$. The salt front is obtained by using the continuity of pressure on the interface $Z = (1 + \alpha) \bar{\Phi}_s - \alpha \bar{\Phi}_f$. The upper surface Z_T is replaced by $\bar{\Phi}_f$ in the case of a free aquifer and by a constant in the confined case.

2.3.5 Mathematical model of the sharp interface problem

In this subsection, we present the seawater intrusion sharp interface model, where freshwater and saltwater heads are the unknowns. Let Ω be an open polygonal domain, $\partial\Omega = \Gamma = \bar{\Gamma}_D \cup \bar{\Gamma}_N$, $x = (x_1, x_2) \in \mathbb{R}^2$ and $]0, T[$ a time interval. Let $\Omega_T =]0, T[\times \Omega$. We note $u = \bar{\Phi}_f$, $v = \bar{\Phi}_s$ and $\bar{\mathbf{D}}_i = \mathbf{D}_i, i = f, s$. The mathematical system is given by:

$$\begin{cases} \beta_f(u, v) \frac{\partial u}{\partial t} - \omega(\cdot) \frac{\partial v}{\partial t} - \operatorname{div} (b_f(u, v) \mathbf{D}_f \nabla u) & = Q_f & \text{in } \Omega_T, \\ \beta_s(u, v) \frac{\partial v}{\partial t} - \lambda(\cdot) \frac{\partial u}{\partial t} - \operatorname{div} (b_s(u, v) \mathbf{D}_s \nabla v) & = Q_s & \text{in } \Omega_T, \\ u(0, \cdot) = u^0(\cdot), \quad v(0, \cdot) = v^0(\cdot) & & \text{in } \Omega, \\ v = v_D, \quad u = u_D & & \text{on }]0, T[\times \Gamma_D, \\ b_f(u, v) \mathbf{D}_f \nabla u \cdot \vec{n} = 0, \quad b_s(u, v) \mathbf{D}_s \nabla v \cdot \vec{n} = 0 & & \text{on }]0, T[\times \Gamma_N. \end{cases} \quad (2.3.16)$$

with

$$\begin{aligned} \beta_f(u, v) &= S_f b_f(u, v) + \phi(x)(\beta + \alpha), & \omega(x) &= \phi(x)(1 + \alpha), \\ \beta_s(u, v) &= S_s b_s(u, v) + \phi(x)(1 + \alpha), & \text{and } \lambda(x) &= \phi(x)\alpha. \end{aligned}$$

The thickness of freshwater is given by

$$b_f(u, v) = \begin{cases} (1 + \alpha)(u - v) & \text{free aquifer,} \\ Z_T - (1 + \alpha)v + \alpha u & \text{confined aquifer,} \end{cases}$$

while that of saltwater is as follows $b_s(u, v) = \alpha u - (1 + \alpha)v - Z_B$. The initial conditions $u^0(x)$ and $v^0(x)$ are given for u and v at ($t=0$) to describe the initial state of the aquifer.

The problem is a coupled system of two nonlinear parabolic partial differential equations simulating two immiscible fluids. The unknowns are u the hydraulic head of freshwater and v the hydraulic head of saltwater. The depth of the freshwater/saltwater surface can be calculated from the following relationship

$$Z = (1 + \alpha)v - \alpha u.$$

2.4 Conclusion

In this section, we conclude the work carried out in the context of marine intrusion modeling. We first presented a state of the art of saline intrusion models. Three approaches were outlined. The classical 2D sharp interface approach, which assumes that the two fluids are immiscible. This approach simulates respectively the location of the salt front and the depth of the free surface. The second is the 3D variable density approach, which assumes that the two masses of water interact with each other. It is characterized by the variation of the salt concentration and the hydraulic head of the freshwater. Furthermore, we presented a new approach [25] corresponding to the sharp-diffuse interfaces model. It is a combination of the two previous approaches. The two fluids are assumed to be immiscible and the dynamics of the transition zones are taken into account.

The other part of this chapter is devoted to the formulation of the mathematical model using the sharp interface approach. We first introduced the physical laws of the continuity equation and Darcy's law. Moreover, we consider Bear's hypothesis and Dupuit's approximation to upscale the initial 3D problem. We presented the mathematical model of the marine intrusion using the sharp interface approach in a free and confined aquifer. The system of equations simulating freshwater and saltwater heads is further completed with Neumann and Dirichlet boundary conditions. The elevation of the salt front is predicted as a function of the head of freshwater and saltwater. The numerical resolution of this model will be the purpose of the next chapter.

Chapter 3

A finite volume method for numerical simulation of the sharp interface model

Contents

| | | |
|------------|--------------------------------------------------------|-----------|
| 3.1 | Introduction | 23 |
| 3.2 | A fully implicit finite volume numerical scheme | 24 |
| 3.2.1 | Discretization and basic notations | 25 |
| 3.2.2 | Resolution of the nonlinear system | 29 |
| 3.3 | Implementation of the numerical scheme | 32 |
| 3.4 | Numerical simulations | 32 |
| 3.4.1 | Test 1: The rotating interface problem | 33 |
| 3.4.2 | Test 2: a field-scale free aquifer problem | 37 |
| 3.4.3 | Test 3: Souss-Chtouka case study | 47 |
| 3.4.4 | Test 4: Tripoli aquifer case study | 60 |
| 3.5 | Conclusion | 67 |

3.1 Introduction

This chapter deals with a numerical method for performing numerical simulations of the sharp interface model in a coastal aquifer. In this work, we develop a fully implicit, cell-centered finite volume method to predict seawater intrusion by means of this approach. A complete presentation of the derivation of the numerical scheme is presented in section 3.2. To approximate the diffusive terms, a Two-Point Flux Approximation (TPFA) method [42] on structured mesh is performed. An upwind scheme is used to evaluate the convective fluxes. The nonlinear system is solved by a Newton's method, wherein each iteration a linear system is solved by an iterative Krylov method.

After that, we have implemented and integrated this scheme in a new module in the DuMuX framework [1]. A short introduction of the platform is presented in section 3.3. The developed module enables us to solve a coupled system of two parabolic equations modeling saline intrusion in coastal aquifers. Our numerical scheme has been tested and validated by different 1D, 2D test cases, including real-scale Benchmarks. First of all, we validate our model in the case of a confined aquifer with the rotating interface problem of Keulegan [61]. Numerical results, presented in subsection 3.4.1, are compared to the analytical solution and showed a good agreement with those presented in [8, 67]. After that, we validate our model in the case of an unconfined aquifer. We proceed to the study of the numerical convergence of the scheme on different grid resolutions. Then, we applied our approach to two real test cases: the first test "field-scale free aquifer" is presented in [71]. Numerical simulations over 30 years of exploitation of the aquifer are presented in subsection 3.4.2. The comparison between our results and those presented in [71] for eleven scenarios illustrates the robustness and efficiency of our approach. The second test case, presented in [5], corresponds to the Souss-Chtouka plain located in the southwest of Morocco. Hydrological data and physical parameters are used to predict seawater intrusion in the Souss-Chtouka aquifer. The numerical results showing the evolution of different quantities during 80 years of over-exploitation of the aquifer are presented in subsection 3.4.3. Afterwards, we validated our implemented module on a real test case corresponding to the Tripoli aquifer in the northeast of Lebanon. Numerical simulations over 20 years of exploitation are presented in section 3.4.4. The comparison of our numerical results and those presented in [57] showed a good agreement, which ensures the validity of our module to provide efficient and accurate results in real scale test cases. Section 3.5 contains concluding remarks.

3.2 A fully implicit finite volume numerical scheme

This section aims to develop a finite volume numerical scheme for the sharp interface approach. We consider the system of equations, presented in chapter 2, which simulates freshwater head (u) and saltwater head (v) into confined and unconfined aquifers:

$$\left\{ \begin{array}{l} \beta_f(u, v) \frac{\partial u}{\partial t} - \omega(\cdot) \frac{\partial v}{\partial t} - \operatorname{div}(b_f(u, v) \mathbf{D}_f \nabla u) = Q_f \quad \text{in } \Omega_T, \\ \beta_s(u, v) \frac{\partial v}{\partial t} - \lambda(\cdot) \frac{\partial u}{\partial t} - \operatorname{div}(b_s(u, v) \mathbf{D}_s \nabla v) = Q_s \quad \text{in } \Omega_T, \\ u(0, \cdot) = u^0(\cdot), \quad v(0, \cdot) = v^0(\cdot) \quad \text{in } \Omega, \\ v = v_D, \quad u = u_D \quad \text{on }]0, T[\times \Gamma_D, \\ b_f(u, v) \mathbf{D}_f \nabla u \cdot \vec{n} = 0, \quad b_s(u, v) \mathbf{D}_s \nabla v \cdot \vec{n} = 0 \quad \text{on }]0, T[\times \Gamma_N. \end{array} \right. \quad (3.2.1)$$

which involve the following functions:

$$\begin{aligned} \beta_f(u, v) &= S_f b_f(u, v) + \phi(x)(\beta + \alpha), & \omega(x) &= \phi(x)(1 + \alpha), \\ \beta_s(u, v) &= S_s b_s(u, v) + \phi(x)(1 + \alpha), & \lambda(x) &= \phi(x)\alpha. \end{aligned}$$

The thickness of freshwater is given by

$$b_f(u, v) = \begin{cases} (1 + \alpha)(u - v) & \text{free aquifer,} \\ Z_T - (1 + \alpha)v + \alpha u & \text{confined aquifer,} \end{cases}$$

while that of saltwater is as follows $b_s(u, v) = \alpha u - (1 + \alpha)v - Z_B$. We generalize our model in both cases of free and confined aquifers by introducing a parameter

$$\beta = \begin{cases} 1, & \text{if the aquifer is free,} \\ 0, & \text{if the aquifer is confined.} \end{cases}$$

The source terms Q_f and Q_s represent the amount of freshwater and saltwater injected (or pumped) per unit surface, respectively. The domain Ω is illustrated in Figure 3.1

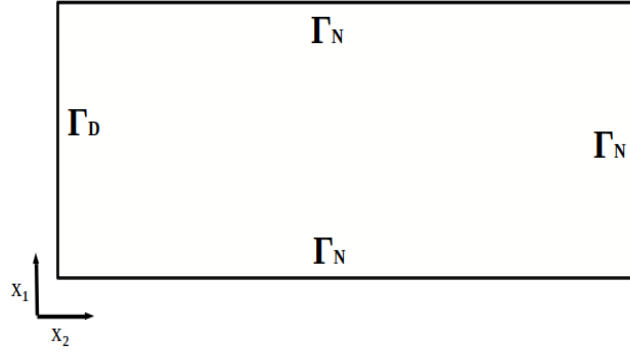


Figure 3.1: Geometry of the domain Ω .

3.2.1 Discretization and basic notations

In this subsection, we give the parameters and the notations which used in the derivation of the numerical scheme. Here, we choose a cell-centered finite volume methods for the discretization in space. For the sake of simplicity, we present the scheme on a structured mesh which suitable with TPFA method. The main advantage of this scheme is to preserve the conservation property of the mass and the positivity of the freshwater and saltwater thicknesses. The extension to unstructured grids will be presented in the next chapter for the so called the Multi Point Flux Approximation (MPFA)[3].

We introduce the following notations

- Let $\{t_0, \dots, t_N\}$ be a partition of $[0, T]$, $\Delta t^n = t_{n+1} - t_n$ the time step size and $\Delta t = \max_n \Delta t^n$.
- let (\mathcal{T}) be a rectangular partition of $\bar{\Omega}$, such that $\bar{\Omega} = \cup_{V_k \in \mathcal{T}} \bar{V}_k$. $\partial V_k = \bar{V}_k \setminus V_k$ the boundary of V_k .

- The physical parameters are given as constant values on each cell. One has

$$\phi_k = \frac{1}{|\mathbf{V}_k|} \int_{\mathbf{V}_k} \phi(x) dx, \quad w_k = \frac{1}{|\mathbf{V}_k|} \int_{\mathbf{V}_k} w(x) dx \quad \text{and} \quad \lambda_k = \frac{1}{|\mathbf{V}_k|} \int_{\mathbf{V}_k} \lambda(x) dx$$

- The freshwater thickness can be written as $b_f(u, v) = \chi(u) - (1 + \alpha)v$ with

$$\chi(u) = \begin{cases} (1 + \alpha)u, & \text{in the case of free aquifer,} \\ Z_T + \alpha u, & \text{in the case of confined aquifer.} \end{cases}$$

We define the nonlinear function $\eta \in \mathbb{C}^1(\Omega)$ by:

$$\eta(u) = \int_0^u \chi(s) ds.$$

Also, we define the function

$$\varphi(v) = \frac{(1 + \alpha)}{2} v^2.$$

- For an initial condition $u_0 \in \mathbf{L}^\infty(\Omega)$ (resp. v_0), we put : $u_k^0 = \frac{1}{|V_k|} \int_{V_k} u^0(x) dx$ (resp. v_k^0).

Other notations are presented in Figure 3.2.

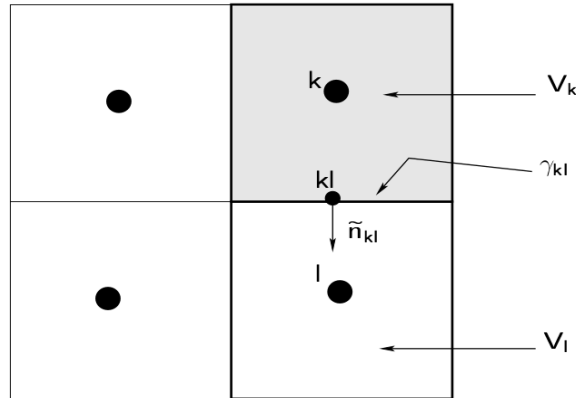


Figure 3.2: Discretisation by a cell-centred finite volume method.

We present the derivation of the numerical scheme using a cell-centered finite volume method in space. For the time discretization, we use an Euler implicit method. The approximation of the convective subfluxes is done with an upwind scheme. In the diffusion term, we approximate the gradient on the interface by a TPF method. The control volume V_k where the numerical scheme will be written is illustrated in Figure 3.2.

We integrate the freshwater and the saltwater equations in the system (3.2.1) on $]t_n, t_{n+1}[\times V_k$, we obtain:

- The freshwater equation:

$$\begin{aligned} & \int_{t_n}^{t_{n+1}} \int_{V_k} \beta_f(u, v) \frac{\partial u}{\partial t} dx dt - \int_{t_n}^{t_{n+1}} \int_{V_k} \omega(x) \frac{\partial v}{\partial t} dx dt - \int_{t_n}^{t_{n+1}} \int_{V_k} \text{div}(b_f(x, u, v) \mathbf{D}_f \nabla u) dx dt \\ & = \int_{t_n}^{t_{n+1}} \int_{V_k} Q_f dx dt. \end{aligned}$$

- The saltwater equation:

$$\begin{aligned} & \int_{t_n}^{t_{n+1}} \int_{\mathbf{V}_k} \beta_s(u, v) \frac{\partial v}{\partial t} dx dt - \int_{t_n}^{t_{n+1}} \int_{\mathbf{V}_k} \lambda(x) \frac{\partial u}{\partial t} dx dt - \int_{t_n}^{t_{n+1}} \int_{\mathbf{V}_k} \operatorname{div}(b_s(x, u, v) \mathbf{D}_s \nabla v) dx dt \\ &= \int_{t_n}^{t_{n+1}} \int_{\mathbf{V}_k} Q_s dx dt. \end{aligned}$$

Let $u_k^n = \frac{1}{|\mathbf{V}_k|} \int_{\mathbf{V}_k} u(x, t^n) dx$ (resp. $v_k^n = \frac{1}{|\mathbf{V}_k|} \int_{\mathbf{V}_k} v(x, t^n) dx$) be the approximate value of u (resp. v) in the control volume \mathbf{V}_k at time t_n . Using an implicit approximation in time, the numerical scheme can be written as follows

$$\begin{aligned} & \frac{|\mathbf{V}_k|}{\Delta t^n} \{ \beta_f(u_k^{n+1}, v_k^{n+1}) (u_k^{n+1} - u_k^n) - w_k (v_k^{n+1} - v_k^n) \} \\ & - \sum_{l \in \partial V(k)} \int_{\gamma_{kl}} \left\{ \mathbf{D}_f \nabla \eta(u^{n+1}) - (1 + \alpha) \mathbf{D}_f v^{n+1} \nabla u^{n+1} \right\}_{kl} \cdot \vec{n}_{kl} d\gamma \\ &= Q_{f,k}^{n+1}, \\ & \frac{|\mathbf{V}_k|}{\Delta t^n} \{ \beta_s(u_k^{n+1}, v_k^{n+1}) (v_k^{n+1} - v_k^n) - \lambda_k (u_k^{n+1} - u_k^n) \} \\ & - \sum_{l \in \partial V(k)} \int_{\gamma_{kl}} \left\{ \mathbf{D}_s \nabla \varphi(v^{n+1}) - \mathbf{D}_s (\alpha u^{n+1} + Z_B) \nabla v^{n+1} \right\}_{kl} \cdot \vec{n}_{kl} d\gamma \\ &= Q_{s,k}^{n+1}, \end{aligned}$$

where \vec{n}_{kl} is the unit outer normal to γ_{kl} and $V(k)$ is the set of adjacent elements of \mathbf{V}_k . We denote by $Q_{f,k}^{n+1}$ (resp. $Q_{s,k}^{n+1}$) the average value of Q_f (resp. Q_s) on V_k at time t_{n+1} . The exact diffusion fluxes are given by

$$F_{kl}(u^{n+1}) = - \int_{\gamma_{kl}} \{ \mathbf{D}_f \}_{kl} \{ \nabla \eta(u^{n+1}) \}_{kl} \cdot \vec{n}_{kl} d\gamma_{kl}, \quad F_{kl}(v^{n+1}) = - \int_{\gamma_{kl}} \{ \mathbf{D}_s \}_{kl} \{ \nabla \varphi(v^{n+1}) \}_{kl} \cdot \vec{n}_{kl} d\gamma_{kl},$$

while the exact convectif fluxes are given by

$$\begin{aligned} G_{kl}(u^{n+1}) &= (1 + \alpha) \int_{\gamma_{kl}} \{ \mathbf{D}_f \}_{kl} \{ v^{n+1} \}_{kl} \nabla u^{n+1} \cdot \vec{n}_{kl} d\gamma_{kl}, \\ G_{kl}(v^{n+1}) &= \int_{\gamma_{kl}} \{ \mathbf{D}_s \}_{kl} (\alpha \{ u^{n+1} \}_{kl} + Z_B) \nabla v^{n+1} \cdot \vec{n}_{kl} d\gamma_{kl}. \end{aligned}$$

The next step consist to approximate the exact fluxes.

Numerical diffusion fluxes:

The gradient of the freshwater and saltwater heads on the interface γ_{kl} are approximated by a TPFA method. For the computation of the diffusion coefficients \mathbf{D}_f (resp. \mathbf{D}_s), we use an harmonic average between two adjacent elements. Here is the expression of the numerical fluxes defined as a function of the main unknowns:

$$\begin{aligned} F_{kl}^*(u_k^{n+1}) &= - \{ \mathbf{D}_f \}_{kl}^{har} \frac{\eta(u_l^{n+1}) - \eta(u_k^{n+1})}{d_{kl}} |\gamma_{kl}|, \\ F_{kl}^*(v_k^{n+1}) &= - \{ \mathbf{D}_s \}_{kl}^{har} \frac{\varphi(v_l^{n+1}) - \varphi(v_k^{n+1})}{d_{kl}} |\gamma_{kl}|, \end{aligned}$$

where $\{\mathbf{D}_f\}_{kl}^{har}$ is the harmonic average of $\{\mathbf{D}_f\}_k$ and $\{\mathbf{D}_f\}_l$, while d_{kl} is the distance between the centers of the control volume \mathbf{V}_k and \mathbf{V}_l .

Numerical convective fluxes:

For the approximation of the convective terms, we use a fully implicit upwind scheme. The freshwater and saltwater heads are therefore evaluated implicitly and dependently on the sign of the freshwater velocity. The numerical convective fluxes at the interface γ_{kl} are given by:

$$\begin{aligned} G_{kl}^*(u_k^{n+1}) &= \{v^{n+1}\}_{kl}^{up} \{\mathbf{D}_f\}_{kl} \{\nabla u^{n+1}\}_{kl} \cdot \vec{n}_{kl} |\gamma_{kl}| (1 + \alpha), \\ G_{kl}^*(v_k^{n+1}) &= (\alpha \{u^{n+1}\}_{kl}^{up} + Z_B) \{\mathbf{D}_s\}_{kl} \{\nabla v^{n+1}\}_{kl} \cdot \vec{n}_{kl} |\gamma_{kl}|. \end{aligned}$$

with

$$\{v^{n+1}\}_{kl}^{up} = \begin{cases} v_k^{n+1} & \text{if } \{\mathbf{D}_f\}_{kl} \{\nabla u^{n+1}\}_{kl} \cdot \vec{n}_{kl} > 0 \\ v_l^{n+1} & \text{else} \end{cases} \quad (3.2.2)$$

In an analogue way, the discrete value $\{u^{n+1}\}_{kl}^{up}$ is evaluated on the interface γ_{kl} .

Finally, the fully implicit cell-centered finite volume numerical scheme issued from the sharp interface model (3.2.1) yields to the nonlinear coupled equations:

$$\begin{aligned} & \frac{|\mathbf{V}_k|}{\Delta t^n} \left\{ \beta_f(u_k^{n+1}, v_k^{n+1}) (u_k^{n+1} - u_k^n) - w_k (v_k^{n+1} - v_k^n) \right\} \\ & - \sum_{l \in \partial V(k)} \{\mathbf{D}_f\}_{kl}^{har} |\gamma_{kl}| \left(\frac{\eta(u_l^{n+1}) - \eta(u_k^{n+1})}{d_{kl}} - (1 + \alpha) \{v^{n+1}\}_{kl}^{up} \frac{u_l^{n+1} - u_k^{n+1}}{d_{kl}} \right) \\ & = Q_{f,k}^{n+1}, \end{aligned} \quad (3.2.3)$$

$$\begin{aligned} & \frac{|\mathbf{V}_k|}{\Delta t^n} \left\{ \beta_s(u_k^{n+1}, v_k^{n+1}) (v_k^{n+1} - v_k^n) - \lambda_k (u_k^{n+1} - u_k^n) \right\} \\ & - \sum_{l \in \partial V(k)} \{\mathbf{D}_s\}_{kl}^{har} |\gamma_{kl}| \left(\frac{\varphi(v_l^{n+1}) - \varphi(v_k^{n+1})}{d_{kl}} - (\alpha \{u^{n+1}\}_{kl}^{up} + Z_B) \frac{v_l^{n+1} - v_k^{n+1}}{d_{kl}} \right) \\ & = Q_{s,k}^{n+1}. \end{aligned} \quad (3.2.4)$$

The initial conditions are given by

$$u_k^0 = \frac{1}{|\mathbf{V}_k|} \int_{\mathbf{V}_k} u^0(x) dx, \quad \text{and} \quad v_k^0 = \frac{1}{|\mathbf{V}_k|} \int_{\mathbf{V}_k} v^0(x) dx. \quad (3.2.5)$$

For the discretization of the boundary conditions, we distinguish between two cases

- Homogeneous Neumann BCs on Γ_N , one has

$$F_N^*(u_k^{n+1}) = F_N^*(v_k^{n+1}) = G_N^*(u_k^{n+1}) = G_N^*(v_k^{n+1}) = 0. \quad (3.2.6)$$

- Dirichlet BCs on Γ_D , we have

$$\begin{aligned} F_D^*(u_k^{n+1}) &= -\{\mathbf{D}_f\}_k \frac{\eta(u_D) - \eta(u_k^{n+1})}{d_{kl}} |\gamma_k|, \\ F_k^*(v_k^{n+1}) &= -\{\mathbf{D}_f\}_k \frac{\eta(v_D) - \eta(u_k^{n+1})}{d_{kl}} |\gamma_k|, \end{aligned} \quad (3.2.7)$$

$$G_D^*(u_k^{n+1}) = \{v^{n+1}\}_D^{up} \{\mathbf{D}_f\}_k \{\nabla u^{n+1}\}_D \cdot \vec{n}_D |\gamma_k|, \quad (3.2.8)$$

$$G_D^*(v_k^{n+1}) = \{u^{n+1}\}_D^{up} \{\mathbf{D}_f\}_k \{\nabla v^{n+1}\}_D \cdot \vec{n}_D |\gamma_k|, \quad (3.2.9)$$

with

$$\{v^{n+1}\}_D^{up} = \begin{cases} v_k^{n+1} & \text{if } \{\mathbf{D}_f\}_k \{\nabla u^{n+1}\}_{kl} \cdot \vec{n}_{kl} > 0 \\ v_D^{n+1} & \text{else} \end{cases}$$

3.2.2 Resolution of the nonlinear system

The numerical scheme (3.2.3)-(3.2.8) derived from the TPFA method is formulated by two coupled nonlinear equations. Solving the governing equations is not obvious. The difficulty arises from the nonlinearity and the coupling of the system. To linearise the coupled system at each time step Δt^n , we use Newton's method wherein each iteration, a linear system is solved using iterative linear solvers provided by the external library of DUNE [2]. The residual of the system of equations (3.2.3)-(3.2.4) which is a function of the discrete solution (u_k^{n+1}, v_k^{n+1}) can be written by the two equations: $\forall k \in \mathcal{T}$, and $n \in \{0, \dots, N-1\}$

$$\begin{cases} \{\mathcal{R}_f\}_k^{n+1}(u_k^{n+1}, v_k^{n+1}) = 0, \\ \{\mathcal{R}_s\}_k^{n+1}(u_k^{n+1}, v_k^{n+1}) = 0. \end{cases} \quad (3.2.10)$$

We note that the local residual function \mathcal{R}_f (resp. \mathcal{R}_s) of the discrete freshwater (resp. saltwater) equation is given at each element \mathbf{V}_k and any time t_{n+1} . In our implemented module, we use some numerical differentiation techniques to approximate the derivatives of the residual in the calculation of the Jacobian matrix. Adding or subtracting epsilon from the solution in the numerical differential for each coefficient of the local Jacobian matrix requests more time within the numerical context (CPU time). However, in practice, we do not recalculate the whole matrix at each Newton iteration, but only a part of it according to the local residual error. Thereafter, using some numerical strategies, we assemble the global residual and then the global matrix. To show and illustrate the matrix form of the linear system solved at each Newton's iteration, we propose to compute explicitly the derivatives of the local residue from our numerical scheme (3.2.3)-(3.2.4). To do so, we consider a control volume \mathbf{V}_k sharing an edge $l \in \partial V(k)$ with its neighbor \mathbf{V}_l . We begin by computing the local residual of freshwater and saltwater with respect to the discrete solution u_k^{n+1} and v_k^{n+1} . We introduce the following notations

$$\alpha_{kl}^v = \begin{cases} 1 & \text{if } \{\mathbf{D}_f\}_{kl} \{\nabla u^{n+1}\}_{kl} \cdot \vec{n}_{kl} > 0 \\ 0 & \text{else} \end{cases} \quad \alpha_{kl}^u = \begin{cases} 1 & \text{if } \{\mathbf{D}_f\}_{kl} \{\nabla v^{n+1}\}_{kl} \cdot \vec{n}_{kl} > 0 \\ 0 & \text{else} \end{cases} \quad (3.2.11)$$

The derivatives of the local freshwater residue $\mathcal{R}_f(u_k^{n+1}, v_k^{n+1})$ on the element \mathbf{V}_k and at time t^{n+1} with respect to u_k^{n+1} and v_k^{n+1} are the following:

$$\begin{aligned} \frac{\partial \{\mathcal{R}_f\}_k^{n+1}}{\partial u_k^{n+1}} &= \frac{|\mathbf{V}_k|}{\Delta t^n} \left\{ \frac{\partial \beta_f(u_k^{n+1}, v_k^{n+1})}{\partial u_k^{n+1}} (u_k^{n+1} - u_k^n) + \beta_f(u_k^{n+1}, v_k^{n+1}) \right\} \\ &\quad - \sum_{l \in \partial V(k)} \{\mathbf{D}_f\}_{kl}^{har} \frac{\partial}{\partial u_k^{n+1}} \left(\frac{\eta(u_l^{n+1}) - \eta(u_k^{n+1})}{d_{kl}} \right) |\gamma_{kl}| \end{aligned}$$

$$+ (1 + \alpha) \sum_{l \in \partial V(k)} \{\mathbf{D}_f\}_{kl}^{har} \alpha_{kl}^v v_k^{n+1} \frac{\partial}{\partial u_k^{n+1}} \left(\frac{u_l^{n+1} - u_k^{n+1}}{d_{kl}} \right) |\gamma_{kl}|, \quad (3.2.12)$$

$$\begin{aligned} \frac{\partial \{\mathcal{R}_f\}_k^{n+1}}{\partial v_k^{n+1}} &= \frac{|\mathbf{V}_k|}{\Delta t^n} \left\{ \frac{\partial \beta_f(u_k^{n+1}, v_k^{n+1})}{\partial u_k^{n+1}} (u_k^{n+1} - u_k^n) - \omega_k \right\} \\ &+ (1 + \alpha) \sum_{l \in \partial V(k)} \{\mathbf{D}_f\}_{kl}^{har} \alpha_{kl}^v \left(\frac{u_l^{n+1} - u_k^{n+1}}{d_{kl}} \right) |\gamma_{kl}|. \end{aligned} \quad (3.2.13)$$

Now, we calculate the derivative of the local residual $\{\mathcal{R}_f\}_k^{n+1}$ with respect to the approximate solutions on the element \mathbf{V}_l .

$$\begin{aligned} \frac{\partial \{\mathcal{R}_f\}_k^{n+1}}{\partial u_l^{n+1}} &= - \sum_{l \in \partial V(k)} \{\mathbf{D}_f\}_{\mathbf{D}l}^{har} \frac{\partial}{\partial u_l^{n+1}} \left(\frac{\eta(u_l^{n+1}) - \eta(u_{\mathbf{D}}^{n+1})}{d_{kl}} \right) |\gamma_{kl}| \\ &+ (1 + \alpha) \sum_{l \in \partial V(k)} \{\mathbf{D}_f\}_{kl}^{har} \alpha_{kl}^v v_l^{n+1} \frac{\partial}{\partial u_l^{n+1}} \left(\frac{u_l^{n+1} - u_k^{n+1}}{d_{kl}} \right) |\gamma_{kl}|, \end{aligned} \quad (3.2.14)$$

$$\frac{\partial \{\mathcal{R}_f\}_k^{n+1}}{\partial v_l^{n+1}} = (1 + \alpha) \sum_{l \in \partial V(k)} \{\mathbf{D}_f\}_{kl}^{har} \alpha_{kl}^v \left(\frac{u_l^{n+1} - u_k^{n+1}}{d_{kl}} \right) |\gamma_{kl}|. \quad (3.2.15)$$

The derivative of the local saltwater residual $\{\mathcal{R}_s\}_k^{n+1}$ on the element \mathbf{V}_k at time t^{n+1} with respect to the discrete unknowns v_k^{n+1} and u_k^{n+1} are as follows respectively:

$$\begin{aligned} \frac{\partial \{\mathcal{R}_s\}_k^{n+1}}{\partial v_k^{n+1}} &= \frac{|\mathbf{V}_k|}{\Delta t^n} \left\{ \frac{\partial \beta_s(u_k^{n+1}, v_k^{n+1})}{\partial v_k^{n+1}} (v_k^{n+1} - v_k^n) + \beta_s(u_k^{n+1}, v_k^{n+1}) \right\} \\ &- \sum_{l \in \partial V(k)} \{\mathbf{D}_s\}_{kl}^{har} \frac{\partial}{\partial v_k^{n+1}} \left(\frac{\varphi(v_l^{n+1}) - \varphi(v_k^{n+1})}{d_{kl}} \right) |\gamma_{kl}| \\ &+ \sum_{l \in \partial V(k)} \{\mathbf{D}_s\}_{kl}^{har} \alpha_{kl}^u u_k^{n+1} \frac{\partial}{\partial v_k^{n+1}} \left(\frac{v_l^{n+1} - v_k^{n+1}}{d_{kl}} \right) |\gamma_{kl}|, \end{aligned} \quad (3.2.16)$$

$$\begin{aligned} \frac{\partial \{\mathcal{R}_s\}_k^{n+1}}{\partial u_k^{n+1}} &= \frac{|\mathbf{V}_k|}{\Delta t^n} \left\{ \frac{\partial \beta_s(u_k^{n+1}, v_k^{n+1})}{\partial u_k^{n+1}} (v_k^{n+1} - v_k^n) - \lambda_k \right\} \\ &+ \sum_{l \in \partial V(k)} \{\mathbf{D}_s\}_{kl}^{har} (\alpha \alpha_{kl}^v + Z_B) \left(\frac{v_l^{n+1} - v_k^{n+1}}{d_{kl}} \right) |\gamma_{kl}|. \end{aligned} \quad (3.2.17)$$

For the derivative of the local residue of the saltwater equation with respect to the discrete unknowns u_l^{n+1} and v_l^{n+1} , we have

$$\frac{\partial \{\mathcal{R}_s\}_k^{n+1}}{\partial v_l^{n+1}} = - \sum_{l \in \partial V(k)} \{\mathbf{D}_s\}_{kl}^{har} \frac{\partial}{\partial v_l^{n+1}} \left(\frac{\varphi(v_l^{n+1}) - \varphi(u_k^{n+1})}{d_{kl}} \right) |\gamma_{kl}|$$

$$+ \sum_{l \in \partial V(k)} \{\mathbf{D}_s\}_{kl}^{har} (\alpha_{kl}^u u_l^{n+1} + Z_B) \frac{\partial}{\partial v_l^{n+1}} \left(\frac{v_l^{n+1} - v_k^{n+1}}{d_{kl}} \right) |\gamma_{kl}|, \quad (3.2.18)$$

$$\frac{\partial \{\mathcal{R}_s\}_k^{n+1}}{\partial u_l^{n+1}} = \sum_{l \in \partial V(k)} \{\mathbf{D}_s\}_{kl}^{har} \alpha_{kl}^u \left(\frac{v_l^{n+1} - v_k^{n+1}}{d_{kl}} \right) |\gamma_{kl}|. \quad (3.2.19)$$

Now we consider two adjacent elements \mathbf{V}_k and \mathbf{V}_l . We illustrate the blocks of the matrix on these two cells without considering the other cells. Therefore, the structure of the Jacobian matrix is given by

$$\begin{pmatrix} \mathbb{J}_{kk} & \mathbb{J}_{kl} \\ \mathbb{J}_{lk} & \mathbb{J}_{ll} \end{pmatrix} \quad (3.2.20)$$

- The block \mathbb{J}_{kk} (resp. \mathbb{J}_{ll}) represents the derivative of the residual issued from the system (3.2.3)-(3.2.4) on the control volume \mathbf{V}_k (resp. \mathbf{V}_l) with respect to the discrete unknowns of freshwater and the saltwater heads on the element \mathbf{V}_k (resp. \mathbf{V}_l). The explicit form of the blocks is given by

$$\mathbb{J}_{kk} = \begin{pmatrix} \frac{\partial \{\mathcal{R}_f\}_k^{n+1}}{\partial u_k^{n+1}} & \frac{\partial \{\mathcal{R}_f\}_k^{n+1}}{\partial v_k^{n+1}} \\ \frac{\partial \{\mathcal{R}_s\}_k^{n+1}}{\partial u_k^{n+1}} & \frac{\partial \{\mathcal{R}_s\}_k^{n+1}}{\partial v_k^{n+1}} \end{pmatrix} \quad (3.2.21)$$

$$\mathbb{J}_{ll} = \begin{pmatrix} \frac{\partial \{\mathcal{R}_f\}_l^{n+1}}{\partial u_l^{n+1}} & \frac{\partial \{\mathcal{R}_f\}_l^{n+1}}{\partial v_l^{n+1}} \\ \frac{\partial \{\mathcal{R}_s\}_l^{n+1}}{\partial u_l^{n+1}} & \frac{\partial \{\mathcal{R}_s\}_l^{n+1}}{\partial v_l^{n+1}} \end{pmatrix} \quad (3.2.22)$$

- The blocks \mathbb{J}_{kl} (resp. \mathbb{J}_{lk}) corresponds to the derivative of the residual on the control volume \mathbf{V}_k (resp. \mathbf{V}_l) with respect to the discrete unknowns u_l^{n+1}, v_l^{n+1} on the element \mathbf{V}_l (resp. u_k^{n+1}, v_k^{n+1} on the element \mathbf{V}_k for the flux \mathbb{J}_{lk}). The explicit form of this terms is as follows

$$\mathbb{J}_{kl} = \begin{pmatrix} \frac{\partial \{\mathcal{R}_f\}_k^{n+1}}{\partial u_l^{n+1}} & \frac{\partial \{\mathcal{R}_f\}_k^{n+1}}{\partial v_l^{n+1}} \\ \frac{\partial \{\mathcal{R}_s\}_k^{n+1}}{\partial u_l^{n+1}} & \frac{\partial \{\mathcal{R}_s\}_k^{n+1}}{\partial v_l^{n+1}} \end{pmatrix} \quad (3.2.23)$$

$$\mathbb{J}_{lk} = \begin{pmatrix} \frac{\partial \{\mathcal{R}_f\}_l^{n+1}}{\partial u_k^{n+1}} & \frac{\partial \{\mathcal{R}_f\}_l^{n+1}}{\partial v_k^{n+1}} \\ \frac{\partial \{\mathcal{R}_s\}_l^{n+1}}{\partial u_k^{n+1}} & \frac{\partial \{\mathcal{R}_s\}_l^{n+1}}{\partial v_k^{n+1}} \end{pmatrix} \quad (3.2.24)$$

3.3 Implementation of the numerical scheme

The implementation of the code is done in the platform [DuMu^X](#). It is based on the [DUNE](#) library (Distributed and Unified Numerical Environment). It offers a variety of tools to numerically solve PDEs by the finite volume methods, finite element methods, finite difference methods and discontinuous Galerkin method. It also provides other features such as mesh management, discretization, linear and nonlinear solvers...etc.

The main feature of [DuMu^X](#) is the modularity of the concepts. It can be easily integrated and combine different properties depending on the problem to be solved. For each [DuMu^X](#) module, different elements interact with each other via common interfaces. The user can select different properties according to the nature of the problem.

[DuMu^X](#) has two types of numerical schemes: the fully implicit approach and the sequential approach. The global implicit strategy employs an implicit Euler discretization in time, combined with the "Cell-Centered" or "Vertex-Centered" method in space. The derived equations are assembled into a single nonlinear system, solved at each time step. The sequential approach deals with conservation equations where the flow equation is approximated implicitly, while the transport equations are solved using an explicit scheme. Flow and transport equations are solved sequentially at each time step. Besides, there is a general module for solving flow and transport problems, called "*NpMc*", where N is the number of phases and M is the number of components. Moreover, the choice of linear and nonlinear solvers, the type of grids as provided by the [DUNE](#) library, is maintained by the user in the problem file. Finally, we have the parameters, properties and physical law for each problem solved in the source files.

In this work, we have developed a new module, called *2p-SWI*, to predict seawater intrusion problem using the sharp interface approach by means of the fully implicit approach. This method enable us to decrease in a significant way the CPU time while maintaining a good accuracy of the results. The nonlinear system is linearized by Newton's method, wherein each iteration a linear system is solved by a BiConjugate Gradient STABILized (BiCGSTAB) combined to the preconditionor (ILU). Other iterative linear solvers and preconditioners are available in the [DUNE](#) library. For the approximation of the derivatives in the Jacobian matrix, we use numerical differentiation techniques. This is mainly to ensure the occurrence and efficiency of the implemented model. The management of the time-step is based on the number of iterations required by the Newton method to achieve convergence for the last time iteration. The time-step is reduced if the number of iterations exceeds a specified threshold, whereas it is increased if the method converges within less iterations.

3.4 Numerical simulations

This section aims to present numerical simulations of seawater intrusion problem using the sharp interface approach. Several 1D, 2D test cases are used to validate

our method. Numerical results for each test case are presented. In the case of a confined aquifer, we have tested our module *2p-SWI* against a linear analytical solution of Keulegan. The obtained results correspond well to the analytical solution and are in agreement with those proposed in [67]. After that, we have tested and validated our strategy in the case of an unconfined aquifer by proceeding to the study of the numerical convergence of the scheme. Furthermore, we examined three test cases: the first is proposed in [70] and the two others are realistic test cases with real data and complex geometry. The complete similarity of our results with those presented in [67, 70] validates our approach and proves that our module is applicable and able to simulate seawater intrusion in coastal aquifers.

We note that all computations were performed on a laptop with Intel Xeon(R) CPU E3-1505M Processor (3.00 GHz) and 8 GB RAM.

Finally, a remarkable property of the TPFA scheme is that the discrete maximum principles (nonnegativity of the thickness of freshwater and saltwater in the aquifer) is satisfied which is crucial to obtain physically meaningful approximate solutions. This has been verified in all our simulations. A proof of this result for a simplified model could be found in [76].

3.4.1 Test 1: The rotating interface problem

To verify and validate the numerical model obtained from the TPFA method, the numerical results are compared with an analytical solution proposed in [61]. This test consists to observe the movement of the interface without any external forces. In this case, we consider a confined aquifer of uniform thickness D with saltwater on the $x < 0$ part and freshwater on the $x > 0$ part. Homogeneous Neumann conditions are imposed at the borders. At the time $t = 0$, the interface starts to move due to the density difference α . The elevation of the interface is therefore described by a linear profile passing through a fixed point $(0, -D/2)$ in each time $t \geq 0$. It is given by the following equation

$$Z(x, t) = -\frac{D}{2} \left(1 + \frac{x}{L(t)} \right). \quad (3.4.1)$$

The intersection of the interface with the base of the aquifer (toe the interface) is given for $Z = -D$ by

$$L(t) = \sqrt{\frac{DD_f t}{\alpha \phi}}. \quad (3.4.2)$$

The initial position of the interface is given for $L(t_0) = 20$ m, position corresponding to $t_0 = 12.28$ days. The aquifer is approximated by a square $] -50, 50[\times] 0, 100[$. The physical and geometric parameters used are those used in [40, 83] and they are summarized in Table 3.1.

| Parameters | D [m] | α | ϕ | \mathbf{D}_f [m/day] | \mathbf{D}_s [m/day] | S_f, S_s [m ⁻¹] |
|------------|-------|----------|--------|------------------------|------------------------|-------------------------------|
| Values | 10 | 40 | 0.3 | 39.024 | 40 | 0.0 |

Table 3.1: Parameter values for the rotating interface problem.

Simulations were conducted over a 20-day period from the initial position. The simulations start run with a resolution of 100×100 . Figure 3.3 shows the position of the interface obtained with this model (curves "Z-App1t') and the analytical solution (curves "Zexact') at time $t = 1, 10$ and 20 days.

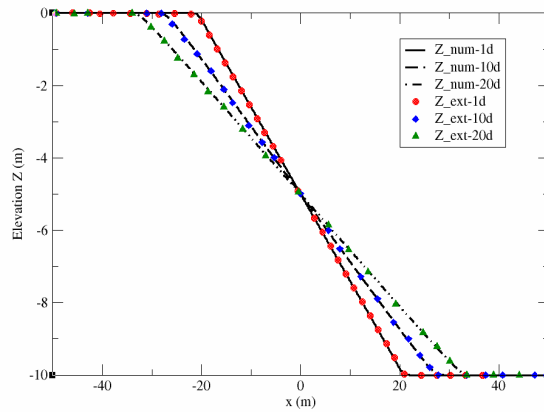


Figure 3.3: Position of the interface obtained with the present model and the analytical solution at different simulation times.

The results issued from the finite volume method are consistent with the exact solution and other numerical results presented in [40, 67, 72, 83]. Figure 3.4 shows the movement of the toe of the interface compared to the exact solution calculated by the formula (3.4.2). It can be seen that the toe of the interface moves exactly at the theoretical speed.

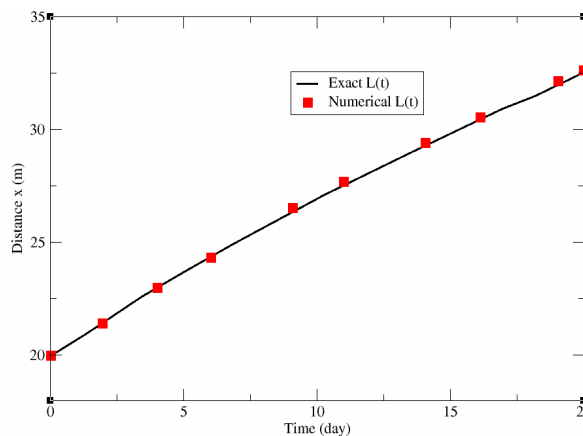


Figure 3.4: The progress of the numerical and analytical toe.

To visualize the state of equilibrium of the salt front, a second simulation was performed with the same initial condition as the previous test. The interface between these two liquids rotates counterclockwise until it becomes horizontal as shown in Figure 3.5. The simulations described below permit to follow the rotation of the interface.

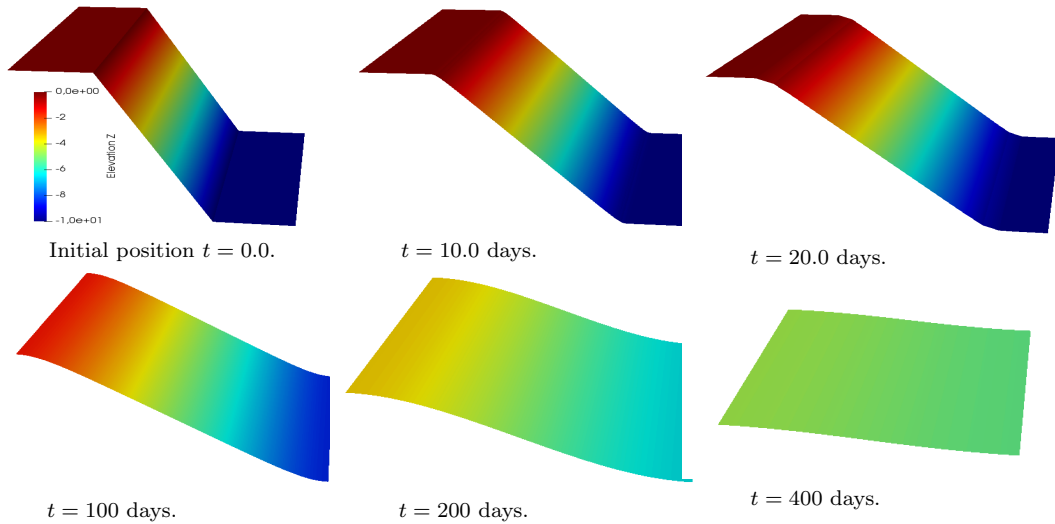


Figure 3.5: Evolution of the salt interface at different times.

We refer to Figure 3.6 for better visualization of the rotary character of the interface. Here, we plot its evolution along the section $x_2 = 50$. The equilibrium state of the interface achieved at $t = 800$ days.

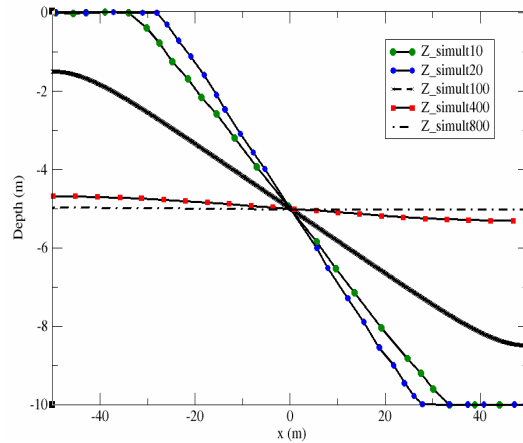


Figure 3.6: Rotary character of the freshwater/saltwater interface at times $t = 10, 20, 100, 400$ and 800 days.

Injection and pumping processes

We consider the case of a free aquifer with soil compressibility. We associate homogeneous Neumann boundary conditions to our problem, which allows the solution to evolve freely. We examine two cases:

- Injection of a significant amount of freshwater for a short period of 0.8 days through a well with a radius of 1.0 m centered at $(15, 50)$.
- Pumping freshwater through a well with a radius of 1.0 m centered at $(15, 50)$.

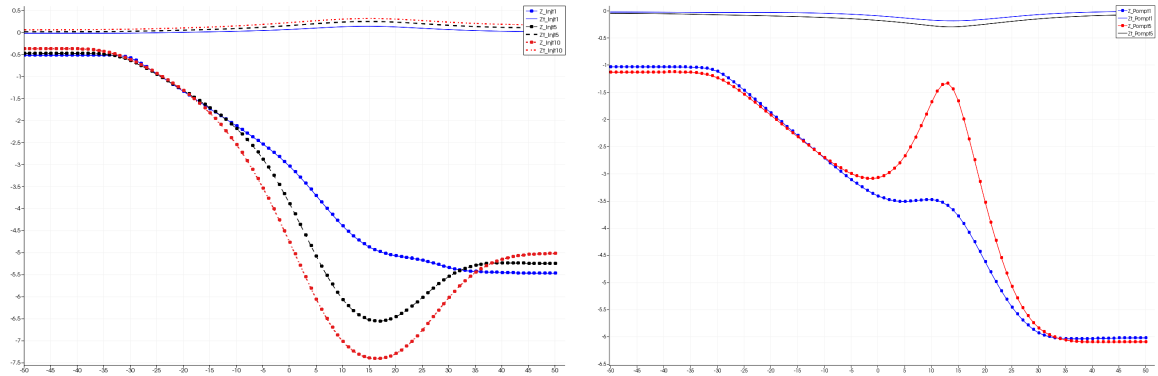


Figure 3.7: Evolution of the groundwater surface Z_T and the salt front Z in an injection (left) and pumping (right) process at time: $t=1.5$ and 10 days.

Figure 3.7 shows the movement of the interfaces Z_T and Z during a pumping and injection processes. We observe a local depression of the water table and the appearance of a salt cone ”upconing” in the pumping area. The salt interface rises globally towards the horizon, which can be dangerous for the users. As to the injection scenario, the effects of freshwater filling with a decrease in the depth of salt water are observed, especially in the injection zone.

The complete similarity of our results with those presented in [8, 67] validate our model.

The soil Compressibility

The purpose of this subsection is to visualize the effect of soil compressibility on the evolution of the groundwater surface Z_T and the salt front Z . The higher the storage coefficient S_f , the more water the soil can contain.

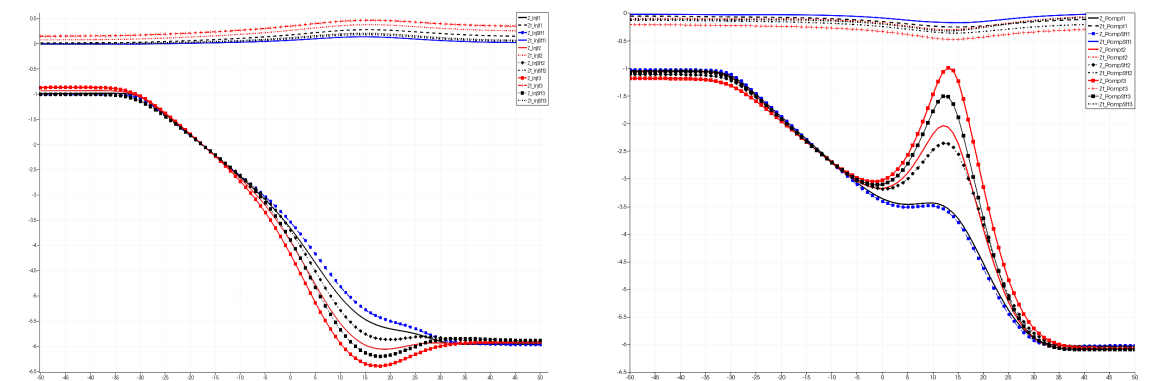


Figure 3.8: Left: Injection process. Right: pumping scenario.

Figure 3.8 shows a comparison of the interfaces Z_T and Z in the case of a compressible soil ($S_f = 0.25$, the Z-InjSft curves) and in the case of an incompressible environment ($S_f = 0$, the Z-Injt curves) at time $t = 1, 2, 3$ days. We can see an overestimation of the groundwater interface level Z_T and an underestimation of the salt front interface elevation Z when S_f is zero. Usually, the injection process is

used to decrease the salt cone and limit the marine intrusion problem. However, we remark the opposite phenomenon during a pumping process. Therefore, we see here that neglecting the compressibility of the soil can produce estimation errors on the evolution of the Z_T and Z interfaces, particularly in the injection area.

3.4.2 Test 2: a field-scale free aquifer problem

We consider a test case presented in [70] which aims to ensure the applicability of the sharp-interface approach for an unconfined coastal aquifer subjected to pumping by comparison with dispersive approach results. The validity of the sharp interface approach is based on two parameters: the pumping rate and the position of the well. Numerical simulations for several scenarios have been considered. We briefly review the main results of this comparison. The sharp interface gives better results compared to the dispersive approach for higher pumping rates where the saltwater has reached the well screen. Moreover, it's produce good results when the pumping wells are deep and close to the coast. As a conclusion, for such problems, the sharp interface approach models well the saline intrusion.

To prove the performance of our developed module in the case of a free aquifer, we proceed to the study of the numerical convergence of the TPGA scheme. The efficiency and the accuracy are investigated through 2D simulations with different grid resolutions. After that, we compared our numerical results with those presented in [70] for several senarios. A good agreement between both results is observed.

3.4.2.1 Test description

We consider a hypothetical free aquifer of thickness 30 m and length 500 m. A Dirichlet condition for the saltwater head $v = 30$ m is imposed at the seaside boundary ($x = 500$ m). The constant freshwater flux $0.1 \text{ m}^3/\text{day}$ at land boundary ($x = 0$) is considered. Homogeneous Neumann boundary conditions are imposed on the rest of the boundaries. The total extraction rate in the pumping wells is assumed to be constant irrespective of the proportions of saltwater and freshwater: $Q_t = Q_f + Q_s$. The last quantities are calculated in the same manner proposed in [84]. One has,

$$Q_f = \frac{\mathbf{D}_f l_f}{\mathbf{D}_f l_f + \mathbf{D}_s l_s} Q_t, \quad Q_s = \frac{\mathbf{D}_s l_s}{\mathbf{D}_f l_f + \mathbf{D}_s l_s} Q_t.$$

The thickness of the freshwater l_f and the saltwater l_s in the well screen respectively are calculated as follow

$$l_f = \max\{\min(Z_{wt}, u) - \max(Z_{wb}, Z), 0\},$$

$$l_s = \min\{Z_{wt}, u\} - \max\{Z_{wb}, Z_B\} - l_f.$$

Z_{wt} and Z_{wb} are respectively the elevation of the top and the bottom of the well screen. The freshwater head is noted by u and Z_B is the elevation of the bottom of the aquifer. The physical well screen length is about 2 m while the diameter is set at 1 m. Other notations are presented in Figure 3.9.

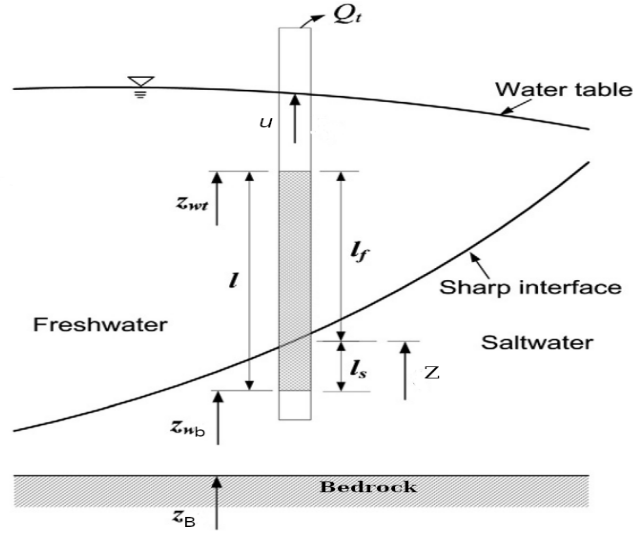


Figure 3.9: Schematic of the well screen in an unconfined aquifer [84].

First of all, we have run the model under steady state conditions. In this case, the aquifer is assumed to be static (no pumping). The obtained results are used as initial conditions for the transient model (after pumping). The time required for the simulation is approximately 30 years. The properties and parameters of the aquifer are summarized in Table 3.2.

| Parameters | α | D_f | D_s | ϕ | ρ_f | ρ_s | S_f | S_s |
|------------|----------|-------|-------|--------|----------|----------|-------|-------|
| Values | 40 | 1.0 | 41.0 | 0.35 | 1000 | 1025 | 0.0 | 0.0 |

Table 3.2: Parameters and properties of the aquifer.

Different scenarios of the pumping rate and the wells position are presented in Table 3.3. Q_t represents the amount of water pumped, x_w is the distance between the well and the sea while z_w is the depth of the well.

| Scenarios | Sc-1 | Sc-2 | Sc-3 | Sc-4 | Sc-5 | Sc-6 | Sc-7 | Sc-8 | Sc-9 | Sc-10 | Sc-11 |
|-----------------------------|------|------|------|------|------|------|------|------|------|-------|-------|
| Q_t [m ³ /day] | 0.1 | 0.05 | 0.07 | 0.15 | 0.1 | 0.1 | 0.1 | 0.1 | 0.1 | 0.07 | 0.07 |
| x_w [m] | 150 | 150 | 150 | 150 | 150 | 150 | 200 | 300 | 100 | 150 | 150 |
| z_w [m] | 15 | 15 | 15 | 15 | 0 | 25 | 15 | 15 | 15 | 0 | 25 |

Table 3.3: Different pumping scenarios.

3.4.2.2 Numerical convergence

In order to validate our implemented module, we proceed to the study of the numerical convergence. To do so, we select a scenario in the test case described in [70], for example Scenario 2. In this case, the pumping well is placed at a depth of 15 m and at a distance of $x_w = 350$ m from the shoreline. We pump a constant amount of freshwater with $Q_t = 0.05$ m³/day. We calculate the solution of the problem,

corresponding to the saltwater and freshwater heads, for different grids. We have refined the initial mesh several times by the factor 2. The grids considered for the study of the numerical convergence are summarized in Table 3.4.

| Grid levels | Number of cells |
|-------------|----------------------------|
| 1 | $400 = 100 \times 4$ |
| 2 | $1600 = 200 \times 8$ |
| 3 | $6400 = 400 \times 16$ |
| 4 | $25600 = 800 \times 32$ |
| 5 | $102400 = 1600 \times 64$ |
| 6 | $409600 = 3200 \times 128$ |

Table 3.4: Grids considered in the study of the numerical convergence.

The reference solution is calculated on a refined mesh, corresponding to 409600 cells with a resolution 3200×128 in the x_1/x_2 direction with a very small time step equal to $dt = 12$ hours.

To visualize the convergence of the solution calculated on different grids to the reference solution, we make several sections in space and time. In Figure 3.10, we plot different sections in space from the point $(0, 10)$, which represents the seashore, to the point $(500, 10)$ at the landside. This section allows us to visualize the evolution of the solution, corresponding to the freshwater and saltwater heads and salt front, during the 30 years of activity. In Figure 3.10, we observe the convergence of the solution calculated on different grids towards the reference solution.

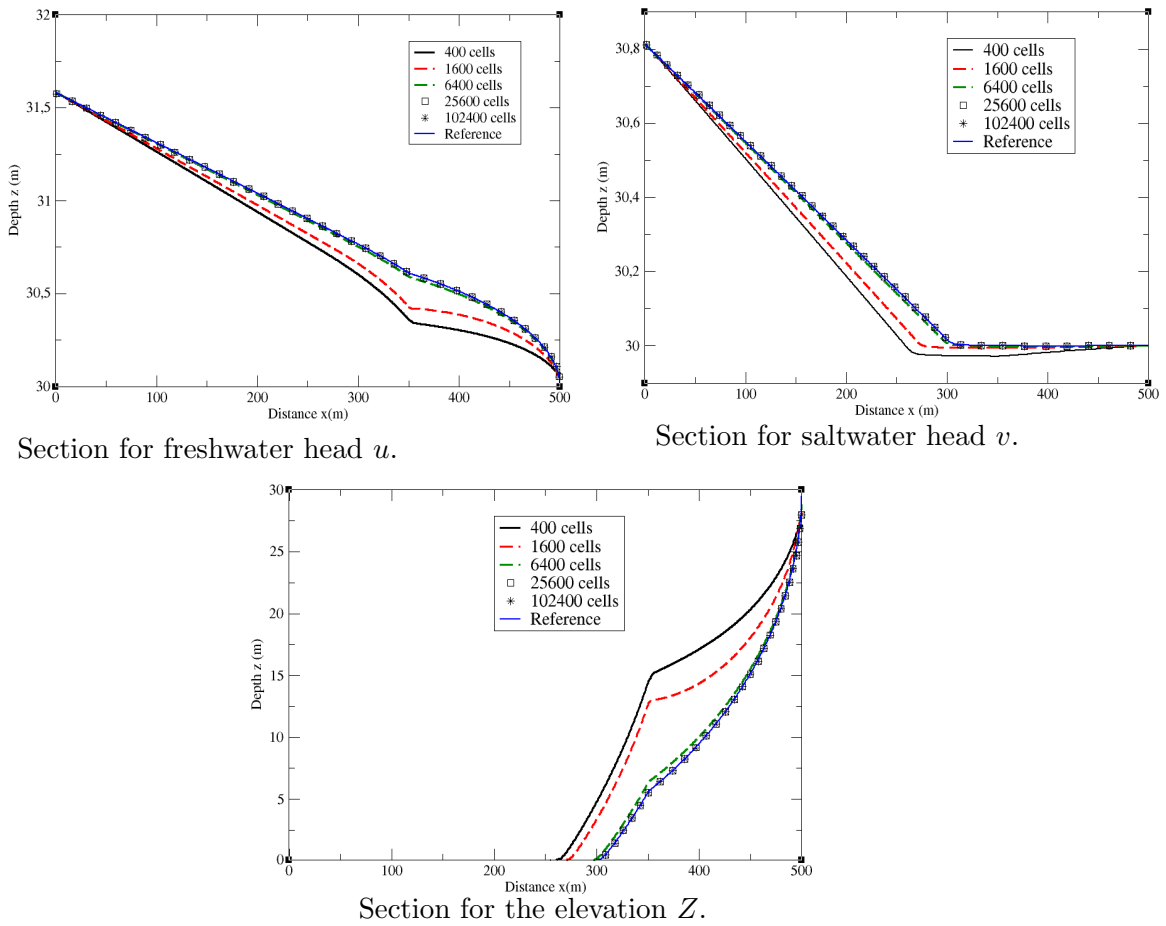


Figure 3.10: Convergence of solutions on different grids to the reference solution during 30 years of activity on the main section $(0, 10) - (500, 10)$.

In the sequel, we visualize the convergence of the solutions in time. To do so, we select a point in the zone of pumping of freshwater corresponding to the point $(350, 10)$. In Figure 3.11, we plot the curves of the freshwater head u , the saltwater head v and the salt front elevation Z on 30 years (9.4×10^8 s). The evolution of the solution calculated on different grids is compared to the reference solution computed on a fine mesh. We can see a good convergence of these quantities to the reference solution during 30 years of activity.

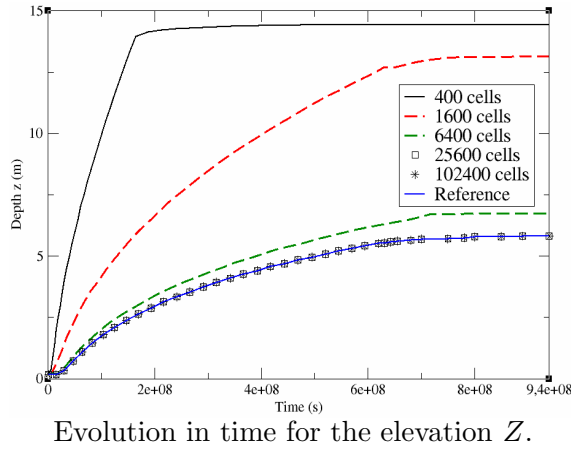
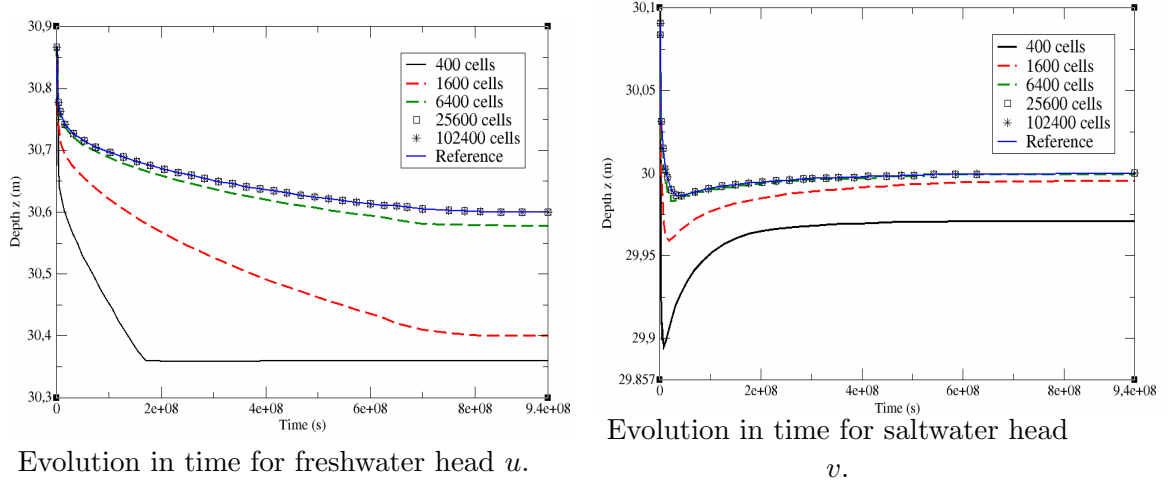


Figure 3.11: Evolution of the solutions on each grid and convergence to the reference solution for 30 years at the point of pumping (350, 10).

As we are interested in the accuracy of the scheme, we are going to evaluate the error of the numerical scheme. We denote by er_{l^2} the discrete l^2 -relative norm. Moreover, we study the error between the reference solution and the numerical one in l^∞ and we note by er_{l^∞} the discrete l^∞ -relative norm. Let

$$er_{l^2} = \frac{\sqrt{\sum_{i=1}^{NRef} |u_h(i) - u_{ref}(i)|^2}}{\sqrt{\sum_{i=1}^{NRef} |u_{ref}(i)|^2}}$$

and

$$er_{l^\infty} = \frac{\sup_{i=1, \dots, NRef} |u_h(i) - u_{ref}(i)|}{\sup_{i=1, \dots, NRef} |u_{ref}(i)|}.$$

$u_{ref}(i)$ is the reference solution and $u_h(i)$ is the numerical solution calculated on a certain grid at element i while $NRef$ represents the number of elements in the fine mesh. We present in Table 3.5 the discrete l^2 -relative norm and in Table 3.6 the discrete l^∞ -relative norm.

| | | | | | |
|---------------------|--------------|--------------|--------------|--------------|--------------|
| Number of cells | 400 | 1600 | 6400 | 25600 | 102400 |
| Freshwater head u | $4.37e^{-3}$ | $2.05e^{-3}$ | $6.29e^{-4}$ | $3.01e^{-4}$ | $9.15e^{-5}$ |
| Saltwater head v | $2.00e^{-3}$ | $1.08e^{-3}$ | $3.77e^{-4}$ | $1.76e^{-4}$ | $6.28e^{-5}$ |
| Elevation Z | 0.63 | 0.31 | $8.01e^{-2}$ | $4.03e^{-2}$ | $1.72e^{-2}$ |

Table 3.5: Numerical convergence of the scheme in l^2 -relative norm.

| | | | | | |
|---------------------|--------------|--------------|--------------|--------------|--------------|
| Number of cells | 400 | 1600 | 6400 | 25600 | 102400 |
| Freshwater head u | $6.45e^{-3}$ | $3.2e^{-3}$ | $9.86e^{-4}$ | $5.08e^{-4}$ | $2.05e^{-4}$ |
| Saltwater head v | $4.44e^{-3}$ | $2.85e^{-3}$ | $6.54e^{-4}$ | $4.21e^{-4}$ | $1.96e^{-4}$ |
| Elevation Z | 0.32 | 0.18 | $6.46e^{-2}$ | $3.66e^{-2}$ | $1.5e^{-2}$ |

Table 3.6: Numerical convergence of the scheme in l^∞ -relative norm.

Let p be the order of convergence of the scheme in space. Then, there exists a constant C such that: $er_{l^2}(h) \simeq Ch^p$. To estimate the order of convergence numerically, we have refined the initial mesh several times by a factor of 2 for example. For two successive mesh sizes h and $h/2$, one has

$$er_{l^2}\left(\frac{h}{2}\right) \approx C \left(\frac{h}{2}\right)^p \approx \frac{er_{l^2}(h)}{2^p}.$$

We obtain

$$p \approx \frac{\log\left(\frac{er_{l^2}(h)}{er_{l^2}\left(\frac{h}{2}\right)}\right)}{\log(2)}. \quad (3.4.3)$$

The next step consists to calculate the order of convergence using equation (3.4.3). Tables 3.7-3.8 represent the order of convergence of the scheme calculated for u, v and Z in the l^2 and l^∞ relative norms. It is of order 1 for the primary variables, which seems logical considering the complexity and nonlinearity of the problem.

| | | | | | |
|---------------------|-----|------|------|-------|--------|
| Number of cells | 400 | 1600 | 6400 | 25600 | 102400 |
| Freshwater head u | - | 1.06 | 1.2 | 1.3 | 1.46 |
| Saltwater head v | - | 0.88 | 1.09 | 1.23 | 1.34 |
| Elevation Z | - | 1.02 | 1.12 | 1.2 | 1.3 |

Table 3.7: Order of convergence for the l^2 -relative norm.

| | | | | | |
|---------------------|-----|------|------|-------|--------|
| Number of cells | 400 | 1600 | 6400 | 25600 | 102400 |
| Freshwater head u | - | 0.95 | 1.01 | 1.25 | 1.3 |
| Saltwater head v | - | 0.63 | 0.7 | 0.86 | 1.1 |
| Elevation Z | - | 0.83 | 0.94 | 1.17 | 1.28 |

Table 3.8: Order of convergence for the l^∞ -relative norm.

Finally, we present in Table 3.9 the value of the CPU time corresponding to each simulation.

| | | | | | | |
|-----------------|------|------|------|-------|--------|--------|
| Number of cells | 400 | 1600 | 6400 | 25600 | 102400 | 409600 |
| Time CPU (min) | 0.06 | 0.3 | 1.3 | 4.06 | 17.46 | 80.49 |

Table 3.9: CPU time taken for each simulation.

3.4.2.3 Numerical results

For the simulations of this test, we use a uniform rectangular mesh of 250×10 cells in the x_1/x_2 direction for the control volumes. We performed the simulations with an initial time step of 0.01 s and a maximum time step of 1 day. The time step is incremented or decremented according to the number of iterations required by Newton's method in the previous time iteration. If Newton's method does not converge to a fixed maximum number of iterations, the time step is then divided by 2. In the opposite case, the time step is multiplied by two. This process runs until the maximum time step is reached.

The tolerances for the Newton's method and the linear solver BICGSTAB are respectively 10^{-8} and 10^{-6} . For this simulation, Newton's method converges quickly with less than 5 iterations while the CPU time required is inferior to 1 min. In the following, we will compare our developed model $2p$ -SWI implemented in DuMu^X (Curves: SWI-DuMu^X) with the one presented in [70] (Curves: Mehdizadeh and al) while changing the pumping rate and well position. The well position is represented by a solid rectangular on Figure 3.12. The plots below illustrate that our numerical solutions lead to results similar to those obtained in [70].

a) Case 1: varying the pumping rates

The objective here is to visualize the effect of the quantity of water pumped on the variation of the saline front. In this case, the well screen is fixed and its central point is located at $(x_w = 350, x_2 = 0)$ with a diameter of 0.5 m. The depth of the well with respect to the horizontal surface is $z_w = 15$ m. We simulate the saltwater interface with different pumping rates, which correspond respectively to $0.1 \text{ m}^3 \cdot \text{d}^{-1}$ (Sc-1), $0.05 \text{ m}^3/\text{day}$ (Sc-2), $0.07 \text{ m}^3/\text{day}$ (Sc-3) and $0.15 \text{ m}^3/\text{day}$ (Sc-4). The numerical results corresponding to each scenario are shown in Figure 3.12.

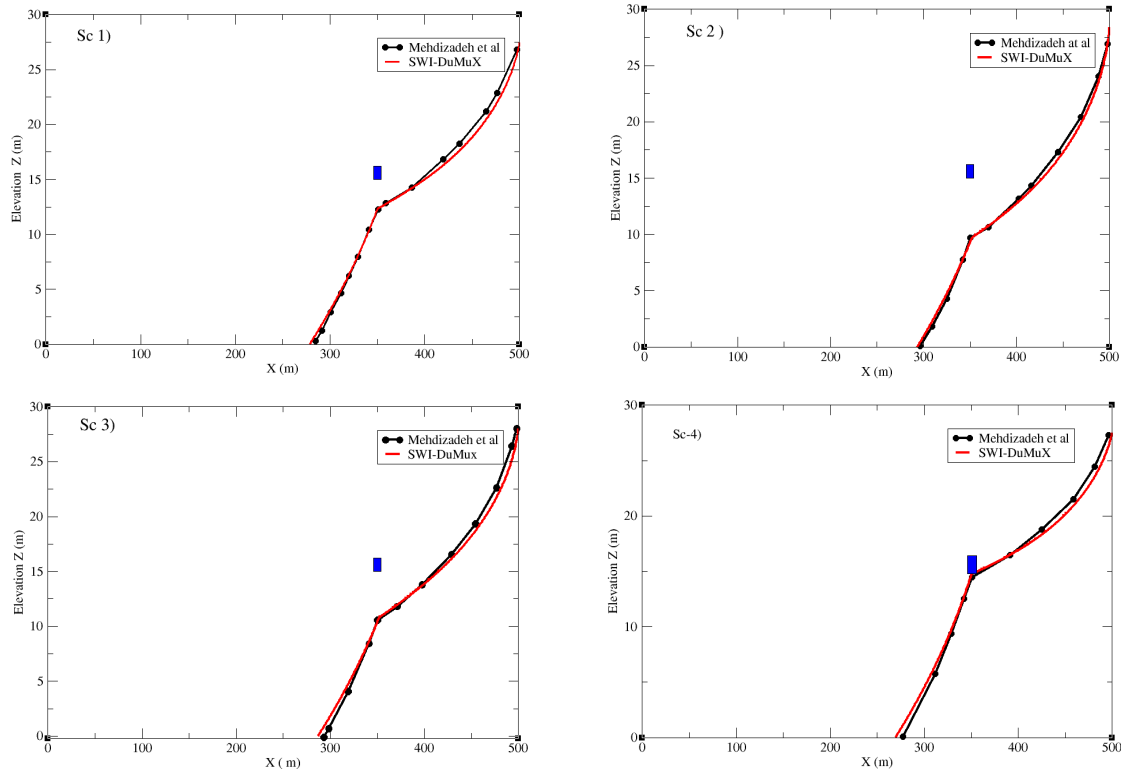


Figure 3.12: Variation of the salt front while changing the pumping rate and fixing the position of the well.

throughout the pumping time, the salt interface gradually rises and the cone of the polluted water tends towards the pumping well. The progression of the cone is related to the quantity of the water pumped. The interface is too far from the base of the well in (Sc-2) which corresponds to the smallest amount of freshwater pumped. In this case, pumping do not present any risk of pollution. However, saltwater reaches the base of the well in (Sc-4). The latter is salinized by the seawater, which can be dangerous for the users. The interface is little far from the well bottom in (Sc-1, Sc-3) but the risk is still present. It can, therefore, be deduced that the salinization of the well increases with the increase in the quantity of water pumped.

b) Case 2: changing the depth of the well

In this test, we mainly concentrate on the effect of the well position together with the pumping rate on the variation of the sharp interface. The well is placed in the center, at the bottom and at the upper part of the aquifer. We consider two different pumping rates $Q_t = 0.1 \text{ m}^3/\text{day}$, correspond to (Sc-1, Sc-5, Sc-6), and $Q_t = 0.07 \text{ m}^3/\text{day}$ for (Sc-3, Sc-10, Sc-11). We plot in Figure (3.13) the salt front for different position of the well screen.

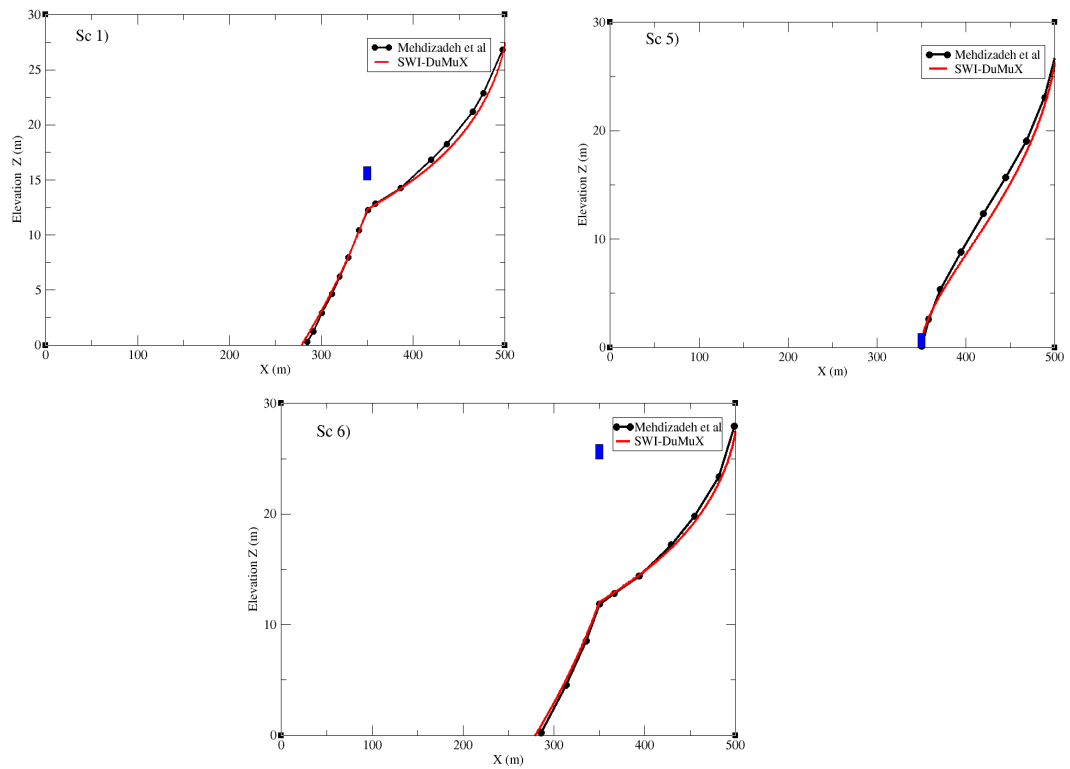


Figure 3.13: Evolution of the salt front by varying the depth of the well and fixing the pumping rate at $Q_t = 0.1 \text{ m}^3/\text{day}$.

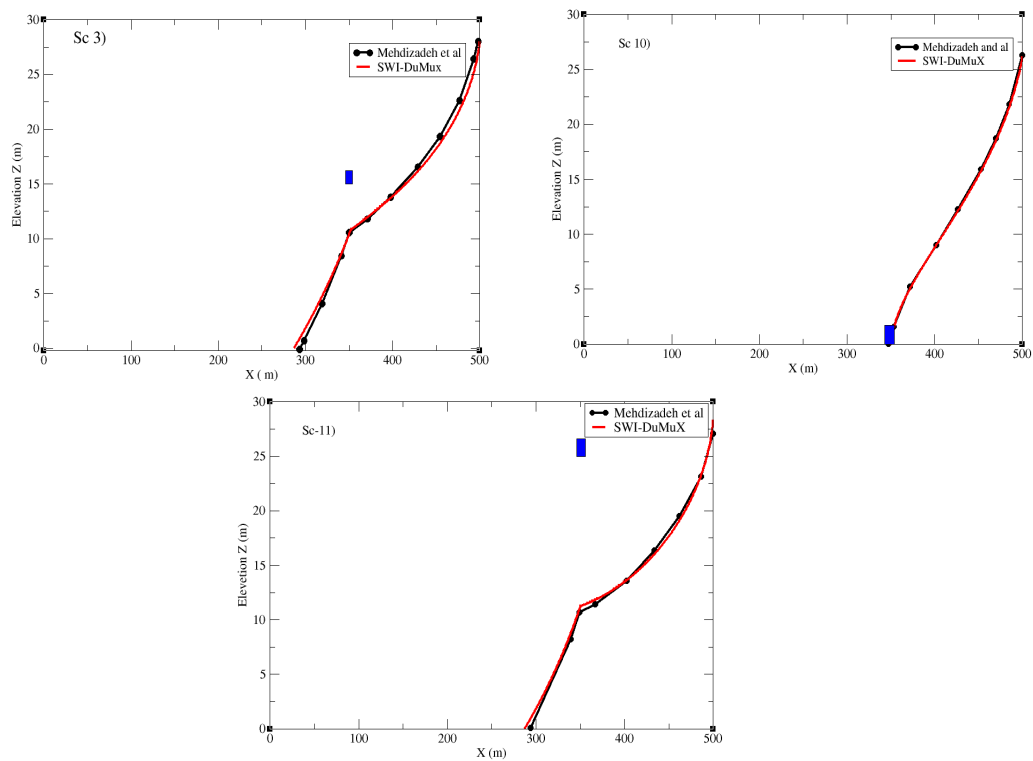


Figure 3.14: Evolution of the salt front by varying the depth of the well and fixing the pumping rate at $Q_t = 0.07 \text{ m}^3/\text{day}$.

As shown in Figure 3.13 (Sc-5) and Figure 3.14 (Sc-10), the well screen is placed at the bottom of the aquifer. We are talking about the full penetration of the pumping well where the salt cone has disappeared and the well is completely filled with saltwater. Steady-state conditions are reached quickly with $Q_t = 0.1 \text{ m}^3/\text{day}$, where more time is needed for $Q_t = 0.07 \text{ m}^3/\text{day}$.

For the other simulations, we have a partial penetration of the strainer. We observe the evolution of the salt interface and the appearance of the "upconing". The progress of the latter depends in particular on the location of the well. In (Sc-6), the polluted cone is too far from the base, which does not present any risk, while it is too close in (Sc-1). We can conclude that the deeper the well, the faster the saltwater reaches the base.

The same remarks can be made when we decrease the pumping rate to $Q_t = 0.07 \text{ m}^3/\text{day}$ but the effects are less than those obtained with $Q_t = 0.1 \text{ m}^3/\text{day}$.

c) Case 3: varying the longitudinal position of the well

Four scenarios are considered to study the effect of the distance of the well from the coast on the evolution of the salt front. To do so, we fixed the amount of freshwater at $Q_t = 0.1 \text{ m}^3/\text{day}$ and we varied the distance from the coast x_w . The obtained results in this case are presented in Figure 3.15.

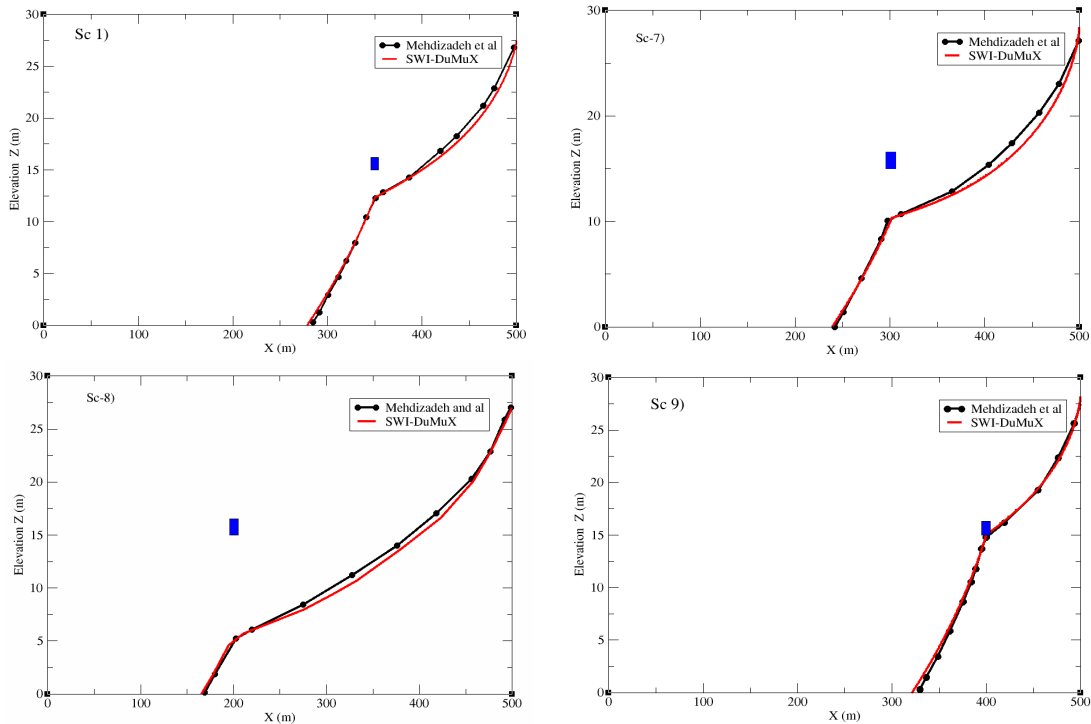


Figure 3.15: Evolution of the salt front for Sc-1, Sc-7, Sc-8 and Sc-9 scenarios, while changing the longitudinal positions of the wells.

Figure 3.15 shows the evolution of the interface saltwater/freshwater for different values of x_w . (Sc-8) corresponds to the greatest distance from the coast compared to the other simulations, it can be seen that the saltwater is too far from the well

position, whereas it is completely polluted in the nearest one (Sc-9). The saltwater cone is too close in (Sc-1, Sc- 7) which means that the risk is higher in these cases. We conclude that if the pumping well is close to the coast, the probability of its pollution by seawater is higher. In addition, the risk decreases as you move away from the coast.

Remark 3.4.1. *We have presented a comparison of our results versus those obtained in [70] for a test case dealing with a homogeneous unconfined aquifer subject to eleven scenarios with different pumping rates and different well locations. We can observe a very good agreement between both calculations, ensures the validity of our developed model. From these series of simulations, it can be seen that if the well position is deep and close to the coast, the risk of pollution is higher, the same remarks can be made with a large quantity of water pumped.*

We note that these simulations are carried out until steady-state conditions are obtained, which means that the aquifer will be exploited for many years. It can be noted, therefore, that these simulations can be useful to control the use of water resources and avoid pollution of the aquifer.

3.4.3 Test 3: Souss-Chtouka case study

In this subsection, we present numerical results obtained using the $2p$ -SWI module in the case of the Souss-Chtouka test case presented in [5]. We start by giving a short description of the Geographical location of the Souss-Massa basin. Moreover, we present different parameters corresponding to the geometry, boundary conditions, geological data and pumping rates, used for the prediction of saline intrusion in the Souss and Chtouka aquifer. The plain is under coastal groundwater conditions and assumed to be static before 1986. Therefore, the model is first run under steady state conditions. The comparison between the approximate and the measured piezometric map of 1968 showed a good agreement. The obtained results are used as initial conditions for the transition model. Different sections in space and time are used to visualize the saltwater intrusion under 80 years of over-exploitation of the plain. Numerical simulations have shown that the salt front elevation has moved to the landside and that the groundwater flow decreases in the whole plain. This means that our module is efficient and able to simulate the saltwater intrusion in a realistic test case.

3.4.3.1 Geographical location

The Souss-Massa basin is located in the south-western of Morocco (see Figure 3.16), which contains an important hydrological catchments with an area of 27000 Km². The natural limits of the Souss-Massa river basin are: the Anti-Atlas mountains in the south, the High Atlas mountains in the north, the Siroua massif in the east, and the Atlantic ocean in the west (see Figure 3.16). In this region, significant groundwater tables have been identified occupying the Souss plain (4500 Km²), the Chtouka plain (1260 Km²) and Tiznit plain (1200 Km²). Deep aquifers are identified in this hydrogeologic structure, in addition of the generalized phreatic aquifer, subject of this study. The phreatic aquifer of the Souss and Chtouka plains

consists of heterogeneous fitting material of the valley. According to its geology, the deposits correspond to the quaternary alluvial sands and gravels of the Oued-Souss river, to the Moghrebian sandstones and coastal marine sands, to the Pliocene limestone with marl and conglomeratic intercalations of the down-land areas of the Souss plain and to fluvial-lacustrine deposits of the Souss unit extending to the Anti-Atlas chain border [5].

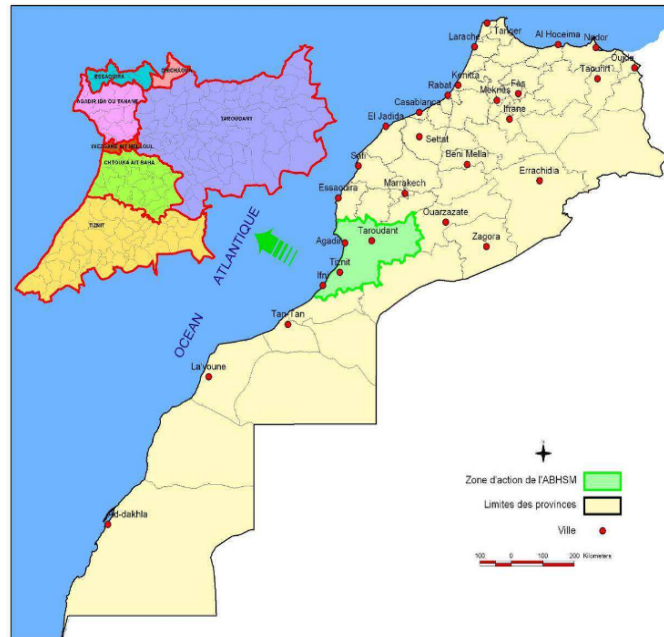


Figure 3.16: The situation of the Souss-Massa basin and the Souss-Chtouka groundwater.

3.4.3.2 The studied domain and discretization

The studied domain, which is approximately 24 Km², corresponds to the down-land part of the Souss-Aval valley and the Chtouka plain. It is located between the Haut-Atlas chain at the north, the 100 m contour of the 1968's piezometry at the east, the Oued-Massa river at the south and the Atlantic ocean at the west.

The geometry and boundaries of the aquifer are given in the left of Figure 3.18. For the mesh, we used a triangulation mesh of 19520 elements and 9871 vertexes as shown in the right of Figure 3.18.



Figure 3.17: 3D representation of the studied domain.

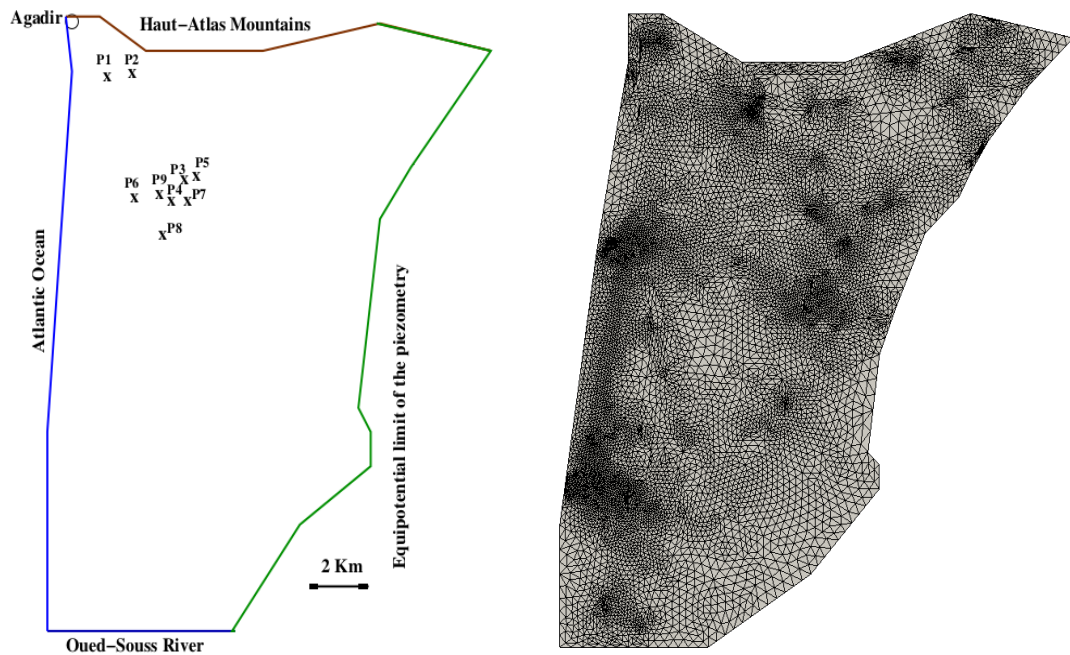


Figure 3.18: Left: geometry and boundaries of the aquifer and well locations. Right: mesh for the aquifer.

In passing, we remark that the horizontal surface area of the aquifer is about 24 Km², while the thickness of the aquifer is less than 1 Km (about 600 m in the north and 100 m in the south). In spite of the presence, locally, of relatively high depth regions in the northern part of the Souss–Chtouka coastal aquifer, the thickness of the latter remains small when compared to its lateral extent, which allows the Dupuit assumption to be valid. The fluid movement is therefore assumed to be horizontal.

3.4.3.3 Physical parameters and boundary conditions

Hydraulic conductivity of different geologic units that constitute the Souss–Chtouka aquifer, are determined following trial-and-error calibration operations in [5]. Ten zones have been recognized, for which the spatial hydraulic conductivity values vary between 1.21 m/day and 40 m/day. The value is higher in the lower part of the valley, especially in the north-west, where agricultural activity is very important, than in the upper part. Porosity values varying between 0.1 and 0.25 have been used, depending on the geologic material lithology. The porosity and hydraulic conductivity distributions are specified in Figure 3.19.

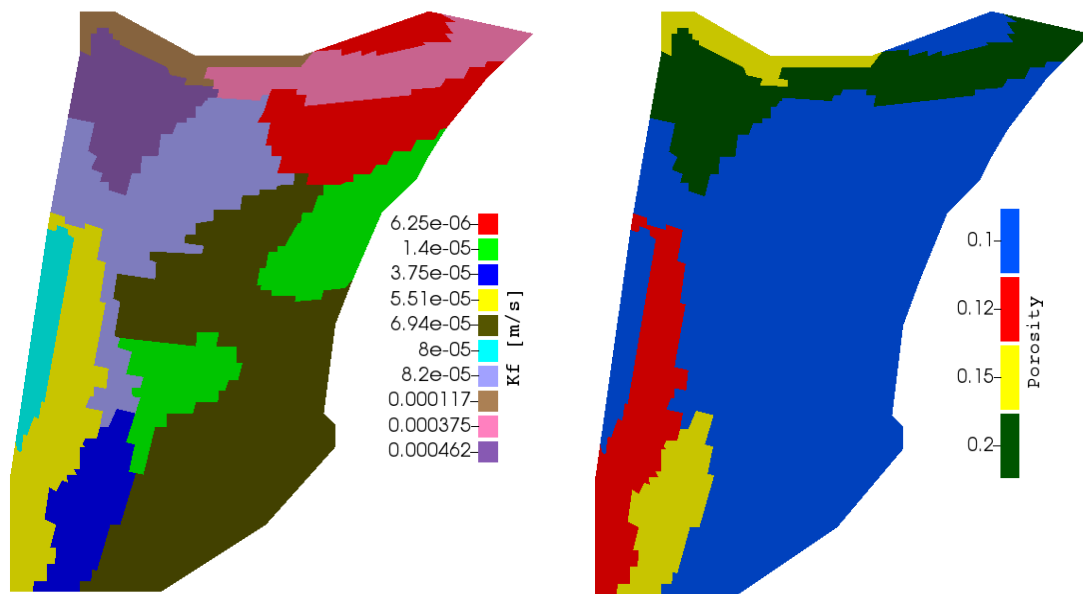


Figure 3.19: Left: hydraulic conductivity (D_f) of the aquifer. Right: porosity (ϕ) of the soil.

The specific storage coefficient values varying between $10^{-5}m^{-1}$ and $4 \times 10^{-5} m^{-1}$ and taken to be the same for fresh and salty phases are specified at the right hand-side of Figure 3.20.

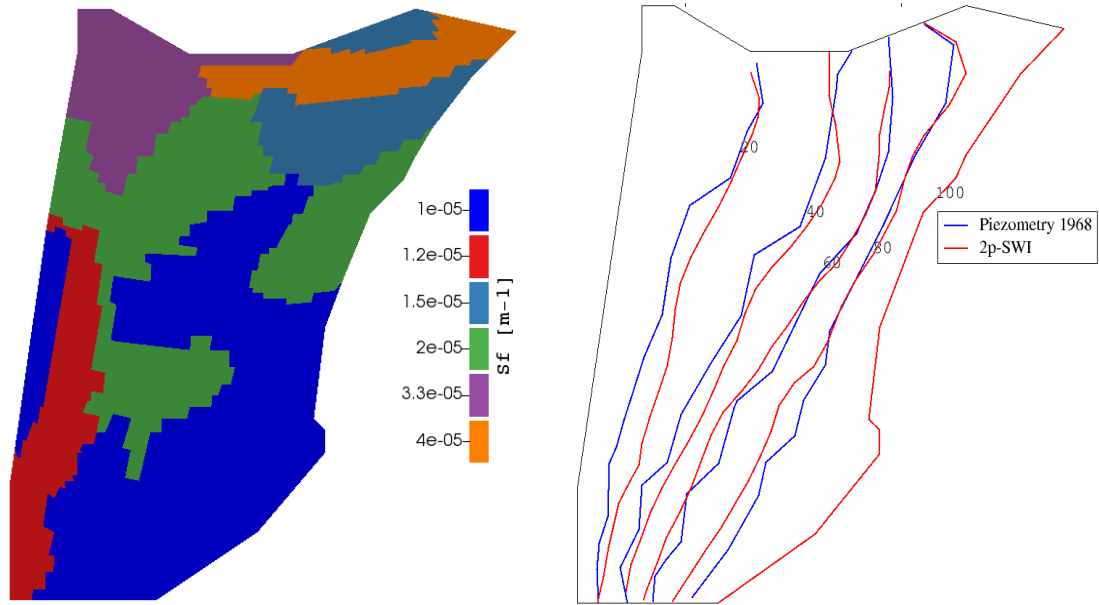


Figure 3.20: Left: the freshwater storage coefficient S_f . Right: comparison between our developed module $2p$ -SWI model and the measured piezometric map of 1968.

For the initial conditions, the plain is supposed to be in hydrostatic equilibrium. Saltwater is static and freshwater is in dynamic. The problem is, therefore, run under steady-state conditions, using the parameters obtained from the calibrations done in [5]. The obtained results are compared with the measuring head of 1968 piezometric (see Figure 3.20 right). The results are satisfactory and used as initial conditions for the transition regime.

Figure 3.21 presents different values of the topography of the aquifer. The depth of the aquifer varies between -690 m and 35 m where the sea level is used as a reference. Negative values expressed the depth below sea level. The deeper values are located to the northwest of the domain while the higher values are located at the southeast.

The Souss—Chtouka aquifer is fed, mainly, by the precipitation, the irrigation returns, the vertical leakance of the underlain Turonian limestone, the infiltration from the Oued-Souss river and the recharge from the Haut-Atlas chain at the north. In [5], the author delimited 8 zones in the study area with fluxes values varying between 1.05×10^{-6} m/day and 8.06×10^{-5} m/day.

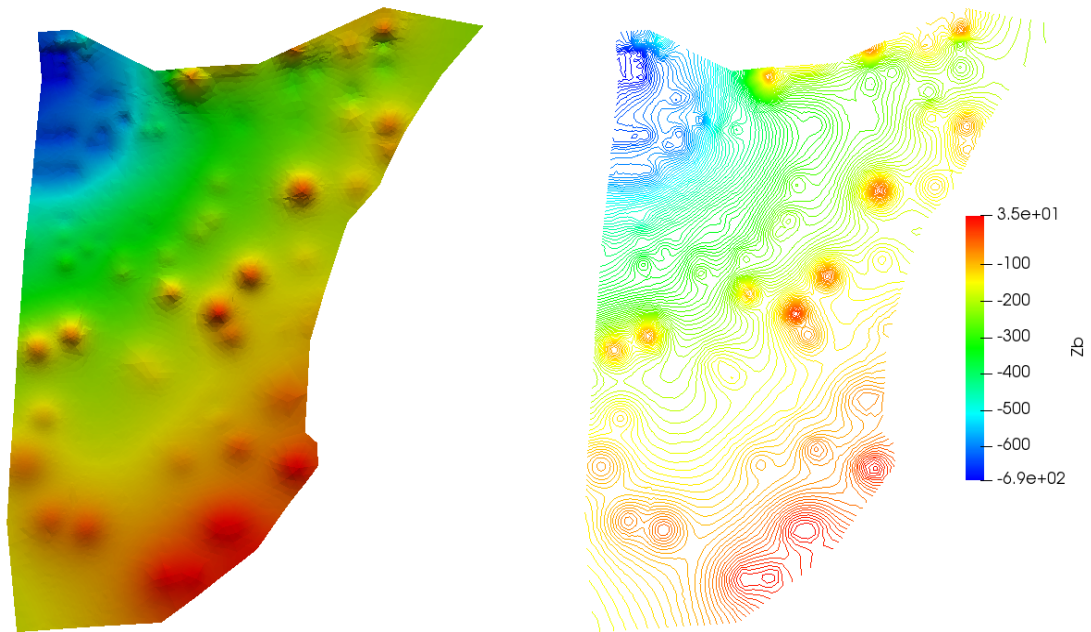


Figure 3.21: Topography of the aquifer bottom.

Owing to the intensive exploitation of the Souss–Chtouka aquifer and the difficulty to have appropriate data, a general lowering of the water table is assumed. Many pumping wells given by the Moroccan authority of water (ONEP) are presented in Table 3.10. However, the numerical simulations obtained with these data show that the interface does not move for almost 80 years. In order to predict a significant displacement of the interface in the long term, we have multiplied the pumping rates given by the ONEP by a factor of 10.

| | | | | | | |
|----------------------------|---------|---------|---------|--------|--------|---------|
| Points | P1 | P2 | P3 | P4 | P5 | P6 |
| X [m] | 99811 | 100277 | 101250 | 100750 | 102000 | 99507 |
| Y [m] | 384285 | 383966 | 374280 | 374280 | 375400 | 375246 |
| Rate [m ³ /day] | 2918.84 | 2686.99 | 1011.10 | 673.31 | 710.22 | 1113.03 |
| | P7 | P8 | P9 | | | |
| | 101710 | 100062 | 100000 | | | |
| | 374431 | 372311 | 374996 | | | |
| | 1533.89 | 1402.35 | 1488.54 | | | |

Table 3.10: Well position and associated rates.

To close the problem, boundary conditions have to be specified. Fixed head ($u = 100$ m) is used on the upstream of the domain, at the east. At the northwest, at the contact with the Haut-Atlas chain and the south, fixed heads are also imposed representing the measured head [5]. On the western boundary, at the contact with the ocean a zero head is imposed ($u = v = 0$ m).

For all simulations, a triangulation mesh of 19,520 cells is used for control volumes. We have ensured that the orthogonality condition is satisfied while constructing the mesh. This condition is necessary for consistent and efficient approximations of the TPFA method. Simulations were achieved with an initial time step of 10 s. The tolerances for the Newton method and the BICGSTAB solver are respectively 10^{-8} and 10^{-6} . In this case, Newton's method converges in less than 5 iterations. As expected, the time-step is increased when Newton's algorithm converges within less iterations. A remarkable attribute of the algorithm is that the total CPU time required for a 80 years simulation is less than 5 min on a laptop.

Let us end this section with the following remark. A second simulation for the Souss—Chtouka aquifer was performed with a refined mesh (37,320 cells and 18,861 vertex). The obtained results are very close to those of the previous coarse mesh. However, the CPU time is 15 min. In the sequel, we will present results corresponding to the coarse mesh.

3.4.3.4 Numerical results

In this subsection, we will present numerical results obtained using our $2p$ -SWI module for modeling seawater intrusion into the Souss-Chtouka aquifer. We consider the hydrogeological data and physical parameters described above. The model is, thereafter, run under transition condition over an 80-year period. Figure 3.22 illustrates the piezometry of freshwater in 1968 and after 80 years of exploitation.

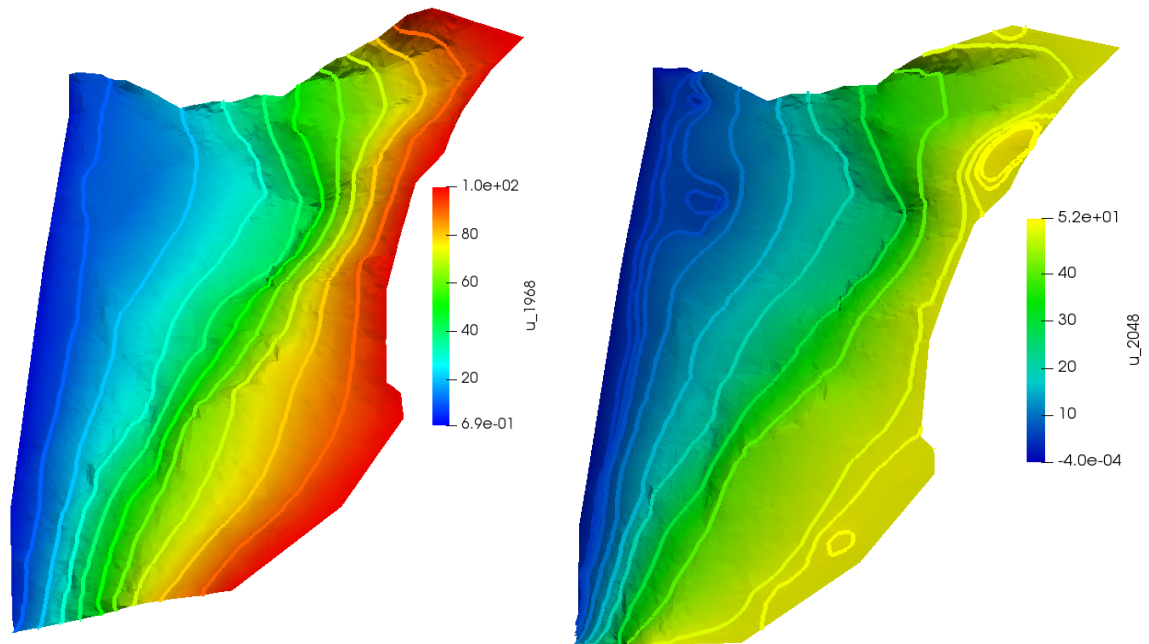


Figure 3.22: Plan view of the piezometry of the plain Souss—Chtouka before (left) and after (right) solicitation.

Up to 1968, the Souss-Chtouka aquifer was not subject to any exploitation. It follows the principle of the functioning of coastal aquifers. It is supposed to be in hydrostatic equilibrium. The aquifer is inflated and the equipotentials are regular and vary from 0 downstream to 100 upstream as shown in Figure 3.22 at left. However, for the 2048 predictions, equipotentials are no longer regular. Indeed, after 80 years of drastic exploitation, consisting of a general decline of the water table from the coast to the upstream ($u(t) = 100 - 0.625t$), the level of freshwater is decreased by 50 m in the upper part of the aquifer and a local depression of the water table in pumping wells position illustrated by negative values of the freshwater head.

To give a more realistic vision of the freshwater potential and to visualize the impact of the dramatic exploitation of the Souss-Chtouka Plain, we illustrate the piezometric contours of the freshwater head on the bottom of the aquifer (see Figure 3.23).

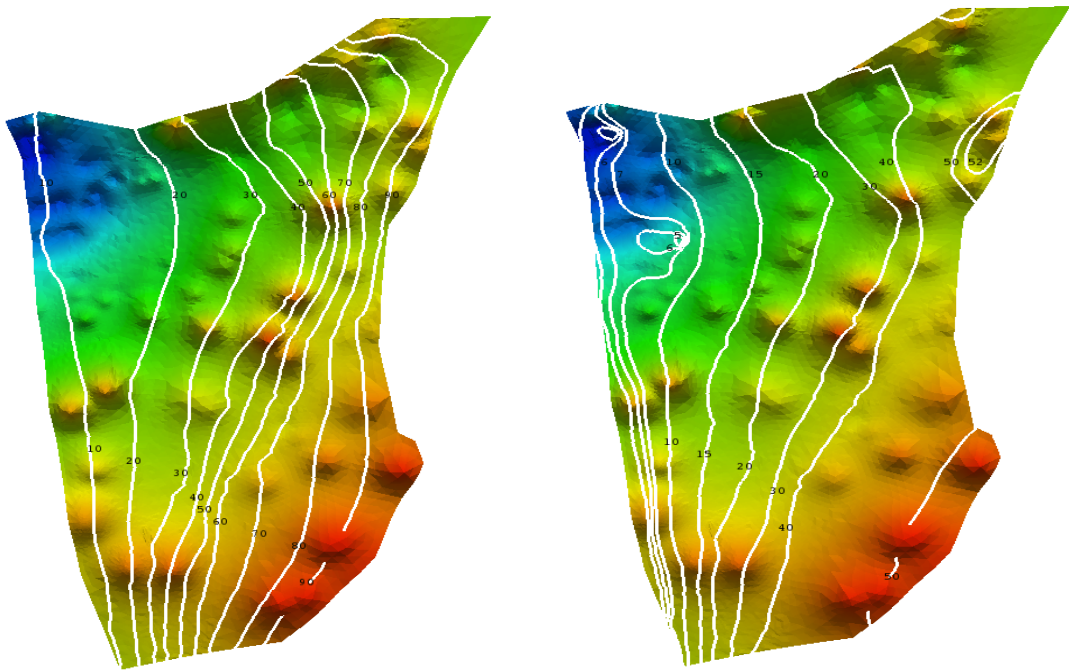


Figure 3.23: Contours representing the freshwater potential of the Souss-Chtouka plain illustrated on the bottom of the aquifer in 1968 (left) and 2048 (right).

Figure 3.24 shows the piezometric of saltwater in its initial state, corresponding to 1968, and after 80 years of service.

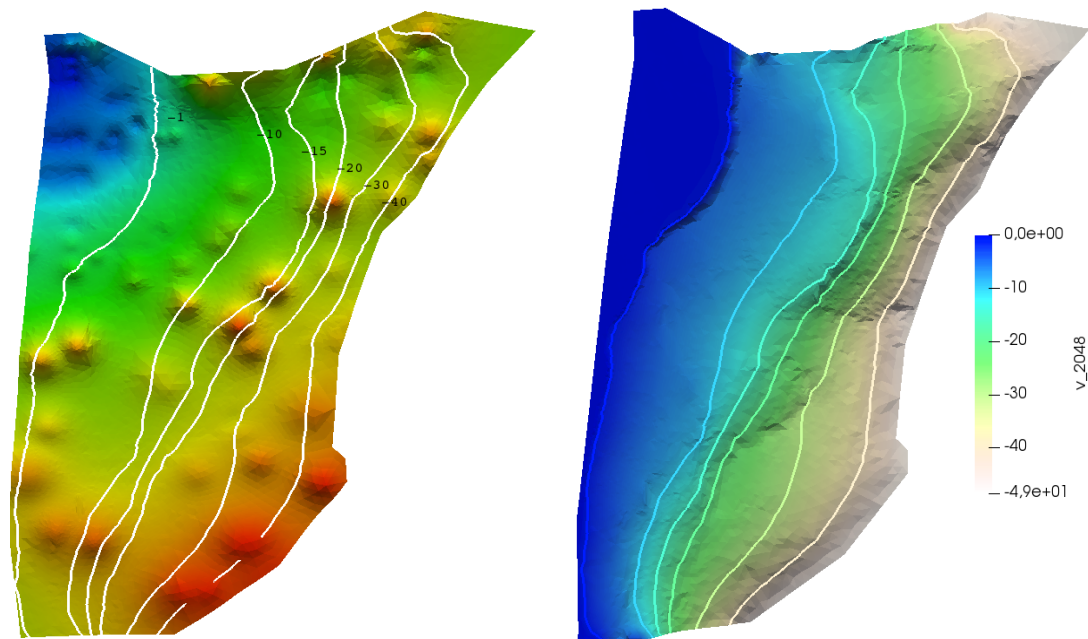


Figure 3.24: Plan view of the piezometry of the saltwater in its initial state in 1968 (left) and after 80 years of exploitation (right).

Until 1968, the plain follows the principle of coastal aquifers in stable conditions. The only fluid in movement is freshwater. The saltwater level is supposed to be identified with the sea level, which is equal to zero. After 80 years of drastic exploitation, the aquifer has experienced a general decrease in seawater level from the coast to the whole basin illustrated by negative values.

Figure 3.25 illustrates the extension of the salt wedge, which is more prominent in the north towards the east (the depth of the reservoir reaches 650 m) and remains practically parallel to the western limit when going south. After 80 years of activity, the salt bevel has experienced a significant displacement in the north caused by intensive freshwater pumping, especially in regions where pumping wells are placed.

However, in the southwestern region, Figure 3.25 shows that the salt bevel is stable and does not advance in the continent (in regions with low permeability).

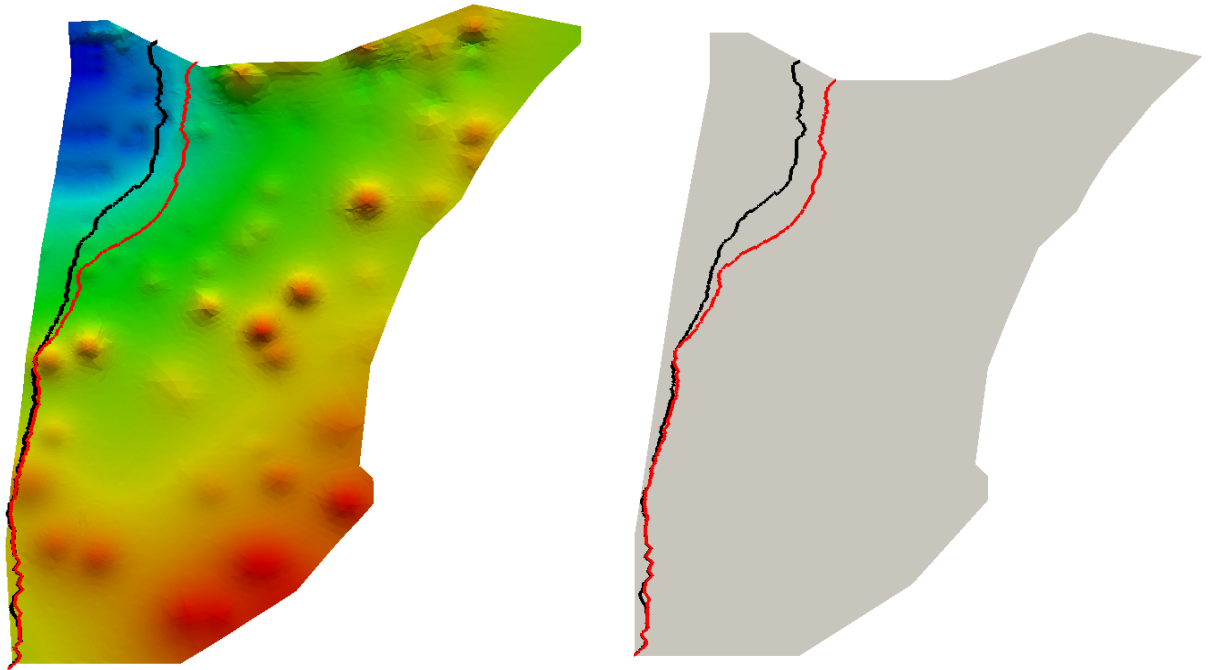
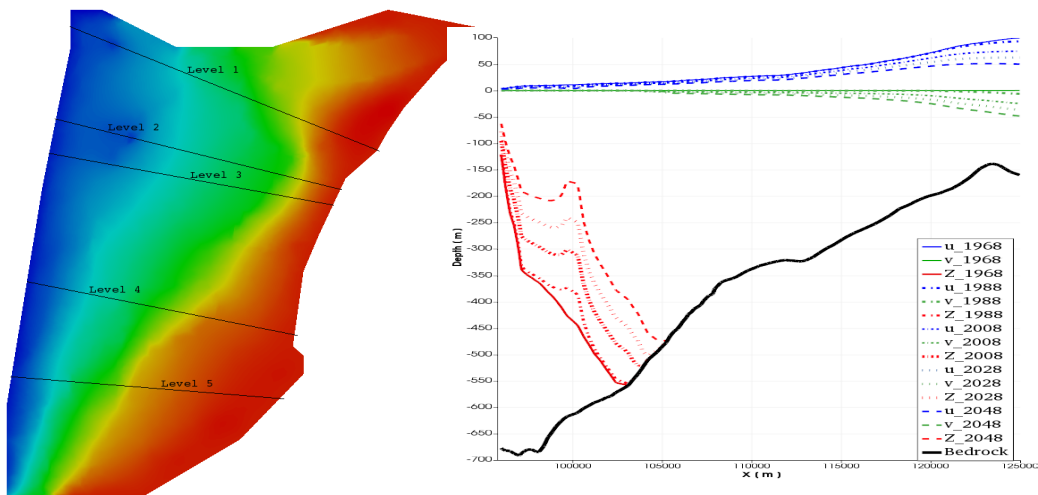


Figure 3.25: Position of the interface freshwater/saltwater in 1968 (black line) and in 2048 (red line).

In order to show the extent of the salt intrusion according to the location, we chose five sections perpendicular to the Atlantic coast and oriented from the East to the West. The profiles of u, v and Z according to different sections over a 20-year package are presented in Figures 3.26-3.28.



Level positions

Level 1

Figure 3.26: Left: Plan view of level positions. Right: vertical cross section showing the interface position (red line), the free surface position (blue line) and the variation of the saltwater hydraulic head (green line) for different time: cut on the level 1.

The first remark we can make is the progress of the freshwater/saltwater interface for the great depths to the east in the Agadir region, over a distance estimated at 7000 m on the substratum at a depth of 600 m. In fact, in the concerned area, the high value of the permeability of the formations contributes to the advance of the bevel. Significant vertical advancement of the interface is noticed in the first section and an “upconing” is developed under a large flow well. The pumping well is close to the coast, which accelerates the advancement of the salt bevel during the 80 years of activity (Figure 3.26 (left)).

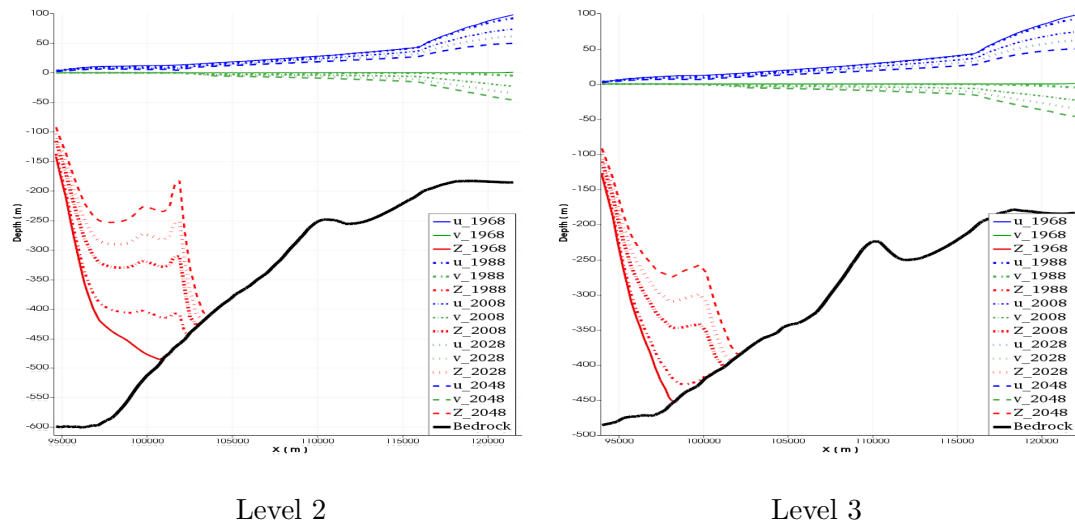


Figure 3.27: Vertical cross section showing the interface position (red line), the free surface position (blue line) and the variation of the saltwater hydraulic head (green line), for different time: cut on the levels 2 (left) and 3 (right).

On the second section, (Figure 3.27 (left)), we can see a significant displacement of the salt bevel laterally around 4 Km and especially vertically, so that an “upconing” developed below a large flow of three pumping wells. A slight cone of depression can also be noted at the location of these wells.

Along the third section, (Figure 3.27 (right)), the salt bevel is displaced laterally over a distance of at least 6K m after 80 years of activity and an “upconing” is developed below the pumping well. The pumping effects are less visible compared to the first two sections since the corresponding flow rate is low. On the other hand, a strong cone of depression developed at the well site. The regular shape of the bedrock and the high permeability values in this region contributed to the lateral advancement of the salt bevel.

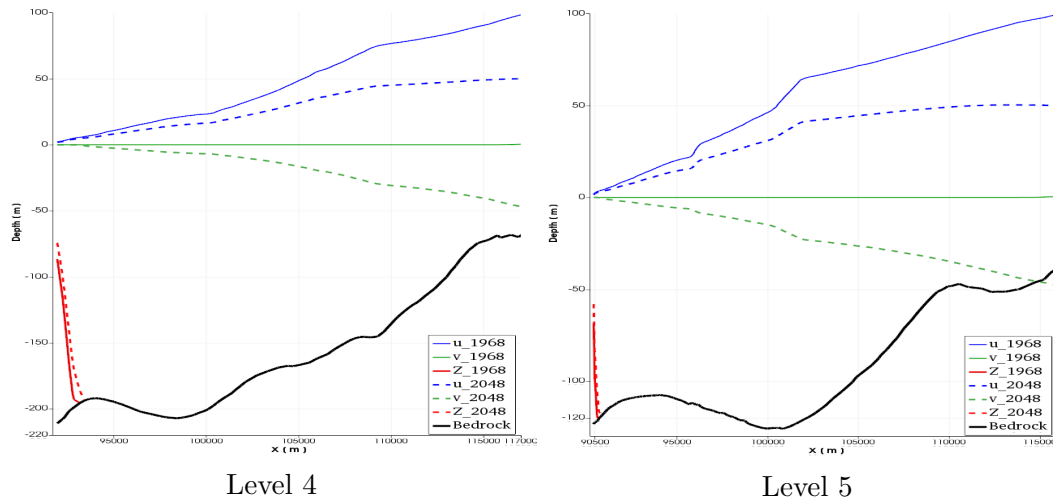


Figure 3.28: Vertical cross section showing the interface position (red line), the free surface position (blue line) and the variation of the saltwater hydraulic head (green line), for different times: cut on the levels 4 (left) and 5 (right).

On the fourth section, (Figure 3.28 (right)), there is always a sustained movement of the salt bevel over the years to reach its maximum value after 80 years of service. Finally, the fifth section, (Figure 3.28 (left)), shows almost no movement of the salt bevel despite a linear decrease in the free surface area, which is generalized to the entire basin. It should be noted that the region interested in logging is free of any pumping zones.

To understand the functioning of the Souss-Chtouka aquifer during the period of its activity, we propose to visualize the evolution of several quantities over time. To do so, we have selected five points on the surface of the aquifer. Figures 3.29 show the evolution of u , v and Z over time.

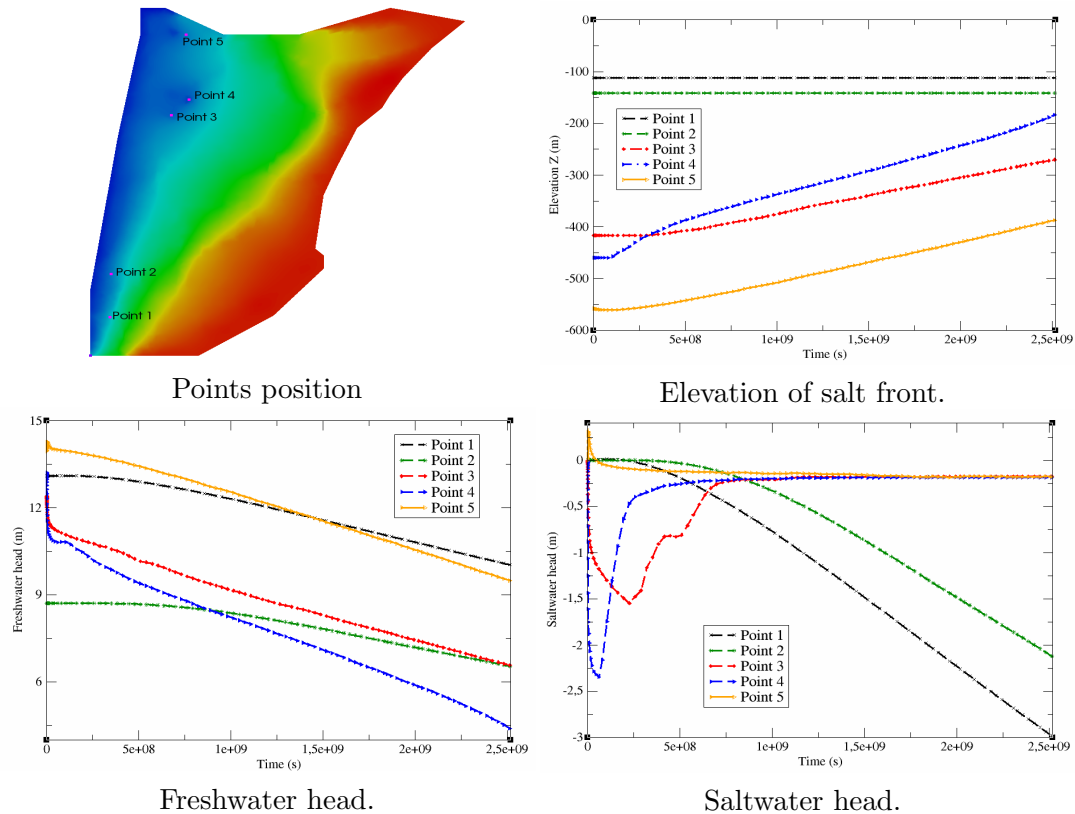


Figure 3.29: Evolution in time of the salt front (top right) freshwater head (left) and saltwater head (right).

The results show that the salt front elevation is stable and did not move during the period of its exploitation at the second and third points. This seems physically logical since the corresponding area is free of any external exploitation. At the third and fifth points, the salt interface has moved about 150 m towards the ground during the 80 years of operation. The area concerned is under immense stress. In addition, the hydrogeological parameters (high permeability and porosity) improve the progression of the salt front. The third point is located at the position of the pumping well with a rate of $2686.99 \text{ m}^3/\text{day}$. As a result, the interface has moved rapidly about 250 m to the surface, particularly over the past 50 years. This is the result of a combination of over-exploitation and the nature of the soil.

A general decline in freshwater levels is observed in Figure 3.29 (right) over the 80-years period. At the fifth point, the freshwater level decreases by 13 m during the pumping period. The evolution of the saltwater level is shown in Figure 3.29 (left). The saltwater level in the area subjected to stress decreases in the first few years and then stabilizes again.

Remark 3.4.2. *The numerical results of the "Souss-Chtouka" test case proved that the new module developed is capable of providing an accurate solution and can predict the location, shape and extent of the water table and of the the freshwater/saltwater interface in coastal aquifers under a variety of different stress conditions, thereby illustrating its robustness with a sufficient convergence rate.*

To end this section, we have the following remark. For numerous tests, the obtained results are satisfactory and the numerical computations for the coupled system have demonstrated that this approach yields physically realistic flow fields in heterogeneous fields. Furthermore, the fully coupled fully implicit scheme greatly reduce the CPU time of the simulations.

3.4.4 Test 4: Tripoli aquifer case study

In this section, we present the numerical results obtained in the case of the Tripoli test case proposed in [57] using the sharp interface module. It deals with the impact of demographic evolution on seawater intrusion in the lower Tripoli aquifer in Lebanon. We present a brief description of the geographical location of the Tripoli aquifer and the different physical parameters employed in the simulations. To ensure the validity of our developed module in a real case, we propose to compare our numerical results with those presented in [57]. Different scenarios are considered and presented based on the available hydrological data. Numerical simulations have shown a reduction of the water potential and an advance of the freshwater/saltwater interface.

3.4.4.1 Geographical location

The city of Tripoli is the second pole of attraction located in northern Lebanon (see Figure 3.30), which covers a total area of 400 Km². It is located between the Mediterranean Sea (about 15 Km) in the west, the Mountain of "Bcharré" in the east and the Mountains of Qalhat and Torbol from the south and the north, respectively. The groundwater is mainly supplied by precipitation and snow-melt from the "Bcharré" region located at the east of the Tripoli aquifer (see Figure 3.30).

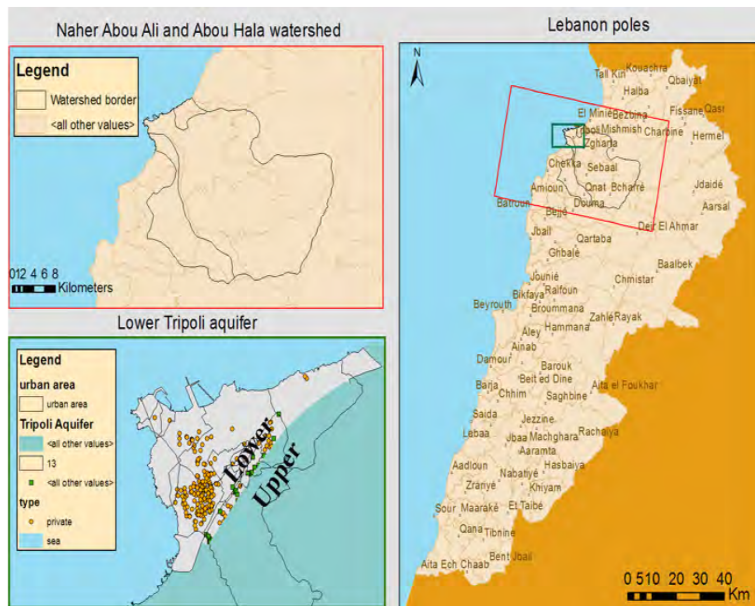


Figure 3.30: Position of the Tripoli aquifer, study zone and wells position (cf. [56]).

In this work, we consider only the lower Tripoli aquifer. The bedrock of the aquifer is the impermeable layer "C6" formed by marl and marl limestone (See Figure 3.31). The thickness of the aquifer above the impermeable layer is about 200 m.

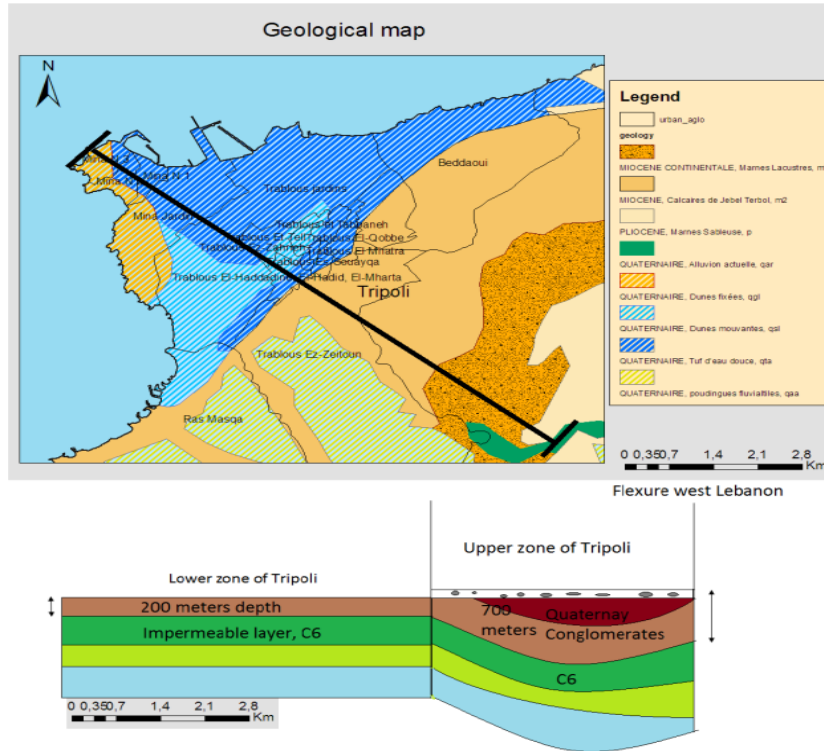


Figure 3.31: Geological map and stratigraphy of Tripoli (cf. [56]).

3.4.4.2 The studied domain and physical parameters

The study area is approximately $3 \text{ Km} \times 6 \text{ Km}$. The Tripoli aquifer is an homogeneous porous medium with a thickness of 200 m. The geometry and boundaries of the aquifers are given in Figure 3.32. For the mesh, we use a triangulation mesh of 37568 elements and 10285 vertices.

The boundary conditions are divided into two parts: Γ_1 represents the shoreline of the aquifer and Γ_2 corresponds to a fracture separating the lower and the upper zone of the city. A Dirichlet boundary condition ($u = v_0 = 200 \text{ m}$) is used on Γ_1 while a freshwater inflow Q_{inflow} is imposed on Γ_2 . This flux has been calibrated in [56] for the year 2008.

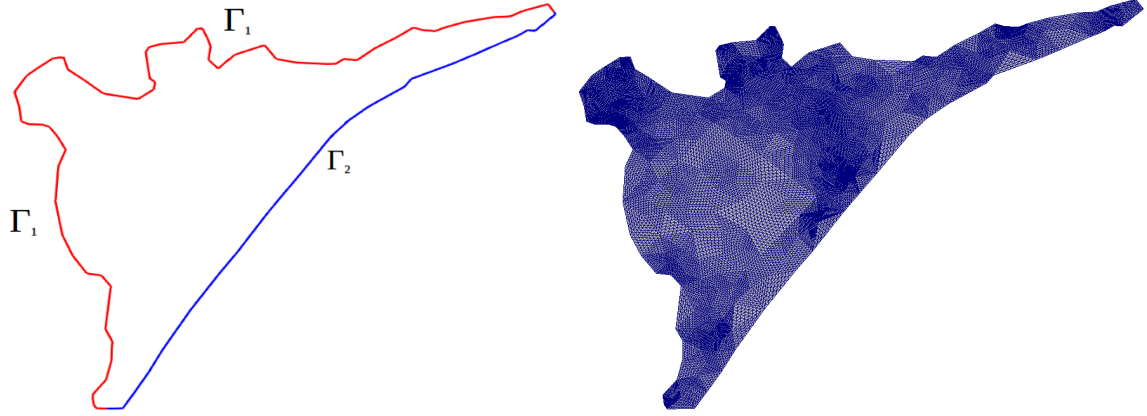


Figure 3.32: Geometry and Boundaries of the aquifer (left). The mesh of the studied domain (right).

The physical parameters used in the simulation are listed in Table 3.11.

| Parameters | symbol | value | Unit |
|-------------------------|--------------|-------|-------------------------|
| Bottom of the aquifer | Z_B | 0 | [m] |
| Porosity of the medeuim | ϕ | 0.15 | [-] |
| Sea level | v_0 | 200 | [m] |
| Hydraulic conductivity | \mathbf{D} | 1.156 | [m/day] |
| Density of freshwater | ρ_f | 1000 | [kg · m ⁻³] |
| Density of saltwater | ρ_s | 1025 | [kg · m ⁻³] |
| Density contrast | γ | 0.025 | [-] |
| Well raduis | — | 10;40 | [m] |
| Storage coefficient | S_f | 0.0 | [-] |
| Freshwater inflow | Q_{inflow} | 26.0 | m ³ /day |

Table 3.11: Parameters and properties of the aquifer (cf. [56])

The direction of the flow in the Tripoli plain can be assumed mainly horizontal since its thickness (200 m) is negligible compared to its horizontal surface (18 Km). This ensures the validity of the Dupuit approximation and allows us to vertically integrate the freshwater and saltwater equations in 3D.

Due to the increase in population over the past decades in the city of Tripoli, the high demand for drinking water threatens the freshwater potential. Figure 3.33 represents the pumping areas as described in [56, 57]. Private wells are located in the center of Tripoli city and represented by a blue rectangle in Figure 3.33. In addition, six active public wells maintained by the Tripoli Water Authority are considered and presented by yellow markings in Figure 3.33. Four wells are located in the village of "Bahsas" and two others in the neighborhoods of "El-Jisr" and "Malouleh".

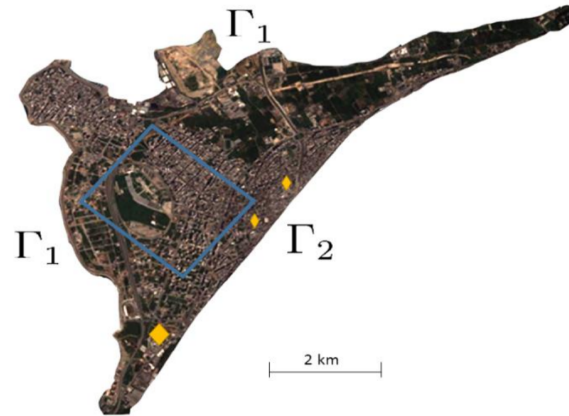


Figure 3.33: Location of pumping zones (cf. [56]). The rectangle in blue corresponds to the private wells and the public wells are represented by a yellow zone. The yellow zone in the south of the aquifer contain 4 wells in Bhsas while the two other wells are in El-jisr and Malouleh respectively.

Table 3.12 summarized the associated pumping rates for public wells.

| Wells | Number of wells | Pumping rate [m^3/day] | Well raduis [m] |
|---------------|-----------------|------------------------------------------|-----------------|
| Private wells | — | 21 000 | — |
| Bahsas | 4 | 4680 | 40 |
| Malouleh | 1 | 3264 | 10 |
| El-Jisr | 1 | 4896 | 10 |

Table 3.12: Wells position and associated rates.

Four scenarios are used to predict the extent and progression of the salt wedge in the lower Tripoli aquifer:

- "NOP": represents the no pumping scenario and corresponds to the results of the year 2008. In this case, the plain is assumed to be in hydrostatic equilibrium and the model is run under steady state conditions.
- "REC": refers to a scenario with 150 L/day as required by the water authorities after 10 years of exploitation.
- "10 Y": refers to a scenario with the current pumping rate of 250 L/day for 10 years of exploitation.
- "20 Y": refers to a scenario with the current pumping rate of 250 L/day after 20 years of exploitation.

3.4.4.3 Numerical results

In this subsection, we will present numerical results obtained using our developed module to predict seawater intrusion into Tripoli case study. We performed the simulations with an initial time step of 0.01 s and a maximum time step of 20

days. The tolerances for the Newton's method and the linear solver BICGSTAB are respectively 10^{-8} and 10^{-6} . For this simulation, Newton's method converges quickly with less than 4 iterations while the CPU time required is less than 13 min. In the following, we will compare the result obtained with our developed model $2p$ -SWI implemented in DuMu^X with the one presented in [57] in different situations. The comparison between our numerical results and those presented in [57] showed good agreement between both calculations.

We consider the hydrogeological data and the physical parameters described above. The model is run under steady state conditions. The obtained results are labeled as "NOP" pumping scenario and used as initial conditions for the other scenarios. Figure 3.34 presents the evolution of the freshwater/saltwater interface in 2008 in the natural conditions.

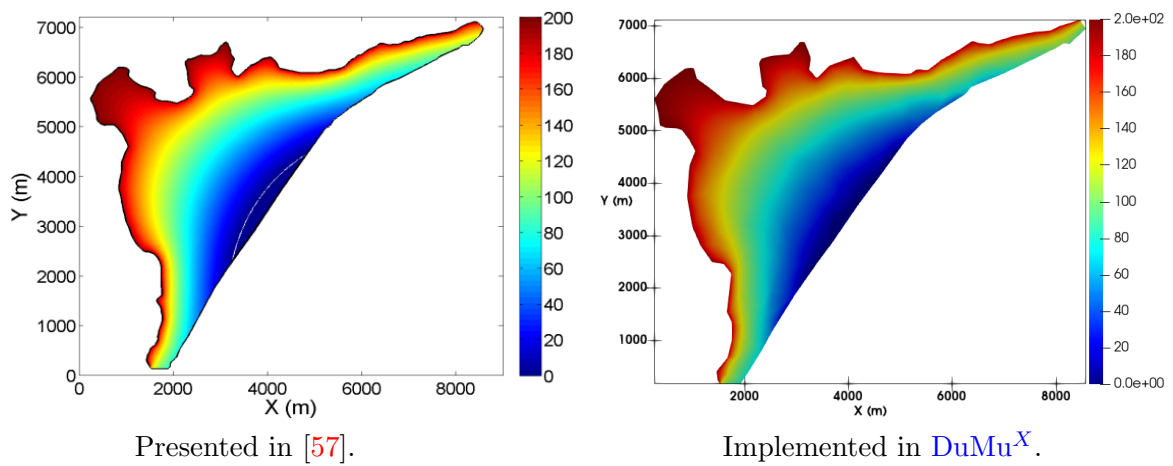


Figure 3.34: Evolution of the saltwater/freshwater interface in 2008. "NOP" scenario

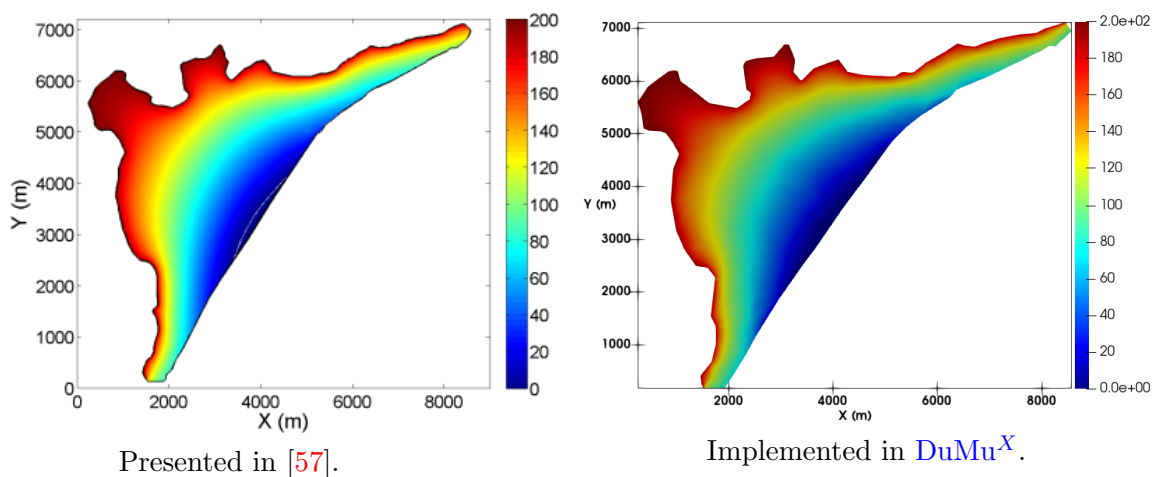


Figure 3.35: Evolution of the saltwater/freshwater interface in 2018 with a rate of 150 L/day as recommended by the water authorities.

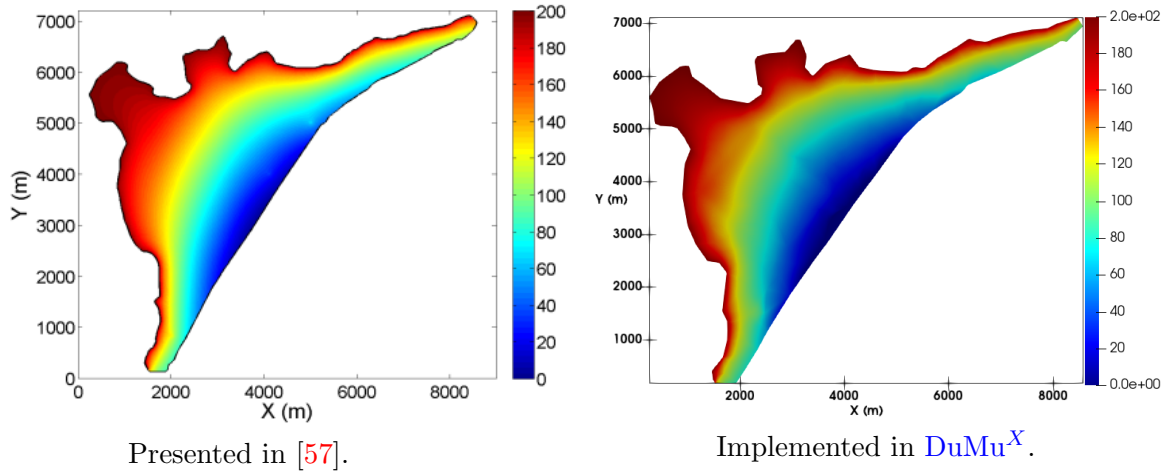


Figure 3.36: Evolution of the saltwater/freshwater interface in 2018 with a rate of 250 L/day.

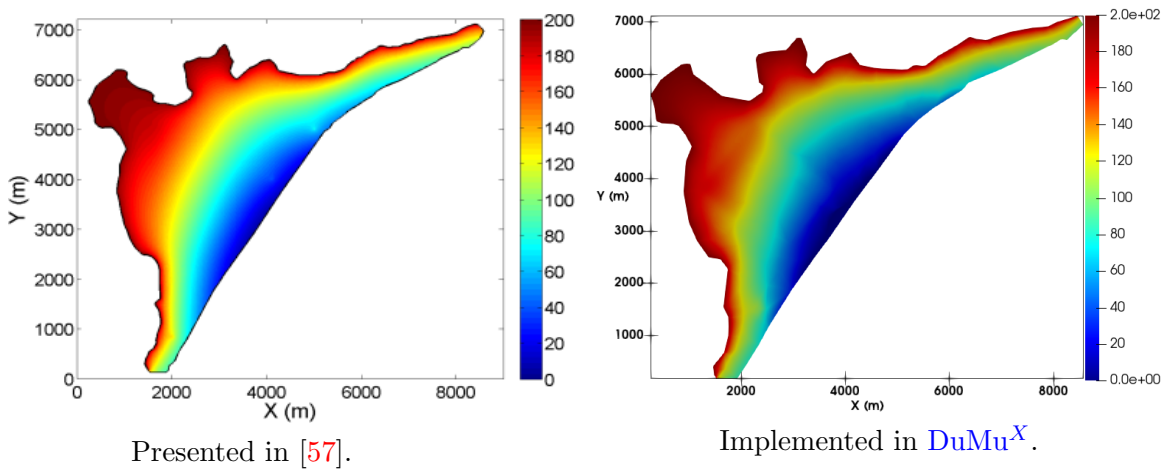


Figure 3.37: Evolution of the saltwater/freshwater interface in 2028 with a rate of 250 L/day.

Up to 2008, the aquifer is not subjected to any external forces and is assumed to be in natural equilibrium. A significant movement of the interface towards the interior of the domain is observed. In Figure 3.35, the salt level is stable and the saltwater/freshwater interface has not moved during 10 years of pumping at the rate of 150 L/day recommended by the water authorities. Using the current rate of 250 L/day for 10 years of exploitation, we can see a significant advance of the interface in Figure 3.36 towards the landward side, especially in the position of the private wells. In Figure 3.37, the salt wedge has intruded about 300 m into the domain after 20 years of pumping.

We illustrate in 3.38 the piezometric head of freshwater in natural conditions. We can see that the equipotentials are regular and vary from 200 m at the coast to 206 m at the landside. In Figure 3.39, we illustrate the position of the freshwater head u in different situations. In Figure 3.39a), the pumping rate in private wells as recommended by the water authorities is about 150 L/day. We can observe that

the water potential is stable and has not changed during 10 years of activity while it decreases with a rate of 250 L/day for the same period. During 20 years of over-exploitation with a rate of 250 L/day, the freshwater level is decreased in the whole plain and an exceptional depression is located around the position of the pumping wells.

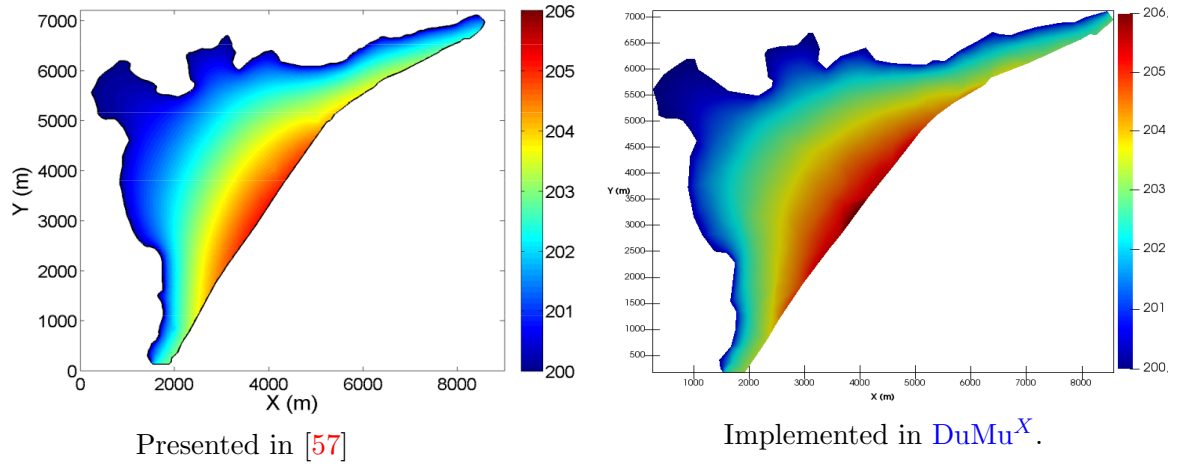


Figure 3.38: Evolution of the piezometric head of freshwater in 2008.

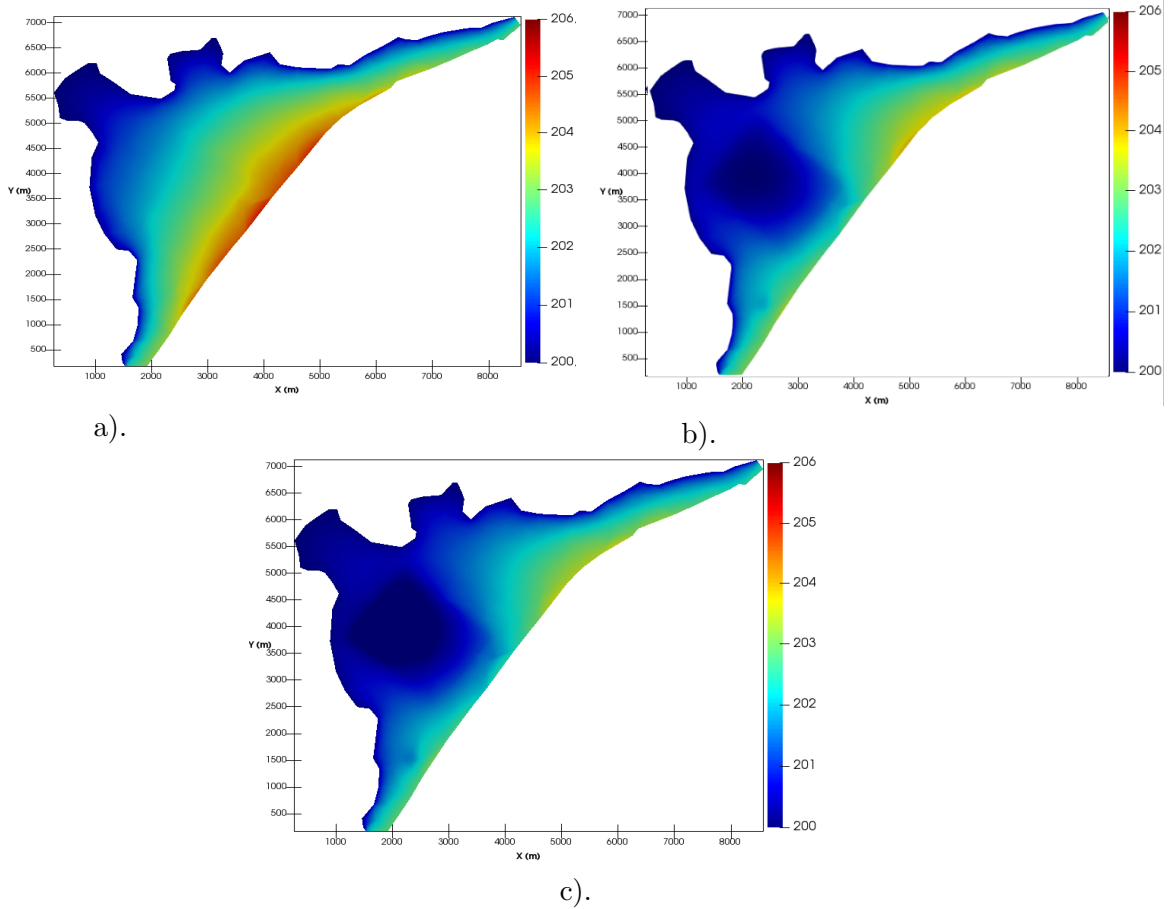


Figure 3.39: Position of the freshwater head scenarios. a) After 10 years of pumping with 150 L/day: "REC" scenario. b) After 10 years of pumping with 250 L/day: "10Y" scenario. c) After 20 years of pumping with 250 L/day: "20Y" scenario.

In this section, we presented a comparison between our results and those presented in [57] for a homogeneous test case dealing with the impact of demographic change on seawater intrusion in the lower Tripoli aquifer in Lebanon. We can see good agreements between the two calculations, which ensures the validity of our developed model. The numerical results of the test case "Tripoli aquifer" showed the ability and capacity of our model to predict the seawater intrusion in real scale test cases.

3.5 Conclusion

In this chapter, we have developed a fully coupled, fully implicit approach of the sharp interface seawater intrusion problem. The first part deals with the numerical scheme of the mathematical model. The coupled system is discretized by a cell-centered finite volume method in space. For the time discretization, we used an implicit Euler method, which allows us to take large time steps. The CPU time is, therefore, significantly decreasing while maintaining a good accuracy of the scheme. The nonlinear system is solved by Newton's method, wherein each iteration a linear system is solved by a preconditioned gradient BiConjugate STA-

Bilized (BiCGSTAB). The time step is chosen according to the number of iterations required by the Newton method to achieve convergence in the last iteration. Thereafter, We have developed and implemented a new module, called 2p-SWI, in the context of the parallel open-source platform [DuMu^X](#), based on [DUNE](#). A short description of the platform is also provided. Afterwards, the *2p-SWI* module has been validated in several examples.

The first test case is described in [\[67\]](#). Numerical simulations are compared to an analytical solution proposed in [\[61\]](#). The obtained results are satisfactory and in good agreement with those in [\[67\]](#). Next, we have considered the field-scale free aquifer test case [\[70\]](#). Our numerical simulations are compared to those in [\[70\]](#). The numerical results demonstrate the accuracy and robustness of our approach.

After that, we have applied our model to the Souss-Chtouka field case located in the southwestern of Morocco. The numerical model is based on available hydrogeological data in real scale by simulating the progress of seawater intrusion during 80 years. Until 1968, the aquifer is supposed to be in hydrostatic equilibrium. To do so, the model is first performed under steady-state conditions. The obtained results constitute, therefore, the initial values of the transition model. After 80 years of exploitation, the salt front has moved to the landside. Also, the level of the freshwater head decreases in the entire basin. The numerical results show that marine intrusion is dependent on several factors, such as the amount of extraction carried out and the location of wells close to the shoreline. It should also be noted that marine intrusion is favored in areas of high permeability, even in the absence of pumping. Afterwards, we validated our implemented module on a real test case corresponding to the Tripoli aquifer in the northeast of Lebanon. Numerical simulations over 20 years of exploitation are presented. The comparison of our numerical results and those presented in [\[57\]](#) showed a good agreement, which ensures the validity of our module to provide efficient and accurate results in real scale test cases.

Chapter 4

A finite volume method for numerical simulation of the sharp-diffuse interfaces model

Contents

| | |
|------------------------------------------------------------------------|-----------|
| 4.1 Introduction | 69 |
| 4.2 Mathematical model of the sharp-diffuse interfaces problem | 70 |
| 4.3 Numerical simulations of the sharp-diffuse interfaces model | 72 |
| 4.3.1 Test 1: Pumping of freshwater | 72 |
| 4.3.2 Test 2: Tidal effects | 78 |
| 4.3.3 Test 3: 3D variable density test | 82 |
| 4.4 Conclusion | 89 |

4.1 Introduction

In this chapter, we present a finite volume scheme and numerical simulation of the sharp-diffuse interfaces model into coastal aquifers, which was recently introduced in [25, 26]. We present the derivation of the mathematical model in section 4.2. Such flows are governed by a coupled system of two parabolic partial differential equations describing a two-phase immiscible seawater/freshwater flow and integrating the dynamics of transition zones. The non-degeneracy of the equations comes from the presence of the term modeling the transition zones.

In section 4.3, we developed a fully coupled, fully implicit finite volume scheme to discretize the governing equations. Precisely, we employ a TPFA method in space on a structured mesh where the orthogonality condition is satisfied. We apply an implicit Euler scheme for the time discretization, which allows us to take large time steps and thus reduce the CPU time. An upwind scheme is used to approximate the convective flux. In this context, we have developed and integrated a two phase diffuse module in the framework of DuMu^X. The validity of the implemented

module is examined through the study of the numerical convergence of the scheme. Moreover, a 2D simulations on different grid resolution prove the ability of the developed module to predict the position of the interface in the presence of the transition zones. This has been discussed and presented in section 4.3.

Thereafter, we propose to compare the numerical results of our 2D module with those obtained with the classical 3D model for miscible displacements. The 2D model yields information on the position of the salt front whereas the 3D model describes the evolution of the salt concentration. Numerical simulations of both models are afterwards compared to those presented in [23]. The numerical results showed that this approach gives physically consistent and performance results. Finally, section 4.4 presents some concluding comments.

4.2 Mathematical model of the sharp-diffuse interfaces problem

In this section, we present the mathematical modeling of seawater intrusion using a mixed sharp-diffuse interfaces approach [24, 25]. Let us mention that the derivation of this model is done in [25]. Therefore, we only present here the outlines to obtain the governing equations modeling saltwater intrusion using the mixed approach. Freshwater and saltwater fluxes are modeled by mass conservation and Darcy's laws for each fluid. By neglecting the vertical variation of the fluids, the flow is assumed to be horizontal. The problem is therefore reduced to a 2D model that takes into account the dynamics of the transition zones. Neglecting the saltwater storage coefficient, the governing equations modeling the freshwater and saltwater flows are as follows

$$S_f b_f \frac{\partial u}{\partial t} - \operatorname{div}(b_f \mathbf{D} \nabla u) + F(u) - F(Z) = Q_f, \quad (4.2.1)$$

$$- \operatorname{div}((1 + \gamma) b_s \mathbf{D} \nabla v) + F(Z) = Q_s. \quad (4.2.2)$$

where u is the freshwater head, Z is the salt front elevation and v is the saltwater head. The other notations are summarized in Figure 4.1 and given as follows

- S_f : the storage coefficient of freshwater,
- $b_f = u - Z$: thickness of the freshwater.
- $b_s = Z - Z_B$: thickness of the saltwater.
- Q_i : quantity of the fluid $i = f, s$ pumped or injected per unit of surface.
- \mathbf{D} : the hydraulic conductivity of freshwater.
- $\gamma = \frac{\rho_s - \rho_f}{\rho_f}$: the density contrast and ρ_i is the density of the fluid $i = f, s$.
- $F(\cdot)$: the approximated flux on the saturated/unsaturated and freshwater/saltwater zones.

The aquifer is presented by a domain $\Omega \times (Z_B, Z_T)$ with $\Omega \subset \mathbb{R}^2$ represents a part of its horizontal surface. The function Z_B [resp. Z_T] describes its lower [resp. upper] topography.

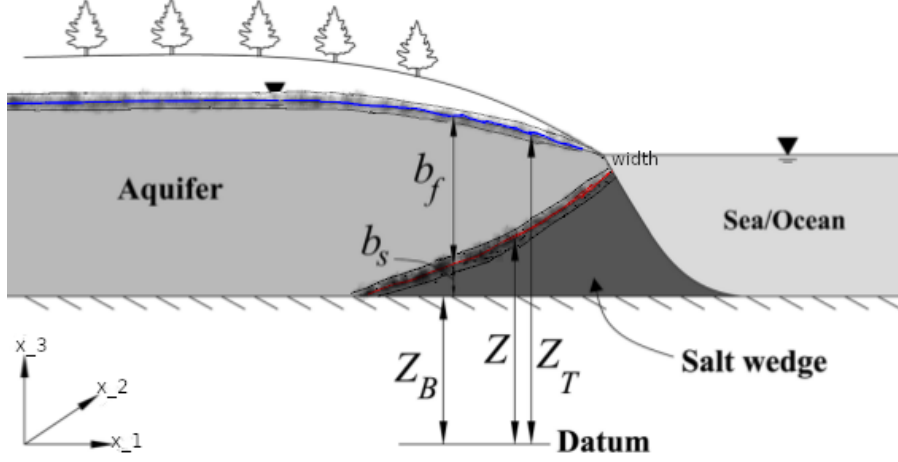


Figure 4.1: Schematic representation of a coastal aquifer.

For modeling the transition zones, a phase field model developed in [10] is employed. For more details on the approximation of the fluxes across the transition zones, the authors can refer to [24]. The expression for the approximate fluxes describing the dynamics of diffusive transition zones is as follows:

$$F(u) = \phi\beta \left[\frac{\partial u}{\partial t} - \delta \operatorname{div}(\mathbf{D}\nabla u) \right],$$

$$F(Z) = \phi \left(\frac{\partial Z}{\partial t} - \delta \Delta Z \right).$$

where ϕ and δ are respectively the porosity of the medium and the width of the transition zones. The elevation of the salt front is written $\gamma Z = (1 + \gamma)v - u$, while the parameter β is used to combine the two cases: free and confined aquifers,

$$\beta = \begin{cases} 1, & \text{if the aquifer is free,} \\ 0, & \text{if the aquifer is confined.} \end{cases}$$

Let Ω be an open polygonal domain, $\partial\Omega = \Gamma$, $x = (x_1, x_2) \in \mathbb{R}^2$ and $]0, T[$ a time interval. Let $\Omega_T =]0, T[\times \Omega$ and $\partial\Omega_T =]0, T[\times \partial\Omega$. Summing equations (4.2.1)-(4.2.2) and invoking the expression of the approximated fluxes, the mathematical system is given by

$$\begin{cases} (S_f b_f + \beta\phi) \frac{\partial u}{\partial t} - \operatorname{div}(\mathbf{D}(b_s + b_f)\nabla u) - \operatorname{div}(\gamma\mathbf{D}b_s\nabla Z) - \beta\delta \operatorname{div}(\phi\mathbf{D}\nabla u) = Q_f + Q_s & \text{in } \Omega_T, \\ \phi \frac{\partial Z}{\partial t} - \operatorname{div}(\mathbf{D}b_s\nabla u) - \operatorname{div}(\gamma\mathbf{D}b_s\nabla Z) - \delta \operatorname{div}(\phi\mathbf{D}\nabla Z) = Q_s & \text{in } \Omega_T, \\ \mathbf{D}\nabla u \cdot \vec{n} = 0, \quad \mathbf{D}\nabla Z \cdot \vec{n} = 0, \quad \mathbf{D}b_s\nabla u \cdot \vec{n} = 0 & \text{on } \partial\Omega_T, \\ \mathbf{D}(b_s + b_f)\nabla u \cdot \vec{n} = 0, \quad \mathbf{D}b_s\nabla Z \cdot \vec{n} = 0 & \text{on } \partial\Omega_T, \\ u(., 0) = u_0, \quad Z(., 0) = Z_0 & \text{in } \Omega, \end{cases}$$

where the main unknowns are, from now on, the freshwater head u and the salt front elevation Z . The initial conditions $u^0(x)$ and $Z^0(x)$ are given for u and Z at $(t = 0)$ to describe the initial state of the aquifer while \vec{n} is the unit outward normal to $\partial\Omega$. The other physical parameters used in the system are defined above.

The problem consists of a coupled system of two nonlinear parabolic partial differential equations simulating two immiscible fluids and taking into account the dynamics of the transition zones.

4.3 Numerical simulations of the sharp-diffuse interfaces model

Let us mention that the finite volume numerical scheme for the sharp-diffuse interfaces model using the TPFM finite volume method is similar to that presented in chapter 3. Therefore, this subsection discusses numerical simulations of this model using the TPFM method to predict seawater intrusion in coastal aquifers.

The numerical scheme afterwards is implemented and integrated in the framework [DuMu^X](#). We validate our scheme on different test cases. First, we proceed to the numerical convergence of the scheme in the case of a free aquifer. Besides, we have tested our 2pdiff-SWI module against an analytical solution derived from Ferris model [45]. The obtained results match well with the analytical solution and are in good agreement with those presented in [7, 23]. Our results are completely equivalent to the results given in [7, 23] thus validate our methodology and demonstrate the usability and capacity of our module to simulate marine intrusion into coastal aquifers.

4.3.1 Test 1: Pumping of freshwater

Here, we consider a test case described in [25] dealing with the effect of pumping on the displacement of the salt front in an unconfined aquifer where diffusion in the transition zones is not neglected. First, we proved the validity of our sharp-diffuse interfaces model implemented in [DuMu^X](#) by studying the numerical convergence of the TPFM scheme. Different meshes resolution are used to visualize the convergence of the solutions to the reference solution. Numerical results, proving the efficiency and accuracy of our model to predict saltwater intrusion, are presented.

4.3.1.1 Test description

We consider a free aquifer of thickness 10 m and horizontal surface $\Omega =]-50 \text{ m}, 50 \text{ m}[\times]-20 \text{ m}, 20 \text{ m}[$. Homogeneous Neumann boundary conditions are imposed on the boundaries to let the interfaces evolve freely. We pump a constant amount of freshwater with different rates ranging from $0.8 \text{ m}^3/\text{day}$ to 0 according to the position (x_1, x_2) for three days. The main pumping point is located at $(x_1 = 15 \text{ m}, x_2 = 0 \text{ m})$ with a maximum rate of $0.8 \text{ m}^3/\text{day}$. The rate decreases as it approaches the boundaries. .

Numerically, the pumping (or injection) is modeled by a term source imposed in a specified part of the domain. In this case, let the term source of the freshwater equation $Q_f = -0.8 \exp(-0.01((x-15)^2 + y^2))$. The initial position of the saltwater/freshwater interface is computed with an analytical solution proposed in [61]. The position of the intersection of the interface with the base of the aquifer is initially set at 30 m.

The physical parameters and properties of the aquifer are summarized in Table 4.1.

| Parameters | δ | ϕ | $\mathbf{D}[\text{m/day}]$ | S_f |
|------------|----------|--------|----------------------------|-------|
| Values | 0.1 | 0.3 | 39.024 | 0.0 |

Table 4.1: Parameter values for the pumping scenario.

4.3.1.2 Numerical convergence

First, we proceed to the study of the numerical convergence. We calculate the solution of the problem for different cells. The initial mesh is refined several times. For example by a factor 2. We consider the following grids as presented in Table 4.2

| Grid levels | Number of cells |
|-------------|--------------------------|
| 1 | $40 = 10 \times 4$ |
| 2 | $160 = 20 \times 8$ |
| 3 | $640 = 40 \times 16$ |
| 4 | $2560 = 80 \times 32$ |
| 5 | $10240 = 160 \times 64$ |
| 6 | $40960 = 320 \times 128$ |

Table 4.2: Different grids used in the numerical convergence.

We calculate the reference solution on a fine grid corresponding to $40960 = 320 \times 128$ cells. We start by making several sections in space and time. In Figure 4.2, we plot the section in space from the point $(-50, 0)$ to the point $(50, 0)$. The section passes through the main part of the pumping. Figure 4.2 shows the evolution of several quantities in a free aquifer subjected to pumping for 3 days. We observe the convergence of the solution calculated on different grids towards the reference solution.

In addition, we consider a plot selection over time taken at point $(-10, 0)$ that belongs to the main part of the pumping. Figure 4.3 shows the evolution of the freshwater head, the saltwater head and the elevation of the salt front over time. We see that during 3 days of pumping, the solution calculated on different grids converges towards the reference solution.

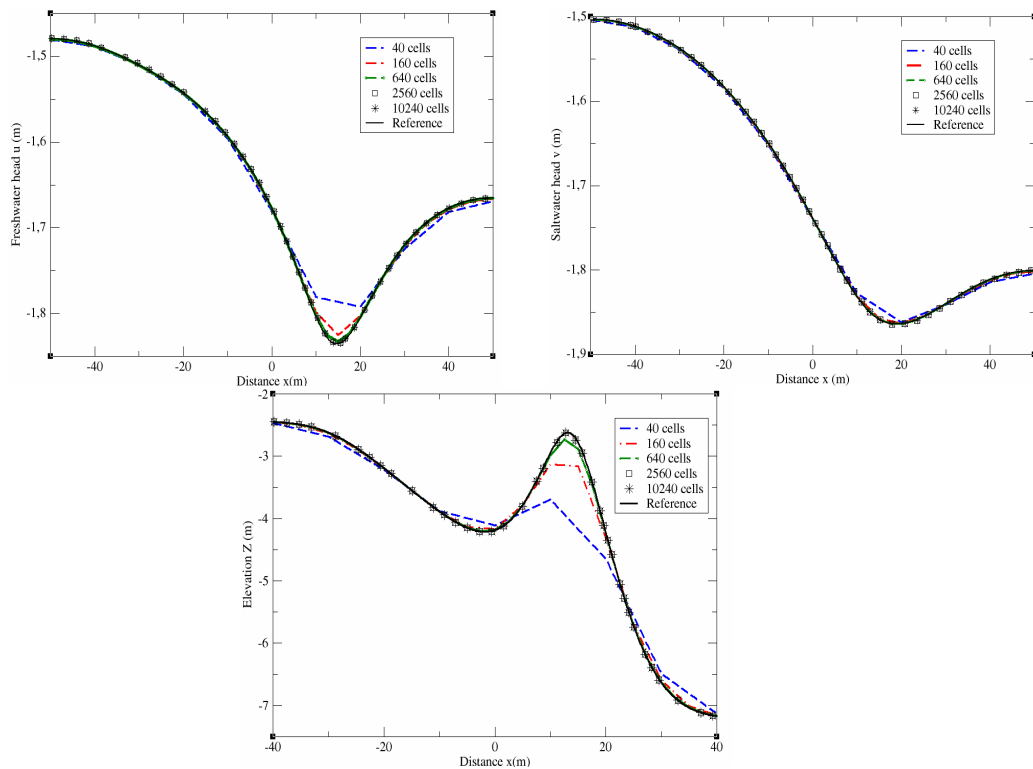


Figure 4.2: Convergence of solutions on each grid to the reference solution during 3 days of pumping on cross-section $(-50, 0) - (50, 0)$.

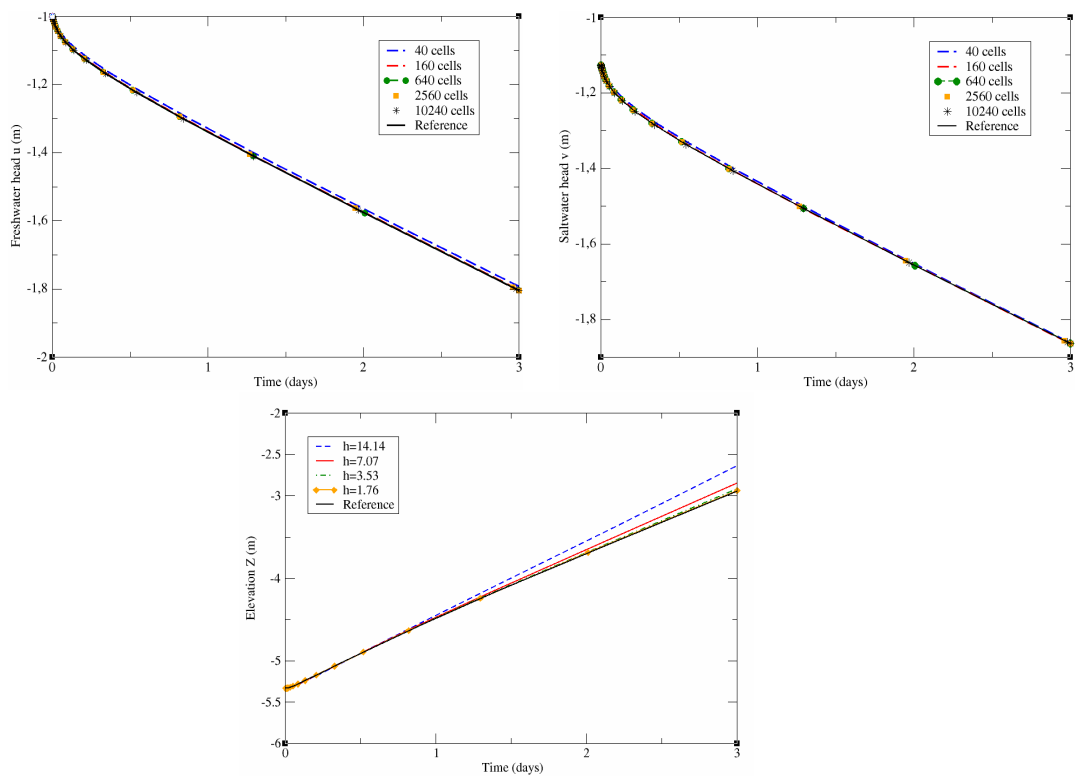


Figure 4.3: Evolution of the solutions on each grid and convergence to the reference solution for 3 days at the point $(-10, 0)$.

Finally, we make an analysis of the error starting from an initial value 40 cells, then we will calculate the numerical convergence order. The tables 4.3-4.5 below represent the standard l^2 and l^∞ relative norms as well as the order of convergence.

| Cells | 40 | 160 | 640 | 2560 | 10240 |
|---------------------|--------------|--------------|--------------|--------------|--------------|
| Freshwater head u | $1.05e^{-2}$ | $4.92e^{-3}$ | $2.4e^{-3}$ | $1.16e^{-3}$ | $5.22e^{-4}$ |
| Saltwater head v | $8.9e^{-3}$ | $4.23e^{-3}$ | $2.07e^{-3}$ | $1.01e^{-3}$ | $4.52e^{-4}$ |
| Elevation Z | $6.03e^{-2}$ | $2.96e^{-2}$ | $1.46e^{-2}$ | $7.13e^{-3}$ | $3.18e^{-3}$ |

Table 4.3: Numerical convergence of the scheme in l^2 -relative norm.

| Cells | 40 | 160 | 640 | 2560 | 10240 |
|---------------------|--------------|--------------|--------------|--------------|--------------|
| Freshwater head u | $8.35e^{-2}$ | $4.18e^{-2}$ | $1.95e^{-2}$ | $8.29e^{-3}$ | $2.79e^{-3}$ |
| Saltwater head v | $5.74e^{-2}$ | $2.73e^{-2}$ | $1.23e^{-2}$ | $5.3e^{-3}$ | $1.8e^{-3}$ |
| Elevation Z | 2.03 | 1.08 | 0.48 | 0.2 | $6.98e^{-2}$ |

Table 4.4: Numerical convergence of the scheme in l^∞ norm

| Number of cells | 40 | 160 | 640 | 2560 | 10240 |
|---------------------|----|------|------|------|-------|
| Freshwater head u | — | 1.09 | 1.03 | 1.04 | 1.15 |
| Saltwater head v | — | 1.07 | 1.03 | 1.03 | 1.16 |
| Elevation Z | — | 1.02 | 1.01 | 1.03 | 1.16 |

Table 4.5: Order of convergence

Figure 4.4 shows the exact total amount of freshwater pumped against the numerical amount. The aquifer is closed. The total amount of freshwater pumped over 3 days is founded exactly using the numerical model. As a consequence, the mass conservation law is satisfied. Numerically, we represent the pumping process in the term source by a negative value and the injection by a positive value.

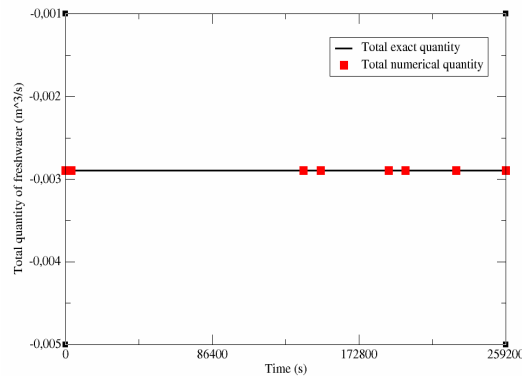


Figure 4.4: Conservation of the total amount of freshwater pumped

The last stage of our study concerns the CPU time and the number of iterations

required by Newton’s method to achieve convergence. Table 4.6 summarizes the CPU time and the number of iterations calculated on different grids.

| | | | | | | |
|--------------|------|-------|-------|------|-------|-------|
| Cells | 40 | 160 | 640 | 2560 | 10240 | 40960 |
| Time CPU (s) | 0.06 | 0.249 | 0.971 | 4.06 | 17.46 | 80.29 |

Table 4.6: CPU time and the number of iterations required by Newton’s method to converge

By refining the initial grid several times, the program takes more time to complete the process. The CPU time therefore gradually increase.

Simulations have been performed with an initial time step of 10 s and a maximum time step of 0.5 day. The time step size increases if Newton’s method converges with less iterations in the last time iteration and decreases otherwise. This process is manipulated during the simulation according to the function *SuggestStepTimeSize()* implemented in DuMu^X. The tolerances for the Newton method and the BICGSTAB solver are respectively 10^{-8} and 10^{-6} . In this test, Newton’s method converges in less than 4 iterations.

4.3.1.3 Numerical results

This subsection aims to illustrate the displacement of the interface of the salt front and the ground water level in a free aquifer subjected to pumping during 3 days. In this test, we consider an uniform rectangular resolution of 80×32 in the direction $x_1 \times x_2$. In Figure 4.5, we can see that the "upconing" is appeared and grow up quickly and a local depression is located at the main zone of pumping. The presence of the freshwater/saltwater transition zone and the saturated/unsaturated zone promotes diffusion and advancement of the free surface and salt front.

The velocity of freshwater and saltwater flows during 3 days of pumping is illustrated in Figure 4.6. The flow velocity of both fluids is maximum in the main pumping zone. Moreover the direction of the freshwater flow tends downward while tends to upper for the saltwater fluid. Furthermore, the direction of freshwater flow tends downward, corresponding to the decrease in freshwater level, while the saltwater flow tends toward the upper surface. This proves the ability of our model to predict saltwater intrusion into an unconfined aquifer and its ability to provide physically satisfactory results.

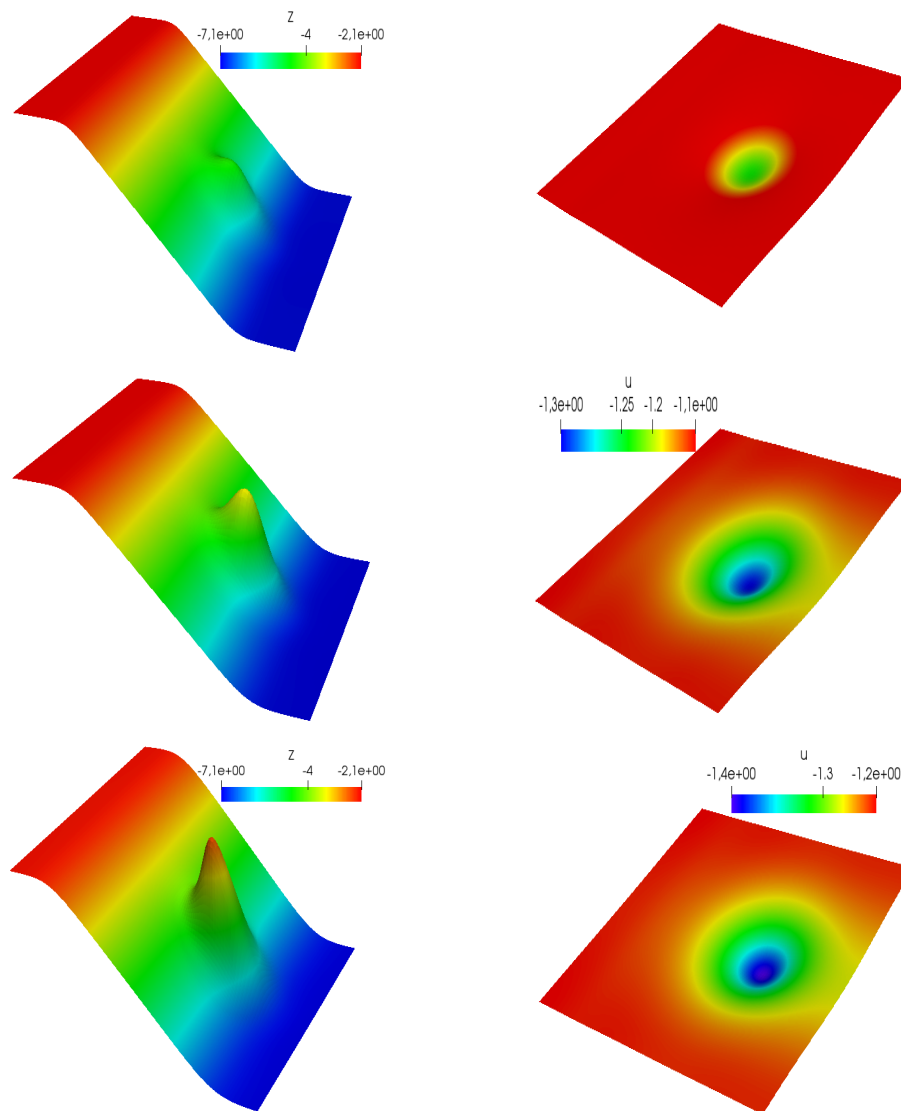
Salt front elevation Z .Freshwater head u .

Figure 4.5: Evolution of the elevation of sharp-diffuse interfaces (left) and the freshwater head (right) in 1, 2 and 3 days.

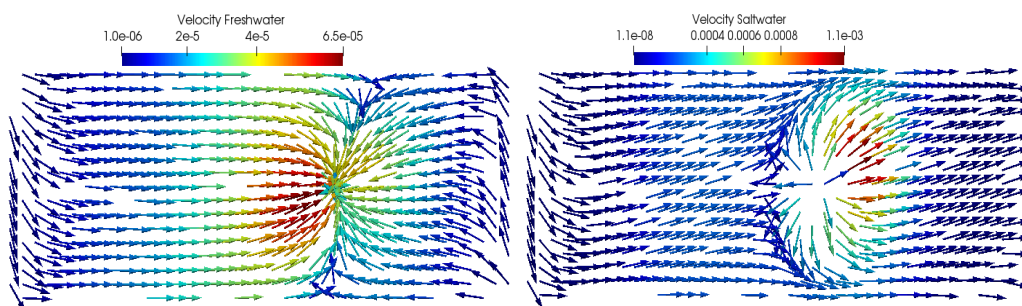


Figure 4.6: Velocity of freshwater (left) and saltwater (right) flows during 3 days of pumping.

4.3.2 Test 2: Tidal effects

The purpose of this test is to assess the validity of our implemented module in the case of a free aquifer. For this purpose, we consider a test case presented in [7, 25], which mainly focuses on the interface displacement coupling with tidal fluctuation effects. We propose to compare our numerical results with an analytical solution derived from the Ferris model [45]. The obtained results are promising and show a good agreement for both calculations. Afterwards, we compare our obtained results to those presented in [7, 25] in different situations. The numerical simulations prove that our module is efficient and able to predict seawater intrusion in a free aquifer taking into account the width of the transition zones and sea fluctuations effects.

4.3.2.1 Test description

We consider a free aquifer represented by $]0, 50[\times]0, 50[$. The depth of the aquifer is fixed at 10 m. We combine the problem, of rotary character, with tidal effects. The oscillations of the sea progressively generate pressure waves close to the aquifer. For this test case, we use the parameters proposed in [30] after a scaling of our aquifer. We take $\mathbf{D} = 39.024\text{m/day}$ for the hydraulic head of freshwater and $\phi = 0.3$ for the porosity. We impose a Dirichlet boundary condition at the seashore, which corresponds to $\{x_1 = -50\}$, for the salt front Z (while the freshwater head u evolves freely on the impermeable side). The Dirichlet value is calculated using an analytical solution proposed in [7, 45]. Homogeneous boundary conditions are imposed on the rest of the boundary. The amplitude of the transition zone δ is evaluated from the equation for the width of the dispersive zone (eq. (2) in [30]). Its value is approximately $\delta = 0.1$. We performed the simulations with an initial time step of 0.01 s and a maximum time step of 1 day.

4.3.2.2 Numerical results

In order to ensure the validity of our developed module in the case of a free aquifer, we propose to compare our numerical results issued from our developed module with an analytical solution computed with Ferris model. In this case, the aquifer is not subjected to any external forces. For these simulations, we consider two uniform rectangular mesh with mesh 1 = 100×100 and mesh 2 = 200×200 in the $x_1 \times x_2$ direction. Figure 4.7 illustrate the position of the interface obtained with this present model compared to the analytical solution after a period and a half-period sea fluctuations.

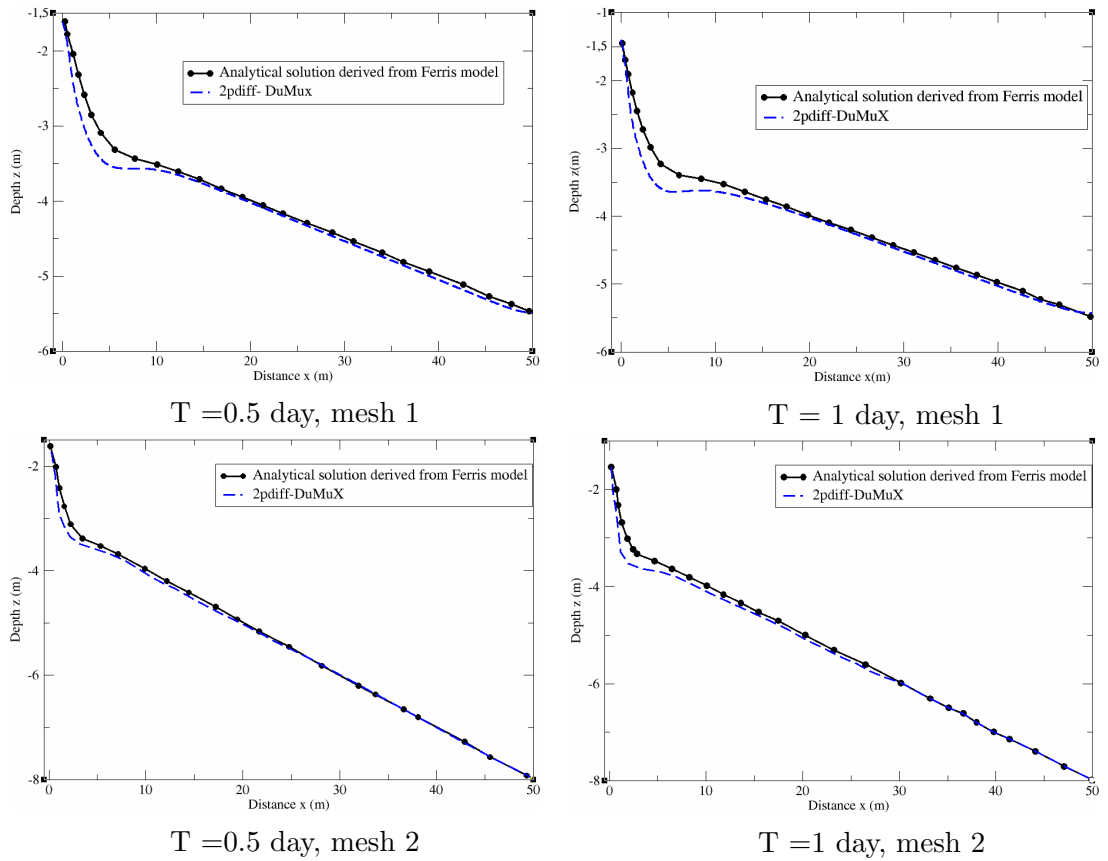


Figure 4.7: Convergence of the interface obtained with the present model towards the analytical solution derived from Ferris model. Times $T = 0.5$ day (left) and $T = 1$ day (right).

By refining the mesh twice, we can observe the convergence of the numerical solution to the analytical solution derived from the Ferris model at both times $T = 0.5, 1$ days. After one day, the interface evolves freely on the landside and returns to its initial position on the seaward side. The wave pressure causes oscillations on the seaside and accelerates the movement of the interface in the whole domain. Next, we propose to compare our obtained results with those presented in [6] in two different cases. The objective here is to evaluate the ability of our module to handle different physical phenomena. For the spatial discretization, we use the resolution of mesh 1. We illustrate in Figure 4.8 the evolution of the interface at different times without any external force while Figure 4.9 presents its position during a pumping scenario.

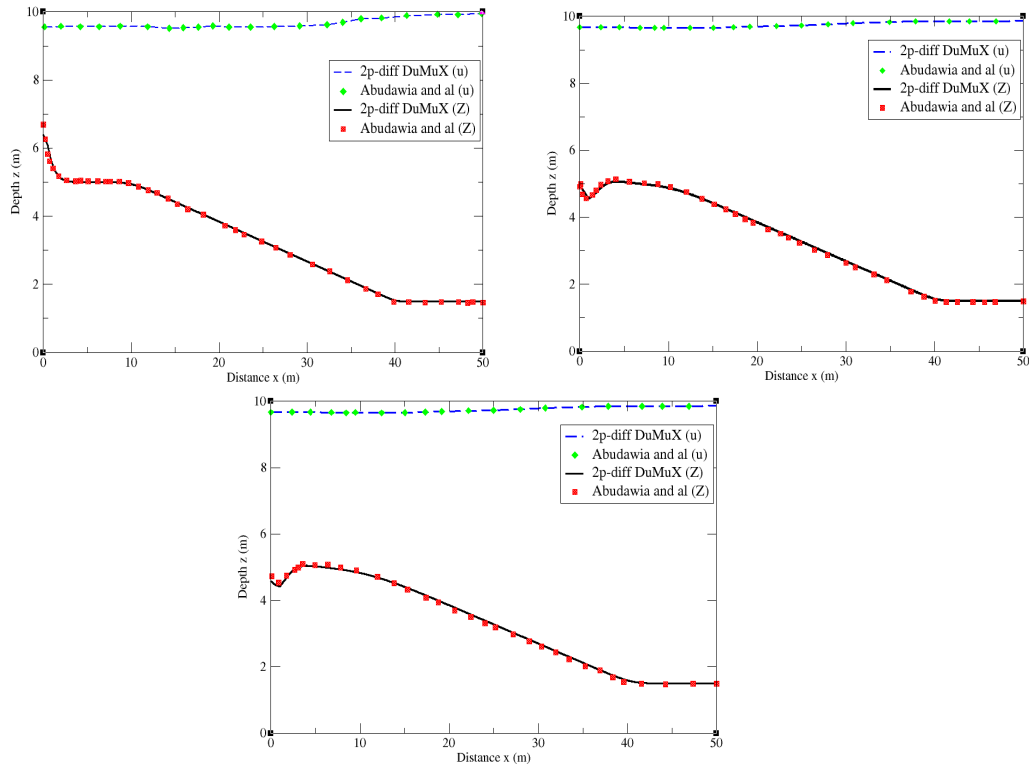


Figure 4.8: Evolution of the freshwater head and the salt front elevation in different times without any external forces. $T= 0.1, 0.5$ and 1 day.

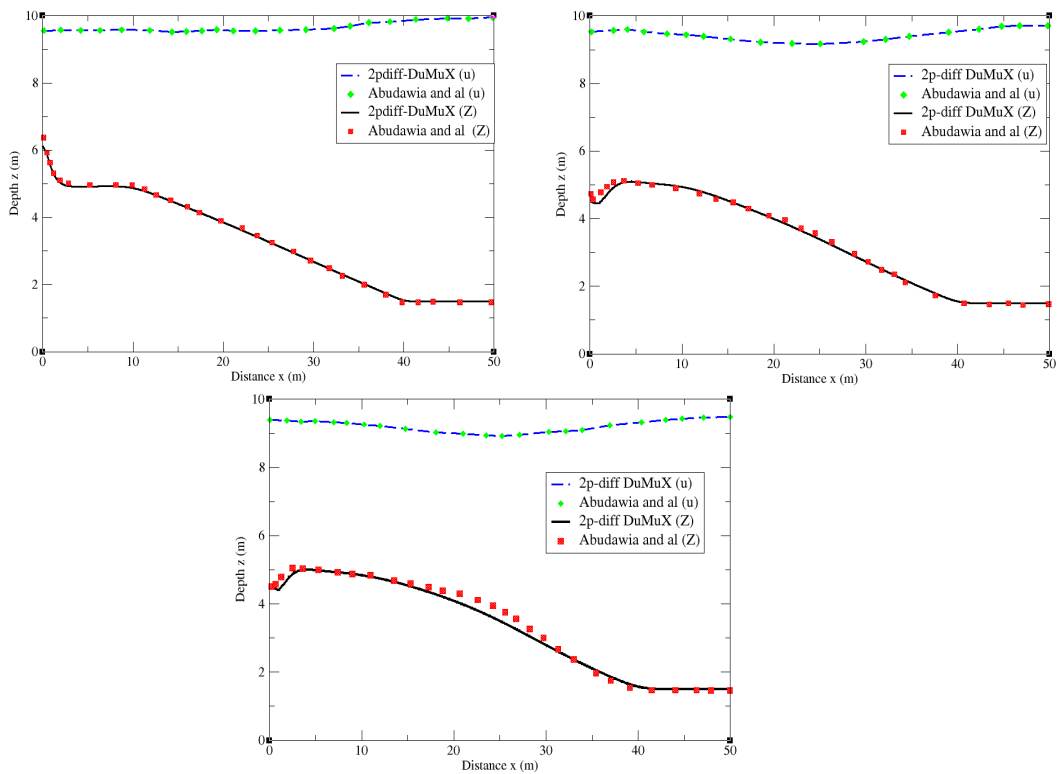


Figure 4.9: Displacement of the freshwater head and the salt front elevation in different times during a pumping scenario. $T=0.1, 0.5, 1$ day.

We place a hydrograph artifacts at $x = -35$ to illustrate the behavior of the salt interface over time. Figure 4.10 shows the results predicted by the hydrograph artifacts for the sharp interface model ($\delta = 0.0$) and the sharp-diffuse interfaces model ($\delta \neq 0$). The obtained results for both models are then compared to the analytical solution derived from Ferris. Afterwards, our numerical results for both models (sharp and sharp-diffuse interfaces model) are compared to those presented in [25]. The Dirichlet value at the seaside evolves over time and take into account the tidal effect. The impact of tidal fluctuations is illustrated in both situations. The interface evolves freely as in natural conditions despite the oscillations at the seashore. In addition, pumping effects are observed at the well position.

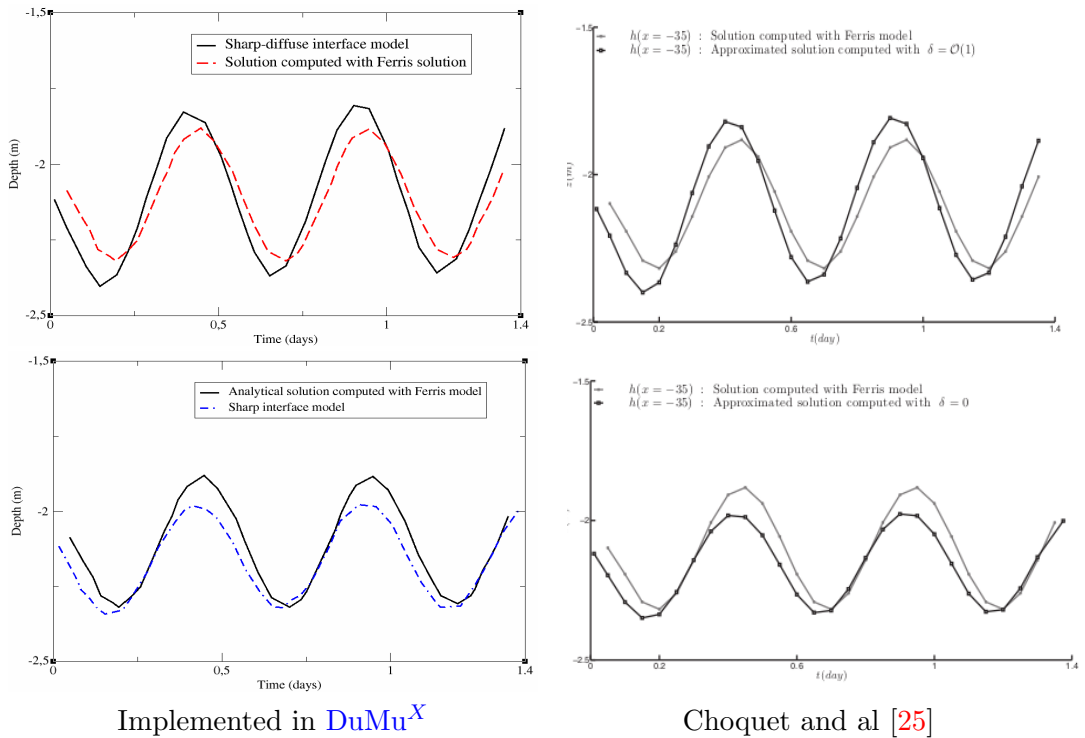


Figure 4.10: Oscillations on the salt front elevation, predicted by the hydrograph artifacts ($\delta = 0$ (left) and $\delta \neq 0$ (right)) and comparison between both models.

The first comment we can make is the similarity of our results implemented in [DuMu^X](#) (left) with those presented in [25]. The oscillations are more noticeable in the model with ($\delta \neq 0$). Comparing the two models to the analytical solution derived from the Ferris model, we observe that the model with a sharp-diffuse interfaces matches the analytical solution well. The evolution of the freshwater head u in this case for both models is illustrated in Figure 4.11.

Now, we concentrate on the behavior of the freshwater head when setting up seaside oscillations and with Neumann homogeneous BCs for both variables u and Z . In Figure 4.12, we present the result presented by the hydro-graph over time.

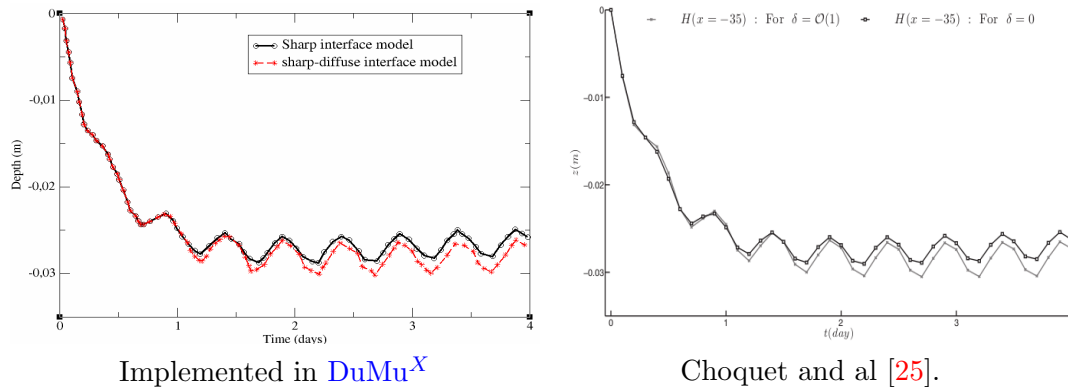


Figure 4.11: Sea oscillations effects on the freshwater head u . Simulations with $\delta = 0$ and $\delta \neq 0$.

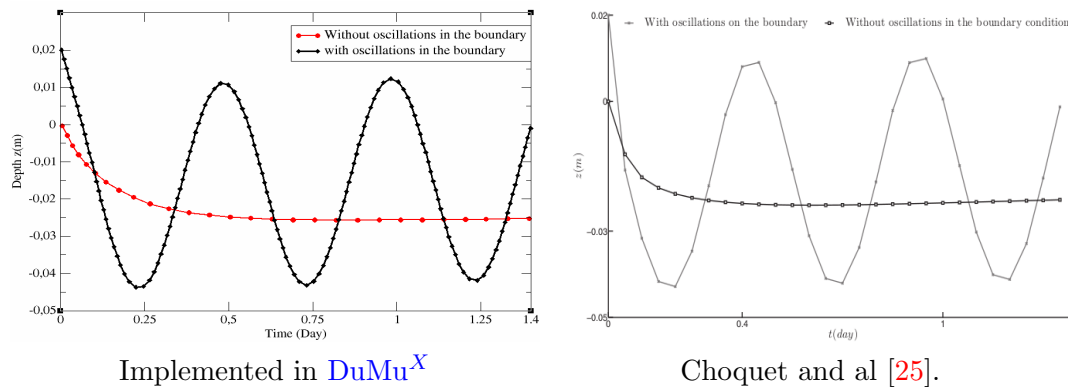


Figure 4.12: Evolution of the freshwater head u with and without oscillations in the boundary.

We distinguish here two cases: with and without oscillations on the boundary. By imposing the Dirichlet value calculated with the Ferris model, we can observe sinusoidal oscillations caused by tidal effects at the hydrograph located at $x_1 = -35$. Using homogeneous Neumann boundary conditions, we observe that the water table level decreases and stabilizes after 0.25 days.

4.3.3 Test 3: 3D variable density test

We consider a test case described in [23] that aims to numerically compare the 3D variable density model with the 2D sharp-diffuse interfaces model. The 3D model describes the evolution of the salt concentration while the 2D model gives the position of the salt front and takes into account the width of the transition zone. For the validation of our 2D and 3D models implemented in **DuMu^X**, we propose to compare our numerical results obtained for both models with those presented in [23]. The CPU time required for the 2D simulations is less than one minute, while it takes about 2 hours and 30 minutes for the 3D model.

4.3.3.1 Test description

We consider a confined aquifer presented by $\Omega_{3D} =]-5, 5[\times]0, 3[\times]-3, 0[$ which its horizontal surface is given by $\Omega_{2D} =]-5, 5[\times]0, 3[$. The depth of the aquifer for the 2D model is fixed at -3 . The physical parameters and data used in the simulations are summarized in table 4.7.

| Parameters | values |
|----------------------------------------------|------------------|
| Diffuse interface width δ [m] | 0.2 |
| Freshwater head Z_T [m] | 0.0 |
| Porosity [-] | 0.3 |
| Hydraulic conductivity \mathbf{D} [m/d] | 39.02 |
| Storage coefficient S_f [m ⁻¹] | 0.0 |
| Diffusion coefficient [m/s] | 10 ⁻⁷ |
| Longitudinal dispersivity α_L [m] | 0.2 |
| Transverse dispersivity α_T [m] | 0.0 |

Table 4.7: Parameters and properties of the aquifer

For the mesh, we use a uniform rectangular mesh of 200×60 for the 2D model and a resolution of $50 \times 50 \times 50$ for the 3D model in the direction $x_1 \times x_2 \times x_3$. The initial time step is set at 0.01s while the maximum time step is fixed at 0.1 day for both 2D and 3D models. Now, let's specify the initial conditions for both models. The freshwater head is set to $Z_T = 0.0$ while the initial position of the interface is given in Figure 4.13. In the salt part, the concentration is fixed at 0.2055, while it is zero in the freshwater side. The concentration in the transition zone is set to 0.1 with a width of 0.2 m. A 3D presentation of the quasi-interface is shown in Figure 4.14.

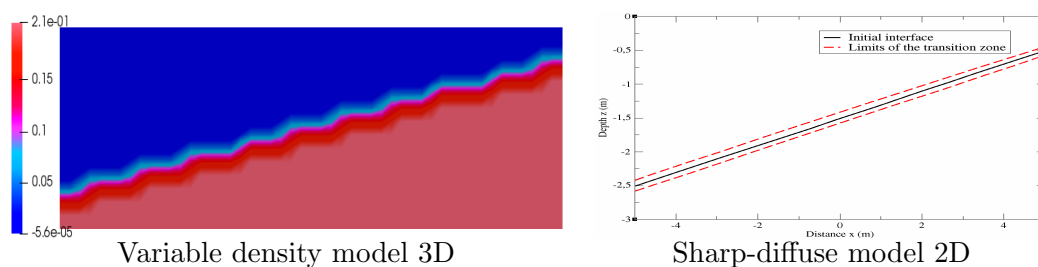


Figure 4.13: Initial conditions : initial salt concentration for the 3D model (left) and initial position of the transition zone between freshwater/saltwater for the 2D model (right).

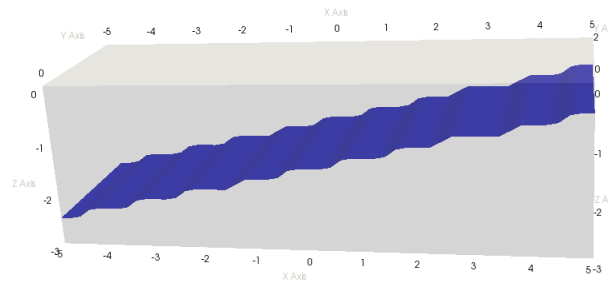


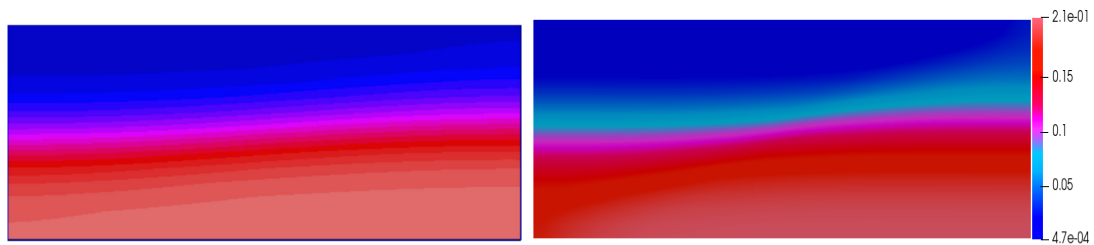
Figure 4.14: 3D presentation of the initial position of the interface.

4.3.3.2 Numerical results

In this sub-section, we will present numerical results for each model (3D and 2D models) implemented in DuMu^X compared to those of [23]. We consider the data and the physical parameters described above. Different cases dealing with saltwater pollution of an aquifer are analyzed.

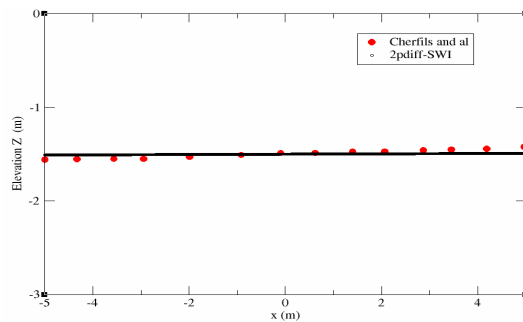
Case 1: rotating interface problem

In this test, we focus on the behavior of the interface at normal conditions where the aquifer is not subjected to any external forces (i.e., $Q_1 = Q_2 = 0.0$). To do so, we consider that the boundaries of the domain are impermeable. The storage coefficient S_f is neglected and we fix the density contrast $\gamma = 0.025$. The figure 4.15 shows the evolution of the salt concentration and the salt front obtained by the 3D and 2D models.



Cherfils and al [23].

3D density variable.



Sharp-diffuse interfaces model 2D.

Figure 4.15: Evolution of the freshwater and saltwater flows in the normal conditions during $T = 10$ days.

The first remark we can make concerns the consistency between our results and

those presented in [23]. The simulations start with a quasi-horizontal interface and, under the density contrast the interface evolves freely to reach its equilibrium state after 10 days. On the other hand, we can see that the diffuse interfaces issued from the 2D model is consistent with the 50 % contour of the transition zone in the 3D model. This can be confirmed with the result presented in figure 4.16.

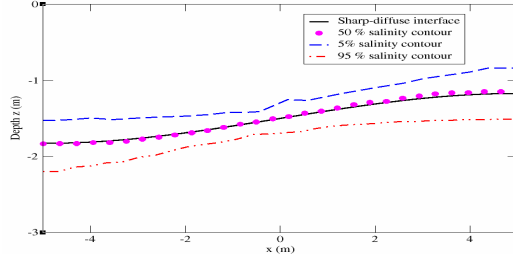


Figure 4.16: Representation of sharp-diffuse interfaces and 3D density variable results (50 % salinity contour and 5 % and 95% salinity contour) for $T=5$ days.

The dotted lines indicate 5 and 95 % salinity contours in the 3D model while the solid line represents the salt front elevation issued from the 2D model. We can see a good agreement between the results issued from both models. We illustrate in Figure 4.17 the gradient of the freshwater head.

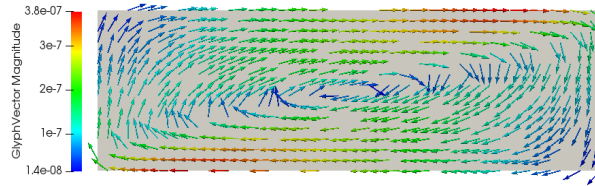


Figure 4.17: The velocity field in the rotating interface problem at $t = 10$ days.

Case 2: pumping process

We associate to the previous test a pumping well with a surface of 1 m^2 and a depth of 0.5 m with a pumping rate fixed at $0.6 \text{ m}^3/\text{day}$ per unit volume. This process is modeled numerically by positing $Q_2 = -0.6 \chi_{[-2,-3] \times [1,2] \times [-0.5,0]}$ and $Q_1 = 0.0$. We have reduced the effect of the density contrast $\gamma = 0.0025$ to better visualize the pumping effect. The interface is assumed to be fixed at the edge of the sea. Dirichlet boundary conditions are imposed on the right hand side of the domain. The model is performed for 5 days.

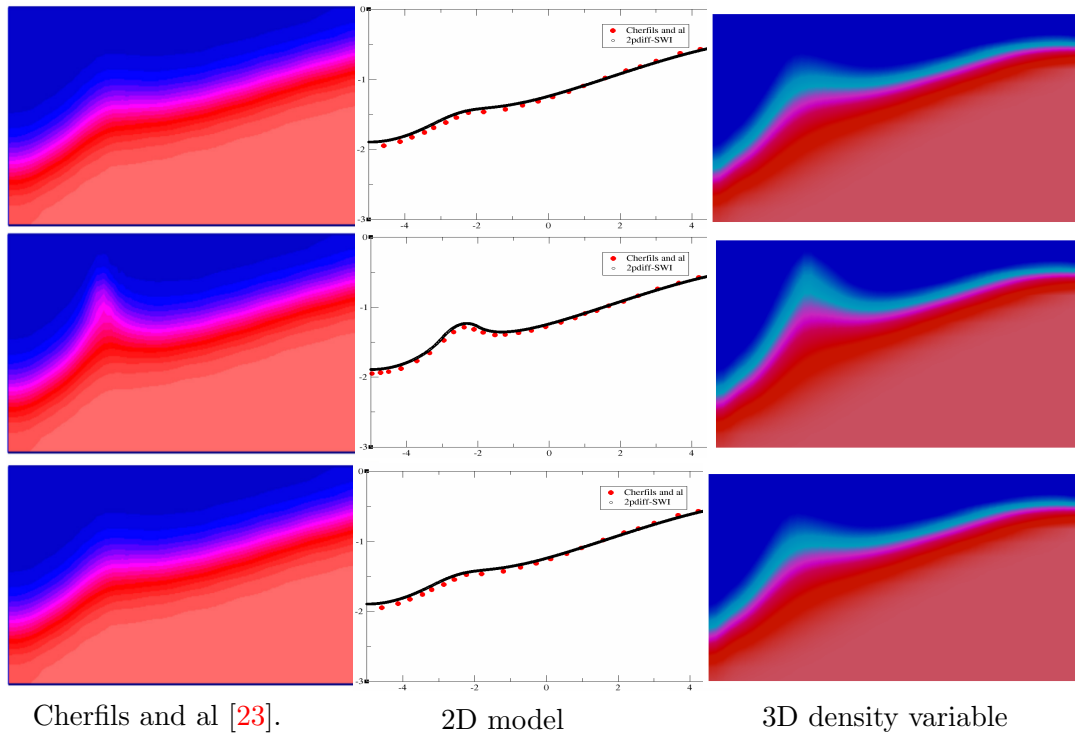


Figure 4.18: Numerical results for pumping scenario: $x_2 = 0.5$ (top) $x_2 = 1.5$ (center) and $x_2 = 2.5$ (below).

Figure 4.18 shows the evolution of the concentration and the salt front in a confined aquifer subjected to pumping. To visualize such a behavior in this case, we made three slices. Then, we consider the slice defined on $x_2 = 1.5$ and on $x_2 = 2.5$. The pumping effect appears more in slice $x_2 = 1.5$. Under the impact of a significant pumping flux, an "upconing" is formed and tends towards the horizon. The same behavior is shown in the 2D model in both slices. This leads to the conclusion that the 2D model fits well with the realistic 3D model. We perform the same experiment for a higher pumping rate and a higher density contrast. Let $Q_2 = -4.0\chi_{[-2,-3]\times[1,2]\times[-0.5,0]}$ and $\gamma = 0.025$. The objective of this experiment is to assess the validity of the 2D sharp-diffuse interfaces model with a large amount of pumping.

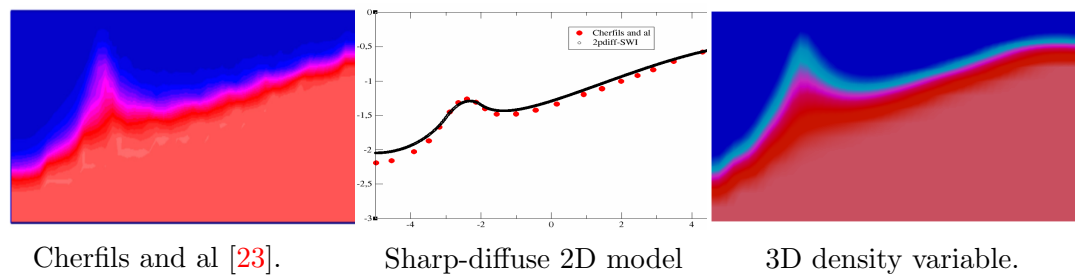


Figure 4.19: Evolution of the concentration (3D model) and the salt front (2D model) under a large amount of pumping: slice on $x_2 = 1.5$.

In Figure 4.19, the upconing shown by the sharp-diffuse 2D model is not a pike as

it is known for the classical sharp interface model. This is due to the existence of the width of the transition zone in the system of equations.

Case 3: injection process

In the following experiment, we add some form of injection to the problem. This is numerically modeled by a positive value imposed in a specific part of the domain. In our case, suppose that $Q_2 = 0.7\chi_{[1,2]\times[1,2]\times[-0.5,0]}$ and $\gamma = 0.00025$

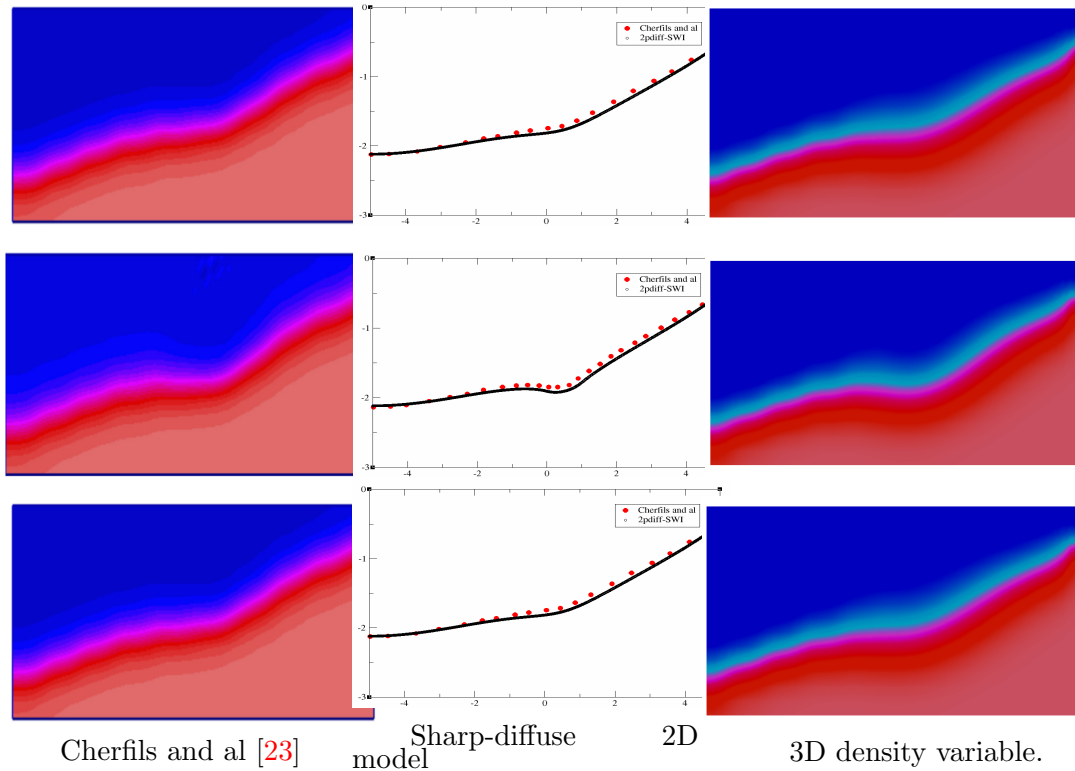


Figure 4.20: Numerical results during an injection experiment. $x_2 = 0.5$ (top), $x_2 = 1.5$ m (center) and $x_2 = 0.5$ (bottom)

Figure 4.20 illustrates the evolution of the transition zone during a 5 day injection scenario. A local depression in the injection zone is observed in both models. The density contrast is decreased. The salt front thereby tends downwards under the large freshwater flux injected. The effects of the injection are visible in the 2D model, especially in the third slice $y = 1.5$ m. The transition zone in the 3D model is wider due to dispersion and diffusion effects, which is not visible in the 2D model.

Case 4: Double pumping scenario

Here, we present two test cases for a large aquifer with two exploitation zones. We represent the aquifer by $\Omega_{3D} =]-10, 10[\times]0, 5[\times]-5, 0[$. Its horizontal surface is given by $\Omega_{2D} =]-10, 10[\times]0, 5[$. The depth of the aquifer for the 2D model is fixed at -5 . Dirichlet boundary conditions are imposed at the seaside ($x_1 = -10$) and the initial conditions are shown in Figure 4.21.

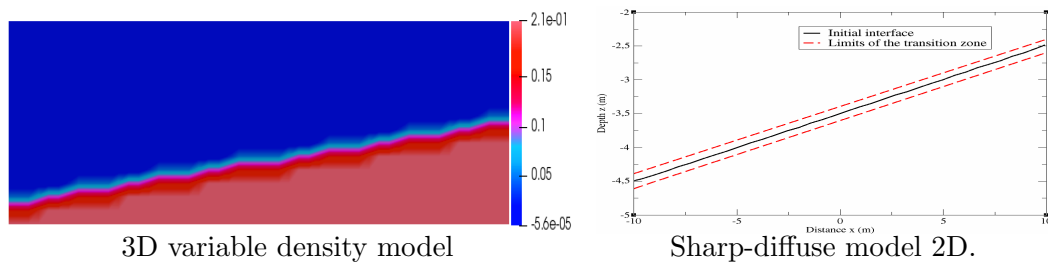


Figure 4.21: Initial conditions: initial salt concentration for 3D model (left) and initial position of the salt front for the 2D model (right).

We consider two zones of pumping wells with different rates. Let $Q_1 = 0.0$ and $Q_2 = -1.8 \cdot \chi_{[-5.5, -4.5] \times [2, 3] \times [-0.5, 0]} - 1.0 \chi_{[4.5, 5.5] \times [2, 3] \times [-0.5, 0]}$. The density contrast is fixed at $\gamma = 0.0025$. Figure 4.22 presents numerical results for a double pumping wells during 7.5 days.

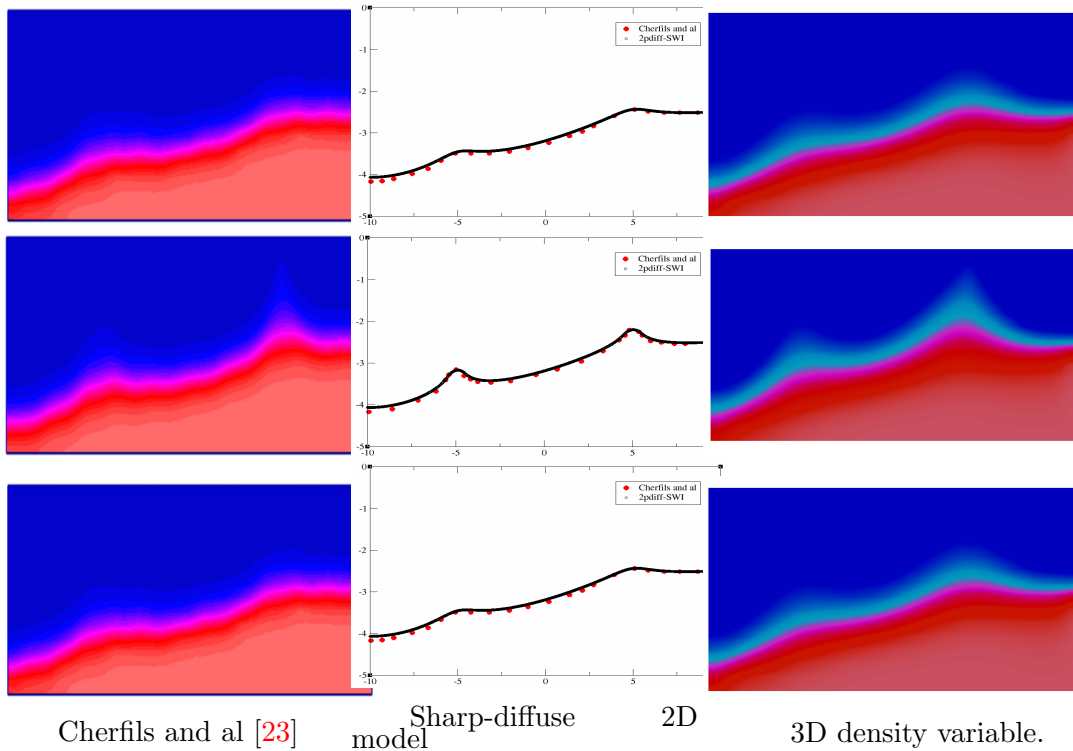


Figure 4.22: Numerical results for double pumping wells. Slice $x_2 = 0.5$ m (top), slice $x_2 = 1.5$ m (center) and slice $x_2 = 2.5$ m.

The pumping effect is visualized in both models. Two upconings are formed and tend to the surface under the high pumping rate. The 2D model is able to visualize the pumping effect as does the 3D model and the transition zone is large due to the force applied in this region.

Case 5: pumping and injection experiment

For the last test, we combine the effect of injection and pumping at the same time. We choose a production well at the left and an injection well at the right. The source term in this case is given by $Q_1 = 0.0$ and $Q_2 = -1 \cdot \chi_{[-5.5, -4.5] \times [2, 3] \times [-0.5, 0]} +$

$0.4\chi_{[4.5,5] \times [2.3] \times [-0.5,0]}$. Figure 4.23 represents the numerical results of the corresponding test.

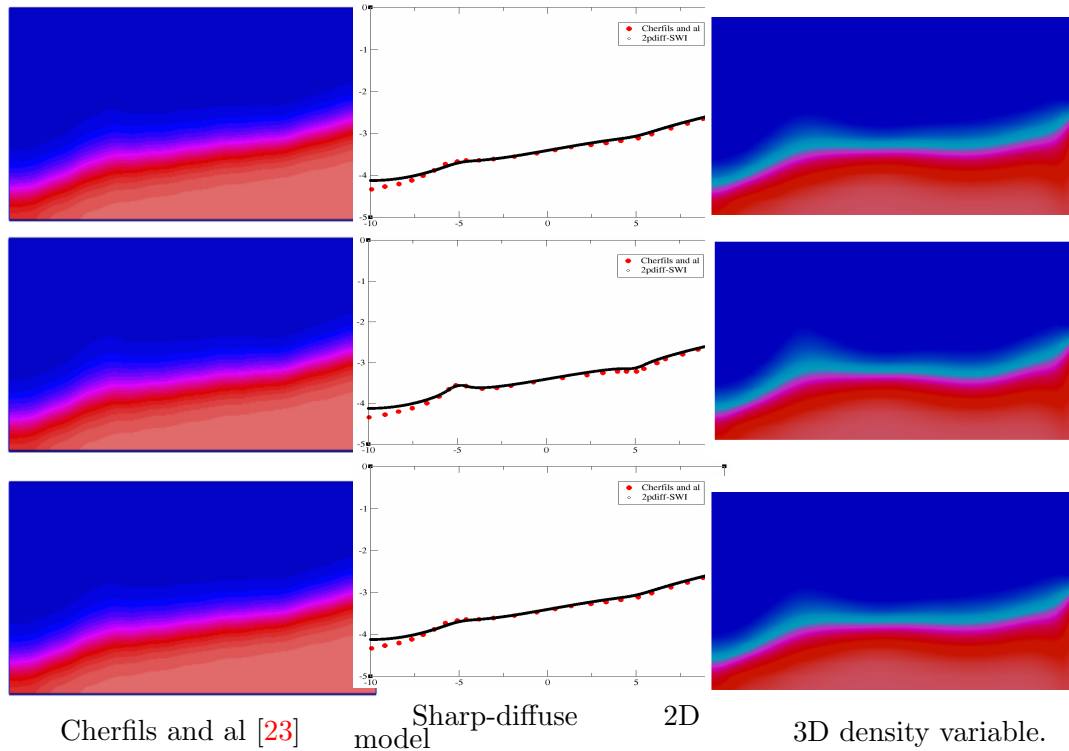


Figure 4.23: Numerical results: injection and pumping, $T = 10.5$ days $\gamma = 0.00025$.

The pumping effect does not appear too much and a stabilization of the interface in the whole domain is observed due to the injection process. Also in this case, we can see that the 2D model yields physically efficient and accurate results.

Remark 4.3.1. *We have compared our results with those presented in [23] for both 2D and 3D modes for a test case handling the contamination of a confined aquifer by saltwater in different situations. The obtained results proved a good agreement for both models, which ensures the validity of our methodology. This comparison is used to show the ability of the 2D model to predict seawater intrusion in different cases. The numerical results proved that the sharp-diffuse interfaces 2D model provides physically efficient results and take into account the width of the transition zone.*

4.4 Conclusion

This chapter deals with a finite volume numerical method for modeling seawater intrusion problem using the mixed sharp-diffuse interfaces approach in coastal aquifer. First, we outlined the main steps of the derivation of the mathematical model. The construction of the numerical scheme is established by integrating the governing equations on each control volume and evaluating the flows on each edge. We adopt a fully coupled, fully implicit TPFA finite volume method for the discretization of these equations in space while we use an implicit Euler scheme for the discretization in time. An upwind scheme is used to approximate the convective fluxes.

Afterwards, the numerical scheme is integrated and implemented in the framework [DuMu^X](#). The developed module has been validated by performing a numerical convergence of the scheme. The numerical simulations showed that the existence of a diffuse freshwater/saltwater and saturated/unsaturated zones favors the advance and diffusion of the salt front and water surface level. Moreover, we tested the ability of our developed module to take into account physical and hydrogeological phenomena such as tidal fluctuations. To do so, we consider a test case described in [\[7, 25\]](#) that aims to illustrate the impact of tidal fluctuations caused by waves motion on the displacement of interfaces. Our numerical results are compared to an analytical solution derived from Ferris model and showed good agreement with the results presented in [\[7, 25\]](#) in different cases. Besides, the validity of our module is examined by comparing our results obtained for the 2D model with the classical 3D model for miscible fluid flows. Our results for both models (2D and 3D) are then compared with those presented in [\[23\]](#) and presents good correspondence.

From these series of simulations, it can be seen that the 2D sharp-diffuse interfaces model can provide an efficient and accurate results and take into account various hydraulic and physical phenomena with a reasonable CPU time. The numerical analysis of an extension of this method to a more efficient and accurate scheme to deal with heterogeneity and anisotropy on an unstructured mesh will be discussed in the next chapter.

Chapter 5

Numerical analysis of a multi-point flux approximation finite volume scheme for a sharp-diffuse interfaces model

Contents

| | | |
|------------|---------------------------------------------------|------------|
| 5.1 | Introduction | 91 |
| 5.2 | Mathematical model | 92 |
| 5.3 | Finite volume discretization | 93 |
| 5.3.1 | Discretization and notations | 94 |
| 5.3.2 | Fully coupled fully implicit finite volume scheme | 95 |
| 5.4 | Discrete maximum principle | 98 |
| 5.5 | Energy estimates and compactness results | 101 |
| 5.5.1 | A priori estimates | 101 |
| 5.5.2 | Existence of the discrete solution | 107 |
| 5.5.3 | Space and time translates estimates | 109 |
| 5.6 | Convergence results | 112 |
| 5.7 | Numerical results | 116 |
| 5.7.1 | Studied domain and physical data | 117 |
| 5.7.2 | Test case 1: homogeneous aquifer | 118 |
| 5.7.3 | Test case 2: fractured aquifer | 120 |
| 5.8 | Conclusion | 121 |

5.1 Introduction

This chapter aims to present the convergence of the finite volume Multi-Point Flux Approximation (MPFA) scheme for a sharp-diffuse seawater intrusion problem. The derivation of the mathematical model is presented in Chapter 4. Here, we consider

a sharp-diffuse interfaces model in an anisotropic and heterogeneous free aquifer. Such a process is governed by a coupled system of two parabolic partial differential equations simulating respectively the freshwater head and the salt front elevation. To handle such a system numerically, we propose a fully implicit MPFA finite volume approach that solves the governing equations at each time step using Newton's method. In fact, this method tackles the non-linearity of the problem, the anisotropy and the heterogeneity of the aquifer on unstructured mesh, which improves the efficiency and accuracy of the numerical computations of such system. In section ??, we present the numerical discretization of the system of equations. For the approximation of the convective flux, we use an upwind scheme. To discretize in time, we employ an Euler implicit scheme.

The present chapter has several objectives. First, we will develop a fully coupled fully implicit approach which combines advantages of the MPFA method to accurately solve the diffusion terms with an upwind method for space discretization on unstructured grids. The second objective of this paper is to present a proof of the convergence of this scheme. The proof of convergence is established due to some compactness properties. Moreover, we have demonstrate the weak convergence of the discrete gradient of the freshwater head and the salt front elevation. Passing to the limit, we have proved that the approximate solution is a weak solution to the continuous problem. Lastly, we have developed and implemented this scheme in a new module in the context of the parallel open source platform DuMu^X [1], based on the Distributed and Unified Numerics Environment (DUNE) [2], allowing simulations for large-scale field applications involving seawater intrusion in coastal aquifers. The overall objective of this part is the development of a new-generation framework and reservoir simulator suitable for massively parallel processors. Some numerical examples are presented, one of which is related to flows in a fractured porous medium.

The outline of the paper is as follows. Section 5.2 is devoted to the statement of the problem. Namely, in this section, we introduce the system of equations for the sharp-diffuse interfaces model in a free coastal aquifer [24, 25]. Then we formulate the main assumptions on the data. In Section 5.3 we recall the general FV framework and formulate the fully coupled fully implicit MPFA FV scheme that will be studied. A discrete maximum principle, that will be used in the energy estimates for the scheme, is proven in Section 5.4. In Section 5.5.2, we first establish some energy estimates followed by the existence of discrete solution to the FV scheme. In Section 5.5.3, we establish some compactness results corresponding to space and time translate estimates. In Section 5.6, the convergence of the scheme is proved by compactness arguments. In Section 5.7, a description of the implementation of our strategy in DuMu^X is given. Then, to validate our approach, we consider two test cases. The first test case is a simulation in a homogeneous domain, while the second one is in a heterogenous free surface aquifer where two intersecting fractures are considered. Finally, concluding remarks are summarized in section 5.8.

5.2 Mathematical model

We consider an open bounded domain Ω of \mathbb{R}^2 , describing the projection of the aquifer on the horizontal surface, over a time period $]0, T[$. Let $\Omega_T =]0, T[\times \Omega$, $\partial\Omega_T =]0, T[\times \partial\Omega$ and \vec{n} the unit outward normal to $\partial\Omega$. We consider the sharp-diffuse interfaces model for seawater intrusion problem in coastal free aquifers describing two immiscible phase seawater/freshwater flow and tacking into account the width of transition zones. Then the mathematical model is given by a coupled nonlinear system of parabolic PDEs (see [25]) where the main unknowns are the freshwater head u [m] and the salt front elevation Z [m]:

$$(P) \quad \begin{cases} \phi \frac{\partial u}{\partial t} - \operatorname{div}(D\nabla\varphi(u)) - \operatorname{div}(D\nabla\varphi(Z)) - \operatorname{div}(\phi\delta D\nabla u) = 0 & \text{in } \Omega_T, \\ \phi \frac{\partial Z}{\partial t} - \operatorname{div}(Db_s(Z)\nabla u) - \operatorname{div}(D\nabla\varphi(Z)) - \operatorname{div}(\phi\delta D\nabla Z) = 0 & \text{in } \Omega_T, \\ D\nabla u \cdot \vec{n} = 0, \quad D\nabla Z \cdot \vec{n} = 0, \quad Db_s(Z)\nabla u \cdot \vec{n} = 0 & \text{on } \partial\Omega_T, \\ D\nabla\varphi(u) \cdot \vec{n} = 0, \quad D\nabla\varphi(Z) \cdot \vec{n} = 0 & \text{on } \partial\Omega_T, \\ u(0, \cdot) = u_0(\cdot), \quad Z(0, \cdot) = Z_0(\cdot) & \text{in } \Omega. \end{cases}$$

ϕ [%] is the porosity of the medium, D [$\text{m} \cdot \text{day}^{-1}$] the hydraulic conductivity of the freshwater, ρ_s, ρ_f [$\text{kg} \cdot \text{m}^{-3}$] the densities of the fresh and the saltwater, $\gamma = \frac{\rho_s - \rho_f}{\rho_f}$ [%] the density contrast, δ [m] the width of the transition zone, Z_B [m] the bottom of the aquifer, $b_s(u) = u - Z_B$ [m] the thickness of the aquifer, $b_s(Z) = Z - Z_B$ [m] the thickness of the freshwater, $\varphi(u) = \frac{1}{2}(u - Z_B)^2$, u_0 and Z_0 are given functions. We have to mention, that for simplicity, we have neglected the source terms and taken $\gamma = 1$.

The main assumption on the data are as follows:

(A.1) The tensor D is assumed to be bounded symmetric and uniformly elliptic in Ω . There exists constants $D^+ \geq D^- > 0$ such that

$$0 < D^- |\xi|^2 \leq D(x)\xi \cdot \xi \leq D^+ |\xi|^2 < \infty \quad \text{for any } \xi \in \mathbb{R}^2 \text{ and } \xi \neq 0, \text{ a.e. in } \Omega.$$

(A.2) The porosity belongs to $L^\infty(\Omega)$, and there exists two positives values ϕ^- and ϕ^+ such that $0 < \phi^- \leq \phi(x) \leq \phi^+ < \infty$ a.e. in Ω .

(A.3) u_0 and Z_0 are in $L^2(\Omega)$ and the initial thicknesses satisfy: $0 < u_0 - Z_0 \leq M$, $0 < Z_0 - Z_B \leq M$, a.e. in Ω where M is a positive constant.

Remark 5.2.1. *The assumptions (A.1)–(A.3) are classical and physically meaningful for seawater intrusion into coastal free aquifers. They are similar to the assumptions made in [24, 27] that dealt with the existence of a weak solution. Let us mention that with the assumption (A.3) and by introducing "sufficiently pumping" source terms, a maximum principle is shown in [27] that is the thicknesses $u - Z$ and $Z - Z_B$ are bounded and positive.*

5.3 Finite volume discretization

We now introduce our notation and the general form of the FV approximations that will be considered in the rest of the paper. We formulate a fully coupled

fully implicit cell-centered FV scheme for the spatial discretization and a first-order (backward Euler) scheme for the integration in time. We present an MPFA [3, ?] method which has high potential to improve efficiency and accuracy of numerical simulations for seawater intrusion in anisotropic and heterogeneous porous media. Furthermore, the orthogonality condition of the mesh is no more required which is necessary for the TPFM, see for instance [41].

5.3.1 Discretization and notations

For sake of simplicity, we consider an uniform partition $\{t_0, \dots, t_N\}$ of $[0, T]$ with $\delta t = t_{n+1} - t_n$ the time step size and $t^n = n\delta t$ for all $n \in \{0, \dots, N\}$. Furthermore, let $(\mathcal{T}_h)_{h>0}$ be an admissible triangulation in the sense of [42], such that $\bar{\Omega} = \cup_{K \in \mathcal{T}_h} \bar{K}$. $\partial K = \bar{K} \setminus K$ the boundary of K . Let us note by $\mathcal{E} = \mathcal{E}_{\text{int}} \cup \mathcal{E}_{\text{ext}}$ the interior and exterior edges of the \mathcal{T}_h . We denote $\sigma = K \setminus L$ the interface between the adjacent triangles K and L . Let $|K|$ be the 2-dimensional Lebesgue measure of K and $|\sigma|$ the 1-dimensional Lebesgue measure of σ . $\mathcal{P} = \left((x_K)_{K \in \mathcal{T}_h}, (x_\sigma)_{\sigma \in \mathcal{E}} \right)$ is a set of points in Ω with x_K represents the barycentric point of the control volume K while x_σ is the point of continuity on the edge σ . \mathcal{V} is the set of vertices of the mesh \mathcal{T}_h and we note by \mathcal{V}_K the set of vertices of the triangle K . The size of the mesh \mathcal{T}_h can be given by $h = \max_{K \in \mathcal{T}_h} \text{diam}(K)$. We construct for each $K \in \mathcal{T}_h$ three sub-volume controls K_r as presented in Figure 5.1. We note P_i, P_j and P_k the vertices of the triangle K . The points P_{ij}, P_{ki} and P_{jk} are the midpoints of the edges $(P_i P_j), (P_i P_k)$ and $(P_j P_k)$ respectively. We denote $\sigma_{K_i}^1$ (resp. $\sigma_{K_i}^2$) the segment made by the points P_i and P_{ij} [resp. P_{ki}] with a measure noted $|\sigma_{K_i}^1|$ [resp. $|\sigma_{K_i}^2|$]. Let $\vec{n}_{\sigma_{K_i}^1}$ [resp. $\vec{n}_{\sigma_{K_i}^2}$] the outward unit normal vector to $\sigma_{K_i}^1$ [resp. $\sigma_{K_i}^2$]. For any vertex $r \in \{i, j, k\}$, the sub-volume control K_r is the quadrilateral made by $x_K, P_{.,r}, P_r$ and $P_{.,r}$, as shown in Figure 5.1 .

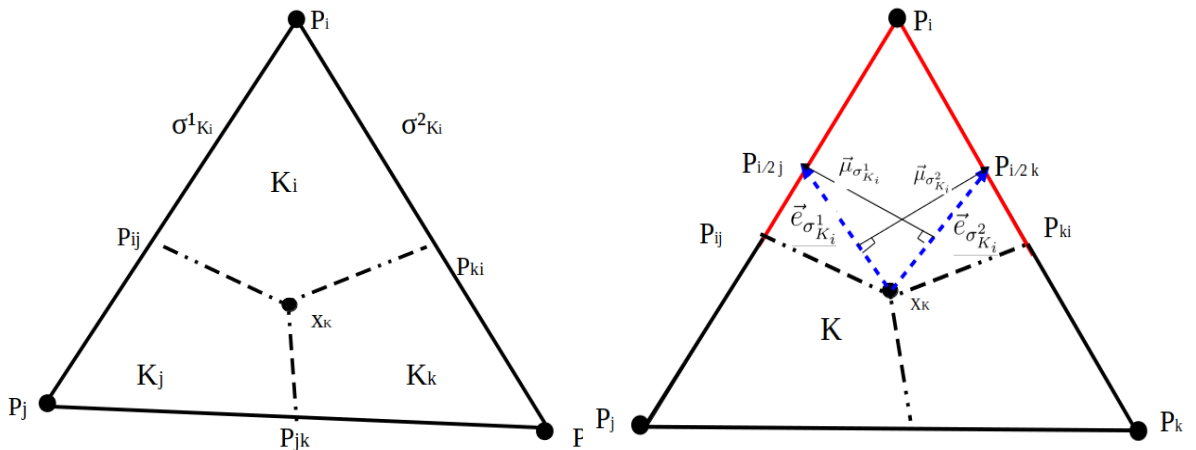


Figure 5.1: The control volume K and associated notations.

Let us state the following notations:

- $D_K = \frac{1}{|K|} \int_K D(x) dx, \phi_K = \frac{1}{|K|} \int_K \phi(x) dx.$

- $u_K(t) \simeq \frac{1}{|K|} \int_K u(x, t) dx$, $u_K^n = u_K(t_n)$ and $u_K^0 = \frac{1}{|K|} \int_K u_0(x) dx$, $t \in]t_n, t_{n+1}]$.
- $Z_K(t) \simeq \frac{1}{|K|} \int_K Z(x, t) dx$, $Z_K^n = Z_K(t_n)$ and $Z_K^0 = \frac{1}{|K|} \int_K Z_0(x) dx$, for $t \in]t_n, t_{n+1}]$.
- The discrete space-time solution corresponds to an approximate solution of the continuous problem (P) given by

$$\begin{aligned} u_h^{\delta t}(t, x) &= u_K^{n+1} \text{ for } x \in K \text{ and } t \in]t_n, t_{n+1}], \\ Z_h^{\delta t}(t, x) &= Z_K^{n+1} \text{ for } x \in K \text{ and } t \in]t_n, t_{n+1}]. \end{aligned}$$

Following [20], the point $P_{i/2,j}$ is set on the segment $(P_i P_j)$ such $\frac{|P_i P_{i/2,j}|}{|P_i P_j|} = \frac{1}{3}$. We note by $\vec{e}_{\sigma_{K_i}^1} = \overrightarrow{x_K P_{i/2,j}}$ and $\vec{e}_{\sigma_{K_i}^2} = \overrightarrow{x_K P_{i/2,k}}$. The vectors $\vec{\mu}_{\sigma_{K_r}^1}$ and $\vec{\mu}_{\sigma_{K_r}^2}$ satisfied the following property

$$\begin{cases} \vec{\mu}_{\sigma_{K_r}^{Id}} \cdot \vec{e}_{\sigma_{K_i}^{Id}} = 1, \\ \vec{\mu}_{\sigma_{K_r}^{3-Id}} \cdot \vec{e}_{\sigma_{K_i}^{Id}} = 0, \end{cases} \quad \text{for all } Id = 1, 2. \quad (5.3.1)$$

Definition 5.3.1 (Discrete gradient). We denote $u_{\sigma_{K_r}^{Id}}^n$ the discrete values on the continuity points $(x_\sigma)_{\sigma \in \mathcal{E}}$. Using (5.3.1), the discrete gradients of $u_h^{\delta t}$ and $Z_h^{\delta t}$ on the quadrilateral K_r are written as in [20] by

$$\nabla_{K_r} u_h^{\delta t} = \left(u_{\sigma_{K_r}^1}^{n+1} - u_K^{n+1} \right) \vec{\mu}_{\sigma_{K_r}^1} + \left(u_{\sigma_{K_r}^2}^{n+1} - u_K^{n+1} \right) \vec{\mu}_{\sigma_{K_r}^2}, \quad (5.3.2)$$

$$\nabla_{K_r} Z_h^{\delta t} = \left(Z_{\sigma_{K_r}^1}^{n+1} - Z_K^{n+1} \right) \vec{\mu}_{\sigma_{K_r}^1} + \left(Z_{\sigma_{K_r}^2}^{n+1} - Z_K^{n+1} \right) \vec{\mu}_{\sigma_{K_r}^2}. \quad (5.3.3)$$

5.3.2 Fully coupled fully implicit finite volume scheme

In this subsection, we provide a description of the fully coupled fully implicit FV scheme for the system (P) modeling sharp-diffuse interfaces for seawater intrusion in heterogeneous porous media. It is based on the MPFA method for fluxes and diffusive terms and upstream for advective terms with implicit Euler's time discretization. The main idea of the MPFA scheme [3, ?] is to obtain a consistent approximation of the flux on each edge of the control volume. Moreover, This scheme gives a linear formulation of the flux across the edges.

The main unknowns are the freshwater head $(u_K^{n+1})_{K \in \mathcal{T}_h}$ and the salt elevation $(Z_K^{n+1})_{K \in \mathcal{T}_h}$ for any $n \in \{0, \dots, N-1\}$. By integrating the coupled system (P) in $[t_n, t_{n+1}] \times K$, we obtain the following scheme:

$$\phi_K (u_K^{n+1} - u_K^n) - \frac{1}{|K|} \int_{t_n}^{t_{n+1}} \sum_{\sigma \in \partial K} \int_{\sigma} [D\nabla\varphi(u) + D\nabla\varphi(Z) + \delta\phi D\nabla u] \cdot \vec{n}_{K,\sigma} d\sigma dt = 0, \quad (5.3.4)$$

$$\phi_K (Z_K^{n+1} - Z_K^n) - \frac{1}{|K|} \int_{t_n}^{t_{n+1}} \sum_{\sigma \in \partial K} \int_{\sigma} [Db_s(Z)\nabla u + D\nabla\varphi(Z) + \delta\phi D\nabla Z] \cdot \vec{n}_{K,\sigma} d\sigma dt = 0, \quad (5.3.5)$$

with $\vec{n}_{K,\sigma}$ is the external normal to σ . Using a fully implicit approach and $\sum_{\sigma \in \partial K} \int_{\sigma} = \sum_{r=i,j,k} \sum_{Id=1,2} \int_{\sigma_{K_r}^{Id}}$, yields to the following equations

$$\phi_K (u_K^{n+1} - u_K^n) + \frac{\delta t}{|K|} \sum_{r=i,j,k} \sum_{Id=1,2} F_{\sigma_{K_r}^{Id}}(u_h^{\delta t}) + F_{\sigma_{K_r}^{Id}}(Z_h^{\delta t}) + G_{\sigma_{K_r}^{Id}}(u_h^{\delta t}) = 0, \quad (5.3.6)$$

$$\phi_K (Z_K^{n+1} - Z_K^n) + \frac{\delta t}{|K|} \sum_{r=i,j,k} \sum_{Id=1,2} H_{\sigma_{K_r}^{Id}}(Z_h^{\delta t}, u_h^{\delta t}) + F_{\sigma_{K_r}^{Id}}(Z_h^{\delta t}) + G_{\sigma_{K_r}^{Id}}(Z_h^{\delta t}) = 0, \quad (5.3.7)$$

where $\vec{n}_{\sigma_{K_r}^{Id}}$ is the external normal to $\sigma_{K_r}^{Id}$ and the exact diffusive sub-fluxes on each half edge $\sigma_{K_r}^{Id}$ ($r = i, j, k, Id = 1, 2$) are given by the following expressions:

$$F_{\sigma_{K_r}^{Id}}(u_h^{\delta t}) = - \int_{\sigma_{K_r}^{Id}} D_{K|\sigma_{K_r}^{Id}} \nabla \varphi(u_h^{\delta t}) \cdot \vec{n}_{\sigma_{K_r}^{Id}} d\sigma, \quad (5.3.8)$$

$$F_{\sigma_{K_r}^{Id}}(Z_h^{\delta t}) = - \int_{\sigma_{K_r}^{Id}} D_{K|\sigma_{K_r}^{Id}} \nabla \varphi(Z_h^{\delta t}) \cdot \vec{n}_{\sigma_{K_r}^{Id}} d\sigma, \quad (5.3.9)$$

and

$$G_{\sigma_{K_r}^{Id}}(u_h^{\delta t}) = - \int_{\sigma_{K_r}^{Id}} \delta \phi_{K|\sigma_{K_r}^{Id}} D_{K|\sigma_{K_r}^{Id}} \nabla u_h^{\delta t} \cdot \vec{n}_{\sigma_{K_r}^{Id}} d\sigma, \quad (5.3.10)$$

$$G_{\sigma_{K_r}^{Id}}(Z_h^{\delta t}) = - \int_{\sigma_{K_r}^{Id}} \delta \phi_{K|\sigma_{K_r}^{Id}} D_{K|\sigma_{K_r}^{Id}} \nabla Z_h^{\delta t} \cdot \vec{n}_{\sigma_{K_r}^{Id}} d\sigma. \quad (5.3.11)$$

In addition, the exact convective sub-flux is as follows

$$H_{\sigma_{K_r}^{Id}}(Z_h^{\delta t}, u_h^{\delta t}) = - \int_{\sigma_{K_r}^{Id}} b_s(Z_h^{\delta t})_{K|\sigma_{K_r}^{Id}} D_{K|\sigma_{K_r}^{Id}} \nabla u_h^{\delta t} \cdot \vec{n}_{\sigma_{K_r}^{Id}} d\sigma. \quad (5.3.12)$$

Now, the construction of the MPFA scheme requires a consistent approximation of the sub-fluxes on each half edge of the control volume K . However, each vertex $r = \{i, j, k\}$ is associated with two half edges $\sigma_{K_r}^1$ and $\sigma_{K_r}^2$. The exact sub-fluxes (5.3.8)–(5.3.12) are then approximated by the numerical sub-fluxes on each half edge of the control volume. By using the discrete gradient operator (5.3.2)–(5.3.3) on K_r in the diffusive term, the numerical sub-fluxes on each inner half edge are given, for all $K \in \mathcal{T}_h$ and around each vertex $r = \{i, j, k\}$, by

$$F_{\sigma_{K_r}^{Id}}^*(u_h^{\delta t}) = -|\sigma_{K_r}^{Id}| D_K \left[\left(\varphi(u_{\sigma_{K_r}^1}^{n+1}) - \varphi(u_K^{n+1}) \right) \vec{\mu}_{\sigma_{K_r}^1} + \left(\varphi(u_{\sigma_{K_r}^2}^{n+1}) - \varphi(u_K^{n+1}) \right) \vec{\mu}_{\sigma_{K_r}^2} \right] \cdot \vec{n}_{\sigma_{K_r}^{Id}}, \quad (5.3.13)$$

$$F_{\sigma_{K_r}^{Id}}^*(Z_h^{\delta t}) = -|\sigma_{K_r}^{Id}| D_K \left[\left(\varphi(Z_{\sigma_{K_r}^1}^{n+1}) - \varphi(Z_K^{n+1}) \right) \vec{\mu}_{\sigma_{K_r}^1} + \left(\varphi(Z_{\sigma_{K_r}^2}^{n+1}) - \varphi(Z_K^{n+1}) \right) \vec{\mu}_{\sigma_{K_r}^2} \right] \cdot \vec{n}_{\sigma_{K_r}^{Id}}, \quad (5.3.14)$$

and

$$G_{\sigma_{K_r}^{Id}}^*(u_h^{\delta t}) = -|\sigma_{K_r}^{Id}|\delta\phi_K D_K \left[\left(u_{\sigma_{K_r}^1}^{n+1} - u_K^{n+1} \right) \vec{\mu}_{\sigma_{K_r}^1} + \left(u_{\sigma_{K_r}^2}^{n+1} - u_K^{n+1} \right) \vec{\mu}_{\sigma_{K_r}^2} \right] \cdot \vec{n}_{\sigma_{K_r}^{Id}}, \quad (5.3.15)$$

$$G_{\sigma_{K_r}^{Id}}^*(Z_h^{\delta t}) = -|\sigma_{K_r}^{Id}|\delta\phi_K D_K \left[\left(Z_{\sigma_{K_r}^1}^{n+1} - Z_K^{n+1} \right) \vec{\mu}_{\sigma_{K_r}^1} + \left(Z_{\sigma_{K_r}^2}^{n+1} - Z_K^{n+1} \right) \vec{\mu}_{\sigma_{K_r}^2} \right] \cdot \vec{n}_{\sigma_{K_r}^{Id}}. \quad (5.3.16)$$

For the convective flux, we evaluate the function $b_s(Z)$ in the equation (5.3.12) by an upwind scheme. Using the discrete gradient definition in the equation (5.3.2), the numerical convective sub-flux on each half-edge is expressed as follows

$$H_{\sigma_{K_r}^{Id}}^*(Z_h^{\delta t}, u_h^{\delta t}) = -|\sigma_{K_r}^{Id}| D_K b_s(Z_h^{\delta t})_{\sigma_{K_r}^{Id}}^{up} \nabla_{K_r} u_h^{\delta t} \cdot \vec{n}_{\sigma_{K_r}^{Id}}. \quad (5.3.17)$$

with

$$b_s \left(Z_h^{\delta t} \right)_{\sigma_{K_r}^{Id}}^{up} = \begin{cases} b_s \left(Z_K^{n+1} \right) & \text{if } -|\sigma_{K_r}^{Id}| D_K \nabla_{K_r} u_h^{\delta t} \cdot \vec{n}_{\sigma_{K_r}^{Id}} \geq 0, \\ b_s \left(Z_L^{n+1} \right) & \text{if } -|\sigma_{K_r}^{Id}| D_K \nabla_{K_r} u_h^{\delta t} \cdot \vec{n}_{\sigma_{K_r}^{Id}} < 0. \end{cases} \quad (5.3.18)$$

L is the neighboring element of K which has in common the edge $\sigma_{K_r}^{Id}$.

Finally, the scheme of the problem (P) is expressed by the following nonlinear coupled (5.3.19)-(5.3.25) system:

$\forall K \in \mathcal{T}_h$ and $\forall n = 0, \dots, N-1$,

$$\begin{aligned} & \phi_K |K| (u_K^{n+1} - u_K^n) \\ & - \delta t \sum_{r=i,j,k} \sum_{Id=1,2} |\sigma_{K_r}^{Id}| D_K \left[\left(\varphi(u_{\sigma_{K_r}^1}^{n+1}) - \varphi(u_K^{n+1}) \right) \vec{\mu}_{\sigma_{K_r}^1} + \left(\varphi(u_{\sigma_{K_r}^2}^{n+1}) - \varphi(u_K^{n+1}) \right) \vec{\mu}_{\sigma_{K_r}^2} \right] \cdot \vec{n}_{\sigma_{K_r}^{Id}} \\ & - \delta t \sum_{r=i,j,k} \sum_{Id=1,2} |\sigma_{K_r}^{Id}| D_K \left[\left(\varphi(Z_{\sigma_{K_r}^1}^{n+1}) - \varphi(Z_K^{n+1}) \right) \vec{\mu}_{\sigma_{K_r}^1} + \left(\varphi(Z_{\sigma_{K_r}^2}^{n+1}) - \varphi(Z_K^{n+1}) \right) \vec{\mu}_{\sigma_{K_r}^2} \right] \cdot \vec{n}_{\sigma_{K_r}^{Id}} \\ & - \delta t \sum_{r=i,j,k} \sum_{Id=1,2} \delta\phi_K |\sigma_{K_r}^{Id}| D_K \left[\left(u_{\sigma_{K_r}^1}^{n+1} - u_K^{n+1} \right) \vec{\mu}_{\sigma_{K_r}^1} + \left(u_{\sigma_{K_r}^2}^{n+1} - u_K^{n+1} \right) \vec{\mu}_{\sigma_{K_r}^2} \right] \cdot \vec{n}_{\sigma_{K_r}^{Id}} = 0, \end{aligned} \quad (5.3.19)$$

$$\begin{aligned} & \phi_K |K| (Z_K^{n+1} - Z_K^n) \\ & - \delta t \sum_{r=i,j,k} \sum_{Id=1,2} |\sigma_{K_r}^{Id}| D_K \left[\left(\varphi(Z_{\sigma_{K_r}^1}^{n+1}) - \varphi(Z_K^{n+1}) \right) \vec{\mu}_{\sigma_{K_r}^1} + \left(\varphi(Z_{\sigma_{K_r}^2}^{n+1}) - \varphi(Z_K^{n+1}) \right) \vec{\mu}_{\sigma_{K_r}^2} \right] \cdot \vec{n}_{\sigma_{K_r}^{Id}} \\ & - \delta t \sum_{r=i,j,k} \sum_{Id=1,2} |\sigma_{K_r}^{Id}| D_K b_s(Z_h^{\delta t})_{\sigma_{K_r}^{Id}}^{up} \left[\left(u_{\sigma_{K_r}^1}^{n+1} - u_K^{n+1} \right) \vec{\mu}_{\sigma_{K_r}^1} + \left(u_{\sigma_{K_r}^2}^{n+1} - u_K^{n+1} \right) \vec{\mu}_{\sigma_{K_r}^2} \right] \cdot \vec{n}_{\sigma_{K_r}^{Id}} \\ & - \delta t \sum_{r=i,j,k} \sum_{Id=1,2} \delta\phi_K |\sigma_{K_r}^{Id}| D_K \left[\left(Z_{\sigma_{K_r}^1}^{n+1} - Z_K^{n+1} \right) \vec{\mu}_{\sigma_{K_r}^1} + \left(Z_{\sigma_{K_r}^2}^{n+1} - Z_K^{n+1} \right) \vec{\mu}_{\sigma_{K_r}^2} \right] \cdot \vec{n}_{\sigma_{K_r}^{Id}} = 0. \end{aligned} \quad (5.3.20)$$

The flux continuity on each half edge reads

$$D_K \left[\left(\varphi(u_{\sigma_{K_r}^1}^{n+1}) - \varphi(u_K^{n+1}) \right) \vec{\mu}_{\sigma_{K_r}^1} + \left(\varphi(u_{\sigma_{K_r}^2}^{n+1}) - \varphi(u_K^{n+1}) \right) \vec{\mu}_{\sigma_{K_r}^2} \right] \cdot \vec{n}_{\sigma}$$

$$+ D_L \left[\left(\varphi(u_{\sigma_{L_r}^{n+1}}) - \varphi(u_L^{n+1}) \right) \vec{\mu}_{\sigma_{L_r}^1} + \left(\varphi(u_{\sigma_{L_r}^{n+1}}) - \varphi(u_L^{n+1}) \right) \vec{\mu}_{\sigma_{L_r}^2} \right] \cdot \vec{n}_\sigma = 0, \quad (5.3.21)$$

$$D_K \left[\left(\varphi(Z_{\sigma_{K_r}^{n+1}}) - \varphi(Z_K^{n+1}) \right) \vec{\mu}_{\sigma_{K_r}^1} + \left(\varphi(Z_{\sigma_{K_r}^{n+1}}) - \varphi(Z_K^{n+1}) \right) \vec{\mu}_{\sigma_{K_r}^2} \right] \cdot \vec{n}_\sigma \\ + D_L \left[\left(\varphi(Z_{\sigma_{L_r}^{n+1}}) - \varphi(Z_L^{n+1}) \right) \vec{\mu}_{\sigma_{L_r}^1} + \left(\varphi(Z_{\sigma_{L_r}^{n+1}}) - \varphi(Z_L^{n+1}) \right) \vec{\mu}_{\sigma_{L_r}^2} \right] \cdot \vec{n}_\sigma = 0, \quad (5.3.22)$$

$$D_K \left[\left(u_{\sigma_{K_r}^{n+1}} - u_K^{n+1} \right) \vec{\mu}_{\sigma_{K_r}^1} + \left(u_{\sigma_{K_r}^{n+1}} - u_K^{n+1} \right) \vec{\mu}_{\sigma_{K_r}^2} \right] \cdot \vec{n}_\sigma \\ + D_L \left[\left(u_{\sigma_{L_r}^{n+1}} - u_L^{n+1} \right) \vec{\mu}_{\sigma_{L_r}^1} + \left(u_{\sigma_{L_r}^{n+1}} - u_L^{n+1} \right) \vec{\mu}_{\sigma_{L_r}^2} \right] \cdot \vec{n}_\sigma = 0, \quad (5.3.23)$$

$$D_K \left[\left(Z_{\sigma_{K_r}^{n+1}} - Z_K^{n+1} \right) \vec{\mu}_{\sigma_{K_r}^1} + \left(Z_{\sigma_{K_r}^{n+1}} - Z_K^{n+1} \right) \vec{\mu}_{\sigma_{K_r}^2} \right] \cdot \vec{n}_\sigma \\ + D_L \left[\left(Z_{\sigma_{L_r}^{n+1}} - Z_L^{n+1} \right) \vec{\mu}_{\sigma_{L_r}^1} + \left(Z_{\sigma_{L_r}^{n+1}} - Z_L^{n+1} \right) \vec{\mu}_{\sigma_{L_r}^2} \right] \cdot \vec{n}_\sigma = 0, \quad (5.3.24)$$

$$D_K b_s(Z_h^{\delta t})_\sigma^{up} \left[\left(u_{\sigma_{K_r}^{n+1}} - u_K^{n+1} \right) \vec{\mu}_{\sigma_{K_r}^1} + \left(u_{\sigma_{K_r}^{n+1}} - u_K^{n+1} \right) \vec{\mu}_{\sigma_{K_r}^2} \right] \cdot \vec{n}_\sigma \\ + D_L b_s(Z_h^{\delta t})_\sigma^{up} \left[\left(u_{\sigma_{L_r}^{n+1}} - u_L^{n+1} \right) \vec{\mu}_{\sigma_{L_r}^1} + \left(u_{\sigma_{L_r}^{n+1}} - u_L^{n+1} \right) \vec{\mu}_{\sigma_{L_r}^2} \right] \cdot \vec{n}_\sigma = 0. \quad (5.3.25)$$

The discrete initial conditions are given by

$$u_K^0 = \frac{1}{|K|} \int_K u_0(x) \, dx, \quad Z_K^0 = \frac{1}{|K|} \int_K Z_0(x) \, dx, \quad \forall K \in \mathcal{T}_h. \quad (5.3.26)$$

5.4 Discrete maximum principle

In this section, we prove a discrete maximum principle for the approximate solutions freshwater head and the salt front elevation respectively. To do so, we suppose the existence of at least a solution to the numerical scheme. The existence result is proved in the next section. The nonnegativity of the thickness of the freshwater and saltwater issued from the numerical scheme is presented in the following proposition.

Proposition 5.4.1. *Let assumptions (A.1)–(A.3) be fulfilled. Then the following inequalities hold:*

$$Z_K^{n+1} - Z_B \geq 0 \text{ and } u_K^{n+1} - Z_K^{n+1} \geq 0, \text{ for any } K \in \mathcal{T}_h \text{ and } n \in \{0, \dots, N-1\}.$$

The approximate freshwater and saltwater thicknesses are non-negative.

Proof. We demonstrate this result by induction. This statement is hold up for $n=0$. We assume that this property is valid for any $k \leq n$, and we will demonstrate the validity of this property for $k = n + 1$. We select a control volume K such that $Z_K^{n+1} = \min_{L \in \mathcal{T}_h} \{Z_L^{n+1}\}$ and $w_K^{n+1} = \min_{L \in \mathcal{T}_h} \{w_L^{n+1}\}$. Let us start by proving $Z_K^{n+1} - Z_B \geq 0$, i.e. we want to show the non-negativity of the saltwater thickness.

To do so, we note by $\omega_K^{n+1} = Z_K^{n+1} - Z_B$ and we assume that $\omega_K^{n+1} < 0$. We multiply the saltwater equation (5.3.20) by $(\omega_K^{n+1})^- = \min\{\omega_K^{n+1}, 0\} \leq 0$. We obtain

$$\phi_K \frac{|K|}{\delta t} (Z_K^{n+1} - Z_K^n) (\omega_K^{n+1})^- + A_1 + A_2 + A_3 = 0,$$

with

$$\begin{aligned} A_1 &= \sum_{r=i,j,k} \sum_{Id=1,2} (\omega_K^{n+1})^- b_s(Z_h^{\delta t})_{\sigma_{K_r}^{Id}}^{up} \mathcal{V}_{\sigma_{K_r}^{Id}}^{n+1}, \text{ with } \mathcal{V}_{\sigma_{K_r}^{Id}}^{n+1} = -|\sigma_{K_r}^{Id}| D_K \nabla_{K_r} u_h^{\delta t} \cdot \vec{n}_{\sigma_{K_r}^{Id}}, \\ A_2 &= -D_K \sum_{r=i,j,k} \sum_{Id=1,2} |\sigma_{K_r}^{Id}| (\omega_K^{n+1})^- \nabla_{K_r} \phi(Z_K^{n+1}) \cdot \vec{n}_{\sigma_{K_r}^{Id}}, \\ A_3 &= -\delta \phi_K D_K \sum_{r=i,j,k} \sum_{Id=1,2} |\sigma_{K_r}^{Id}| (\omega_K^{n+1})^- \nabla_{K_r} Z_K^{n+1} \cdot \vec{n}_{\sigma_{K_r}^{Id}}. \end{aligned}$$

We start by proving that the convective term A_1 is positive. Using the upstream values of $b_s(Z_h^{\delta t})^{up}$, we get

- if $\mathcal{V}_{\sigma_{K_r}^{Id}}^{n+1} \geq 0$, then $b_s(Z_h^{\delta t})_{\sigma_{K_r}^{Id}}^{up} = b_s(Z_K^{n+1})$. Therefore,

$$b_s(Z_h^{\delta t})_{\sigma_{K_r}^{Id}}^{up} \mathcal{V}_{\sigma_{K_r}^{Id}}^{n+1} (w_K^{n+1})^- = b_s(Z_K^{n+1}) \mathcal{V}_{\sigma_{K_r}^{Id}}^{n+1} (w_K^{n+1})^- = 0,$$

where we used the fact that the function $b_s(Z_K^{n+1})$ is extended by 0 whenever $Z_K^{n+1} < Z_B$ (i.e. $w_K^{n+1} < 0$).

- If $\mathcal{V}_{\sigma_{K_r}^{Id}}^{n+1} < 0$, one has $b_s(Z_h^{\delta t})_{\sigma_{K_r}^{Id}}^{up} = b_s(Z_L^{n+1})$. So,

$$b_s(Z_L^{n+1}) \mathcal{V}_{\sigma_{K_r}^{Id}}^{n+1} (w_K^{n+1})^- \geq b_s(Z_K^{n+1}) \mathcal{V}_{\sigma_{K_r}^{Id}}^{n+1} (w_K^{n+1})^- = 0.$$

Combining the two cases, we get

$$b_s(Z_h^{\delta t})_{\sigma_{K_r}^{Id}}^{up} \mathcal{V}_{\sigma_{K_r}^{Id}}^{n+1} (w_K^{n+1})^- \geq b_s(Z_K^{n+1}) \mathcal{V}_{\sigma_{K_r}^{Id}}^{n+1} (w_K^{n+1})^- = 0.$$

Following the same steps we get that A_2 is also positive. As a result

$$\phi_K |K| (Z_K^{n+1} - Z_K^n) (\omega_K^{n+1})^- \leq 0.$$

Since $(\omega_K^{n+1})^-$ is negative and using the induction assumption of Z_K^n , we get

$$Z_K^{n+1} - Z_B \geq Z_K^n - Z_B \geq 0.$$

That yields a contradiction with $w_K^{n+1} = Z_K^{n+1} - Z_B < 0$. Hence,

$$Z_K^{n+1} \geq Z_B \text{ for any } n = 0, \dots, N-1 \text{ and } K \in \mathcal{T}.$$

Now let us prove that $u_K^{n+1} - Z_K^{n+1} \geq 0$, i.e. the freshwater thickness is non-negative. We note by $(u_K^{n+1} - Z_K^{n+1})^- = \min\{u_K^{n+1} - Z_K^{n+1}, 0\}$. We multiply the freshwater equation (5.3.19) and the saltwater equation (5.3.20) by $(u_K^{n+1} - Z_K^{n+1})^- < 0$. Subtracting the freshwater equation from the saltwater equation, we get

$$\phi \frac{|K|}{\delta t} \left(u_K^{n+1} - Z_K^{n+1} - (u_K^n - Z_K^n) \right) (u_K^{n+1} - Z_K^{n+1})^- + B_1 + B_2 = 0,$$

with

$$B_1 = -\delta\phi_K D_K \sum_{r=i,j,k} \sum_{Id=1,2} |\sigma_{K_r}^{Id}| (u_K^{n+1} - Z_K^{n+1})^- \nabla_{K_r} (u_K^{n+1} - Z_K^{n+1}) \cdot \vec{n}_{\sigma_{K_r}^{Id}},$$

$$B_2 = \sum_{r=i,j,k} \sum_{Id=1,2} (u_K^{n+1} - Z_K^{n+1})^- \left[-D_K \nabla_{K_r} \varphi(u_h^{\delta t}) \cdot \vec{n}_{\sigma_{K_r}^{Id}} - b_s(Z_h^{\delta t})_{\sigma_{K_r}^{Id}}^{up} \mathcal{V}_{\sigma_{K_r}^{Id}}^{n+1} \right].$$

To prove that these terms are positives, we follow the same idea as done in the previous step. To compute B_1 , we multiply equations (5.3.23) and (5.3.24) by $-\left(u_{\sigma_{K_r}^{Id}}^{n+1} - Z_{\sigma_{K_r}^{Id}}^{n+1}\right)^-$. Substrating the first one from the second and adding the result to B_1 , we get

$$B_1 = \delta\phi_K D_K \sum_{r=i,j,k} \sum_{Id=1,2} -|\sigma_{K_r}^{Id}| (u_K^{n+1} - Z_K^{n+1})^- \nabla_{K_r} (u_K^{n+1} - Z_K^{n+1}) \cdot \vec{n}_{\sigma_{K_r}^{Id}}$$

$$- \left(u_{\sigma_{K_r}^{Id}}^{n+1} - Z_{\sigma_{K_r}^{Id}}^{n+1} \right)^- \left(G_{\sigma_{K_r}^{Id}}^* (Z_K^{n+1}) - G_{\sigma_{K_r}^{Id}}^* (u_K^{n+1}) + G_{\sigma_{K_r}^{Id}}^* (Z_L^{n+1}) - G_{\sigma_{K_r}^{Id}}^* (u_L^{n+1}) \right).$$

Using the non-decreasing property of the function $G_{\sigma_{K_r}^{Id}}^*$ with respect to $u_K^{n+1} - Z_K^{n+1}$, we have

$$-G_{\sigma_{K_r}^{Id}}^* (u_L^{n+1} - Z_L^{n+1}) \left(u_{\sigma_{K_r}^{Id}}^{n+1} - Z_{\sigma_{K_r}^{Id}}^{n+1} \right)^- \geq -G_{\sigma_{K_r}^{Id}}^* (u_K^{n+1} - Z_K^{n+1}) \left(u_{\sigma_{K_r}^{Id}}^{n+1} - Z_{\sigma_{K_r}^{Id}}^{n+1} \right)^-.$$

This yields to the following inequality

$$B_1 \geq \delta\phi_K D_K \sum_{r=i,j,k} \sum_{Id=1,2} |K_r| \nabla_{K_r} (u_K^{n+1} - Z_K^{n+1}) \cdot \nabla_{K_r} (u_K^{n+1} - Z_K^{n+1})^-$$

$$\geq 0.$$

It remains to prove that B_2 is positive. We have

$$B_2 = \sum_{r=i,j,k} \sum_{Id=1,2} (Z_K^{n+1} - u_K^{n+1})^- \left[-D_K |\sigma_{K_r}^{Id}| \nabla_{K_r} \varphi(u_h^{\delta t}) \cdot \vec{n}_{\sigma_{K_r}^{Id}} - b_s(Z_h^{\delta t})_{\sigma_{K_r}^{Id}}^{up} \mathcal{V}_{\sigma_{K_r}^{Id}}^{n+1} \right].$$

Using the following inequality $-\varphi(b) - \varphi(a) \geq -b_s(a)(b - a)$ for any $a, b \in \mathbb{R}$, we obtain that

$$-|\sigma_{K_r}^{Id}| D_K \nabla_{K_r} \varphi(u_h^{\delta t}) \cdot \vec{n}_{\sigma_{K_r}^{Id}} \geq -|\sigma_{K_r}^{Id}| D_K b_s(u_K^{n+1}) \nabla_{K_r} u_h^{\delta t} \cdot \vec{n}_{\sigma_{K_r}^{Id}},$$

$$\geq b_s(u_K^{n+1}) \mathcal{V}_{\sigma_{K_r}^{Id}}^{n+1}.$$

Therefore

$$-|\sigma_{K_r}^{Id}| D_K \nabla_{K_r} \varphi(u_h^{\delta t}) \cdot \vec{n}_{\sigma_{K_r}^{Id}} - b_s(Z_h^{\delta t})_{\sigma_{K_r}^{Id}}^{up} \mathcal{V}_{\sigma_{K_r}^{Id}}^{n+1} \geq \left(b_s(u_K^{n+1}) - b_s(Z_h^{\delta t})_{\sigma_{K_r}^{Id}}^{up} \right) \mathcal{V}_{\sigma_{K_r}^{Id}}^{n+1}.$$

- If $\mathcal{V}_{\sigma_{K_r}^{Id}}^{n+1} > 0$, then $(b_s(u_K^{n+1}) - b_s(Z_K^{n+1})) \mathcal{V}_{\sigma_{K_r}^{Id}}^{n+1} = 0$, since the function $b_s(u)$ is extended by zero if $u < 0$ (i.e. $u_K^{n+1} - Z_K^{n+1} < 0$).
- If $\mathcal{V}_{\sigma_{K_r}^{Id}}^{n+1} \leq 0$, then $(b_s(u_K^{n+1}) - b_s(Z_h^{\delta t})_{\sigma_{K_r}^{Id}}^{up}) \mathcal{V}_{\sigma_{K_r}^{Id}}^{n+1} \geq (b_s(u_K^{n+1}) - b_s(Z_K^{n+1})) \mathcal{V}_{\sigma_{K_r}^{Id}}^{n+1} = 0$.

Combining both cases, we get that B_2 is positive. As a result, we have

$$|K| \phi_K \left(u_K^{n+1} - Z_K^{n+1} - (u_K^n - Z_K^n) \right) (u_K^{n+1} - Z_K^{n+1})^- \leq 0.$$

Therefore, we have $u_K^{n+1} - Z_K^{n+1} \geq 0$ according to the induction assumption on $u_K^{n+1} - Z_K^{n+1}$ which gives

$$u_K^{n+1} \geq Z_K^{n+1} \text{ for every } n = 0, \dots, N-1 \text{ and } K \in \mathcal{T}_h.$$

This completes the proof of Proposition 5.4.1. \square

5.5 Energy estimates and compactness results

In this section we first present some energy estimates followed by the existence of discrete solutions to the FV scheme and a compactness result which will be used for the convergence of the numerical scheme.

5.5.1 A priori estimates

In this subsection, we present a set of preliminary results which are needed for the analysis of the scheme.

Proposition 5.5.1. *Let assumptions (A.1)–(A.3) be fulfilled. Then there exists a constant $C > 0$ independent of h and δt such that*

$$\begin{aligned} & \sum_{n=0}^{N-1} \delta t \sum_{K \in \mathcal{T}_h} D_K \sum_{r=i,j,k} |K_r| \nabla_{K_r} \varphi(u_h^{\delta t}) \cdot \nabla_{K_r} \varphi(u_h^{\delta t}) \\ & + \sum_{n=0}^{N-1} \delta t \sum_{K \in \mathcal{T}_h} D_K \sum_{r=i,j,k} |K_r| \nabla_{K_r} \varphi(Z_h^{\delta t}) \cdot \nabla_{K_r} \varphi(Z_h^{\delta t}) \leq C. \end{aligned}$$

Proof. First, we multiply equation (5.3.19) by u_K^{n+1} and equations (5.3.21)–(5.3.22) and (5.3.23) by $|\sigma_{K_r}^{Id}| u_{\sigma_{K_r}^{Id}}^{n+1}$. Adding the equalities and summing over $K \in \mathcal{T}_h$, we get

$$\sum_{K \in \mathcal{T}_h} \phi_K |K| (u_K^{n+1} - u_K^n) u_K^{n+1} + A_1 + A_2 + A_3 = 0, \quad (5.5.1)$$

with

$$A_1 =$$

$$\begin{aligned} & \delta t \sum_{K \in \mathcal{T}_h} D_K \sum_{r=i,j,k} \sum_{\text{Id}=1,2} -|\sigma_{K_r}^{\text{Id}}| u_K^{n+1} \left[\left(\varphi(u_{\sigma_{K_r}^1}^{n+1}) - \varphi(u_K^{n+1}) \right) \vec{\mu}_{\sigma_{K_r}^1} + \left(\varphi(u_{\sigma_{K_r}^2}^{n+1}) - \varphi(u_K^{n+1}) \right) \vec{\mu}_{\sigma_{K_r}^2} \right] \cdot \vec{n}_{\sigma_{K_r}^{\text{Id}}} \\ & + |\sigma_{K_r}^{\text{Id}}| u_{\sigma_{K_r}^{\text{Id}}}^{n+1} \left[\left(\varphi(u_{\sigma_{K_r}^1}^{n+1}) - \varphi(u_K^{n+1}) \right) \vec{\mu}_{\sigma_{K_r}^1} + \left(\varphi(u_{\sigma_{K_r}^2}^{n+1}) - \varphi(u_K^{n+1}) \right) \vec{\mu}_{\sigma_{K_r}^2} \right] \cdot \vec{n}_{\sigma_{K_r}^{\text{Id}}}, \end{aligned}$$

$$A_2 =$$

$$\begin{aligned} & \delta t \sum_{K \in \mathcal{T}_h} D_K \sum_{r=i,j,k} \sum_{\text{Id}=1,2} -|\sigma_{K_r}^{\text{Id}}| u_K^{n+1} \left[\left(\varphi(Z_{\sigma_{K_r}^1}^{n+1}) - \varphi(Z_K^{n+1}) \right) \vec{\mu}_{\sigma_{K_r}^1} + \left(\varphi(Z_{\sigma_{K_r}^2}^{n+1}) - \varphi(Z_K^{n+1}) \right) \vec{\mu}_{\sigma_{K_r}^2} \right] \cdot \vec{n}_{\sigma_{K_r}^{\text{Id}}} \\ & + |\sigma_{K_r}^{\text{Id}}| u_{\sigma_{K_r}^{\text{Id}}}^{n+1} \left[\left(\varphi(Z_{\sigma_{K_r}^1}^{n+1}) - \varphi(Z_K^{n+1}) \right) \vec{\mu}_{\sigma_{K_r}^1} + \left(\varphi(Z_{\sigma_{K_r}^2}^{n+1}) - \varphi(Z_K^{n+1}) \right) \vec{\mu}_{\sigma_{K_r}^2} \right] \cdot \vec{n}_{\sigma_{K_r}^{\text{Id}}}, \end{aligned}$$

and

$$A_3 =$$

$$\begin{aligned} & \delta t \sum_{K \in \mathcal{T}_h} D_K \delta \phi_K \sum_{r=i,j,k} \sum_{\text{Id}=1,2} -|\sigma_{K_r}^{\text{Id}}| u_K^{n+1} \left[\left(u_{\sigma_{K_r}^1}^{n+1} - u_K^{n+1} \right) \vec{\mu}_{\sigma_{K_r}^1} + \left(u_{\sigma_{K_r}^2}^{n+1} - u_K^{n+1} \right) \vec{\mu}_{\sigma_{K_r}^2} \right] \cdot \vec{n}_{\sigma_{K_r}^{\text{Id}}} \\ & + |\sigma_{K_r}^{\text{Id}}| u_{\sigma_{K_r}^{\text{Id}}}^{n+1} \left[\left(u_{\sigma_{K_r}^1}^{n+1} - u_K^{n+1} \right) \vec{\mu}_{\sigma_{K_r}^1} + \left(u_{\sigma_{K_r}^2}^{n+1} - u_K^{n+1} \right) \vec{\mu}_{\sigma_{K_r}^2} \right] \cdot \vec{n}_{\sigma_{K_r}^{\text{Id}}}. \end{aligned}$$

We use the following formulas from [20], $|\sigma_{K_r}^1| \vec{n}_{\sigma_{K_r}^1} = |K_r| \vec{\mu}_{\sigma_{K_r}^1}$ and $|\sigma_{K_r}^2| \vec{n}_{\sigma_{K_r}^2} = |K_r| \vec{\mu}_{\sigma_{K_r}^2}$, in the last terms, we obtain after factoring

$$\begin{aligned} A_1 &= \delta t \sum_{K \in \mathcal{T}_h} D_K \sum_{r=i,j,k} |K_r| \left[\left(\varphi(u_{\sigma_{K_r}^1}^{n+1}) - \varphi(u_K^{n+1}) \right) \left(u_{\sigma_{K_r}^1}^{n+1} - u_K^{n+1} \right) |\vec{\mu}_{\sigma_{K_r}^1}|^2 + \left(\varphi(u_{\sigma_{K_r}^2}^{n+1}) - \varphi(u_K^{n+1}) \right) \left(u_{\sigma_{K_r}^2}^{n+1} - u_K^{n+1} \right) |\vec{\mu}_{\sigma_{K_r}^2}|^2 \right. \\ & \left. + \left(\left(\varphi(u_{\sigma_{K_r}^1}^{n+1}) - \varphi(u_K^{n+1}) \right) \left(u_{\sigma_{K_r}^2}^{n+1} - u_K^{n+1} \right) + \left(\varphi(u_{\sigma_{K_r}^2}^{n+1}) - \varphi(u_K^{n+1}) \right) \left(u_{\sigma_{K_r}^1}^{n+1} - u_K^{n+1} \right) \right) \vec{\mu}_{\sigma_{K_r}^1} \cdot \vec{\mu}_{\sigma_{K_r}^2} \right] \\ &= \delta t \sum_{K \in \mathcal{T}_h} D_K \sum_{r=i,j,k} |K_r| \nabla_{K_r} \varphi \left(u_h^{\delta t} \right) \cdot \nabla_{K_r} u_h^{\delta t}. \\ A_2 &= \delta t \sum_{K \in \mathcal{T}_h} D_K \sum_{r=i,j,k} |K_r| \left[\left(\varphi(Z_{\sigma_{K_r}^1}^{n+1}) - \varphi(Z_K^{n+1}) \right) \left(u_{\sigma_{K_r}^1}^{n+1} - u_K^{n+1} \right) |\vec{\mu}_{\sigma_{K_r}^1}|^2 + \left(\varphi(Z_{\sigma_{K_r}^2}^{n+1}) - \varphi(Z_K^{n+1}) \right) \left(u_{\sigma_{K_r}^2}^{n+1} - u_K^{n+1} \right) |\vec{\mu}_{\sigma_{K_r}^2}|^2 \right. \\ & \left. + \left(\left(\varphi(Z_{\sigma_{K_r}^1}^{n+1}) - \varphi(Z_K^{n+1}) \right) \left(u_{\sigma_{K_r}^2}^{n+1} - u_K^{n+1} \right) + \left(\varphi(Z_{\sigma_{K_r}^2}^{n+1}) - \varphi(Z_K^{n+1}) \right) \left(u_{\sigma_{K_r}^1}^{n+1} - u_K^{n+1} \right) \right) \vec{\mu}_{\sigma_{K_r}^1} \cdot \vec{\mu}_{\sigma_{K_r}^2} \right] \\ &= \delta t \sum_{K \in \mathcal{T}_h} D_K \sum_{r=i,j,k} |K_r| \nabla_{K_r} \varphi \left(Z_h^{\delta t} \right) \cdot \nabla_{K_r} u_h^{\delta t}, \\ A_3 &= \delta t \sum_{K \in \mathcal{T}_h} D_K \sum_{r=i,j,k} |K_r| \left[\left(u_{\sigma_{K_r}^1}^{n+1} - u_K^{n+1} \right)^2 |\vec{\mu}_{\sigma_{K_r}^1}|^2 + \left(u_{\sigma_{K_r}^2}^{n+1} - u_K^{n+1} \right)^2 |\vec{\mu}_{\sigma_{K_r}^2}|^2 \right. \\ & \left. + 2 \left(u_{\sigma_{K_r}^1}^{n+1} - u_K^{n+1} \right) \left(u_{\sigma_{K_r}^2}^{n+1} - u_K^{n+1} \right) \vec{\mu}_{\sigma_{K_r}^1} \cdot \vec{\mu}_{\sigma_{K_r}^2} \right], \\ &= \delta t \sum_{K \in \mathcal{T}_h} D_K \sum_{r=i,j,k} |K_r| \nabla_{K_r} u_h^{\delta t} \cdot \nabla_{K_r} u_h^{\delta t}. \end{aligned}$$

Summing the result over $n = 0$ to $N - 1$, equation (5.5.1) can be written as

$$A_{0N} + A_{1N} + A_{2N} + A_{3N} = 0, \quad (5.5.2)$$

where

$$\begin{aligned} A_{0N} &= \sum_{n=0}^{N-1} \sum_{K \in \mathcal{T}_h} \phi_K |K| (u_K^{n+1} - u_K^n) u_K^{n+1}, \\ A_{1N} &= \sum_{n=0}^{N-1} \delta t \sum_{K \in \mathcal{T}_h} D_K \sum_{r=i,j,k} |K_r| \nabla_{K_r} \varphi(u_h^{\delta t}) \cdot \nabla_{K_r} u_h^{\delta t}, \\ A_{2N} &= \sum_{n=0}^{N-1} \delta t \sum_{K \in \mathcal{T}_h} D_K \sum_{r=i,j,k} |K_r| \nabla_{K_r} \varphi(Z_h^{\delta t}) \cdot \nabla_{K_r} u_h^{\delta t}, \\ A_{3N} &= \sum_{n=0}^{N-1} \delta t \sum_{K \in \mathcal{T}_h} D_K \phi_K \sum_{r=i,j,k} |K_r| \delta \nabla_{K_r} u_h^{\delta t} \cdot \nabla_{K_r} u_h^{\delta t}. \end{aligned}$$

Next, using the identity: for any $a, b \in \mathbb{R}$, $(a - b)a = \frac{1}{2}[(a - b)^2 + (a^2 - b^2)]$, A_{0N} can be written as

$$\begin{aligned} A_{0N} &= \frac{1}{2} \sum_{K \in \mathcal{T}_h} \phi_K |K| \left((u_K^N)^2 - (u_K^0)^2 + \sum_{n=0}^{N-1} (u_K^{n+1} - u_K^n)^2 \right), \\ &= \frac{1}{2} \sum_{K \in \mathcal{T}_h} \phi_K |K| (u_K^N)^2 - \frac{1}{2} \sum_{K \in \mathcal{T}_h} \phi_K |K| (u_K^0)^2 + \frac{1}{2} \sum_{n=0}^{N-1} \sum_{K \in \mathcal{T}_h} \phi_K |K| (u_K^{n+1} - u_K^n)^2, \\ &\geq -\frac{1}{2} \phi_+ \sum_{K \in \mathcal{T}_h} |K| (u_K^0)^2 = -\frac{1}{2} \phi_+ \|u_0\|_{\mathbf{L}^2(\Omega)}^2. \end{aligned}$$

From the fact that φ is a non-decreasing Lipschitz continuous function with λ its Lipschitz constant, we obtain the following estimate for the term A_{1N} :

$$\begin{aligned} A_{1N} &= \sum_{n=0}^{N-1} \delta t \sum_{K \in \mathcal{T}_h} D_K \sum_{r=i,j,k} |K_r| \left[\left(\varphi(u_{\sigma_{K_r}^1}^{n+1}) - \varphi(u_K^{n+1}) \right) \left(u_{\sigma_{K_r}^1}^{n+1} - u_K^{n+1} \right) |\vec{\mu}_{\sigma_{K_r}^1}|^2 + \left(\varphi(u_{\sigma_{K_r}^2}^{n+1}) - \varphi(u_K^{n+1}) \right) \left(u_{\sigma_{K_r}^2}^{n+1} - u_K^{n+1} \right) |\vec{\mu}_{\sigma_{K_r}^2}|^2 \right. \\ &\quad \left. + \left(\left(\varphi(u_{\sigma_{K_r}^1}^{n+1}) - \varphi(u_K^{n+1}) \right) \left(u_{\sigma_{K_r}^2}^{n+1} - u_K^{n+1} \right) + \left(\varphi(u_{\sigma_{K_r}^2}^{n+1}) - \varphi(u_K^{n+1}) \right) \left(u_{\sigma_{K_r}^1}^{n+1} - u_K^{n+1} \right) \right) \vec{\mu}_{\sigma_{K_r}^1} \cdot \vec{\mu}_{\sigma_{K_r}^2} \right] \\ &\geq \frac{1}{\lambda} \sum_{n=0}^{N-1} \delta t \sum_{K \in \mathcal{T}_h} D_K \sum_{r=i,j,k} |K_r| \left[\left(\varphi(u_{\sigma_{K_r}^1}^{n+1}) - \varphi(u_K^{n+1}) \right)^2 |\vec{\mu}_{\sigma_{K_r}^1}|^2 + \left(\varphi(u_{\sigma_{K_r}^2}^{n+1}) - \varphi(u_K^{n+1}) \right)^2 |\vec{\mu}_{\sigma_{K_r}^2}|^2 \right. \\ &\quad \left. + 2 \left(\varphi(u_{\sigma_{K_r}^1}^{n+1}) - \varphi(u_K^{n+1}) \right) \left(\varphi(u_{\sigma_{K_r}^2}^{n+1}) - \varphi(u_K^{n+1}) \right) \vec{\mu}_{\sigma_{K_r}^1} \cdot \vec{\mu}_{\sigma_{K_r}^2} \right], \\ &\geq \frac{1}{\lambda} \sum_{n=0}^{N-1} \delta t \sum_{K \in \mathcal{T}_h} D_K \sum_{r=i,j,k} |K_r| \nabla_{K_r} \varphi(u_h^{\delta t}) \cdot \nabla_{K_r} \varphi(u_h^{\delta t}), \end{aligned}$$

In an analogue way, we get

$$\begin{aligned}
A_{2N} &= \sum_{n=0}^{N-1} \delta t \sum_{K \in \mathcal{T}_h} D_K \sum_{r=i,j,k} |K_r| \left[\right. \\
&\quad \left(\varphi(Z_{\sigma_{K_r}^1}^{n+1}) - \varphi(Z_K^{n+1}) \right) \left(u_{\sigma_{K_r}^1}^{n+1} - u_K^{n+1} \right) |\vec{\mu}_{\sigma_{K_r}^1}|^2 + \left(\varphi(Z_{\sigma_{K_r}^2}^{n+1}) - \varphi(Z_K^{n+1}) \right) \left(u_{\sigma_{K_r}^2}^{n+1} - u_K^{n+1} \right) |\vec{\mu}_{\sigma_{K_r}^2}|^2 \\
&\quad + \left(\left(\varphi(Z_{\sigma_{K_r}^1}^{n+1}) - \varphi(Z_K^{n+1}) \right) \left(u_{\sigma_{K_r}^2}^{n+1} - u_K^{n+1} \right) + \left(\varphi(Z_{\sigma_{K_r}^2}^{n+1}) - \varphi(Z_K^{n+1}) \right) \left(u_{\sigma_{K_r}^1}^{n+1} - u_K^{n+1} \right) \right) \vec{\mu}_{\sigma_{K_r}^1} \cdot \vec{\mu}_{\sigma_{K_r}^2} \\
&\geq \frac{1}{\lambda} \sum_{n=0}^{N-1} \delta t \sum_{K \in \mathcal{T}_h} D_K \sum_{r=i,j,k} |K_r| \left[\left(\varphi(Z_{\sigma_{K_r}^1}^{n+1}) - \varphi(Z_K^{n+1}) \right) \left(\varphi(u_{\sigma_{K_r}^1}^{n+1}) - \varphi(u_K^{n+1}) \right) |\vec{\mu}_{\sigma_{K_r}^1}|^2 \right. \\
&\quad + \left(\varphi(Z_{\sigma_{K_r}^2}^{n+1}) - \varphi(Z_K^{n+1}) \right) \left(\varphi(u_{\sigma_{K_r}^2}^{n+1}) - \varphi(u_K^{n+1}) \right) |\vec{\mu}_{\sigma_{K_r}^2}|^2 \\
&\quad + \left(\left(\varphi(Z_{\sigma_{K_r}^1}^{n+1}) - \varphi(Z_K^{n+1}) \right) \left(\varphi(u_{\sigma_{K_r}^2}^{n+1}) - \varphi(u_K^{n+1}) \right) \right. \\
&\quad \left. \left. + \left(\varphi(Z_{\sigma_{K_r}^2}^{n+1}) - \varphi(Z_K^{n+1}) \right) \left(\varphi(u_{\sigma_{K_r}^1}^{n+1}) - \varphi(u_K^{n+1}) \right) \right) \vec{\mu}_{\sigma_{K_r}^1} \cdot \vec{\mu}_{\sigma_{K_r}^2} \right], \\
&\geq \frac{1}{\lambda} \sum_{n=0}^{N-1} \delta t \sum_{K \in \mathcal{T}_h} D_K \sum_{r=i,j,k} |K_r| \nabla_{K_r} \varphi(Z_h^{\delta t}) \cdot \nabla_{K_r} \varphi(u_h^{\delta t}),
\end{aligned}$$

and

$$\begin{aligned}
A_{3N} &= \delta \sum_{n=0}^{N-1} \delta t \sum_{K \in \mathcal{T}_h} D_K \phi_K \sum_{r=i,j,k} |K_r| \left[\right. \\
&\quad \left(u_{\sigma_{K_r}^1}^{n+1} - u_K^{n+1} \right) \left(u_{\sigma_{K_r}^2}^{n+1} - u_K^{n+1} \right) |\vec{\mu}_{\sigma_{K_r}^1}|^2 + \left(u_{\sigma_{K_r}^2}^{n+1} - u_K^{n+1} \right) \left(u_{\sigma_{K_r}^1}^{n+1} - u_K^{n+1} \right) |\vec{\mu}_{\sigma_{K_r}^2}|^2 \\
&\quad + \left(\left(u_{\sigma_{K_r}^1}^{n+1} - u_K^{n+1} \right) \left(u_{\sigma_{K_r}^2}^{n+1} - u_K^{n+1} \right) + \left(u_{\sigma_{K_r}^2}^{n+1} - u_K^{n+1} \right) \left(u_{\sigma_{K_r}^1}^{n+1} - u_K^{n+1} \right) \right) \vec{\mu}_{\sigma_{K_r}^1} \cdot \vec{\mu}_{\sigma_{K_r}^2} \left. \right], \\
&\geq \delta \frac{\phi^-}{\lambda^2} \sum_{n=0}^{N-1} \delta t \sum_{K \in \mathcal{T}_h} D_K \sum_{r=i,j,k} |K_r| \left[\left(\varphi(u_{\sigma_{K_r}^1}^{n+1}) - \varphi(u_K^{n+1}) \right)^2 |\vec{\mu}_{\sigma_{K_r}^1}|^2 + \left(\varphi(u_{\sigma_{K_r}^2}^{n+1}) - \varphi(u_K^{n+1}) \right)^2 |\vec{\mu}_{\sigma_{K_r}^2}|^2 \right. \\
&\quad \left. + \left(\varphi(u_{\sigma_{K_r}^1}^{n+1}) - \varphi(u_K^{n+1}) \right) \left(\varphi(u_{\sigma_{K_r}^2}^{n+1}) - \varphi(u_K^{n+1}) \right) \vec{\mu}_{\sigma_{K_r}^1} \cdot \vec{\mu}_{\sigma_{K_r}^2} \right], \\
&\geq \delta \frac{\phi^-}{\lambda^2} \sum_{n=0}^{N-1} \delta t \sum_{K \in \mathcal{T}_h} D_K \sum_{r=i,j,k} |K_r| \nabla_{K_r} \varphi(u_h^{\delta t}) \cdot \nabla_{K_r} \varphi(u_h^{\delta t}).
\end{aligned}$$

Adding the last inequalities and using equation (5.5.2), we obtain

$$\begin{aligned}
&\left(\frac{1}{\lambda} + \delta \frac{\phi^-}{\lambda^2} \right) \sum_{n=0}^{N-1} \delta t \sum_{K \in \mathcal{T}_h} D_K \sum_{r=i,j,k} |K_r| \nabla_{K_r} \varphi(u_h^{\delta t}) \cdot \nabla_{K_r} \varphi(u_h^{\delta t}) \\
&+ \frac{1}{\lambda} \sum_{n=0}^{N-1} \delta t \sum_{K \in \mathcal{T}_h} D_K \sum_{r=i,j,k} |K_r| \nabla_{K_r} \varphi(Z_h^{\delta t}) \cdot \nabla_{K_r} \varphi(u_h^{\delta t}) \leq \frac{1}{2} \phi^+ \|u_0\|_{\mathbf{L}^2(\Omega)}^2. \quad (5.5.3)
\end{aligned}$$

We now pass to the proof of the discrete gradient estimates for the saltwater equation. We proceed in the same way. We multiply equation (5.3.20) by Z_K^{n+1} and

equations (5.3.22), (5.3.24) and (5.3.25) by $|\sigma_{K_r}^{Id}|Z_{\sigma_{K_r}^{Id}}^{n+1}$. Adding the equalities and summing over $K \in \mathcal{T}_h$ and over $n = 0, \dots, N-1$, we obtain

$$B_{0N} + B_{1N} + B_{2N} + B_{3N} = 0, \quad (5.5.4)$$

where

$$\begin{aligned} B_{0N} &= \sum_{n=0}^{N-1} \sum_{K \in \mathcal{T}_h} \phi_K |K| (Z_K^{n+1} - Z_K^n) Z_K^{n+1}, \\ B_{1N} &= \sum_{n=0}^{N-1} \delta t \sum_{K \in \mathcal{T}_h} D_K \sum_{r=i,j,k} b_s \left(Z_h^{\delta t} \right)^{up} |K_r| \nabla_{K_r} u_K^{n+1} \cdot \nabla_{K_r} Z_K^{n+1}, \\ B_{2N} &= \sum_{n=0}^{N-1} \delta t \sum_{K \in \mathcal{T}_h} D_K \sum_{r=i,j,k} |K_r| \nabla_{K_r} \varphi \left(Z_K^{n+1} \right) \cdot \nabla_{K_r} Z_K^{n+1}, \\ B_{3N} &= \sum_{n=0}^{N-1} \delta t \sum_{K \in \mathcal{T}_h} D_K \delta \phi_K \sum_{r=i,j,k} |K_r| \nabla_{K_r} Z_h^{\delta t} \cdot \nabla_{K_r} Z_h^{\delta t}. \end{aligned}$$

Using the identity: for any $a, b \in \mathbb{R}$, $(a-b)a = \frac{1}{2}[(a-b)^2 + (a^2 - b^2)]$, we have

$$\begin{aligned} B_{0N} &= \frac{1}{2} \sum_{K \in \mathcal{T}_h} \phi_K |K| (Z_K^N)^2 - \frac{1}{2} \sum_{K \in \mathcal{T}_h} \phi_K |K| (Z_K^0)^2 + \frac{1}{2} \sum_{n=0}^{N-1} \sum_{K \in \mathcal{T}_h} \phi_K |K| (Z_K^{n+1} - Z_K^n)^2, \\ &\geq -\frac{1}{2} \phi^+ \|Z_0\|_{\mathbf{L}^2(\Omega)}^2. \end{aligned}$$

For B_{1N} , we use the convexity of φ and the following inequality $b_s(a)(b-a) \geq \varphi(b) - \varphi(a)$ for any $a, b \in \mathbb{R}$, then it follows

$$\begin{aligned} B_{1N} &= \sum_{n=0}^{N-1} \delta t \sum_{K \in \mathcal{T}_h} D_K \sum_{r=i,j,k} |K_r| b_s \left(Z_h^{\delta t} \right)_{\sigma_{K_r}^{Id}}^{up} \left[\right. \\ &\quad \left(Z_{\sigma_{K_r}^1}^{n+1} - Z_K^{n+1} \right) \left(u_{\sigma_{K_r}^1}^{n+1} - u_K^{n+1} \right) |\vec{\mu}_{\sigma_{K_r}^1}|^2 + \left(Z_{\sigma_{K_r}^2}^{n+1} - Z_K^{n+1} \right) \left(u_{\sigma_{K_r}^2}^{n+1} - u_K^{n+1} \right) |\vec{\mu}_{\sigma_{K_r}^2}|^2 \\ &\quad \left. + \left(\left(Z_{\sigma_{K_r}^1}^{n+1} - Z_K^{n+1} \right) \left(u_{\sigma_{K_r}^2}^{n+1} - u_K^{n+1} \right) + \left(Z_{\sigma_{K_r}^2}^{n+1} - Z_K^{n+1} \right) \left(u_{\sigma_{K_r}^1}^{n+1} - u_K^{n+1} \right) \right) \vec{\mu}_{\sigma_{K_r}^1} \cdot \vec{\mu}_{\sigma_{K_r}^2} \right] \\ &\geq \sum_{n=0}^{N-1} \delta t \sum_{K \in \mathcal{T}_h} D_K \sum_{r=i,j,k} |K_r| \left[\right. \\ &\quad \left(\varphi \left(Z_{\sigma_{K_r}^1}^{n+1} \right) - \varphi \left(Z_K^{n+1} \right) \right) \left(u_{\sigma_{K_r}^1}^{n+1} - u_K^{n+1} \right) |\vec{\mu}_{\sigma_{K_r}^1}|^2 + \left(\varphi \left(Z_{\sigma_{K_r}^2}^{n+1} \right) - \varphi \left(Z_K^{n+1} \right) \right) \left(u_{\sigma_{K_r}^2}^{n+1} - u_K^{n+1} \right) |\vec{\mu}_{\sigma_{K_r}^2}|^2 \\ &\quad \left. + \left(\left(\varphi \left(Z_{\sigma_{K_r}^1}^{n+1} \right) - \varphi \left(Z_K^{n+1} \right) \right) \left(u_{\sigma_{K_r}^2}^{n+1} - u_K^{n+1} \right) + \left(\varphi \left(Z_{\sigma_{K_r}^2}^{n+1} \right) - \varphi \left(Z_K^{n+1} \right) \right) \left(u_{\sigma_{K_r}^1}^{n+1} - u_K^{n+1} \right) \right) \vec{\mu}_{\sigma_{K_r}^1} \cdot \vec{\mu}_{\sigma_{K_r}^2} \right] \\ &\geq \frac{1}{\lambda} \sum_{n=0}^{N-1} \delta t \sum_{K \in \mathcal{T}_h} D_K \sum_{r=i,j,k} |K_r| \left[\left(\varphi \left(Z_{\sigma_{K_r}^1}^{n+1} \right) - \varphi \left(Z_K^{n+1} \right) \right) \left(\varphi \left(u_{\sigma_{K_r}^1}^{n+1} \right) - \varphi \left(u_K^{n+1} \right) \right) |\vec{\mu}_{\sigma_{K_r}^1}|^2 \right. \\ &\quad \left. + \left(\varphi \left(Z_{\sigma_{K_r}^2}^{n+1} \right) - \varphi \left(Z_K^{n+1} \right) \right) \left(\varphi \left(u_{\sigma_{K_r}^2}^{n+1} \right) - \varphi \left(u_K^{n+1} \right) \right) |\vec{\mu}_{\sigma_{K_r}^2}|^2 \right] \end{aligned}$$

$$\begin{aligned}
& + \left(\left(\varphi(Z_{\sigma_{K_r}^1}^{n+1}) - \varphi(Z_K^{n+1}) \right) \left(\varphi(u_{\sigma_{K_r}^2}^{n+1}) - \varphi(u_K^{n+1}) \right) \right. \\
& + \left. \left(\varphi(Z_{\sigma_{K_r}^2}^{n+1}) - \varphi(Z_K^{n+1}) \right) \left(\varphi(u_{\sigma_{K_r}^1}^{n+1}) - \varphi(u_K^{n+1}) \right) \right) \vec{\mu}_{\sigma_{K_r}^1} \cdot \vec{\mu}_{\sigma_{K_r}^2} \Big], \\
& \geq \frac{1}{\lambda} \sum_{n=0}^{N-1} \delta t \sum_{K \in \mathcal{T}_h} D_K \sum_{r=i,j,k} |K_r| \nabla_{K_r} \varphi(Z_h^{\delta t}) \cdot \nabla_{K_r} \varphi(u_h^{\delta t}).
\end{aligned}$$

To estimate B_{2N} and B_{3N} , we use the same idea as done in A_{2N} and A_{3N} , to obtain

$$\begin{aligned}
B_{2N} & = \sum_{n=0}^{N-1} \delta t \sum_{K \in \mathcal{T}_h} D_K \sum_{r=i,j,k} |K_r| \nabla_{K_r} \varphi(Z_K^{n+1}) \cdot \nabla_{K_r} Z_K^{n+1}, \\
& \geq \frac{1}{\lambda} \sum_{n=0}^{N-1} \delta t \sum_{K \in \mathcal{T}_h} D_K \sum_{r=i,j,k} |K_r| \nabla_{K_r} \varphi(Z_h^{\delta t}) \cdot \nabla_{K_r} \varphi(Z_h^{\delta t}),
\end{aligned}$$

and

$$\begin{aligned}
B_{3N} & = \sum_{n=0}^{N-1} \delta t \sum_{K \in \mathcal{T}_h} D_K \delta \phi_K \sum_{r=i,j,k} |K_r| \nabla_{K_r} Z_K^{n+1} \cdot \nabla_{K_r} Z_K^{n+1} \\
& \geq \delta \frac{\phi^-}{\lambda^2} \sum_{n=0}^{N-1} \delta t \sum_{K \in \mathcal{T}_h} D_K \sum_{r=i,j,k} |K_r| \nabla_{K_r} \varphi(Z_h^{\delta t}) \cdot \nabla_{K_r} \varphi(Z_h^{\delta t}).
\end{aligned}$$

Adding the previous inequalities and using equation (5.5.4), we get the following estimate

$$\begin{aligned}
& \left(\frac{1}{\lambda} + \delta \frac{\phi^-}{\lambda^2} \right) \sum_{n=0}^{N-1} \delta t \sum_{K \in \mathcal{T}_h} D_K \sum_{r=i,j,k} |K_r| \nabla_{K_r} \varphi(Z_h^{\delta t}) \cdot \nabla_{K_r} \varphi(Z_h^{\delta t}) \\
& + \frac{1}{\lambda} \sum_{n=0}^{N-1} \delta t \sum_{K \in \mathcal{T}_h} D_K \sum_{r=i,j,k} |K_r| \nabla_{K_r} \varphi(Z_h^{\delta t}) \cdot \nabla_{K_r} \varphi(u_h^{\delta t}) \leq \frac{1}{2} \phi^+ \|Z_0\|_{\mathbf{L}^2(\Omega)}^2. \quad (5.5.5)
\end{aligned}$$

Using the estimates (5.5.3) and (5.5.5), we obtain

$$\begin{aligned}
& \sum_{n=0}^{N-1} \delta t \sum_{K \in \mathcal{T}_h} \sum_{r=i,j,k} |K_r| D_K \nabla_{K_r} \varphi(u_h^{\delta t}) \cdot \nabla_{K_r} \varphi(u_h^{\delta t}) \\
& + \sum_{n=0}^{N-1} \delta t \sum_{K \in \mathcal{T}_h} \sum_{r=i,j,k} |K_r| D_K \nabla_{K_r} \varphi(Z_h^{\delta t}) \cdot \nabla_{K_r} \varphi(Z_h^{\delta t}) \\
& + \sum_{n=0}^{N-1} \delta t \sum_{K \in \mathcal{T}_h} \sum_{r=i,j,k} |K_r| D_K \nabla_{K_r} \varphi(Z_h^{\delta t}) \cdot \nabla_{K_r} \varphi(u_h^{\delta t}) \\
& \leq \frac{1}{\min(\delta \phi^- / \lambda, 1)} \frac{\lambda \phi^+}{2} \left(\|Z_0\|_{\mathbf{L}^2(\Omega)}^2 + \|u_0\|_{\mathbf{L}^2(\Omega)}^2 \right).
\end{aligned}$$

Finally, using the following inequality, for any $a, b \in \mathbb{R}^2$, $\frac{1}{2} (\|a\|^2 + \|b\|^2) \leq (\|a\|^2 + \|b\|^2 + a \cdot b)$ in the previous inequality (with $a = \nabla_{K_r} \varphi(Z_h^{\delta t})$, $b = \nabla_{K_r} \varphi(u_h^{\delta t})$), we

obtain

$$\begin{aligned} & \sum_{n=0}^{N-1} \delta t \sum_{K \in \mathcal{T}_h} \sum_{r=i,j,k} |K_r| D_K \nabla_{K_r} \varphi(u_h^{\delta t}) \cdot \nabla_{K_r} \varphi(u_h^{\delta t}) \\ & + \sum_{n=0}^{N-1} \delta t \sum_{K \in \mathcal{T}_h} \sum_{r=i,j,k} |K_r| D_K \nabla_{K_r} \varphi(Z_h^{\delta t}) \cdot \nabla_{K_r} \varphi(Z_h^{\delta t}) \leq C \end{aligned}$$

where $C = \frac{\lambda \phi^+}{\min(\delta \phi^- / \lambda, 1)} \left(\|Z_0\|_{\mathbf{L}^2(\Omega)}^2 + \|u_0\|_{\mathbf{L}^2(\Omega)}^2 \right)$. This concludes the proof of Proposition 5.5.1 \square

5.5.2 Existence of the discrete solution

In this subsection, we will prove an existence result for the nonlinear system of equations (5.3.19)–(5.3.25). To this end, we follow the strategy proposed in [20, 73] and we use Leray-Schauder's fixed point theorem.

Proposition 5.5.2. *Let assumptions (A.1)–(A.3) be fulfilled. The coupled system (5.3.19)–(5.3.25) admits a discrete solution*

$$\mathbf{U} = \left(u_K^{n+1}, u_{\sigma_{K_r}^1}^{n+1}, u_{\sigma_{K_r}^2}^{n+1} \right)_{K \in \mathcal{T}_h, r \in \{i,j,k\}, n \in [0, N-1]} \quad \text{and} \quad \mathbf{Z} = \left(Z_K^{n+1}, Z_{\sigma_{K_r}^1}^{n+1}, Z_{\sigma_{K_r}^2}^{n+1} \right)_{K \in \mathcal{T}_h, r \in \{i,j,k\}, n \in [0, N-1]}.$$

Proof. Let (\mathbf{U}, \mathbf{Z}) be a solution of the system (5.3.19)–(5.3.25). Let $E = \left(\mathbb{R}^{[0, N-1]} \times \mathcal{T}_h \right)^2$ and we define the mapping

$$\begin{aligned} \mathcal{G} : \quad E & \rightarrow E \\ (\mathbf{U}, \mathbf{Z}) & \rightarrow (\tilde{\mathbf{U}}, \tilde{\mathbf{Z}}), \end{aligned}$$

such that $(\tilde{\mathbf{U}}, \tilde{\mathbf{Z}})$ is the solution of the following set of equations: for all $K \in \mathcal{T}_h$,

$$\begin{aligned} & \phi_K |K| (\tilde{u}_K^{n+1} - \tilde{u}_K^n) \\ & - \delta t \sum_{r=i,j,k} \sum_{Id=1,2} |\sigma_{K_r}^{Id}| D_K \left[\left(\varphi(u_{\sigma_{K_r}^1}^{n+1}) - \varphi(u_K^{n+1}) \right) \vec{\mu}_{\sigma_{K_r}^1} + \left(\varphi(u_{\sigma_{K_r}^2}^{n+1}) - \varphi(u_K^{n+1}) \right) \vec{\mu}_{\sigma_{K_r}^2} \right] \cdot \vec{n}_{\sigma_{K_r}^{Id}} \\ & - \delta t \sum_{r=i,j,k} \sum_{Id=1,2} |\sigma_{K_r}^{Id}| D_K \left[\left(\varphi(Z_{\sigma_{K_r}^1}^{n+1}) - \varphi(Z_K^{n+1}) \right) \vec{\mu}_{\sigma_{K_r}^1} + \left(\varphi(Z_{\sigma_{K_r}^2}^{n+1}) - \varphi(Z_K^{n+1}) \right) \vec{\mu}_{\sigma_{K_r}^2} \right] \cdot \vec{n}_{\sigma_{K_r}^{Id}} \\ & - \delta t \sum_{r=i,j,k} \sum_{Id=1,2} \delta \phi_K |\sigma_{K_r}^{Id}| D_K \left[\left(\tilde{u}_{\sigma_{K_r}^1}^{n+1} - \tilde{u}_K^{n+1} \right) \vec{\mu}_{\sigma_{K_r}^1} + \left(\tilde{u}_{\sigma_{K_r}^2}^{n+1} - \tilde{u}_K^{n+1} \right) \vec{\mu}_{\sigma_{K_r}^2} \right] \cdot \vec{n}_{\sigma_{K_r}^{Id}} = 0, \end{aligned}$$

$$\begin{aligned} & \phi_K |K| \left(\tilde{Z}_K^{n+1} - \tilde{Z}_K^n \right) \\ & - \delta t \sum_{r=i,j,k} \sum_{Id=1,2} |\sigma_{K_r}^{Id}| D_K \left[\left(\varphi(Z_{\sigma_{K_r}^1}^{n+1}) - \varphi(Z_K^{n+1}) \right) \vec{\mu}_{\sigma_{K_r}^1} + \left(\varphi(Z_{\sigma_{K_r}^2}^{n+1}) - \varphi(Z_K^{n+1}) \right) \vec{\mu}_{\sigma_{K_r}^2} \right] \cdot \vec{n}_{\sigma_{K_r}^{Id}} \\ & - \delta t \sum_{r=i,j,k} \sum_{Id=1,2} |\sigma_{K_r}^{Id}| D_K b_s(Z_h^{\delta t})_{\sigma_{K_r}^{Id}}^{up} \left[\left(\tilde{u}_{\sigma_{K_r}^1}^{n+1} - \tilde{u}_K^{n+1} \right) \vec{\mu}_{\sigma_{K_r}^1} + \left(\tilde{u}_{\sigma_{K_r}^2}^{n+1} - \tilde{u}_K^{n+1} \right) \vec{\mu}_{\sigma_{K_r}^2} \right] \cdot \vec{n}_{\sigma_{K_r}^{Id}} \end{aligned}$$

$$\begin{aligned}
& -\delta t \sum_{r=i,j,k} \sum_{l=1,2} \delta\phi_K |\sigma_{K_r}^{Id}| D_K \left[\left(\tilde{Z}_{\sigma_{K_r}^1}^{n+1} - \tilde{Z}_K^{n+1} \right) \vec{\mu}_{\sigma_{K_r}^1} + \left(\tilde{Z}_{\sigma_{K_r}^2}^{n+1} - \tilde{Z}_K^{n+1} \right) \vec{\mu}_{\sigma_{K_r}^2} \right] \cdot \vec{n}_{\sigma_{K_r}^{Id}} = 0. \\
& D_K \left[\left(\varphi(u_{\sigma_{K_r}^1}^{n+1}) - \varphi(u_K^{n+1}) \right) \vec{\mu}_{\sigma_{K_r}^1} + \left(\varphi(u_{\sigma_{K_r}^2}^{n+1}) - \varphi(u_K^{n+1}) \right) \vec{\mu}_{\sigma_{K_r}^2} \right] \cdot \vec{n}_\sigma \\
& + D_L \left[\left(\varphi(u_{\sigma_{L_r}^1}^{n+1}) - \varphi(u_L^{n+1}) \right) \vec{\mu}_{\sigma_{L_r}^1} + \left(\varphi(u_{\sigma_{L_r}^2}^{n+1}) - \varphi(u_L^{n+1}) \right) \vec{\mu}_{\sigma_{L_r}^2} \right] \cdot \vec{n}_\sigma = 0, \\
& D_K \left[\left(\varphi(Z_{\sigma_{K_r}^1}^{n+1}) - \varphi(Z_K^{n+1}) \right) \vec{\mu}_{\sigma_{K_r}^1} + \left(\varphi(Z_{\sigma_{K_r}^2}^{n+1}) - \varphi(Z_K^{n+1}) \right) \vec{\mu}_{\sigma_{K_r}^2} \right] \cdot \vec{n}_\sigma \\
& + D_L \left[\left(\varphi(Z_{\sigma_{L_r}^1}^{n+1}) - \varphi(Z_L^{n+1}) \right) \vec{\mu}_{\sigma_{L_r}^1} + \left(\varphi(Z_{\sigma_{L_r}^2}^{n+1}) - \varphi(Z_L^{n+1}) \right) \vec{\mu}_{\sigma_{L_r}^2} \right] \cdot \vec{n}_\sigma = 0, \\
& D_K \left[\left(\tilde{u}_{\sigma_{K_r}^1}^{n+1} - \tilde{u}_K^{n+1} \right) \vec{\mu}_{\sigma_{K_r}^1} + \left(\tilde{u}_{\sigma_{K_r}^2}^{n+1} - \tilde{u}_K^{n+1} \right) \vec{\mu}_{\sigma_{K_r}^2} \right] \cdot \vec{n}_\sigma \\
& + D_L \left[\left(\tilde{u}_{\sigma_{L_r}^1}^{n+1} - \tilde{u}_L^{n+1} \right) \vec{\mu}_{\sigma_{L_r}^1} + \left(\tilde{u}_{\sigma_{L_r}^2}^{n+1} - \tilde{u}_L^{n+1} \right) \vec{\mu}_{\sigma_{L_r}^2} \right] \cdot \vec{n}_\sigma = 0, \\
& D_K \left[\left(\tilde{Z}_{\sigma_{K_r}^1}^{n+1} - \tilde{Z}_K^{n+1} \right) \vec{\mu}_{\sigma_{K_r}^1} + \left(\tilde{Z}_{\sigma_{K_r}^2}^{n+1} - \tilde{Z}_K^{n+1} \right) \vec{\mu}_{\sigma_{K_r}^2} \right] \cdot \vec{n}_\sigma \\
& + D_L \left[\left(\tilde{Z}_{\sigma_{L_r}^1}^{n+1} - \tilde{Z}_L^{n+1} \right) \vec{\mu}_{\sigma_{L_r}^1} + \left(\tilde{Z}_{\sigma_{L_r}^2}^{n+1} - \tilde{Z}_L^{n+1} \right) \vec{\mu}_{\sigma_{L_r}^2} \right] \cdot \vec{n}_\sigma = 0, \\
& D_K b_s(Z_h^{\delta t})_{\sigma_{K_r}^{Id}}^{up} \left[\left(\tilde{u}_{\sigma_{K_r}^1}^{n+1} - \tilde{u}_K^{n+1} \right) \vec{\mu}_{\sigma_{K_r}^1} + \left(\tilde{u}_{\sigma_{K_r}^2}^{n+1} - \tilde{u}_K^{n+1} \right) \vec{\mu}_{\sigma_{K_r}^2} \right] \cdot \vec{n}_\sigma \\
& + D_L b_s(Z_h^{\delta t})_{\sigma_{L_r}^{Id}}^{up} \left[\left(\tilde{u}_{\sigma_{L_r}^1}^{n+1} - \tilde{u}_L^{n+1} \right) \vec{\mu}_{\sigma_{L_r}^1} + \left(\tilde{u}_{\sigma_{L_r}^2}^{n+1} - \tilde{u}_L^{n+1} \right) \vec{\mu}_{\sigma_{L_r}^2} \right] \cdot \vec{n}_\sigma = 0.
\end{aligned}$$

The initial conditions are given by

$$\tilde{u}_K^0 = \frac{1}{|K|} \int_K u_0(x) dx, \quad \text{and} \quad \tilde{Z}_K^0 = \frac{1}{|K|} \int_K Z_0(x) dx.$$

This system of equations is linear and has a unique solution since the associated matrix is symmetric and diagonally dominant. Therefore, the function \mathcal{G} is well defined in E . Moreover, the functions φ and b_s are continuous and the diffusion tensor D is symmetric bounded and uniformly elliptic, we obtain that \mathcal{G} is a continuous mapping in E .

Now, by construction, for any $\alpha \in [0, 1]$, the problem $(\mathbf{U}, \mathbf{Z}) = \alpha \mathcal{G}(\mathbf{U}, \mathbf{Z})$ has exactly the same solutions as the numerical scheme (5.3.19)–(5.3.25) with $\alpha\varphi$, αu_0 and αZ_0 instead of φ , u_0 and Z_0 . Moreover, for any $\alpha \in [0, 1]$, we have, $\|\alpha u_0\| \leq \|u_0\|$, $\|\alpha Z_0\| \leq \|Z_0\|$, and λ is also a Lipschitz constant for $\alpha\varphi$. Then the same a priori estimate in Proposition 5.5.1 is also satisfied for any $\alpha \in [0, 1]$ and for any solution of $(\mathbf{U}, \mathbf{Z}) = \alpha \mathcal{G}(\mathbf{U}, \mathbf{Z})$.

Finally, we have verified all the assumptions of the Leray Schauder theorem [20, 33, 73]. The function \mathcal{G} has then a fixed point and the numerical scheme (5.3.19)–(5.3.25) admits at least a solution. Proposition 5.5.2 is proved. \square

5.5.3 Space and time translates estimates

In this subsection, we derive compactness tools corresponding to space and time translate estimates for the approximate solutions, which allow the application of Kolmogorov's theorem [19, 42]. We start with the definition of the discrete gradient in Ω as introduced in [20]:

$$\nabla^{\mathcal{D}} u_h^{\delta t} = \sum_{K \in \mathcal{T}_h} \sum_{r=i,j,k} \nabla_{K_r} u_h^{\delta t}.$$

The discrete semi-norm in the space $\mathbf{L}^2(0, T; \mathbf{H}^1(\Omega))$ is defined by

$$\|u_h^{\delta t}\|_{1,h,\delta t} = \left(\sum_{n=0}^{N-1} \delta t \sum_{K \in \mathcal{T}_h} \sum_{r=i,j,k} |K_r| \left((u_{\sigma_{K_r}^1}^{n+1} - u_K^{n+1})^2 |\vec{\mu}_{\sigma_{K_r}^1}|^2 + (u_{\sigma_{K_r}^2}^{n+1} - u_K^{n+1})^2 |\vec{\mu}_{\sigma_{K_r}^2}|^2 \right) \right)^{\frac{1}{2}}.$$

Now we present the following lemma about space translations.

Lemma 5.5.1. *Under our standing assumptions, we extend $u_h^{\delta t}$ by 0 outside of $[0, T] \times \Omega$. Then, there exists a constant C independent of the discretization parameters such that the following inequality holds*

$$\int_0^T \int_{\mathbb{R}^2} \left[\varphi(u_h^{\delta t}(t, x + \eta)) - \varphi(u_h^{\delta t}(t, x)) \right]^2 dx dt \leq 2|\eta| (|\eta| + Ch) \|\varphi(u_h^{\delta t})\|_{1,h,\delta t}^2,$$

for any $\eta \in \mathbb{R}^2$. $|\eta|$ is the Euclidean norm of \mathbb{R}^2 .

Proof. The proof can be done by arguments similar to those from Lemma 4.3 in [20], therefore it is omitted here. \square

The estimate for the time translation is given by the following lemma.

Lemma 5.5.2. *Under our standing assumptions, for every $s \in \mathbb{R}^+$, the following uniform in s holds true:*

$$\int_0^{T-s} \int_{\Omega} \left[\varphi(u_h^{\delta t}(t+s, x)) - \varphi(u_h^{\delta t}(t, x)) \right]^2 dx dt \leq Cs \quad (5.5.6)$$

where C is a constant independent of the discretization parameters and s .

Proof. Let $s \in]0, T[$. Since φ is a non-decreasing, Lipschitz function with λ its Lipschitz constant, the following inequality holds

$$\int_0^{T-s} \int_{\Omega} \left[\varphi(u_h^{\delta t}(t+s, x)) - \varphi(u_h^{\delta t}(t, x)) \right]^2 dx dt \leq \lambda \int_0^{T-s} A(t) dt,$$

with

$$A(t) = \int_{\Omega} \left(\varphi(u_h^{\delta t}(t+s, x)) - \varphi(u_h^{\delta t}(t, x)) \right) \left(u_h^{\delta t}(t+s, x) - u_h^{\delta t}(t, x) \right) dx, \quad \forall t \in]0, T-s[.$$

Let $n_0(t) \in \{0, \dots, N-1\}$ such that $t_{n_0(t)} \leq t \leq t_{n_0(t)} + 1$ and $n_1(t) \in \{0, \dots, N-1\}$ such that $t_{n_1(t)} \leq t + s \leq t_{n_1(t)} + 1$. The following equality yields

$$A(t) = \sum_{K \in \mathcal{T}_h} \left(\varphi \left(u_K^{n_1(t)} \right) - \varphi \left(u_K^{n_0(t)} \right) \right) \times \sum_{n=0}^{N-1} \chi_n(t, t+s) \left(u_K^{n+1} - u_K^n \right) |K|,$$

where

$$\chi_n(t, t+s) = \begin{cases} 1, & \text{if } t_{n+1} \text{ belongs to } [t, t+s], \\ 0, & \text{otherwise.} \end{cases}$$

Using the definition of the FV scheme (5.3.19)-(5.3.25) and changing the order of the summations between n and K , one gets

$$\begin{aligned} A(t) &= \delta t \sum_{n=0}^{N-1} \chi_n(t, t+s) \sum_{K \in \mathcal{T}_h} \left[\varphi \left(u_K^{n_1(t)} \right) - \varphi \left(u_K^{n_0(t)} \right) \right] \\ &\quad \times \sum_{r=i,j,k} \sum_{Id=1,2} |\sigma_{K_r}^{Id}| \frac{D_K}{\phi_K} \left[\nabla_{K_r} \varphi \left(u_h^{\delta t} \right) + \nabla_{K_r} \varphi \left(u_h^{\delta t} \right) + \delta \phi_K \nabla_{K_r} u_h^{\delta t} \right] \cdot \vec{n}_{\sigma_{K_r}^{Id}}. \end{aligned}$$

This can be written as follows

$$A(t) = A_1(n_1(t)) - A_1(n_0(t)) + A_2(n_1(t)) - A_2(n_0(t)) + A_3(n_1(t)) - A_3(n_0(t)).$$

Let $\rho = n_1(t)$ or $\rho = n_0(t)$. One has

$$\begin{aligned} A_1(\rho) &= \delta t \sum_{n=0}^{N-1} \chi_n(t, t+s) \sum_{K \in \mathcal{T}_h} \frac{D_K}{\phi_K} \sum_{r=i,j,k} \sum_{Id=1,2} |\sigma_{K_r}^{Id}| \left[\nabla_{K_r} \varphi \left(u_h^{\delta t} \right) \cdot \vec{n}_{\sigma_{K_r}^{Id}} \right] \varphi \left(u_K^\rho \right), \\ A_2(\rho) &= \delta t \sum_{n=0}^{N-1} \chi_n(t, t+s) \sum_{K \in \mathcal{T}_h} \frac{D_K}{\phi_K} \sum_{r=i,j,k} \sum_{Id=1,2} |\sigma_{K_r}^{Id}| \left[\nabla_{K_r} \varphi \left(Z_h^{\delta t} \right) \cdot \vec{n}_{\sigma_{K_r}^{Id}} \right] \varphi \left(u_K^\rho \right), \\ A_3(\rho) &= \delta t \sum_{n=0}^{N-1} \chi_n(t, t+s) \sum_{K \in \mathcal{T}_h} \delta D_K \sum_{r=i,j,k} \sum_{Id=1,2} |\sigma_{K_r}^{Id}| \left[\nabla_{K_r} u_K^{n+1} \cdot \vec{n}_{\sigma_{K_r}^{Id}} \right] \varphi \left(u_K^\rho \right). \end{aligned}$$

In order to obtain an estimate for $A_1(\rho)$, we use the local conservation property of the discrete sub-fluxes on the half-edges. We multiply equation (5.3.21) by $-|\sigma_{K_r}^{Id}| \varphi(u_{\sigma_{K_r}^{Id}}^\rho)$. Adding the obtained results to $A_1(\rho)$, we get

$$\begin{aligned} A_1(\rho) &= \delta t \sum_{n=0}^{N-1} \chi_n(t, t+s) \sum_{K \in \mathcal{T}_h} \frac{D_K}{\phi_K} \sum_{r=i,j,k} |K_r| \\ &\quad \times \left[\left(\varphi \left(u_{\sigma_{K_r}^1}^\rho \right) - \varphi \left(u_K^\rho \right) \right) \left(\varphi \left(u_{\sigma_{K_r}^{n+1}} \right) - \varphi \left(u_K^{n+1} \right) \right) |\vec{\mu}_{\sigma_{K_r}^1}|^2 \right. \\ &\quad + \left(\varphi \left(u_{\sigma_{K_r}^2}^\rho \right) - \varphi \left(u_K^\rho \right) \right) \left(\varphi \left(u_{\sigma_{K_r}^{n+1}} \right) - \varphi \left(u_K^{n+1} \right) \right) |\vec{\mu}_{\sigma_{K_r}^2}|^2 \\ &\quad + \left(\varphi \left(u_{\sigma_{K_r}^1}^\rho \right) - \varphi \left(u_K^\rho \right) \right) \left(\varphi \left(u_{\sigma_{K_r}^{n+1}} \right) - \varphi \left(u_K^{n+1} \right) \right) \vec{\mu}_{\sigma_{K_r}^1} \cdot \vec{\mu}_{\sigma_{K_r}^2} \\ &\quad \left. + \left(\varphi \left(u_{\sigma_{K_r}^2}^\rho \right) - \varphi \left(u_K^\rho \right) \right) \left(\varphi \left(u_{\sigma_{K_r}^{n+1}} \right) - \varphi \left(u_K^{n+1} \right) \right) \vec{\mu}_{\sigma_{K_r}^1} \cdot \vec{\mu}_{\sigma_{K_r}^2} \right]. \end{aligned}$$

Then using the inequality, $ab \leq 1/2(a^2 + b^2)$ for any $a, b \in \mathbb{R}$, leads to

$$\begin{aligned} A_1(\rho) &\leq \frac{D^+}{\phi^-} \sum_{n=0}^{N-1} \delta t \chi_n(t, t+s) \times \sum_{K \in \mathcal{T}_h} \sum_{r=i,j,k} |K_r| \\ &\quad \times \sum_{Id=1,2} \left[\left(\varphi(u_{\sigma_{K_r}^{Id}}^\rho) - \varphi(u_K^\rho) \right)^2 |\vec{\mu}_{\sigma_{K_r}^{Id}}|^2 + \left(\varphi(u_{\sigma_{K_r}^{Id}}^{n+1}) - \varphi(u_K^{n+1}) \right)^2 |\vec{\mu}_{\sigma_{K_r}^{Id}}|^2 \right]. \end{aligned}$$

We proceed in the same way to compute A_2 and A_3 , on has

$$\begin{aligned} A_2(\rho) &\leq \frac{D^+}{\phi^-} \sum_{n=0}^{N-1} \delta t \chi_n(t, t+s) \sum_{K \in \mathcal{T}_h} \sum_{r=i,j,k} |K_r| \\ &\quad \times \sum_{Id=1,2} \left(\varphi(u_{\sigma_{K_r}^{Id}}^\rho) - \varphi(u_K^\rho) \right)^2 |\vec{\mu}_{\sigma_{K_r}^{Id}}|^2 + \left(\varphi(Z_{\sigma_{K_r}^{Id}}^{n+1}) - \varphi(Z_K^{n+1}) \right)^2 |\vec{\mu}_{\sigma_{K_r}^{Id}}|^2, \end{aligned}$$

and

$$\begin{aligned} A_3(\rho) &\leq D^+ \delta \sum_{n=0}^{N-1} \delta t \chi_n(t, t+s) \sum_{K \in \mathcal{T}_h} \sum_{r=i,j,k} |K_r| \\ &\quad \times \sum_{Id=1,2} \left(\varphi(u_{\sigma_{K_r}^{Id}}^\rho) - \varphi(u_K^\rho) \right)^2 |\vec{\mu}_{\sigma_{K_r}^{Id}}|^2 + \left(u_{\sigma_{K_r}^{Id}}^{n+1} - u_K^{n+1} \right)^2 |\vec{\mu}_{\sigma_{K_r}^{Id}}|^2. \end{aligned}$$

For the third term A_3 , φ being a strictly non-decreasing Lipschitz function, there exists $\xi_{Id} \in \mathbb{R}$ for $Id = 1, 2$ such that $\left| \varphi(u_{\sigma_{K_r}^{Id}}^{n+1}) - \varphi(u_K^{n+1}) \right| = \varphi'(\xi_{Id}) \left| u_{\sigma_{K_r}^{Id}}^{n+1} - u_K^{n+1} \right|$. We denote by $\mathcal{C} = \min\{\varphi'(\xi_1), \varphi'(\xi_2)\}$, then we have

$$\begin{aligned} A_3(\rho) &\leq \delta t D^+ \delta \sum_{n=0}^{N-1} \chi_n(t, t+s) \sum_{K \in \mathcal{T}_h} \sum_{r=i,j,k} |K_r| \\ &\quad \times \sum_{Id=1,2} \left(\varphi(u_{\sigma_{K_r}^{Id}}^\rho) - \varphi(u_K^\rho) \right)^2 |\vec{\mu}_{\sigma_{K_r}^{Id}}|^2 + \mathcal{C} \left(\varphi(u_{\sigma_{K_r}^{Id}}^{n+1}) - \varphi(u_K^{n+1}) \right)^2 |\vec{\mu}_{\sigma_{K_r}^{Id}}|^2. \end{aligned}$$

To facilitate the computations, we rewrite the above inequality as follows

$$A(t) \leq \frac{D^+}{\phi^-} \left[(2 + \delta \phi^-)(E_0 + E_1) + (1 + \mathcal{C})E_2 + E_3 \right],$$

with

$$\begin{aligned} E_0 &= \delta t \sum_{n=0}^{N-1} \chi_n(t, t+s) \sum_{K \in \mathcal{T}_h} \sum_{r=i,j,k} \sum_{Id=1,2} |K_r| \left| \varphi(u_{\sigma_{K_r}^{Id}}^{n_0(t)}) - \varphi(u_K^{n_0(t)}) \right|^2 |\vec{\mu}_{\sigma_{K_r}^{Id}}|^2, \\ E_1 &= \delta t \sum_{n=0}^{N-1} \chi_n(t, t+s) \sum_{K \in \mathcal{T}_h} \sum_{r=i,j,k} \sum_{Id=1,2} |K_r| \left| \varphi(u_{\sigma_{K_r}^{Id}}^{n_1(t)}) - \varphi(u_K^{n_1(t)}) \right|^2 |\vec{\mu}_{\sigma_{K_r}^{Id}}|^2, \\ E_2 &= \delta t \sum_{n=0}^{N-1} \chi_n(t, t+s) \sum_{K \in \mathcal{T}_h} \sum_{r=i,j,k} \sum_{Id=1,2} |K_r| \left| \varphi(u_{\sigma_{K_r}^{Id}}^{n+1}) - \varphi(u_K^{n+1}) \right|^2 |\vec{\mu}_{\sigma_{K_r}^{Id}}|^2, \end{aligned}$$

$$E_3 = \delta t \sum_{n=0}^{N-1} \chi_n(t, t+s) \sum_{K \in \mathcal{T}_h} \sum_{r=i,j,k} \sum_{Id=1,2} |K_r| \left| \varphi \left(Z_{\sigma_{K_r}^{Id}}^{n+1} \right) - \varphi \left(Z_K^{n+1} \right) \right|^2 |\vec{\mu}_{\sigma_{K_r}^{Id}}|^2.$$

We have $t \in]0, T-s[$, $n_0(t) \in \{0, \dots, N-1\}$, $m = n_0(t)$ if and only if $t \in [t_m, t_{m+1}]$.
As a consequence

$$\begin{aligned} & \int_0^{T-s} E_0 dt \\ & \leq \sum_{m=0}^{N-1} \int_{t_m}^{t_{m+1}} \delta t \left(\sum_{n=0}^{N-1} \chi_n(t, t+s) \sum_{K \in \mathcal{T}_h} \sum_{r=i,j,k} \sum_{Id=1,2} |K_r| \left| \varphi \left(u_{\sigma_{K_r}^{Id}}^m \right) - \varphi \left(u_K^m \right) \right|^2 |\vec{\mu}_{\sigma_{K_r}^{Id}}|^2 \right) dt, \\ & \leq \sum_{m=0}^{N-1} \delta t \int_{t_m}^{t_{m+1}} \left(\sum_{n=0}^{N-1} \chi_n(t, t+s) \right) dt \sum_{K \in \mathcal{T}_h} \sum_{r=i,j,k} \sum_{Id=1,2} |K_r| \left| \varphi \left(u_{\sigma_{K_r}^{Id}}^m \right) - \varphi \left(u_K^m \right) \right|^2 |\vec{\mu}_{\sigma_{K_r}^{Id}}|^2. \end{aligned}$$

Since

$$\sum_{m=0}^{N-1} \int_{t_m}^{t_{m+1}} \sum_{n=0}^{N-1} \chi_n(t, t+s) dt \leq s,$$

the following inequalities hold

$$\int_0^{T-s} E_0 dt \leq s \|\varphi(u_h^{\delta t})\|_{1, \mathcal{T}_h, \delta t}^2 \quad \text{and} \quad \int_0^{T-s} E_1 dt \leq s \|\varphi(u_h^{\delta t})\|_{1, \mathcal{T}_h, \delta t}^2.$$

In the same way from $\int_0^{T-s} \chi_n(t, t+s) dt \leq s$, we obtain

$$\int_0^{T-s} E_2 dt \leq s \|\varphi(u_h^{\delta t})\|_{1, \mathcal{T}_h, \delta t}^2, \quad \text{and} \quad \int_0^{T-s} E_3 dt \leq s \|\varphi(u_h^{\delta t})\|_{1, \mathcal{T}_h, \delta t}^2.$$

Adding the previous inequalities and using Proposition 5.5.1 lead to the desired result

$$\int_0^{T-s} \int_{\Omega} \left[\varphi(u_h^{\delta t}(t+s, x)) - \varphi(u_h^{\delta t}(t, x)) \right]^2 dx dt \leq Cs,$$

where C is a constant independent of the discretization parameters and s . This completes the proof of Lemma 5.5.2. \square

5.6 Convergence results

In this section, we present some convergence results based on the estimates established in the last sections and Kolmogorov's theorem and we show that the limit of a sub-sequence of the approximate solution (5.3.19)–(5.3.25) tends to a weak solution of the continuous problem, as discretization parameters go to zero.

Theorem 5.6.1. *Let assumptions (A.1)–(A.3) be fulfilled. Let $(\mathcal{T}_{h_m})_{m \in \mathbb{N}^*}$, be a sequence of an admissible triangulation of Ω , h_m being the size of the mesh \mathcal{T}_{h_m} and δt_m is the time step size. Let $(u_{h_m}^{\delta t_m}, Z_{h_m}^{\delta t_m})$ be a sequence of discrete solutions to the FV scheme (5.3.19)–(5.3.25). Then, we can extract a sub-sequence which converges in an adequate sense to a weak solution (u, Z) , when h_m and δt_m tends to zero as $m \rightarrow \infty$, and satisfying the following results:*

1. Convergence results

$$\begin{aligned}
\varphi\left(u_{h_m}^{\delta t_m}\right) &\rightarrow \varphi(u) \text{ strongly in } \mathbf{L}^2(0, T; \Omega), & u_{h_m}^{\delta t_m} &\rightarrow u \quad \text{a.e. in } \Omega_T, \\
\varphi\left(Z_{h_m}^{\delta t_m}\right) &\rightarrow \varphi(Z) \text{ strongly in } \mathbf{L}^2(0, T; \Omega), & Z_{h_m}^{\delta t_m} &\rightarrow Z \quad \text{a.e. in } \Omega_T, \\
\nabla^{\mathcal{D}}\varphi\left(u_{h_m}^{\delta t_m}\right) &\rightharpoonup \nabla\varphi(u) \text{ weakly in } \left(\mathbf{L}^2(0, T; \Omega)\right)^2, \\
\nabla^{\mathcal{D}}\varphi\left(Z_{h_m}^{\delta t_m}\right) &\rightharpoonup \nabla\varphi(Z) \text{ weakly in } \left(\mathbf{L}^2(0, T; \Omega)\right)^2.
\end{aligned}$$

2. The limit (u, Z) is a weak solution to the continuous problem (P) in the following sens

$$\begin{aligned}
&\int_0^T \int_{\Omega} \phi \frac{\partial \psi}{\partial t} u \, dx \, dt - \int_0^T \int_{\Omega} D\left(\nabla\varphi(u) + \nabla\varphi(Z) + \delta\phi\nabla u\right) \cdot \nabla\psi \, dx \, dt + \int_{\Omega} u_0(x)\psi(0, x) \, dx = 0, \\
&\int_0^T \int_{\Omega} \phi \frac{\partial \zeta}{\partial t} Z \, dx \, dt - \int_0^T \int_{\Omega} D\left(b_s(Z)\nabla u + \nabla\varphi(Z) + \delta\phi\nabla Z\right) \cdot \nabla\zeta \, dx \, dt + \int_{\Omega} Z_0(x)\zeta(0, x) \, dx = 0, \\
&\forall(\psi, \zeta) \in \left(C_0^\infty(0, T; \Omega)\right)^2.
\end{aligned}$$

Proof of Theorem 5.6.1

Step 1. Convergence results. From the space and time translations Lemmas 5.5.1 and 5.5.2 and due to Kolmogorov's theorem, the sequence $\varphi\left(u_{h_m}^{\delta t_m}\right)_{m \in \mathbb{N}^*}$ is relatively compact in $\mathbf{L}^2(0, T; \Omega)$. Therefore, there exists a sub-sequence, still denoted by $\varphi\left(u_{h_m}^{\delta t_m}\right)_{m \in \mathbb{N}^*}$, which converges strongly to $\underline{\varphi}$ in $\mathbf{L}^2(0, T; \Omega)$, as $m \rightarrow \infty$. The function φ being a strictly non-decreasing, so there is a continuous reciprocal function φ^{-1} such that

$$u_{h_m}^{\delta t_m} \rightarrow \varphi^{-1}(\underline{\varphi}) \quad \text{a.e. in } \Omega_T.$$

Thanks to the L^∞ bound given in Proposition 5.4.1, we deduce from Lebesgue's dominated convergence theorem that $u_{h_m}^{\delta t_m} \rightarrow u = \varphi^{-1}(\underline{\varphi})$ strongly in $\mathbf{L}^2(0, T; \Omega)$ as $h_m, \delta t_m \rightarrow 0$.

We follow the same method as done for $\varphi\left(u_{h_m}^{\delta t_m}\right)$. We can prove the space and time translation estimates for $\varphi\left(Z_{h_m}^{\delta t_m}\right)$. Then, we apply the same arguments to obtain the compactness of $\varphi\left(Z_{h_m}^{\delta t_m}\right)$ using Kolmogorov's theorem. This yields to the existence of a sub-sequence, still denoted by $\varphi\left(Z_{h_m}^{\delta t_m}\right)$, which converges, as $m \rightarrow \infty$, strongly in $\mathbf{L}^2(0, T; \Omega)$. Using again Lebesgue's dominated convergence theorem, we deduce that $Z_{h_m}^{\delta t_m} \rightarrow Z$ strongly in $\mathbf{L}^2(0, T; \Omega)$ as $h_m, \delta t_m \rightarrow 0$ when $m \rightarrow \infty$.

Now, we demonstrate a weak convergence of the discrete gradient. Proposition 5.5.1 gives an estimate of the discrete gradient in the space $\left(\mathbf{L}^2(0, T; \Omega)\right)^2$, one has

$$\sum_{n=0}^{N_m-1} \delta t_m \|\nabla^{\mathcal{D}}\varphi\left(u_{h_m}^{\delta t_m}\right)\|_2^2 + \sum_{n=0}^{N_m-1} \delta t_m \|\nabla^{\mathcal{D}}\varphi\left(Z_{h_m}^{\delta t_m}\right)\|_2^2 \leq C.$$

From this estimate, one can deduce that $\nabla^{\mathcal{D}}\varphi\left(u_{h_m}^{\delta t_m}\right)$ (resp. $\nabla^{\mathcal{D}}\varphi\left(Z_{h_m}^{\delta t_m}\right)$) is bounded uniformly in $(\mathbf{L}^2(0, T; \Omega))^2$. Then, there exists a sub-sequence such that $\nabla^{\mathcal{D}}\varphi\left(u_{h_m}^{\delta t_m}\right) \rightharpoonup \zeta_1$ and $\nabla^{\mathcal{D}}\varphi\left(Z_{h_m}^{\delta t_m}\right) \rightharpoonup \zeta_2$ weakly in $(\mathbf{L}^2(0, T; \Omega))^2$ as $m \rightarrow \infty$. Using the strong convergence of $\varphi\left(u_{h_m}^{\delta t_m}\right)$ and the weak convergence of the discrete gradient $\nabla^{\mathcal{D}}\varphi\left(u_{h_m}^{\delta t_m}\right)$, we obtain by passing to the limit

$$\int_0^T \int_{\Omega} \nabla^{\mathcal{D}}\varphi\left(u_{h_m}^{\delta t_m}\right) \cdot V + \varphi\left(u_{h_m}^{\delta t_m}\right) \cdot \operatorname{div}V \, dx dt \rightarrow \int_0^T \int_{\Omega} \zeta_1 \cdot V + \varphi(u) \cdot \operatorname{div}V \, dx dt,$$

as $m \rightarrow \infty$ for any $V \in (\mathcal{C}_0^\infty(\bar{\Omega} \times (0, T)))^2$. This prove by the way that $\nabla\varphi(u) = \zeta_1$ (resp. $\nabla\varphi(Z) = \zeta_2$) in the sense of distribution and $\varphi(u), \varphi(Z) \in \mathbf{L}^2(0, T; \mathbf{H}^1(\Omega))$. \square

Step 2. Passage to the limit. Let $\psi \in \mathcal{A}_T = \{\psi \in \mathcal{C}_0^\infty(0, T; \Omega) \mid \nabla\psi \cdot \vec{n} = 0 \text{ on } \partial\Omega_T \text{ and } \psi(\cdot, T) = 0\}$. We denote $\psi_K^{n+1} = \psi(x_K, t^{n+1})$ and $\psi_{\sigma_{K_r}^{Id}}^{n+1} = \psi(x_{\sigma_{K_r}^{Id}}, t_{n+1})$ for $Id = 1, 2$. We multiply equation (5.3.19) by ψ_K^{n+1} and equations (5.3.21)-(5.3.22) and (5.3.23) by $|\sigma_{K_r}^{Id}| \psi_{\sigma_{K_r}^{Id}}^{n+1}$ for $Id=1, 2$. Adding the equalities and summing on $n = 0, \dots, N_m - 1$ and over $K \in \mathcal{T}_{h_m}$. That yields to

$$T_{1m} + T_{2m} + T_{3m} + T_{4m} = 0,$$

with

$$\begin{aligned} T_{1m} &= \sum_{n=0}^{N_m-1} \sum_{K \in \mathcal{T}_{h_m}} |K| \phi_K (u_K^{n+1} - u_K^n) \psi_K^{n+1}, \\ T_{2m} &= \sum_{n=0}^{N_m-1} \delta t_m \sum_{K \in \mathcal{T}_{h_m}} \sum_{r=i,j,k} |K_r| D_K \nabla_{K_r} \varphi\left(u_{h_m}^{\delta t_m}\right) \cdot \nabla_{K_r} \psi_{h_m}^{\delta t_m}, \\ T_{3m} &= \sum_{n=0}^{N_m-1} \delta t_m \sum_{K \in \mathcal{T}_{h_m}} \sum_{r=i,j,k} |K_r| D_K \nabla_{K_r} \varphi\left(Z_{h_m}^{\delta t_m}\right) \cdot \nabla_{K_r} \psi_{h_m}^{\delta t_m}, \\ T_{4m} &= \sum_{n=0}^{N_m-1} \delta t_m \sum_{K \in \mathcal{T}_{h_m}} \sum_{r=i,j,k} |K_r| \delta \phi_K D_K \nabla_{K_r} u_{h_m}^{\delta t_m} \cdot \nabla_{K_r} \psi_{h_m}^{\delta t_m}. \end{aligned}$$

We rearrange the summation of T_{1m} and by using $\psi_K^{N_m} = \psi(x_K, T) = 0$, we get

$$\begin{aligned} T_{1m} &= - \sum_{n=0}^{N_m-1} \sum_{K \in \mathcal{T}_{h_m}} |K| \phi_K u_K^{n+1} (\psi_K^{n+1} - \psi_K^n) + \sum_{K \in \mathcal{T}_{h_m}} |K| \phi_K \left(u_K^{N_m} \psi_K^{N_m} - u_K^0 \psi_K^0 \right), \\ &= - \sum_{n=0}^{N_m-1} \sum_{K \in \mathcal{T}_{h_m}} \int_{t_n}^{t_{n+1}} \int_K u_K^{n+1} \frac{\partial \psi(x_K, t)}{\partial t} \, dx dt - \sum_{K \in \mathcal{T}_{h_m}} |K| \phi_K u_K^0 \psi_K^0. \end{aligned}$$

Now, by the strong convergence of $\psi(x_K, 0)_{K \in \mathcal{T}_{h_m}}$, one has

$$\lim_{m \rightarrow \infty} \sum_{K \in \mathcal{T}_{h_m}} |K| \phi_K u_K^0 \psi_K^0 = \int_{\Omega} \phi(x) u_0(x) \psi(x, 0) \, dx.$$

By the regularity of the function ψ , the $\partial_t \psi(x_K, \cdot)_{K \in \mathcal{T}_{h_m}}$ converges uniformly towards $\partial_t \psi(x, \cdot)$. We deduce from Lebesgue's dominated convergence theorem that

$$\lim_{m \rightarrow \infty} T_{1m} = - \int_{\Omega} \phi(x) u_0(x) \psi(x, 0) dx - \int_0^T \int_{\Omega} \phi(x) u(t, x) \partial_t \psi(t, x) dx dt.$$

We next prove the following limit

$$\lim_{m \rightarrow \infty} T_{2m} = \int_0^T \int_{\Omega} D \nabla \varphi(u) \cdot \nabla \psi dx dt$$

Using the definition of the discrete gradient on Ω , we get

$$T_{2m} = \int_0^T \int_{\Omega} D_K \nabla^{\mathcal{D}} \varphi(u_{h_m}^{\delta t_m}) \cdot \nabla^{\mathcal{D}} \psi_{h_m}^{\delta t_m} dx dt.$$

Following the above, the discrete gradient $\nabla^{\mathcal{D}} \varphi(u_{h_m}^{\delta t_m})$ converges weakly towards $\nabla \varphi(u)$ in $(\mathbf{L}^2(0, T; \Omega))^2$. Due to the regularity property of the function ψ , $\nabla^{\mathcal{D}} \psi_{h_m}^{\delta t_m}$ converges uniformly to $\nabla \psi$. Under the assumption (A.1), we deduce by passing to the limit that

$$\lim_{m \rightarrow \infty} T_{2m} = \int_0^T \int_{\Omega} D \nabla \varphi(u) \cdot \nabla \psi dx dt.$$

In the same way, we obtain the following limits

$$\lim_{m \rightarrow \infty} T_{2m} = \int_0^T \int_{\Omega} D \nabla \varphi(Z) \cdot \nabla \psi dx dt \quad \text{and} \quad \lim_{m \rightarrow \infty} T_{3m} = \int_0^T \int_{\Omega} \delta \phi D \nabla u \cdot \nabla \psi dx dt.$$

For the saltwater equation, we follow the same steps as previously. For any $\zeta \in \mathcal{A}_T$, we multiply equation (5.3.20) by $\zeta_K^{n+1} = \zeta(x_K, t^{n+1})$ and equations (5.3.25), (5.3.22) and (5.3.24) by $|\sigma_{K_r}^{I_d}| \zeta_{\sigma_{K_r}^{I_d}}^{n+1}$. Adding the equalities and summing over $K \in \mathcal{T}_{h_m}$ and over $n = 0, \dots, N_m - 1$, we obtain

$$E_{1m} + E_{2m} + E_{3m} + E_{4m} = 0,$$

with

$$\begin{aligned} E_{1m} &= \sum_{n=0}^{N_m-1} \sum_{K \in \mathcal{T}} |K| \phi_K (Z_K^{n+1} - Z_K^n) \zeta_K^{n+1}, \\ E_{2m} &= \sum_{n=0}^{N_m-1} \delta t_m \sum_{K \in \mathcal{T}_{h_m}} \sum_{r=i,j,k} |K_r| D_K \nabla_{K_r} b_s(Z_{h_m}^{\delta t_m})_{\sigma_{K_r}^{I_d}}^{up} \nabla_{K_r} u_{h_m}^{\delta t_m} \cdot \nabla_{K_r} \zeta_{h_m}^{\delta t_m}, \\ E_{3m} &= \sum_{n=0}^{N_m-1} \delta t_m \sum_{K \in \mathcal{T}_{h_m}} \sum_{r=i,j,k} |K_r| D_K \nabla_{K_r} \varphi(Z_{h_m}^{\delta t_m}) \cdot \nabla_{K_r} \zeta_{h_m}^{\delta t_m}, \\ E_{4m} &= \sum_{n=0}^{N_m-1} \delta t_m \sum_{K \in \mathcal{T}_{h_m}} \sum_{r=i,j,k} |K_r| \delta \phi_K D_K \nabla_{K_r} Z_{h_m}^{\delta t_m} \cdot \nabla_{K_r} \zeta_{h_m}^{\delta t_m}. \end{aligned}$$

As done previously, we have the following limits

$$\lim_{m \rightarrow \infty} E_{1m} = - \int_{\Omega} \phi(x) Z_0(x) \zeta(x, 0) dx - \int_0^T \int_{\Omega} \phi(x) Z(t, x) \frac{\partial \zeta(t, x)}{\partial t} dx dt,$$

$$\lim_{m \rightarrow \infty} E_{3m} = \int_0^T \int_{\Omega} D \nabla \varphi(Z) \cdot \nabla \psi \, dx \, dt \quad \text{and} \quad \lim_{m \rightarrow \infty} E_{4m} = \int_0^T \int_{\Omega} \delta \phi D \nabla u \cdot \nabla \psi \, dx \, dt.$$

We next determinate the limit of E_{2m} , To do so, we consider the residual function R_{2m} defined by

$$\begin{aligned} R_{2m} &= \int_0^T \int_{\Omega} D b_s(Z_{h_m}^{\delta t_m}) \nabla^{\mathcal{D}} u_{h_m}^{\delta t_m} \cdot \nabla^{\mathcal{D}} \zeta_{\mathcal{T}_{h_m}}^{\delta t_m} \, dx \, dt - \int_0^T \int_{\Omega} D b_s(Z) \nabla u \cdot \nabla \zeta \, dx \, dt, \\ &= R_{21_m} + R_{22_m}, \end{aligned}$$

with

$$\begin{aligned} R_{21_m} &= \int_0^T \int_{\Omega} D \left[b_s(Z_{h_m}^{\delta t_m}) \nabla^{\mathcal{D}} u_{h_m}^{\delta t_m} \cdot \nabla^{\mathcal{D}} \zeta_{\mathcal{T}_{h_m}}^{\delta t_m} - b_s(Z) \nabla^{\mathcal{D}} u_{h_m}^{\delta t_m} \cdot \nabla^{\mathcal{D}} \zeta_{\mathcal{T}_{h_m}, \delta t_m} \right] \, dx \, dt, \\ R_{22_m} &= \int_0^T \int_{\Omega} b_s(Z) D \left[\nabla^{\mathcal{D}} u_{h_m}^{\delta t_m} \cdot \nabla^{\mathcal{D}} \zeta_{\mathcal{T}_{h_m}}^{\delta t_m} - \nabla u \cdot \nabla \zeta \right] \, dx \, dt. \end{aligned}$$

The goal here is to show that R_{2m} tends to zero when passing to the limit. Due to the strong convergence of $Z_{h_m}^{\delta t_m}$ towards Z and the continuity of the function b_s , one has $b_s(Z_{h_m}^{\delta t_m}) \rightarrow b_s(Z)$ as $m \rightarrow \infty$. By using the regularity of the test function ζ and the compactness criterion of $\nabla^{\mathcal{D}} u_{h_m}^{\delta t_m}$, we deduce that

$$R_{21_m} \rightarrow 0, \text{ as } m \rightarrow \infty.$$

By the compactness estimate of the discrete gradient and the weak convergence of $\nabla^{\mathcal{D}} u_{h_m}^{\delta t_m} \rightharpoonup \nabla u$ when $m \rightarrow \infty$, we obtain

$$R_{22_m} \rightarrow 0, \text{ as } m \rightarrow \infty.$$

Consequently,

$$\lim_{m \rightarrow \infty} \int_0^T \int_{\Omega} D b_s(Z_{h_m}^{\delta t_m}) \nabla^{\mathcal{D}} u_{h_m}^{\delta t_m} \cdot \nabla^{\mathcal{D}} \zeta_{\mathcal{T}_{h_m}}^{\delta t_m} \, dx \, dt = \int_0^T \int_{\Omega} D b_s(Z) \nabla u \cdot \nabla \zeta \, dx \, dt,$$

which completes the proof of Theorem 5.6.1. □

5.7 Numerical results

In this section, we present the numerical results for two test cases modeling different scenarios of the sharp-diffuse interfaces model for seawater intrusion. The first test case is a simulation in a homogeneous domain, while the second one is in a heterogenous free surface aquifer where two intersecting fractures are considered.

All our developments have been implemented in DuMu^X. It provides many tools to solve numerically PDEs and allowing, among other things, the management of mesh, discretization or linear and nonlinear solvers. The code is an object-oriented software written in C++ and has massively parallel computation capability. The modular concept of DuMu^X makes it easy to integrate new modules adapted to our numerical schemes.

In this context, we have developed and implemented in DuMu^X a new module, named $2p - SWI$, which allows to solve the coupled system (5.3.19)–(5.3.25). The

primary variables are the depth of the saltwater/freshwater interface Z and the hydraulic head of freshwater u . The spatial discretization employs a TPFA or MPFA finite volume method. The time discretization is done by an implicit Euler scheme. The nonlinear system is solved by the Newton method and a BiConjugate Gradient STABILized (BiCGSTAB) method preconditioned by an Algebraic Multigrid (AMG) solver, is used to solve the linear systems. This solver is integrated in the ISTL-Library of DUNE. Dynamic time stepping is used when integrating the equations involved. Time step sizes during transient simulations are dynamically recalculated depending on the convergence behavior of the nonlinear procedure (Newton method). The simulations start with a certain time step which can be increased or reduced, depending on the number of iterations allowed in each nonlinear iteration. Let us mention that throughout all numerical experiments, we observed that in no instance more than a maximum of 10 iterations was needed for the convergence of Newton's method. Consequently, for this study the adopted strategy for the management of the time step is sufficient. Therefore, there is no need to use other types of local time-stepping strategies proposed in the literature.

All computations were performed on a Del PC with Intel Core(R) CPU E3-1505M Processor (3.00 GHz) and 8 GB RAM. One of the objectives of this paper is to deliver computational performance also suitable for limited computational resources. Let us mention that in view of the CPU times required for the examples treated in this paper, all the simulations were performed sequentially. However, the new module developed can be used on multicore/multinode systems. The parallelization in DuMu^X is carried out using the DUNE parallel library package based on MPI providing high parallel efficiency and allowing simulations with several tens of millions of degrees of freedom to be carried out, ideal for large-scale field applications. DuMu^X has the ability to run on anything from single processor systems to highly parallel supercomputers with specialized hardware architectures.

Our approach has been validated by solving several tests, including numerical convergence of the schemes [?]. The numerical results are satisfactory and replicated to those in the literature. The results of these simulations are omitted since nothing startling was found. Instead, we concentrate on the results obtained in two test cases. Finally a remarkable property of the scheme is that the discrete maximum principle (nonnegativity of the thickness of fresh and salt water in the aquifer) is satisfied which is crucial to obtain physically meaningful approximate solutions. This has been verified in all our simulations.

5.7.1 Studied domain and physical data

We consider two test cases by adapting the geometry and data of an example proposed in [25] dealing with the evolution of transition zones under significant solicitations. The example considers a 10 m thick free surface aquifer which the horizontal surface is represented by $\Omega =]-50 \text{ m}, 50 \text{ m}[\times]-20 \text{ m}, 20 \text{ m}[$. Homogeneous Neumann boundary conditions are imposed on the boundaries to allow the interfaces evolve freely. For the initial conditions, a fixed hydraulic head of freshwater $u = -1 \text{ m}$ is imposed and a vertical interface separates the freshwater and saltwater zones.

The example presented above serves to visualize the numerical behavior of the transition zone considering two situations. In the first situation, the aquifer is supposed to be homogeneous, whereas it is taken to be heterogeneous in the second situation. In both situations, two pumping wells, with different flow rates, are also involved. The freshwater extraction rate in the pumping wells is assumed to be constant per day: $Q_f = Q_1 \chi_{]-30, 31[\times]-10, -9.5[} + Q_2 \chi_{]30, 31.5[\times]12, 12.5[}$, where χ is the characteristic function of a subdomain. The properties and parameters of the aquifer are summarized in Table 5.1.

| Parameters | γ [] | δ [m] | ϕ [] | Q_1 [m^3/day] | Q_2 [m^3/day] |
|------------|--------------|--------------|------------|---------------------|---------------------|
| Values | 0.025 | 0.1 | 0.3 | 3 | 20 |

Table 5.1: Parameters and properties of the aquifer.

When dealing with the homogeneous case, the horizontal surface is discretized by a structured mesh with the orthogonality condition being satisfied. The numerical scheme is established using a TPFA method. In the heterogeneous case, the current problem is coupled with a fracture possessing a high conductivity. The domain in this case is discretized using an unstructured triangulation mesh. To deal numerically with such a system, we use the MPFA method. The impact of heterogeneity on the displacement of transition zones is illustrated by numerical investigations. In the following, we present the obtained numerical simulations of each case.

We performed the simulations with an initial time step of 10 seconds and a maximum time step of 1 hour. The tolerances for the Newton method and the BICGSTAB method are respectively 10^{-8} and 10^{-6} . In this case, Newton's method converges rapidly in less than 4 iterations.

5.7.2 Test case 1: homogeneous aquifer

In this case, we focus on the evolution of the transition zones in an homogeneous free aquifer subjected to over-exploitation. The hydraulic conductivity in this case is equal to $D = 4.5 \cdot 10^{-4}$ m/s. Figure 5.2 shows the structured mesh of 21164 cells used in the numerical simulations. To visualize the extent and advancement of

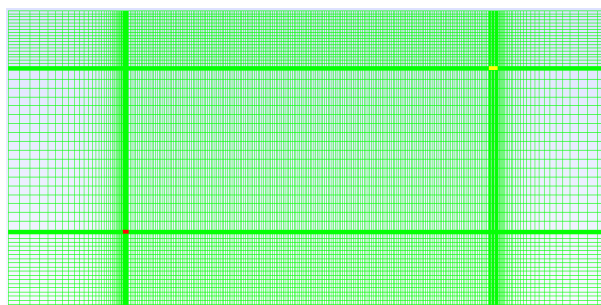


Figure 5.2: Structured mesh of a homogeneous aquifer (21164 cells).

the saltwater intrusion as a function of the location, vertical cross-section through the two pumping wells are performed. Figure 5.3 shows the position of the freshwater/saltwater transition zone at the vertical cross-section 1 through the two pumping

wells, in the free aquifer subjected to pumping during 3 and 10 *days*. Figure 5.4

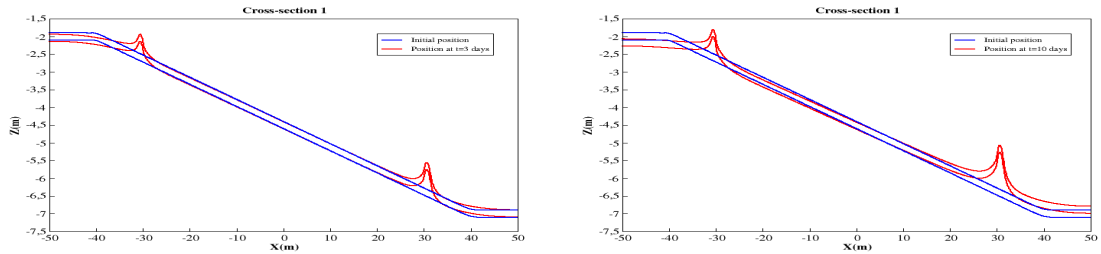


Figure 5.3: Displacement of the freshwater/saltwater transition zone at vertical cross-section through pumping wells in the homogeneous case after 3 *days* (left) and 10 *days* (right).

shows the velocity field in the aquifer after 10 days of over exploitation. It can be seen that the flow velocity is the highest at the pumping wells position and that the freshwater flows upward. The evolution of the freshwater/saltwater interface

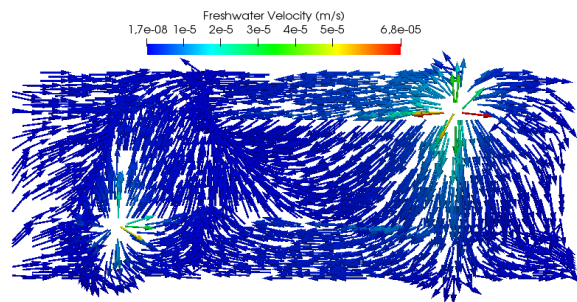


Figure 5.4: Freshwater flow velocity in the homogeneous case after 10 *days*.

is shown in Figure 5.5. It can be observed that "upconings" create beneath the pumping wells and grow up quickly. A local depression, located at the main zone of pumping, is also developed. The presence of the freshwater/saltwater transition zone and the saturated/unsaturated zone promotes diffusion and advancement of the free surface and salt front as it can be seen in Figure 5.6.

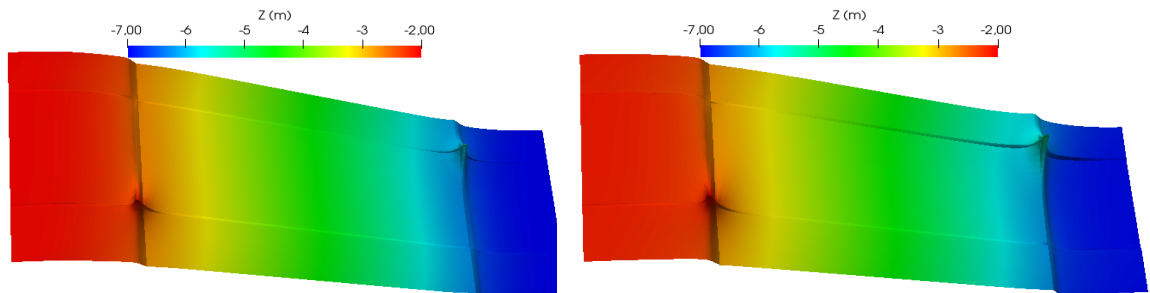


Figure 5.5: Displacement of the freshwater/saltwater interface 2D plot in the homogeneous case after 3 *days* (left) and 10 *days* (right).

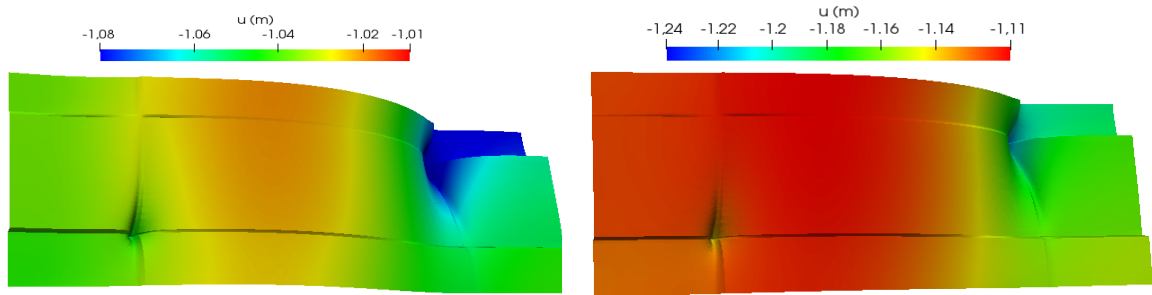


Figure 5.6: Evolution of the freshwater head 2D plot in the homogeneous case after 3 days (left) and 10 days (right).

5.7.3 Test case 2: fractured aquifer

In this case, the impact of heterogeneity on the transition zone is examined. The aquifer described previously is no more homogeneous but crossed by a network of two fractures. The main one is situated in the middle of the aquifer in the length direction, whereas the second one is inclined and located at the right part of the aquifer. The hydraulic conductivity is equal to $D = 4.5 \cdot 10^{-1} m/s$ in the fracture (blue region) and $D = 4.5 \cdot 10^{-4} m/s$ elsewhere. The corresponding mesh (Figure 5.7) is obtained by an unstructured triangulation of 20651 cells and 10418 vertices used in the numerical simulations.

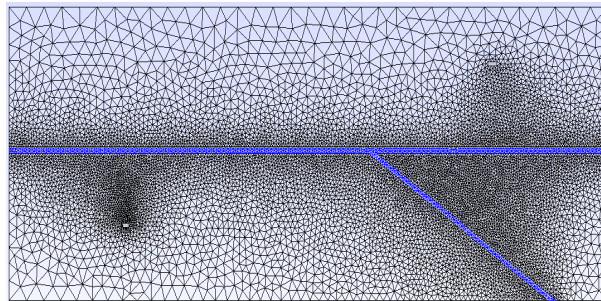


Figure 5.7: Unstructured mesh in the heterogeneous case with two intersecting fractures (20651 cells).

To monitor the location and the extent of the transition zone, three vertical cross-sections are chosen. The first one passes through the two wells (cross-section 1), the second, instead, is lying along the main fracture ($y=0$, cross-section 2) and the third one is lying in the direction of the inclined fracture (cross-section 3). Figure 5.8 shows different behaviors of the transition zone. It can be seen, with respect to the first vertical cross-section, significant vertical progress of the interface and development of two upconings underneath the pumping wells, one of which is exacerbated corresponding to the high flow rate. The second vertical cross-section shows the high mobility of that the transition zone due the high hydraulic conductivity of the fracture. The interface and the transition zone move further and rotate quickly. The third vertical cross-section illustrates the impact of the fracture on the displacement of the interface and the transition zone. One can notice, particularly, on the right-hand side of the domain the high mobility of the

interface and the transition zone with respect to the high hydraulic conductivity of the fracture. There is always a meaningful movement of the salt bevel over the days to achieve its maximum value after 10 *days* of over-exploitation. The existence of the fracture and the transition zones favor the diffusion and advancement of the salt bevel. An advancement of the transition zone due to the greatest amount

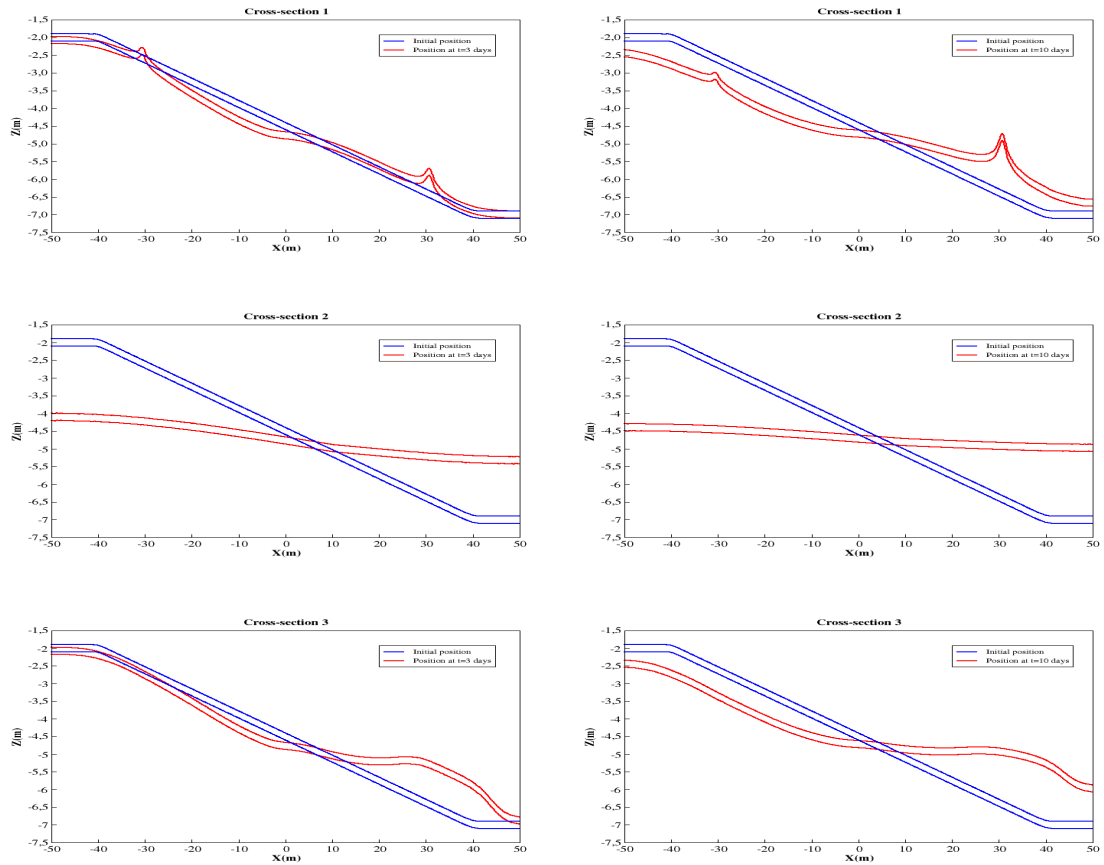


Figure 5.8: Displacement of the freshwater/saltwater transition zone for different sections in the heterogeneous case after 3 *days* (left) and 10 *days* (right).

constitutes a threat for the quality of freshwater extrude in the pumping wells. The existence of the fracture accelerate the freshwater and saltwater flows and contributes to the advancement of the transition zone (Figures 5.9–5.11). After 10 days of over-exploitation, the salt bevel converges to the equilibrium state.

The obtained results are satisfactory and the numerical computations for the coupled system have demonstrated that this approach yields physically realistic flow fields in highly heterogeneous medium.

5.8 Conclusion

In this chapter, we have studied the convergence of an MPFA finite volume method for a sharp-diffuse interfaces model in an heterogeneous free aquifer. A fully implicit, fully coupled finite volume method has been developed to discretize the governing

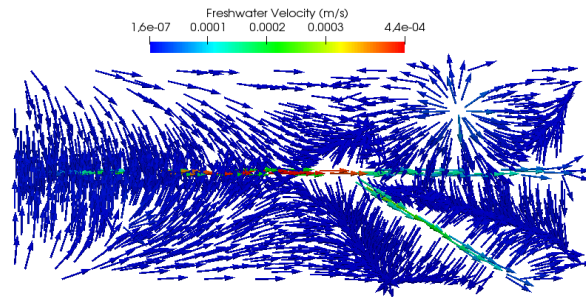


Figure 5.9: Freshwater flow velocity in the heterogeneous case after 10 *days*.

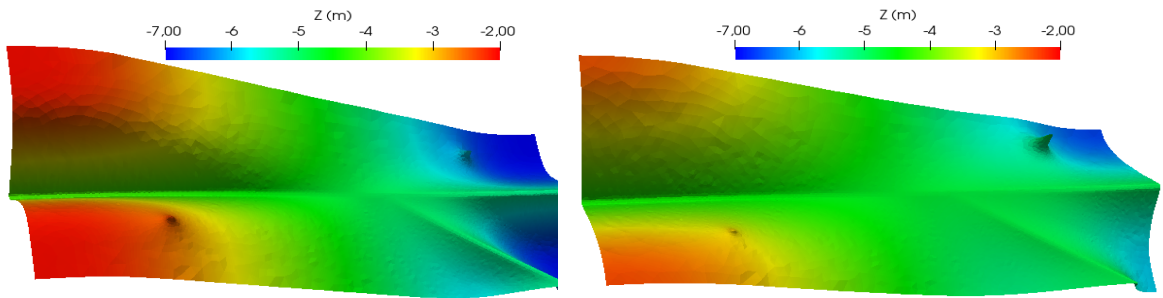


Figure 5.10: Displacement of the freshwater/saltwater interface 2D plot in the heterogeneous case after 3 *days* (left) and 10 *days* (right).

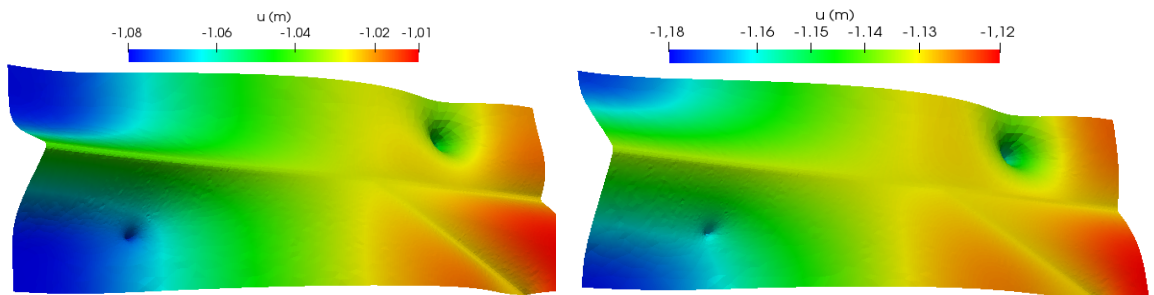


Figure 5.11: Evolution of the freshwater head 2D plot in the heterogeneous case after 3 *days* (left) and 10 *days* (right).

equations. This approach deals well with the anisotropy and heterogeneity of the soil and provides accurate and efficient approximations on an unstructured mesh. The construction of the numerical scheme is established by integrating the governing equations on each control volume and evaluating the fluxes on each half edge. To linearise the coupled system at each time step, we employ a Newton's method wherein each iteration a linear system is solved by an iterative Krylov method.

After that, we have shown that the numerical scheme preserves the positivity of the freshwater and the saltwater thicknesses. Moreover, we have proved an existence result to the nonlinear fully implicit numerical scheme using a fixed point theorem. The strong convergence of the approximate solution to the weak solution of the continuous problem is established via some recent compactness tools corresponding to the space and time translate estimates. In addition, we have proved the weak convergence of the discrete gradients of the freshwater head and salt front elevation.

We have developed and implemented this scheme in the [DuMu^X](#) framework. To ensure the validity of our method, we have studied the numerical convergence of the scheme. To do so, we have considered two test cases. The first test case is a simulation in a homogeneous domain, while the second one is in a heterogenous free surface aquifer where two intersecting fractures are considered. The obtained results proved that our new module based on recent numerical tools is accurate, efficient and able to solve a 2D seawater intrusion model tacking into account the dynamics of the transition zones.

Chapter 6

Conclusion and perspectives

In this chapter, we summarize the main contributions and achievements made in this work in the context of simulating seawater intrusion in coastal aquifers. We have presented accurate and efficient algorithms to solve a seawater intrusion problem using different approaches. A brief presentation of the state of the art of existing approaches is proposed. First of all, we have presented the derivation of the mathematical model using the sharp interface model in a free and confined aquifer. To numerically deal with such a system, we have considered a fully coupled, fully implicit finite volume TPF method on a triangulation mesh where the orthogonality condition is satisfied. The nonlinear system is linearized using Newton's method, in which a linear system is solved at each iteration using iterative Krylov solvers, provided by the external DUNE library. To predict the extent of salt front elevation and water table level in large-scale aquifers, we have integrated the numerical scheme in the framework DuMu^X. The implemented module is based on recent and efficient numerical tools allowing accurate predictions. Different 1D, 2D test cases are used for the validations of our module, including real tests. The obtained results correspond well to those presented in [8, 67, 71]. The numerical module is then applied to the Souss Chtouka plain and the Tripoli aquifer. Numerical solutions based on available hydrogeological data proved the ability of our methodology to predict the progress and the extent of the salt-wedge for several years of over-exploitation of the nappe.

The sharp interface approach assumes that the two fluids are separated by an abrupt interface. This encouraged us to adopt a mixed sharp-diffuse interfaces approach, introduced recently in [24] that takes into account the dynamics of transition zones. In this context, we have developed a fully implicit, fully coupled finite volume method for the numerical resolution of such system. One again, the numerical scheme is implemented in the DuMu^X framework. The developed module is validated on test cases dealing with the progression of the salt front coupled with sea fluctuations. After that, we have compared the numerical result of the 2D model with those obtained with the classical 3D model for miscible displacements. The numerical results are satisfactory and showed good agreement with those presented in [23].

At the real scale, the aquifer is heterogeneous and anisotropic, which is why it is necessary to use a more suitable numerical method on unstructured meshes. In

this work, we have therefore developed a fully coupled, fully implicit MPFA finite volume method for the numerical approximation of the sharp-diffuse model. The numerical analysis of this scheme is presented. We have proved the nonnegativity of the approximate freshwater and saltwater thicknesses. After that, an existence result of the discrete solutions is established by proving a fixed point to the non-linear system. In order to satisfy the assumptions of Kolmogorov's theorem for the convergence of the approximate solution, we proved some compactness tools corresponding to space and time translate estimates. Afterwards, we have presented the theorem of the strong convergence of the discrete solutions. Passing to the limit, we have demonstrate that the approximate solution is a weak solution to the continuous problem. The MPFA numerical scheme is implemented and integrated in the [DuMu^X](#) framework. Let us mention here that all our development and improvement are done in versions 2.12 and 3.0. Our new module is tested and validated in a strongly heterogeneous free aquifer.

We note finally that we encountered difficulties to find reliable and well documented heterogeneous and anisotropic benchmarks. In many articles, some data are missing. We think that a well documented benchmark for a seawater intrusion problem in heterogeneous and anisotropic aquifers would be very useful for the community. Further work on these important issues is in progress.

Bibliography

- [1] DuMu^X DUNE for multi- $\{$ Phase, Component, Scale, Physics, ... $\}$ flow and Transport in Porous Media. Available online: <http://www.dumux.org> (accessed on 1 June 2021).
- [2] DUNE, the Distributed and Unified Numerics Environment. Available online: <https://www.dune-project.org> (accessed on 1 June 2021).
- [3] I. Aavatsmark. An introduction to multipoint flux approximations for quadrilateral grids. *Computational Geosciences*, 6:405–432, 2002.
- [4] A. Abdelkrim, B. Amaziane, M. E. Ossmani, and K. Talali. A fully implicit finite volume scheme for a seawater intrusion problem in coastal aquifers. *Water*, 12(6):1639, 2020.
- [5] N. Abouelmahassine. *Modélisation Préliminaire du Biseau salé par Éléments Finis dans la Zone Côtière de Souss–Chtouka*. Master’s Thesis, Ecole Mohammadia d’Ingénieurs, Rabat, Morocco, 2002.
- [6] A. Abudawia. *Analyse numérique d’une approximation élément fini pour un modèle d’intrusion saline dans les aquifères côtiers*. PhD thesis, Université du Littoral Côte d’Opale, France, 2015.
- [7] A. Abudawia, A. Mourad, J. H. Rodrigues, and C. Rosier. A finite element method for a seawater intrusion problem in unconfined aquifers. *Applied Numerical Mathematics*, 127:349–369, 2018.
- [8] A. Abudawia and C. Rosier. Numerical analysis for a seawater intrusion problem in a confined aquifer. *Mathematics and Computers in Simulation*, 118:2–16, 2015.
- [9] A. Aharmouch and B. Amaziane. Development and evaluation of a numerical model for steady state interface and/or free surface groundwater flow. *Journal of hydrology*, 434:110–120, 2012.
- [10] S. M. Allen, M. Samuel, and J. W. Cahn. A microscopic theory for antiphase boundary motion and its application to antiphase domain coarsening. *Acta metallurgica*, 27:1085–1095, 1979.
- [11] R. Babu, N. Park, S. Yoon, and T. Kula. Sharp interface approach for regional and well scale modeling of small island freshwater lens: Tongatapu island. *Water*, 10:1636, 2018.

- [12] S. Badaruddin, A. D. Werner, and L. K. Morgan. Water table salinization due to seawater intrusion. *Water Resources Research*, 51:8397–8408, 2015.
- [13] J. Bear. *Dynamics of fluids in porous media*. American Elsevier, 1972.
- [14] J. Bear and A. H. D. Cheng. *Modelling Groundwater Flow and Contaminant Transport*. Springer: Dordrecht, The Netherlands, 2000.
- [15] J. Bear, A. H. D. Cheng, S. Sorek, D. Ouazar, and I. Herrera. *Seawater Intrusion in Coastal Aquifers, Concepts, Methods and Practices*. Kluwer Academic Publishers: Dordrecht, The Netherlands, 1999.
- [16] J. Bear and A. Verruijt. *Modelling Groundwater Flow and Pollution*. D. Reidel Publishing Company: Dordrecht, The Netherlands, 1987.
- [17] B. Bouzouf and Z. Chen. A comparison of finite volume method and sharp model for two dimensional saltwater intrusion modeling. *Canadian Journal of Civil Engineering*, 41:191–196, 2014.
- [18] B. Bouzouf, D. Ouazar, M. Himi, A. Casas, I. Elmahi, and F. Benkhaldoun. Integrating hydrogeochemical and geophysical data for testing a finite volume based numerical model for saltwater intrusion. *Transport in porous media*, 43:179–194, 2001.
- [19] H. Brezis. *Functional analysis, Sobolev spaces and partial differential equations*. Springer Science & Business Media, 2010.
- [20] X. Cao, S. F. Nemaadjieu, and I. S. Pop. Convergence of an mpfa finite volume scheme for a two-phase porous media flow model with dynamic capillarity. *IMA Journal of Numerical Analysis*, 39:512–544, 2019.
- [21] A. Cheng. *Multilayered Aquifer Systems. In Fundamentals and Applications*. CRC Press Published: New York, NY, USA, 2000.
- [22] A. Cheng and D. Ouazar. *Coastal Aquifer Management-Monitoring, Modeling, and Case Studies*. CRC Press: New York, NY, USA; Washington, DC, USA, 2003.
- [23] L. Cherfils, C. Choquet, and M. M. Diédhiou. Numerical validation of an upscaled sharp–diffuse interface model for stratified miscible flows. *Mathematics and Computers in Simulation*, 137:246–265, 2017.
- [24] C. Choquet, M. M. Diédhiou, and C. Rosier. Mathematical analysis of a sharp–diffuse interfaces model for seawater intrusion. *Journal of Differential Equations*, 259:3803–3824, 2015.
- [25] C. Choquet, M. M. Diédhiou, and C. Rosier. Derivation of a sharp–diffuse interfaces model for seawater intrusion in a free aquifer. numerical simulations. *SIAM Journal on Applied Mathematics*, 76:138–158, 2016.
- [26] C. Choquet, M. M. Diédhiou, and C. Rosier. Mathematical analysis of a seawater intrusion model including storativity. *SIAM Journal on Mathematical Analysis*, 49:29–63, 2017.

- [27] C. Choquet, C. Rosier, and L. Rosier. Well posedness of general cross-diffusion systems. *Journal of Differential Equations*, 300:386–425, 2021.
- [28] J. Chun, C. Lim, D. Kim, and J. Kimn. Assessing impacts of climate change and sea-level rise on seawater intrusion in a coastal aquifer. *Water*, 10:357, 2018.
- [29] M. Cobaner, R. Yurtal, A. Dogan, and L. H. Motz. Three dimensional simulation of seawater intrusion in coastal aquifers: A case study in the goksu deltaic plain. *Journal of hydrology*, 464:262–280, 2012.
- [30] J. Cooper and H. Hilton. A hypothesis concerning the dynamic balance of fresh water and salt water in a coastal aquifer. *Journal of Geophysical Research*, 64(4):461–467, 1959.
- [31] G. Dagan and J. Bear. Solving the problem of local interface upcoming in a coastal aquifer by the method of small perturbations. *J. Hydrol*, 6:15–44, 1968.
- [32] G. Dagan and D. G. Zeitoun. Seawater-freshwater interface in a stratified aquifer of random permeability distribution. *Journal of Contaminant Hydrology*, 29:185–203, 1998.
- [33] K. Deimling. *Nonlinear functional analysis*. Courier Corporation, 2010.
- [34] M. M. Diédhiou. *Approche mixte interface nette/diffuse pour les problèmes d'intrusion saline en sous-sol: Modélisation, analyse mathématique et illustrations numériques*. PhD thesis, Université de La Rochelle, France, 2015.
- [35] H. Diersch and O. Kolditz. Variable-density flow and transport in porous media: approaches and challenges. *Advances in water resources*, 25:899–944, 2002.
- [36] H. J. G. Diersch. *FEFLOW: Finite Element Modeling of Flow, Mass and Heat Transport in Porous and Fractured Media*. Springer: Berlin/Heidelberg, Germany, 2014.
- [37] J. Droniou. Finite volume schemes for diffusion equations: Introduction to and review of modern methods. *Math. Models Methods Appl. Sci.*, 24(08):1575–1619, 2014.
- [38] J. J. Dupuit. *Traité théorique et pratique de la conduite et de la distribution des eaux*, volume 1. Carilian-Goëury, 1854.
- [39] H. I. Essaid. A comparison of the coupled fresh water-salt water flow and the ghyben-herzberg sharp interface approaches to modeling of transient behavior in coastal aquifer systems. *Journal of Hydrology*, 86:169–193, 1986.
- [40] H. I. Essaid. A multilayered sharp interface model of coupled freshwater and saltwater flow in coastal systems: model development and application. *Water Resources Research*, 26:1431–1454, 1990.
- [41] R. Eymard, T. Gallouët, and R. Herbin. Convergence of finite volume schemes for semilinear convection diffusion equations. *Numerische Mathematik*, 82:91–116, 1999.

-
- [42] R. Eymard, T. Gallouët, and R. Herbin. Finite volume methods. *Handbook of numerical analysis*, 7:713–1018, 2000.
- [43] M. Fahs, B. Koohbor, B. Belfort, B. Ataie-Ashtiani, C. Simmons, A. Younes, and P. Ackerer. A generalized semi-analytical solution for the dispersive Henry problem: effect of stratification and anisotropy on seawater intrusion. *Water*, 10:230, 2018.
- [44] M. Fahs, A. Younes, and T. A. Mara. A new benchmark semi-analytical solution for density-driven flow in porous media. *Advances in water resources*, 70:24–35, 2014.
- [45] J. G. Ferris. Cyclic fluctuations of water level as a basis for determining aquifer transmissibility. Technical report, US Geological Survey, 1952.
- [46] A. Gemitzi and D. Tolikas. Hydra model: Simulation of salt intrusion in coastal aquifers using visual basic and gis. *Environmental Modelling & Software*, 22:924–936, 2007.
- [47] R. E. Glover. The pattern of fresh-water flow in a coastal aquifer. *Journal of Geophysical Research*, 64:457–459, 1959.
- [48] R. R. Goswami and T. P. Clement. Laboratory-scale investigation of saltwater intrusion dynamics. *Water Resources Research*, 43, 2007.
- [49] W. Guo and C. D. Langevin. User’s guide to SEAWAT; a computer program for simulation of three-dimensional variable-density ground-water flow. Technical report, 2002.
- [50] M. Hamidi, S. Reza, and S. Yazdi. Numerical modeling of seawater intrusion in coastal aquifer using finite volume unstructured mesh method. *WSEAS Transactions on Mathematics*, 5:648, 2006.
- [51] M. Hamidi and S. R. Sabbagh-Yazdi. Modeling of 2D density-dependent flow and transport in porous media using finite volume method. *Computers & Fluids*, 37:1047–1055, 2008.
- [52] H. R. Henry. Effects of dispersion on salt encroachment in coastal aquifers, in ” seawater in coastal aquifers”. *US Geological Survey, Water Supply Paper*, 1613:C70–C80, 1964.
- [53] G. J. Houben, L. Stoeckl, K. E. Mariner, and A. S. Choudhury. The influence of heterogeneity on coastal groundwater flow-physical and numerical modeling of fringing reefs, dykes and structured conductivity fields. *Advances in water resources*, 113:155–166, 2018.
- [54] M. S. Hussain, A. A. Javadi, and M. M. Sherif. Three dimensional simulation of seawater intrusion in a regional coastal aquifer in UAE. *Procedia Engineering*, 119:1153–1160, 2015.
- [55] P. S. Huyakorn, Y. S. Wu, and N. S. Park. Multiphase approach to the numerical solution of a sharp interface saltwater intrusion problem. *Water Resources Research*, 32:93–102, 1996.

- [56] O. Kalaoun. *Modélisation de l'intrusion saline dans l'aquifère de Tripoli-Liban: impact des changements globaux*. PhD thesis, Université de Toulouse III-Paul Sabatier, France, 2015.
- [57] O. Kalaoun, A. A. Bitar, J. P. Gastellu-Etchegorry, and M. Jazar. Impact of demographic growth on seawater intrusion: Case of the Tripoli aquifer, Lebanon. *Water*, 8:104, 2016.
- [58] O. Kalaoun, M. Jazar, and A. A. Bitar. Assessing the contribution of demographic growth, climate change, and the refugee crisis on seawater intrusion in the Tripoli aquifer. *Water*, 10:973, 2018.
- [59] N. Karahanoglu and V. Doyuran. Finite element simulation of seawater intrusion into a quarry-site coastal aquifer, Kocaeli-Darica, Turkey. *Environmental Geology*, 44:456–466, 2003.
- [60] H. Ketabchi, D. Mahmoodzadeh, B. Ataie-Ashtiani, and C. T. Simmons. Sea-level rise impacts on seawater intrusion in coastal aquifers: Review and integration. *Journal of Hydrology*, 535:235–255, 2016.
- [61] H. G. Keulegan. *An example report on model laws for density current*. US National Bureau of Standards, Gaithersburg, Md, 1954.
- [62] B. Koohbor, M. Fahs, B. Ataie-Ashtiani, C. T. Simmons, and A. Younes. Semianalytical solutions for contaminant transport under variable velocity field in a coastal aquifer. *Journal of hydrology*, 560:434–450, 2018.
- [63] G. Kopsiaftis, V. Christelis, and A. Mantoglou. Pumping optimization in coastal aquifers: comparison of sharp interface and density dependent models. *European Water*, 57:443–449, 2017.
- [64] H. J. Lin, D. R. Recharads, C. A. Talbot, G. T. Yeh, J. R. Cheng, H. P. Cheng, and N. L. Jones. A three-dimensional finite-element computer model for simulating density-dependent flow and transport in variable saturated media: version 3.1. *US Army Engineering Research and Development Center, Vicksburg, MS*, 1997.
- [65] F. Liu, V. V. Anh, I. Turner, K. Bajracharya, W. J. Huxley, and N. Su. A finite volume simulation model for saturated–unsaturated flow and application to Gooburrum, Bundaberg, Queensland, Australia. *Applied mathematical modelling*, 30:352–366, 2006.
- [66] C. Llopis-Albert and D. Pulido-Velazquez. Discussion about the validity of sharp-interface models to deal with seawater intrusion in coastal aquifers. *Hydrological Processes*, 28:3642–3654, 2014.
- [67] P. Marion, K. Najib, and C. Rosier. Numerical simulations for a seawater intrusion problem in a free aquifer. *Applied Numerical Mathematics*, 75:48–60, 2014.
- [68] G. M. McDonald and A. W. Harbaugh. *A modular three-dimensional finite-difference ground-water flow model*, volume 6. US Geological Survey Reston, VA, 1988.

- [69] S. S. Mehdizadeh, S. E. Karamalipour, and R. Asoodeh. Sea level rise effect on seawater intrusion into layered coastal aquifers (simulation using dispersive and sharp-interface approaches). *Ocean & coastal management*, 138:11–18, 2017.
- [70] S. S. Mehdizadeh, F. Vafaie, and H. Abolghasemi. Assessment of sharp-interface approach for saltwater intrusion prediction in an unconfined coastal aquifer exposed to pumping. *Environmental earth sciences*, 73:8345–8355, 2015.
- [71] S. S. Mehdizadeh, A. D. Werner, F. Vafaie, and S. Badaruddin. Vertical leakage in sharp-interface seawater intrusion models of layered coastal aquifers. *Journal of hydrology*, 519:1097–1107, 2014.
- [72] J. Mercer, S. Larson, and C. Faust. Simulation of salt-water interface motion. *Groundwater*, 18:374–385, 1980.
- [73] A. Michel. A finite volume scheme for two-phase immiscible flow in porous media. *SIAM Journal on Numerical Analysis*, 41:1301–1317, 2003.
- [74] A. Mourad. *Identification de la conductivité hydraulique pour un problème d'intrusion saline: Comparaison entre l'approche déterministe et l'approche stochastique*. PhD thesis, Université du Littoral Côte d'Opale, France, 2017.
- [75] A. A. H. Oulhaj. *Conception et analyse de schémas non-linéaires pour la résolution de problèmes paraboliques: application aux écoulements en milieu poreux*. PhD thesis, Université de Lille 1, France, 2017.
- [76] A. A. H. Oulhaj. Numerical analysis of a finite volume scheme for a seawater intrusion model with cross-diffusion in an unconfined aquifer. *Numerical Methods for Partial Differential Equations*, 34:857–880, 2018.
- [77] T. J. Povich, C. N. Dawson, M. W. Farthing, and C. E. Kees. Finite element methods for variable density flow and solute transport. *Computational Geosciences*, 17:529–549, 2013.
- [78] P. Ranjan, S. Kazama, and M. Sawamoto. Numerical modelling of saltwater-freshwater interaction in the Walawe river basin, Sri Lanka. *IAHS-AISH publication*, pages 306–314, 2007.
- [79] A. Ranjbar and N. Mahjouri. Development of an efficient surrogate model based on aquifer dimensions to prevent seawater intrusion in anisotropic coastal aquifers, case study: the Qom aquifer in Iran. *Environmental earth sciences*, 77:418, 2018.
- [80] S. A. Sakr. Validity of a sharp-interface model in a confined coastal aquifer. *Hydrogeology Journal*, 7:155–160, 1999.
- [81] W. E. Sanford and L. F. Konikow. A two-constituent solute-transport model for ground water having variable density. *United States Geological Survey Water Resources Internal Report*, 85:4279, 1985.
- [82] M. L. Sebben, A. D. Werner, and T. Graf. Seawater intrusion in fractured coastal aquifers: A preliminary numerical investigation using a fractured Henry problem. *Advances in water resources*, 85:93–108, 2015.

- [83] U. Shamir and G. Dagan. Motion of the seawater interface in coastal aquifers: a numerical solution. *Water Resources Research*, 7:644–657, 1971.
- [84] L. Shi, L. Cui, N. Park, and P. S. Huyakorn. Applicability of a sharp-interface model for estimating steady-state salinity at pumping wells—validation against sand tank experiments. *Journal of contaminant hydrology*, 124:35–42, 2011.
- [85] M. Siena and M. Riva. Groundwater withdrawal in randomly heterogeneous coastal aquifers. *Hydrology and Earth System Sciences*, 22:2971–2985, 2018.
- [86] O. D. L. Strack. A single-potential solution for regional interface problems in coastal aquifers. *Water Resources Research*, 12:1165–1174, 1976.
- [87] F. Vafaie and S. S. Mehdizadeh. Investigation of sea level rise effect on salt-water intrusion in an unconfined coastal aquifer using sharp-interface approach. *International Journal of Global Warming*, 8:501–515, 2015.
- [88] V. N. Vappicha and S. H. Nagaraja. An approximate solution for the transient interface in a coastal aquifer. *Journal of Hydrology*, 31:161–173, 1976.
- [89] C. I. Voss. A finite-element simulation model for saturated-unsaturated, fluid-density-dependent ground-water flow with energy transport or chemically-reactive single-species solute transport. *Water Resources Investigation Report*, 84:4369, 1984.
- [90] A. D. Werner. Correction factor to account for dispersion in sharp-interface models of terrestrial freshwater lenses and active seawater intrusion. *Advances in water resources*, 102:45–52, 2017.
- [91] A. D. Werner. On the classification of seawater intrusion. *Journal of hydrology*, 551:619–631, 2017.
- [92] A. D. Werner, M. Bakker, V. E. A. Post, A. Vandenbohede, and D. Barry. Seawater intrusion processes, investigation and management: recent advances and future challenges. *Advances in Water Resources*, 51:3–26, 2013.
- [93] A. Younes and M. Fahs. A semi-analytical solution for the reactive Henry saltwater intrusion problem. *Water, Air, & Soil Pollution*, 224:1779, 2013.
- [94] A. Younes and M. Fahs. Extension of the Henry semi-analytical solution for saltwater intrusion in stratified domains. *Computational Geosciences*, 19:1207–1217, 2015.
- [95] A. Zidane. *Risk of subsidence and aquifer contamination due to evaporite dissolution: Modelization of flow and mass transport in porous and free flow domains*. PhD thesis, University of Basel, Switzerland, 2013.